Observations of High Mass Star Formation Using BLAST and Herschel

by

Sarah Harry

A thesis submitted to

Cardiff University

for the degree of

Doctor of Philosophy

July 2011

DECLARATION

- DECLARATION:
  This work has not previously been accepted in substance for any degree and is not concurrently submitted in candidature for any degree.

  Signed: ..... (candidate) Date: .....

- STATEMENT 1:
  This thesis is being submitted in partial fulfillment of the requirements for the degree of Doctor of Philosophy (PhD).

  Signed: ..... (candidate) Date: .....

- STATEMENT 2:
  This thesis is the result of my own independent work/investigation, except where otherwise stated. Other sources are acknowledged by explicit references.

  Signed: ..... (candidate) Date: .....

- STATEMENT 3
  I hereby give consent for my thesis, if accepted, to be available for photocopying and for inter-library loan, and for the title and summary to be made available to outside organisations.

  Signed: ..... (candidate) Date: .....

SUMMARY OF THESIS

In this thesis, I present BLAST observations of the Carina Nebula and *Herschel* observations of NGC 7538. I use the source extracting routine CSAR to identify 172 source in Carina and 94 sources in NGC 7538. I fit SEDs to all the sources and calculate their mass, luminosity, temperature and radius. For the Carina Nebula I find a mass range of $20-10^4\,M_\odot$, a luminosity range of $10^2-10^5\,L_\odot$, a temperature range of $16-28\,\mathrm{K}$, and source radii range of $0.3-3.2\,\mathrm{pc}$. For NGC 7538 I find a mass range of $5-10^3\,M_\odot$, a luminosity range of $5-10^3\,L_\odot$, a temperature range of $10-40\,\mathrm{K}$ and a source radii range of $0.1-2\,\mathrm{pc}$. I cross-check the source extraction method using the routine, GETSOURCES. This algorithm found a total of 621 sources in NGC 7538. The GETSOURCES catalogue is filtered to removed sources which are present in two or less wavelengths. This filtered catalogue then has a good correlation with the CSAR catalogue. Using both catalogues a robust source list of 75 sources is created from sources found by both routines.

I plot the mass against radius for both the Carin Nebula and NGC 7538. For Carina the data are best fitted by $M \propto R^{1.8}$ which is comparable to the Larson relation of $M \propto R^2$. In NGC 7538 I find no relation. I find no temperature dependence in the Carina Nebula with any other source property but find a weak relation between temperature and luminosity in NGC 7538. Both regions show a relation of $L \propto M$. I find a relation between radius and Luminosity per unit volume where smaller sources have a higher luminosity per unit volume and the larger sources have a lower value. I find sources with a luminosity per unit volume less then $1\,L_\odot\mathrm{pc}^{-3}$ tend to lie in the less dense regions of the nebulae and sources with a luminosity per unit volume greater then $3.5\,L_\odot\mathrm{pc}^{-3}$ lie in the denser regions where the more evolved sources tend to be. This could show that the luminosity per unit volume can trace the evolutionary status of sources in a region.

ACKNOWLEDGMENTS

Firstly I would like to thank my wonderful husband Ian, for all his love, support and friendship over the past six years. You've kept me going when it's got tough and always been there for me. Without you I'd never of made it this far. I also would like to thank Prof. Matt Griffin and Prof. Derek Ward - Thompson for giving me the opportunity to undertake a PhD and take part in some exciting research, also for all their help and support and the occasional trip somewhere sunny.

I would also like to thank all the members of the star formation group, including Prof. Ant Whitworth and especially those in the observation office, Dr. David Nutter, Dr. Jason Kirk, Lucy Wilcock, Ciara Quinn and Adam Rykala, who have had to put up with my rantings during my time here. You have made the last few years enjoyable and I couldn't ask for nicer people to share an office with.

Many thanks goes out to all the friends I have made during my time in Cardiff. Tom Huges, Sara Carver, Matt Smith, Laura Nuttall, Ezzy Pearson, Olly Lomax and the co - founder of cake day, Gwen Raymond. You have all kept me sane. ish. And when you haven't kept me sane you have at least supplied me with cake and pick - and - mix and taken me to the pub. I will miss the intellectual coffee time conversations, they were always very enlightening on subjects such as bolometry and zombies, although we may never know the answer to pig verses swan.

A special thanks to the staff at Cardiff and especially the computing support team for all their help and for fixing my computer every time I broke it. I would like to acknowledge and thank all my collaborators within the BLAST consortium and the *Herschel* HOBYS group.

Finally I would like to thank my parents for all their love and support over the last 26 years, I wouldn't be where I am today without it. And last but not least, my sister Vickie who probably now knows more about star formation then she ever wanted to, but did a great job proof reading.

Contents

List of Figures

List of Tables

Chapter 1

An Introduction to High Mass Star Formation

Star formation is one of the most important processes in the universe. The stars have created almost all of the chemical elements more massive than helium (Shu, Adams, & Lizano, 1987). Low mass stars form and evolve slowly, locking up matter and giving off little energy. The formation and short lives of high mass stars can have a dramatic effect on their surrounding regions and on the galaxy as a whole. High mass stars form quickly, are very luminous for a relatively short time, then die quickly. When they die they give out huge quantities of material and energy into their surroundings in the form of energetic winds, ionising radiation and supernovae shocks. This has a large effect on the interstellar medium, through heating and turbulence, and through sweeping up large volumes of gas and dust which is sometimes enough to kick start more star formation. Massive stars mainly form in large stellar clusters (Lada & Lada, 2003), the fate of which depends on the degree and speed at which the gas is removed. On a larger scale, the evolution

of the galaxy is strongly influenced by the injection of material and energy into the interstellar medium. Finally, the heavy elements from which we and our planet are made, are formed within stars, and the formation of planets from these heavy elements depends on the detailed conditions of the star formation process (McKee & Ostriker, 2007). It is therefore important that we understand how and why stars are created with the properties that have made our existence possible. We also need a good understanding of star formation so we can interpret our observations in other fields of astronomy such as planet formation, galaxy evolution and cosmology.

1.1 Thesis outline

In Chapter 1, I discuss our current understanding of the high mass star formation process. In Section 1.2, I summarise the properties of molecular clouds and the interstellar medium. In Section 1.3, I review the current competing theories and discuss the stages of high mass star formation, and in Section 1.4, why far infrared observations are important is discussed. The problems and observational needs associated with observing in the infrared and submillimetre are discussed in Section 1.5.

In Chapter 2, I describe the observatories past and present that have helped to shape infrared and submillimetre astronomy including the BLAST balloon - borne telescope and the *Herschel* Space Observatory, data from which are used in the final three chapters, and introduce the calibration methods used.

In Chapter 3, I present observations of the Carina Nebula, mapped with BLAST. In Section 3.2 I give a description of the high mass star formation region. The BLAST observations, data reduction and map - making is outlined in

Section 3.3. The BLAST data have been analysed in conjunction with archival *Spitzer* maps which is discussed in Section 3.4. The source extraction methods are described in Section 3.5, and the results are presented in Section 3.6, where I discuss the source sizes, masses, temperatures and luminosities.

In Chapter 4, I present data for NGC 7538, mapped by PACS and SPIRE on *Herschel*. In Section 4.2, I review the region NGC 7538. The observations, data reduction and map making are discussed in Section 4.3, and in Section 4.4 the source extraction method is outlined. A comparison between two source extraction routines, CSAR and GETSOURCES is discussed in Section 4.5. The results are presented in Section 4.6 which includes source sizes, masses, temperatures and luminosities.

In Chapter 5, I present the analysis and discussion of the results from the Carina Nebula and NGC 7538 data. I look at the mass - radius relation for the Carina Nebula and NGC 7538 in Section 5.2. In Sections 5.3 I look at the temperature dependence in both regions. The mass - luminosity relation is discussed in Section 5.4. The global properties of Carina are discussed in Section 5.5 and the global properties for NGC 7538 are discussed in Section 5.6. The use of luminosity per unit volume as a useful parameter to characterise the evolutionary state of high - mass star - forming cores is introduced in Section 5.7.

Finally the results are summarised in Chapter 6, and final conclusions are presented. Possible future work is also discussed.

1.2 The interstellar medium and molecular clouds

The Interstellar Medium (ISM) is the gas and dust that lies between the stars in a galaxy. It consists of about 99% gas and about 1% dust by mass. The gas is made up of about 89% hydrogen, 9% helium and 2% metals and has an average density of roughly one atom per cubic centimetre (e.g., Madden et al. (2006)). The ISM plays a very important role in a galaxy. The dense regions within it allow stars to form, and it also determines the lifespan of active star formation in the galaxy, based on how quickly it depletes its gaseous content.

The dense regions in the ISM are known as molecular clouds (MCs) and it is within these that some of the most important astrophysical processes begin in the form of star formation. Giant molecular clouds (GMCs) are concentrated in the Galactic spiral arms, and are formed by the compression of gas as it enters the denser region of a spiral arm (Williams, Blitz, & McKee, 2000). The masses of GMCs are typically $\sim 10^5 - 10^6\,\mathrm{M}_\odot$, with diameters of $\sim 50\,\mathrm{pc}$. The high density in a GMC is the most important factor in enabling the star formation process to begin. High column densities within the clouds shield the interiors which leads to them being very cold, around $10 - 20\,\mathrm{K}$ (Goldsmith & Langer, 1978). Because of these low temperatures, the thermal support of the cloud is reduced which can lead to gravitational instability with fragments forming which then go on to collapse to form stars. The stars that form in the ISM also help shape it through planetary nebulae, stellar winds, and supernovae. An example of a GMC, the Orion Nebula, is shown in Figure 1.1. The Orion Nebula is one of the closest star forming regions at a distance of around $400\,\mathrm{pc}$ and has an size of approximately $65{\times}60'$ (Hillenbrand, 1997; Menten et al., 2007).

Figure 1.1: Optical image of the Orion Nebula taken using the HST (NASA,ESA, M. Robberto)

1.2.1 Stellar nurseries

The knowledge that stars are formed in GMCs comes from T - Tauri stars, which are the youngest optically visible stars and were first discovered by Joy (1945). The class was named after the prototype star in Taurus. Their properties proved that they had to be formed in GMCs (Herbig, 1977a; Jones & Herbig, 1979). They have irregular variability, strong Hα emission and lithium absorption, ultraviolet and infrared continuum excesses, and associations with nebulosity. They also have radial velocities (Herbig, 1977b) and proper motions (Jones & Herbig, 1979) which were found to be consistent with the bulk motions of their parent molecular clouds.

There are two main categories of stars, low mass and high mass stars. They have different characteristics and need different circumstances to form. Low mass stars are now relatively well understood with clearly defined stages of formation, and can form almost anywhere in a molecular cloud. However we know very little

about the formation processes and early evolution of high mass protostars. A low mass star is classed as anything below 8 $M_{\odot}$, anything with a mass higher then 8 $M_{\odot}$ is considered a high mass star. This boundary is due to the mechanisms involved in forming the protostars. The stages and mechanisms involved in forming high mass stars are discussed in Section 1.3.2.

A GMC can keep producing stars until it depletes its gas and dust, which can take very many years $\sim 10^7$ yrs (Cohen et al., 1980). Low mass stars live for a long time, locking up matter and energy and giving little back to the ISM whereas high mass stars have a much shorter lifespan and dump huge quantities of matter and energy back into the GMC prolonging its life and enriching the cloud with heavy elements.

For star formation to occur in a GMC, a region or regions within the cloud (pre - stellar core) must become gravitationally unstable and collapse. The mechanisms which cause the clouds to fragment are not well understood. There are two main theories as to how this happens, magnetic fields and turbulence, both of which are described below.

The role of magnetic fields

Interstellar magnetic fields have now been known about for over 60 years. They were first discovered by Hall (1949) and Hiltner (1949) who independently detected the polarisation of starlight. It was observed that the degree of polarisation of the starlight was related to the reddening. This led to the realisation that the polarisation was being caused by the dust grains between us and the star. These dust grains had to be aligned by a magnetic field (Verschuur, 1969).

Magnetic fields have been shown to provide support against gravity within a molecular cloud, impeding the cloud from collapsing (Mouschovias, 1976). This process happens due to the partially ionised gas in the cloud. The ions in the cloud feel a resistance as they cross the magnetic field lines, caused by the Lorentz force. This inhibits the gravitational contraction of the cloud due to friction but only in directions perpendicular to the field lines. If the magnetic field is weak enough the contraction drags the field lines in. Eventually the cloud reaches an equilibrium state with its self gravity where it can collapse no further: at this point the cloud is known as magnetically critical. For the cloud to collapse further, the magnetic flux must be removed. This happens through a process called ambipolar diffusion, whereby neutral particles flow past the ions (Mestel & Spitzer, 1956). At this point the magnetically subcritical cloud begins to evolve quasi-statically, building up mass in its core until it is too great for the magnetic field to support. At this stage the core is supercritical and there is nothing to stop it collapsing.

Theoretical magneto-hydrodynamic models of core evolution can be used to explain many of the observed features of prestellar cores. These include the flattened inner density profile (Ward-Thompson et al., 1994), the steep density profiles at large radii (Bacmann et al., 2000), the anti-correlation of core lifetime with central density (Jessop & Ward-Thompson, 2000), and the rapid evolution from the flattened density profile to a centrally condensed one (Ward-Thompson & André, 1999). However they cannot explain the structures present within the molecular clouds, so there must be other processes at work.

The role of turbulence

Turbulence can be used to explain a lot of the structures seen within molecular clouds. It appears to be dynamically important from scales of whole molecular clouds down to individual cores. In recent years it has been realised that turbulence is a fundamental and important feature of molecular clouds, determining properties such as their morphology, lifetimes, rate of star formation etc.

Much of the work on turbulence was inspired by the 'gravitational instability' picture of star formation, in which diffuse nearly uniform clouds collapse and fragment into a hierarchy of successively smaller condensations as the density rises and the Jeans mass decreases (Jeans, 1929). However most molecular clouds do not fit with this simple classical picture: no large, nearly uniform and quiescent clouds that might be in the early stages of star formation have ever been observed, and all large molecular clouds are inhomogeneous and clumpy, showing structure on the smallest resolvable scales.

One of the most influential studies of interstellar turbulence is that of Larson (1981) who identified a power law relationship between the global velocity dispersion, $\Delta v\,(\mathrm{km\ s^{-1}})$ and cloud size, $L\,(\mathrm{pc})$. He studied many molecular clouds of varying sizes and all the regions showed approximately the same power law dependence. This suggests that the observed internal motions in molecular clouds are all part of a common hierarchy of interstellar turbulent motions, and that they have no preferred length scale. This implies that molecular clouds are transient, dynamically evolving features produced by compressive motions of either gravitational or turbulent origin, or even both. This common hierarchy suggests that the energy contributed from internal sources such as individual stellar winds and expanding HII regions may be small with respect to the common external component.

Turbulence in the ISM is transonic, while within molecular clouds it is highly supersonic (Zuckerman & Palmer, 1974; Zuckerman & Evans, 1974). Early studies considered this property mainly as a mechanism of molecular cloud support against gravity, impeding the clouds from collapsing. The transonic flows in the ISM are thought to shape the molecular clouds on a large scale and the supersonic flows to shape the molecular clouds on a small scale (Ballesteros-Paredes et al., 2007).

Both magnetic fields and turbulence have been shown to help shape molecular clouds and enable collapse to form stars. To accurately model the internal structures of the clouds a combination of the two must be needed.

1.2.2 Dust properties

Only 1% of the mass of the ISM is made up of dust but it plays a very important role in how we observe star formation. The typical size of a dust grain is about $1\,\mu$m or smaller, comparable to the wavelength of visible light. The grains are composed of water ice, graphite (carbon), and silicon (e.g., Mathis (1990)). Dust grains can have two effects on light: extinction and reddening. Both of these change the way we see objects. Extinction is the absorption and scattering of radiation emitted by objects, by the dust and gas in the ISM and from circumstellar dust around an object. The concept of interstellar extinction is generally attributed to Robert Trumpler (Trumpler, 1935), though its effects were first identified in 1847 by Friedrich George Wilhelm von Struve (Nyrén, 1905). Reddening occurs due to the light scattering off the dust grains and other matter in the interstellar medium. The emitted blue wavelengths are preferentially scattered more than redder wavelengths, due to the size of the dust grains. Less blue light reaches us so the object appears redder than it should.

Both of these effects have a direct impact on how we observe star formation. All newly forming stars are surrounded by an envelope of gas and dust which absorbs the emitted light and then re-emits it in the infrared. This prevents us from being able to see the early stages of star formation in optical wavelengths.

1.2.3 Mass estimates of molecular clouds from submillimetre observations

We can observe molecular clouds in the submillimetre wavelengths due to the temperature of the clouds interior ($10-20\,\mathrm{K}$). To calculate the mass of a molecular cloud, a method based on the continuum radiation from the thermal emission of the dust grains is used. This method was derived by Hildebrand (1983) who made the assumption that the cloud is optically thin.

The total mass of the dust in a molecular cloud is given by:

$$M_d = \left(\frac{F(\nu)D^2}{B(\nu,T)}\right)\left(\frac{4\rho_g a}{3Q(\nu)}\right), \tag{1.1}$$

where F_ν is the total observed flux at frequency ν, D is the distance to the dust grains, $B(\nu,T)$ is the Planck function at temperature T, ρ_g is the density of a typical dust grain, a is the radius of a dust grain and $Q(\nu)$ is the dust grain emissivity. The first term in equation 1.1 contains all the parameters that need to be found observationally and will be different for every cloud. The second term is equal to the inverse of κ_d, the dust grain mass absorption coefficient. The value of this term is much harder to determine as we can not directly measure the different properties so it is still in dispute.

Hildebrand (1983) made the assumptions that the values for a and ρ_g were $0.1\,\mu$m and $3\,\mathrm{g\,cm^{-3}}$ respectively. The value he used for ρ_g was based on the known densities of graphite and silicates, which are assumed to be the constituents of interstellar dust. The value of a was found by Mathis, Rumpl, & Nordsieck (1977) who discovered that the interstellar extinction is best fitted by grains with a size distribution centred around $0.1\,\mu$m. The value for the emissivity, $Q(\nu)$, is much more difficult to determine.

At infrared wavelengths, $Q(\nu)$ is equal to the extinction efficiency, Q_{ext} which is given by:

$$Q_{ext} = \frac{\sigma_{ext}}{\sigma_{geom}} = \frac{\sigma_{abs} + \sigma_{scat}}{\sigma_{geom}}. \tag{1.2}$$

where σ_{ext} is the extinction cross - section, σ_{geom} is the geometric cross - section, σ_{abs} is the absorption efficiency and σ_{scat} is the scattering efficiency. At UV wavelengths, $\sigma_{abs} = \sigma_{geom} = \sigma_{scat}$ so the extinction efficiency is equal to two. At infrared wavelengths σ_{scat} is negligible so $\sigma_{ext} = \sigma_{abs}$ and therefore the emissivity is equal to the absorption efficiency.

At $250\,\mu$m Hildebrand (1983) found a value of κ_d equal to $0.1\,\mathrm{cm^2\,g^{-1}}$. There have been many studies to try and remove the uncertainties surrounding this parameter and this has led to very different values being adopted. These range from $0.024\,\mathrm{cm^2\,g^{-1}}$ (Draine & Li, 2007) to $0.2\,\mathrm{cm^2\,g^{-1}}$ (Ossenkopf & Henning, 1994). A recent study undertaken by Netterfield et al. (2009) yields the value $0.16\,\mathrm{cm^2\,g^{-1}}$ which is closer to the original value found by Hildebrand (1983).

1.2.4 The Larson relation of mass and radius

Larson (1981), while conducting a study on velocity dispersion found a canonical relation between an objects radius and its mass following $M \propto R^2$. He studied the properties of 57 previously published objects including cloud complexes, individual clouds and clumps. For each of these he found their velocity dispersion, σ_ν, mass, M and size, L. The velocity dispersions were found using the linewidths of ^{13}CO data. The region sizes were found by measuring the largest closed map contour defining the clump, and the masses of the regions were found using the assumption that the ratio of the column density of ^{13}CO to that of H_2 is 2×10^{-6}, and that H_2 constitutes 70 % of the total mass of the source. From his study he found a relation between velocity dispersion and size, and a relation between velocity dispersion and mass. These were then combined using the viral theorem giving,

$$\frac{2\,G\,M}{L} \sim \sigma^2, \tag{1.3}$$

where G is the gravitational constant. He then plotted this against the source length to find the relation,

$$\frac{2\,G\,M}{\sigma^2\,L} \sim 0.92\,L, \tag{1.4}$$

which can be rearragned to give:

$$\frac{G\,M}{\sigma^2} \sim \frac{L^2}{2}, \tag{1.5}$$

This shows a link between the sources mass and size following $M \propto R^2$. By plotting this he found that smaller objects such as prestellar cores showed the strongest correlation and the larger objects such as the cloud complexes showed a

weaker correlation with a dispersion of around an order of magnitude. He noted that his relation is only true for clouds or cores that are in virial balance and are not collapsing, and that some of the spread in his results arises from the difficulty of accurately determining the sizes of the objects. Since this relation appears to be valid over a range of sizes, this implies that it is independent of scale.

1.2.5 Jeans instability

For a cloud to undergo gravitational collapse to form a protostar it needs to overcome its state of equilibrium. To do this is must have a high enough mass and small enough radius. These values were calculated by Jeans (1929) and are known as the Jeans mass, M_J, and Jeans length, R_J. For a spherical cloud, the hydrostatic equilibrium can be expressed as (Shu, 1977):

$$\frac{dp}{dr} = -\frac{G\,\rho(r)\,M_{enc}(r)}{r^2}, \tag{1.6}$$

where p is the pressure , r is the radius, $M_{enc}(r)$ is the enclosed mass at r, $\rho(r)$ is the density of the gas at r and G is the gravitational constant. To estimate the internal pressure of a source we need to make the assumption that the internal pressure at the edge of the source will be zero, $P(r = R) = 0$ (where R is the total radius), and in the centre will be equal to P_c, $P(r = 0) = P_c$. We can then use this to find the average pressure,

$$\frac{dp}{dr} = \frac{P_c - 0}{R} = \frac{P_c}{R}, \tag{1.7}$$

which gives:

$$\frac{P_c}{R} \approx \frac{G\,M\,\rho}{R^2}, \tag{1.8}$$

where M is the typical mass and ρ is the typical density. The typical density of the source is given by:

$$\rho \approx \frac{3\,M}{4\,\pi\,R^3}. \tag{1.9}$$

Substituting this into equation 1.8 gives the pressure at the core of the source:

$$P_c \approx \frac{3\,G\,M^2}{4\,\pi\,R^4}. \tag{1.10}$$

At this pressure the cloud is in equilibrium, so for the cloud to start to collapse it needs to increase in mass. Jeans calculated the critical mass as a function of density and temperature, which when exceeded a process of runaway contraction will begin until another force can stop it. The Jeans mass is givenby:

$$M_J = \left(\frac{4\pi}{3}\right)\rho\,R_J^3, \tag{1.11}$$

where ρ is the mass density, and R_J is given by:

$$R_J = \left(\frac{15 k_B\,T}{4\,\pi\,\rho\,G\,m}\right)^{\frac{1}{2}}, \tag{1.12}$$

where k_B is the Boltzmann constant, T is the temperature in kelvin, and m is the mean mass of a gas particle. Sources with a radius greater then the Jeans radius will be unstable and likely to collapse whereas those with a smaller radius will be more stable. Substituting equation 1.12 into equation 1.11 gives:

$$M_J \geq \left(\frac{5\,k_B\,T}{G\,m}\right)^{\frac{3}{2}}\left(\frac{3}{4\,\pi\,\rho}\right)^{\frac{1}{2}}. \tag{1.13}$$

The Jeans length can be rearranged to give the critical density above which the cloud will start to collapse. This density is given by:

$$\rho_{crit} = \frac{15 k_B T}{4 \pi G m R_J^2}. \tag{1.14}$$

Clouds with a density equal to ρ_{crit} will be stable. If the density increases the cloud will start to collapse and if the density decreases then the cloud may start to disperse.

1.2.6 The Initial Mass Function

The Initial Mass Function (IMF) is an empirical function that describes the mass distribution of a population of stars in terms of their initial mass. The function consists of a three part power law with breaks at 0.08 M and 0.5 M; i.e., with $= 1.3$ for $0.5 < m^*/M < 50$, $= 0.3$ for$0.08 < m^*/M < 0.5$, and $= 0.7$ for $0.01 < m^*/M < 0.08$ (Alves et al., 2007). This is shown in Figure 1.2. The high mass end of the IMF was first quantified by Salpeter (1955). Current studies suggest that the IMF is quite similar in many different locations thoughout our Galaxy. The IMF appears to be independent of the mean density, turbulence level and the magnetic field strength. The origin of the stellar IMF remains one of the major unsolved problems of modern astrophysics. It has been thought that the IMF may originate from the CMF (core mass function), the distribution of masses of dense molecular cores in a cloud (Andre, Ward-Thompson, & Barsony, 2000). Since each protostar forms from the dense core that acts as a reservoir of material surounding it, it would follow that the mass of the protostar would be equal to the mass of the core with some efficiency factor as not all the material will be able to accrete onto the surface of the young star. It has been shown that the CMF and the IMF have a similar shape but shiffted by a factor of 4. This is shown in Figure 1.2 where the mass function of dense molecular cores is plotted as filled

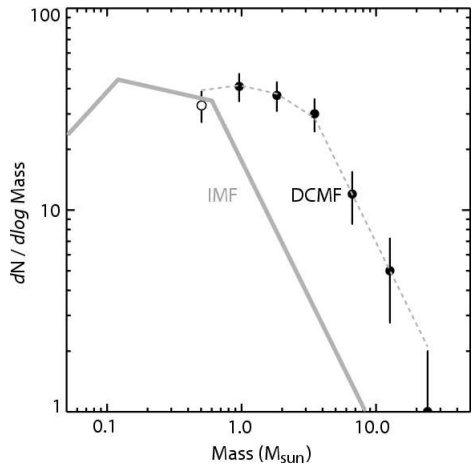

Figure 1.2: Mass function of dense molecular cores plotted as filled circles with error bars. The grey line is the stellar IMF for the Trapezium cluster (Muench et al., 2001). The dashed grey line represents the stellar IMF in binned form matching the resolution of the data and shifted to higher masses by about a factor of 4. The dense core mass function is similar in shape to the stellar IMF function, apart from a uniform star formation efficiency factor. (Alves et al., 2007)

circles with error bars and the grey line is the stellar IMF for the Trapezium cluster (Muench et al., 2001). The dashed grey line represents the stellar IMF in binned form matching the resolution of the data and shifted to higher masses by about a factor of 4. This means that in ever star forming region there should be a similar ratio of protostar masses, so a region with few low mass protostars will have very few high mass stars but regions with a large number of low mass stars should have a larger quantity of higher mass stars.

1.3 High mass star formation

Until recent times it has been very difficult to observe high mass stars as they form, due to their smaller numbers, shorter evolutionary timescales and the fact that they normally form in large clusters at large distances from us. But with new infrared telescopes such as *Herschel* it has become a very exciting research

area with many new discoveries. High mass stars are known to form in large dense clusters with stars having a typical mass of 20 $M_{\odot}$ or higher. In this section I will discuss the two current competing theories on how high mass stars are formed and outline the possible stages. Much of the following section draws on the extensive review of Zinnecker & Yorke (2007).

1.3.1 Competing theories of high mass star formation

There are two main theories as to how high mass stars are formed. Since high mass stars tend to form in large clusters it is observationally very difficult to confirm one over the other. The first proposed mechanism is similar to the mechanism for low mass stars but with a higher accretion rate, the second relies on the cluster environment and involves high mass stars forming by the merging of two or more intermediate mass protostars. Both of these methods are described below.

The accretion scenario

The first proposed method of forming high mass stars is the accretion scenario. This is similar to the mechanism in forming low mass stars but with some key differences. As high mass stars form they produce outflows and strong radiative pressure, which can prevent accretion, so for a star to form with this method it must have a circumstellar disk. The strong winds and radiation create a cavity around the star's polar regions which prevents some matter accreting onto the star but is not strong enough to stop all of it. Most of the gas and dust accretes in the equatorial plane of the circumstellar disk as the angular momentum is transfered outward. For this transfer to take place there must be a weak magnetic field as

discussed in section 1.2.1 (Balbus & Hawley, 1991; Hawley & Balbus, 1991; Balbus, 2003), or turbulence (discussed in Section 1.2.1) present. It is thought that the accretion could also be aided by having other nearby stars. This may be one of the reasons why high mass stars are formed in clusters. It is still unclear how exactly the material in the disk eventually flows onto the star, but there is strong evidence to support this theory.

The coalescence scenario

The second method for the formation of high mass stars is the coalescence scenario. This is where high mass stars are formed by the merging of lower mass stars. This method was first proposed to deal with problems associated with the accretion scenario. It was thought that the radiation pressure on the dust grains was too high to allow accretion and that the high mass clusters studied at the time were too densely packed for there to be enough gas for monolithic collapse. However we now know that not all high mass stars form in such dense clusters, with some forming in more spread out OB associations.

For high mass stars to form by the coalescence scenario, the stars need to be in a very dense cluster where each star already has an intermediate mass. For this method to work the intermediate mass stars need to have a collision time, τ_{coll}, less than the lifespan of the most massive star in the cluster (typically 3 Myr). The collision time is given by (Binney & Tremaine, 1987; Dale & Davies, 2006):

$$\tau_{coll} = \frac{1}{n_{star}\sigma_{grav}v_{rms}}, \tag{1.15}$$

where n_{star} is the density of the stars in the cluster, v_{rms} is the stars average speed and σ_{grav} is the cross section for two stars passing each other, given by:

$$\sigma_{grav} = \pi R_{min}^2, \quad (1.16)$$

where R_{min} is the minimum distance at which the two stars can pass each other, G is the gravitational constant and M_{star} is the mass of the star. It is possible for stars to meet this condition if they are in large and dense enough clusters and have high enough velocities, $\sim 5\,\mathrm{km\,s^{-1}}$ (van Altena et al., 1988). However, it is unlikely that this is the main mechanism for high - mass star formation as many clusters do not meet these requirements.

1.3.2 Stages of high mass star formation

Over the last ten years there has been some progress in identifying an evolutionary sequence similar to the low mass one. This is mainly due to improvements in resolution in observational data. Until there is a universally agreed mechanism for the formation of high mass stars there will not be a definitive evolutionary sequence.

The suggested sequence for high mass star forming cores based on current theories (discussed above) is listed and then each stage is described below (Zinnecker & Yorke, 2007):

- Cold dense massive core (CDMC)
- Hot dense massive core (HDMC)

- Disk - accreting main sequence star (DAMS)
- Zero age main sequence star (ZAMS)

Cold dense massive core

Cold Dense Massive Cores (CDMC) are starless, turbulent and gravitationally bound condensations; they are in a near - virial equilibrium state and are either on the verge of collapsing or already in the process of collapsing (Garay et al., 2004). In the center of the condensation, an intermediate - mass protostar starts to form that will heat up the cold dense massive core, turning it into a hot dense massive core.

Hot dense massive core

At the Hot Dense Massive Core (HDMC) stage, the central star starts to grow in mass by disk accretion. At this point collimated jets and outflows will first appear and can be traced firstly by H_2O and then by methanol maser emission (McKee & Tan, 2003). Once the star starts to gain mass it quickly becomes a disk - accreting main sequence star. It is now powered mainly by hydrogen burning but still has an element of disk accretion.

Disk - accreting main sequence star

At the Disk - Accreting Main Sequence star (DAMS) stage, the accretion disk surrounding the star starts to get photoionised and partly photoevaporated. The collimated outflows which started at the HDMC phase become less collimated

with widening opening angles (Palla & Stahler, 1993). The DAMS star now gives rise to a gravitationally confined hyper - compact HII region with broad hydrogen recombination lines.

Zero age main sequence star

The star enters the Zero Age Main Sequence star (ZAMS) stage when it has attained hydrostatic equilibrium (Mengel et al., 1979). These stars have just begun their hydrogen - burning life - times on the main sequence but have not yet converted any significant fraction of their core mass into helium. The high mass star is now fully formed.

These different stages of high mass star formation are very difficult to observe, but we can also define the observable sequence of the embedded phase that the cores pass through. The phases are listed then describedbelow (Menten, Pillai, & Wyrowski, 2005; Van der Tak & Menten, 2005):

- Infrared dark cloud (IRDC)
- Hot molecular cores (HMCs)
- Hyper - compact and ultra - compact HII regions (UCHII)
- Compact and classical HII regions (HII)

Infrared dark clouds

An infrared dark cloud (IRDC) is a cold, dense molecular cloud core. IRDCs have only recently been discovered (Perault et al., 1996; Egan et al., 1998; Benjamin

et al., 2003) and are a matter of great interest as their high densities ($\geq 10^4\,\mathrm{cm}^{-3}$) and low temperatures ($\leq 15\,\mathrm{K}$) are likely to represent the initial conditions of high mass star formation. IRDCs are very difficult to observe as they are dark even at infrared wavelengths. When observed, these cores are seen as absorption against the bright diffuse mid-infrared background emitted by the Galactic plane.

Hot molecular cores

In the Hot Molecular Core (HMC) phase (Kurtz et al., 2000; Cesaroni, 2005), the high mass stars within the cloud causes it to have temperatures of $\sim 100\,\mathrm{K}$ or greater and it becomes compact with a dusty core. The high temperatures evaporate the organic molecules which had condensated onto the dust grains, causing a cloud of hot molecular gas. The HMCs start to show the common signposts associated with high mass star formation such as masers and luminous infrared sources. To date only a few HMCs have been identified, but as they represent ideal laboratories for testing theories on the formation of OB stars, the interest in them has grown.

Hyper-compact and Ultra-compact HII regions

HMCs can go on to form Hyper-Compact (HCHII) and Ultra-Compact (UCHII) HII regions (Murphy et al., 2010; Hoare et al., 2007). These are small pockets of ionised gas that have stayed confined to the stellar vicinity but are growing steadily. It is thought that HCHII regions represent individual photoevaporating disks (Keto, 2007; Nielbock et al., 2007), and UCHII regions probably represent disk-less stars photoionising their own massive envelopes.

Compact and classical HII regions

As the stars inside the HCHII and UCHII regions evolve, the HII regions expand and become compact and classical HII regions (Mezger et al., 1967; Yorke, 1986). The gas within the HII region becomes globally ionised by one or more stars within it. The region expands hydrodynamically and disrupts the molecular cloud it was formed in. This reveals the embedded high mass stars which were born within it. It is then possible to view these stars not only in the far infrared but in the optical and near - infrared wavebands (Carpenter et al., 1993; Zinnecker, McCaughrean, & Wilking, 1993).

1.4 Why FIR observations are important

Some of the most interesting objects in the Universe are created inside large envelopes of gas and dust. These objects, such as young stars and newly formed planets are hidden from us when viewed in the optical due to extinction. However, it is possible to view them in the far - infrared (FIR). Protostars heat their surroundings as they contract, allowing us not only to see them in the infrared but also the dust around them. Being able to view these very early stages of star formation gives us a great deal of information of how stars like our sun are formed. Infrared observations can also be used to observe how the galaxies are traveling away from us which is important for cosmological studies.

Observing in the optical only gives us one aspect of the larger picture of what is happening in the Universe, so by observing at infrared wavelengths we can reveal the cold emission that would otherwise be hidden from us. An example of the

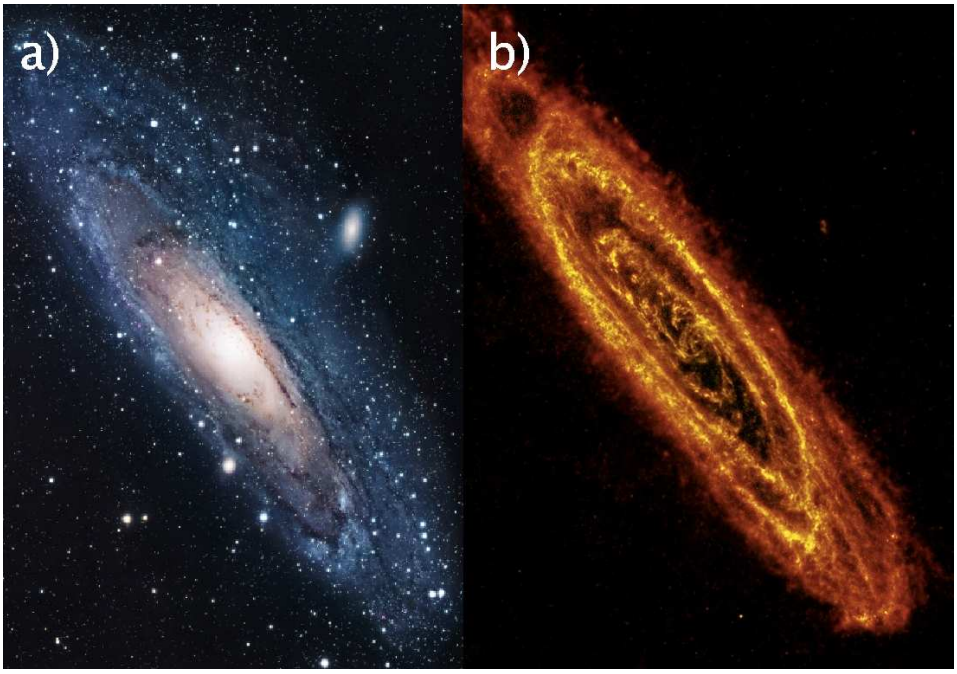

Figure 1.3: a) An optical image of the Andromeda galaxy taken with the HST and (NASA, ESA and T. Lauer (NOAO/AURA/NSF)) b) a far - infrared image taken with Herschel at 250 μm (ESA/Herschel/SPIRE/HELGA).

difference between optical emission and FIR emission is shown in Figure 1.3 which shows the Andromeda galaxy, a) in the optical and b) in the far - infrared (250 μm). From these you can see the dark, cold dust lanes in image a) shine brightly in image b). These dust lanes containregions of active star formation.

Far - infrared observations are particularly important for high mass star formation because it occurs in clusters surrounded by large quantities of gas and dust. Because we know so little about the early stages of high mass star formation, to be able to investigate these clusters is critical to furthering our understanding. To see inside these clusters we also need high angular resolution. Previous FIR telescopes such as IRAS, ISO, and *Spitzer* (discussed in Chapter 2), all with diameters less than 1 m, had limited angular resolutions which were not good enough to pick out individual proto - clusters. BLAST and *Herschel* (discussed in more

detail in Chapter 2) are two recent far - infrared observatories that have allowed major improvements in angular resolution, sensitivity, data quality and sky coverage. BLAST was a balloon - borne telescope operating at 250, 350, and 500 μm, and has provided us with detailed observations of star forming regions such as Vela (Netterfield et al., 2009), Cygnus X (Roy et al., 2011) and Aquila (Rivera-Ingraham et al., 2010). The space - borne *Herschel* observatory observes over a broader wavelength range covering the entire far - infrared/submillimetre region. By observing on both sides of the peak emission, we can get accurate estimates of temperatures, masses and luminosity. Studying these basic properties of star - forming regions is essential to distinguish between temperature and density and to determine the evolutionary status of an individual source.

The temperature of a source can tell us vital information about its evolutionary stage, as a star evolves and contracts, it heats up. For low mass protostars the bolometric temperature (T_{bol}) at each evolutionary stage is well defined. However for high mass protostars it is not, but if a similar classification could be found then determining a high mass protostars evolutionary stage would be made much easier. The temperatures for the evolutionary stages of low mass stars are outlined below (Chen et al., 1995, 1997).

- Class 0 $T_{bol} < 70K$
- Class I $70K < T_{bol} < 650K$
- Class II $650K < T_{bol} < 2880K$
- Class III $T_{bol} > 2880K$

There are many questions yet to be answered about the early stages of high mass star formation including how they evolve, what conditions are necessary for their creation and how they affect the star formation in a region. Using far - infrared

observations can help answer these questions. It is important to look at nearby regions, to get the best possible angular resolution. If we can see how star formation has progressed in a region we can start to understand how and why high mass stars form where they do. To do this we need tofind ways to characterise the evolutionary stages of the sources in a region. Establishing an evolutionary sequence requires observations of large areas of sky towards a number of nearby star forming regions to obtain enough data to make statistically valid conclusions, and this is only really possible to do from space. It also requires identifying some observational features that can be used to trace evolution, (e.g., luminosity vs. mass has been used with low mass star formation (Saraceno et al., 1996)). Such a method couldemerge from a large and coherent data set for nearby high mass star formation regions.

1.5 Problems and observational needs of observing in the FIR

Observing in the infrared and submillimetre presents many problems. The Earth's atmosphere is opaque over most of the far - infrared, and much of the submillimetre, which means most ground - based observations, even at high altitudes, are limited to a few submillimetre spectral windows. To overcome this problem observations have also been taken using balloon - borne and space - based observatories. We discuss these various methods of observing in the IR and submillimetre in this section, including the advantages and disadvantages of each.

1.5.1 Ground - based observatories

Ground - based telescopes are the most common form of astronomical observatories. This is mainly due to their long lifetimes, which are prolonged by having refillable cryogenics, being easy to repair, and being relatively cheap to build compared to space - based observatories. When new technologies are developed, such as more sensitive bolometer arrays, the instruments can be upgraded or replaced. Ground - based telescopes can also have multiple instruments which can be swapped as and when they are needed. There is also no limit (other then engineering problems and cost) on how large the telescopes can be. Observations with the telescopes can be made over several nights increasing the signal to noise ratio and improving the data quality.

There are many disadvantages of ground - based observations for submillimetre astronomy. The telescopes need to be situated in a high, dry and cold location, which limits where they can be built and can make construction difficult. Even at high altitude locations the telescopes still can not get above all the Earth's atmosphere which limits the wavelengths that can be observed. The weather also hugely affects when observing is possible as does the day/night cycle. Being limited to specific wavelengths due to the Earth's atmosphere causes many problems for observing high mass star formation. SCUBA on the JCMT (discussed in detail in Chapter 2) for instance was limited to observing at 450 and 850 μm, which is adequate for observing low mass protostars which tend to be colder, so have a peak emission in these wavelengths, but is not good enough to pick up the higher mass protostars which have emission peaking at around 250 μm. Ground - based telescopes do have the advantage of good angular resolutions which allow more detail to be seen. The 15 m JCMT achieves angular resolutions of 7.5″ and 14″ at

450 and 850 μm respectively.

1.5.2 Balloon - borne observatories

Balloon - borne telescopes are not such a common method for astronomical observations but still have many advantages over ground - based telescopes. They can get above most of the Earth's atmosphere allowing more complete wavelength coverage, and are relatively much cheaper than space - borne observatories.

The disadvantages of balloon - borne telescopes are that they are difficult to control once launched and due to the nature of the balloons there is a limited observing time until the balloon comes back down. The telescopes can be easily damaged during take off and landing which can mean that they may only be usable once. Like ground - based telescopes they are also affected by the weather which can dictate when they can be launched. As the telescopes are carried by a gas balloon there is a restriction to the size that the telescope can have and also at the area of sky that can be viewed. Being able to view objects at a wider range of wavelengths than can be accessed from the ground with balloon - borne telescopes provides excellent opportunities for observing high mass star formation. However the limit to the amount of time an object can be viewed for and the smaller telescope sizes can mean poor angular resolutions and poor signal to noise. BLAST (discussed in Chapter 2) had angular resolutions of 36, 42 and 60 $''$ at 250, 350 and 500 μm which means some of the smaller structures will not be fully resolved.

1.5.3 Space - borne observatories

Space - borne telescopes have major advantages over ground and balloon - borne telescopes. They are above all of the Earth's atmosphere which means they can produce far superior data over a much larger range of wavelengths and can have instruments which are cooled to very low temperatures (a few mK), all of which combine to allow us to observe the very early stages of star formation. These telescopes do not have the same weather or time restrictions as ones on Earth so can observe without significant interruption for the entire length of the mission, which can be several years. Most spaced - based observatories are built as part of large collaborations with members across the world, which means that expertise in many areas is available and there is well developed software available for the data reduction.

The disadvantages of space - based telescopes are that they have much shorter lifetimes compared to ground - based telescopes, as the cryogens can not be refilled and they cannot be repaired in the event of failure. The telescopes are also very expensive and are size - limited as they have to fit into the payload module of a rocket. However, this may be overcome with future space telescopes such as the James Webb Space Telescope, JWST, (Gardner et al., 2006) which plans to have a 6.5 m mirror (nearly twice the size of *Herschel's* mirror) that is capable of being folded when in the payload module and then deployed when in the correct orbit. This type of folding mirror will lead to FIR telescopes with far superior angular resolutions which in turn will allow for more in depth studies of high mass star formation regions.

Space - based telescopes play a crucial role in collecting data for high mass star formation. *Herschel* covers a range of wavelengths from the submillimetre

to the far - infrared which allows us to see a range of objects present in a region. *Herschel's* angular resolution (18, 25 and 36″ at 250, 350, and 500 μm respectively) although better then balloon - borne telescopes is not as high as can be achieved with larger ground - based telescopes. However, a key capability of a space - borne telescope such as *Herschel* is that because of the combination of sensitivity, accurate calibration and stability, large areas of sky can be mapped with great fidelity. The lack of atmospheric turbulence means that the quality of large - scale images is much better than for ground - based telescopes, so that faint and extended emission can be accurately mapped. These features are all important in observing the early stages of star formation and to see how the general cloud environment influences the formation of stars and vice versa. Overall there is not one type of observatory that is better then the others, they all have different advantages and disadvantages. For us to keep obtaining good quality data which advances our knowledge of not only star formation but all the other process in the Universe, all three types of telescopes need to be used.

1.6 Summary

In this chapter, I have discussed our current understanding of the high mass star formation process. There is still a great deal that we do not understand about the formation of high mass stars but I have given an overview of competing theories that try to explain how and why stars form with the properties that we observe. I have explained the need for infrared and submillimetre observations to help us view the early stages of star formation and other objects that are hidden from us at optical wavelengths. I have also discussed the problems which are associated with the infrared and submillimetre wavebands. Finally I have reviewed the three types

of observatories, ground, balloon and spaced - based telescopes, and have given the advantages and disadvantages to each.

Chapter 2

Far Infrared and Submillimetre Observatories

2.1 Introduction

In the last 30 years far - infrared and submillimetre astronomy has benefited from advances in technology, allowing bigger and more advanced telescopes to be developed. Better detector technology has allowed larger arrays to be constructed; larger and more efficient cryogenic systems have lead to colder telescopes which allow more sensitive instruments. Instrument photometric and spectroscopic capabilities have become more advanced allowing more detailed data to be obtained for objects and the development of larger and safer rockets has led to space telescopes with larger mirrors and cryostats providing improved angular resolution and long mission lifetimes.

In this Chapter, I discuss the past and present telescopes and observatories

which have contributed significantly to our knowledge of infrared and submillimetre astronomy, including the two observatories (BLAST and *Herschel*), from which data have been analysed for this work and presented in Chapters 3 – 5. I also describe the observational techniques and calibration methods used.

2.2 IRAS

The Infrared Astronomical Satellite (IRAS) was the first space based observatory to survey the entire sky at infrared wavelengths. Run as a joint project by the United States, NASA, the Netherlands, NIVR and the United Kingdom, SERC, IRAS was launched into a low Earth orbit in January 1983 and observed at 12, 25, 60 and 100 μm with angular resolutions ranging from 30″ at 12 μm to 2′ at 100 μm (Neugebauer et al., 1984).

The satellite consisted of a 0.57 m diameter telescope, a liquid helium cryostat and beryllium mirrors cooled to less than 10 K. The focal plane assembly containing the detectors was cooled to 3 K. The survey array consisted of 62 rectangular infrared detectors arranged in staggered rows. IRAS had two additional instruments on board, a Low Resolution Spectrometer (LRS) and a Chopped Photometric Channel (CPC). The LRS is a slitless spectrometer which observed at 7.5 – 23 μm and the CPC operated during selected pointed observations, mapping infrared sources simultaneously at 50 and 100 μm with higher spatial resolution than normally provided by the survey array.

During its ten month operational lifetime, IRAS mapped 96 % of the sky four times, increasing the number of catalogued infrared sources and detecting approximately 350,000 infrared sources. It revealed for the first time the core of

our galaxy (Soifer, Neugebauer, & Houck, 1987). From all of the data a point source and faint source catalogue were created, both of which are still relevant today even though they are almost 30 years old. IRAS contributed significantly to a young field but it had limitations (angular resolution, wavelength coverage, sensitivity, limited spectroscopic capabilities etc) and follow - up missions were needed.

2.3 ISO

The Infrared Space Observatory (ISO) was built by the European Space Agency (ESA) and launched in November 1995 (Kessler et al., 1996). It observed in the infrared at 2.5 to 240 μm with resolutions ranging from 1.5″ at 2.5 μm to 90″ at 240 μm. This gave ISO a wider wavelength coverage and better spatial resolution than IRAS. ISO had a highly elliptical 24 hr orbit, designed to get it away from the Earth's thermal radiation as much as possible, however this also put it inside the Earth's Van Allen belts of trapped electrons and photons for seven hours per orbit. Inside these regions ISO's detectors were scientifically unusable due to effects caused by radiation impacts.

The ISO satellite consisted of a 0.6 m diameter telescope suspended in the middle of a large cryostat, and four scientific instruments. The detectors on the focal plane array were cooled to 2 K, 1 K cooler then IRAS. The four scientific instruments were: the infrared camera, ISOCAM (Cesarsky et al., 1996) which covered the 2.5 – 17 μm band with two different detector arrays, the photometer and polarimeter, ISOPHOT (Lemke et al., 1996) which covered the wider 2.5 – 240 μm band, the Short Wave Spectrometer, SWS (De Graauw et al., 1996) which covered the 2.4 – 45 μm band and the Long Wave Spectrometer, LWS (Clegg et al.,

1996) which covered the 45 – 196.8 μm band.

ISO had a lifetime of two and a half years, with the cryostat finally exhausting its supply in April 1998. Compared to IRAS, ISO had greater sensitivity, more sophisticated instruments and a longer lifetime, but its mirror was no bigger. During ISO's mission it completed over 900 orbits and performed more than 26,000 observations with many new discoveries being made, including the presence of water vapour in star forming regions such as the Orion Nebula (Cernicharo, Gonzalez-Alfonso, & Lefloch, 1997) and the discovery that the source of the enormous infrared emission from Arp 220 was due to an outburst of star formation (Sturm et al., 1996).

2.4 SCUBA

The Submillimetre Common User Bolometer Array (SCUBA) was built by the Royal Observatory in Edinburgh as a ground based infrared instrument for the 15 m James Clark Maxwell Telescope (JCMT). Located on Mauna Kea in Hawaii, this is an ideal site for infrared astronomy as it is very high and dry, at an elevation of 4000 m, putting it above most of the Earth's atmosphere. First light was achieved in July 1996 (Holland et al., 1999; Di Francesco et al., 2008).

SCUBA combined a dual waveband imaging array which observed at 450 and 850 μm and a three band photometer which observed at 1.1, 1.35 and 2.0 mm. The instrument had two hexagonal arrays of bolometric detectors, the Long - Wave (LW) array and the Short - Wave (SW) array. The LW array had 37 detectors and the SW array had 91 detectors, both of which had a field of view of 2.3′, the three photometer pixels are located around the outside of the LW array. The

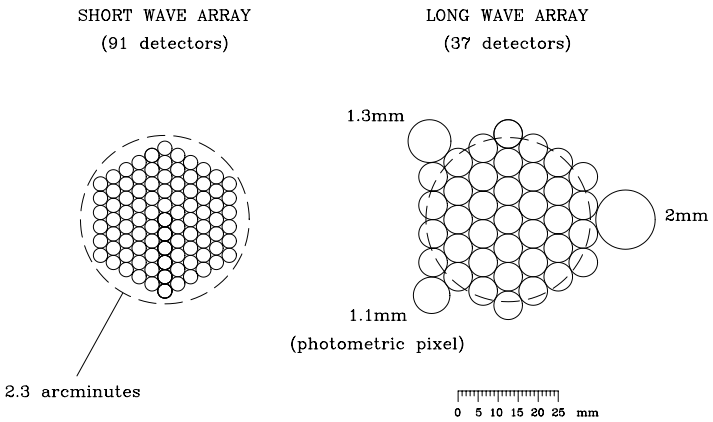

Figure 2.1: The pixel layout for the SCUBA arrays. The locations of the photometric pixels (1.1, 1.35 and 2.0 mm) are also shown (Holland et al., 1999).

arrays are shown in Figure 2.1. Each detector had a diffraction - limited resolution corresponding to approximately 7.5″ at 450 μm and 14″ at 850 μm. The SCUBA detectors were cooled to below 100 mK by means of a dilution refrigerator, which means SCUBA's sensitivity was limited by the photon noise from the sky and telescope background at all wavelengths. SCUBA could also have a polarimeter placed within its beam. SCUBA had three main modes of operation: jiggle mapping, scan mapping and photometry. Jiggle mapping was used for extended sources which are smaller than the array field of view. In this mode the array followed a 64 - point pattern with 3″ spacing, allowing the space between neighbouring bolometers to be sampled, producing a fully sampled map as shown in Figure 2.2. Scan mapping was used to map regions that are large compared with the array field of view. In this mode the telescope scanned across the sky producing a map. Photometry was the preferred mode of observation for a completely isolated point - like source with an accurately known position. Photometry was carried out using the central detector of each array simultaneously or with any of the long wavelength photometers independently. In this mode the secondary mirror moved to observe a small 3×3 grid with 2″ spacing around the source.

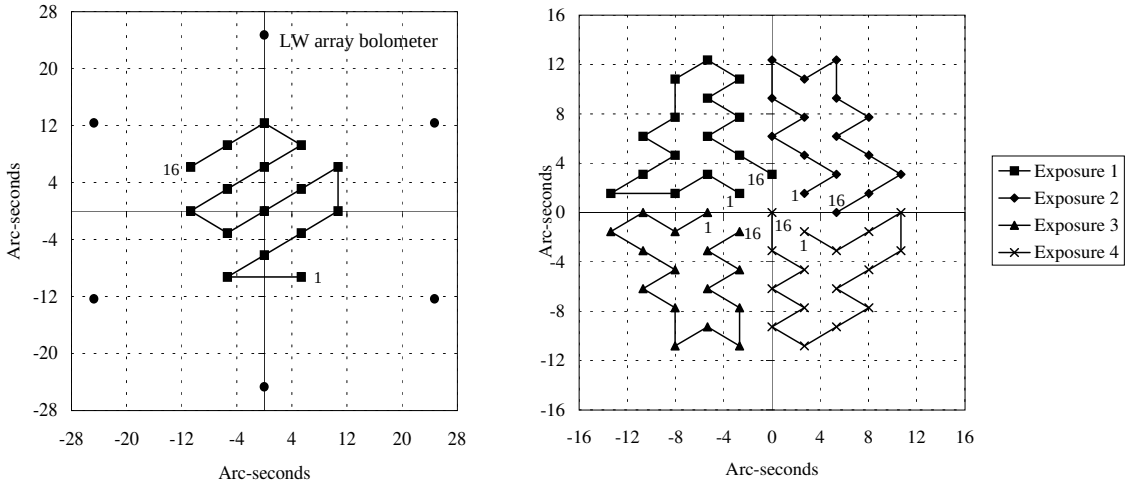

Figure 2.2: (a) Jiggle pattern to fully sample the LW array alone (b) Jiggle pattern to fully sample both arrays simultaneously (Holland et al., 1999).

Using ground - based telescopes such as the JCMT at submillimetre wavelengths has many advantages over spaced based telescopes: ground - based telescopes are cheaper, they have a longer lifetime due to coolants being able to be replaced and repairs can take place, they can be upgraded and can be larger. They also have disadvantages: the warm telescope and the Earth's atmosphere add photon noise which limits sensitivity, atmospheric turbulence produces additional sky noise, weather conditions and day/night cycle limit the time observations can be made. Large parts of the spectrum are blocked completely by the atmosphere and transmission is poor even in the observable parts. The atmospheric transmission for the JCMT is shown in Figure 2.3. SCUBA has now been replaced with the superior SCUBA 2 (Holland et al., 2003, 2006).

SCUBA has been used to carry out many surveys, including the Scuba HAlf Degree Extragalactic Survey, SHADES (Mortier et al., 2005) and the Scuba Local Universe Galaxy Survey, SLUGS (Dunne et al., 2000). For SHADES, SCUBA mapped 0.5 square degrees of sky at a depth sufficient to provide an unbiased

sample of bright submillimetre sources. For SLUGS, SCUBA found the submillimetre properties of the local universe by observing 104 galaxies at submillimetre wavelengths.

SCUBA has contributed many new discoveries to the star formation field. These include the first published maps of magnetic fields in prestellar cores, which are used to test the theoretical ideas about the way in which magnetic field geometry affects the star formation process. This was carried out using the UK - Japan polarimeter placed in the SCUBA beam (Ward-Thompson et al., 2000). SCUBA has also played an important role in low mass star formation by working on Class 0 sources (Andre, Ward-Thompson, & Barsony, 1993; André, Motte, & Bacmann, 1999; Shirley et al., 2000; Visser, Richer, & Chandler, 2002) and giving us insight into the evolutionary sequence.

2.5 SCUBA - 2

SCUBA - 2 (Holland et al., 2003, 2006) is a submillimetre camera with 10,000 detectors, built to replace SCUBA on the JCMT. It is designed to map large areas of sky up to 1000 times faster then SCUBA. The instrument is cooled to 100 mk, 0.2 K colder than SCUBA. SCUBA - 2 consists of detector arrays and sub arrays which image the sky at two wavelengths simultaneously, 450 and 850 μm. It has three observing modes; imaging mode, scan mode and spectroscopic or polarimetric mode. In imaging mode the telescope observes regions of sky equivalent to the array field of view or mosaics offset frames together to produce an image of up to a few arrays in size. In scan mode the telescope maps large areas of sky, potentially up to tens of degrees at a time and in spectroscopic or polarimetric mode, imaging

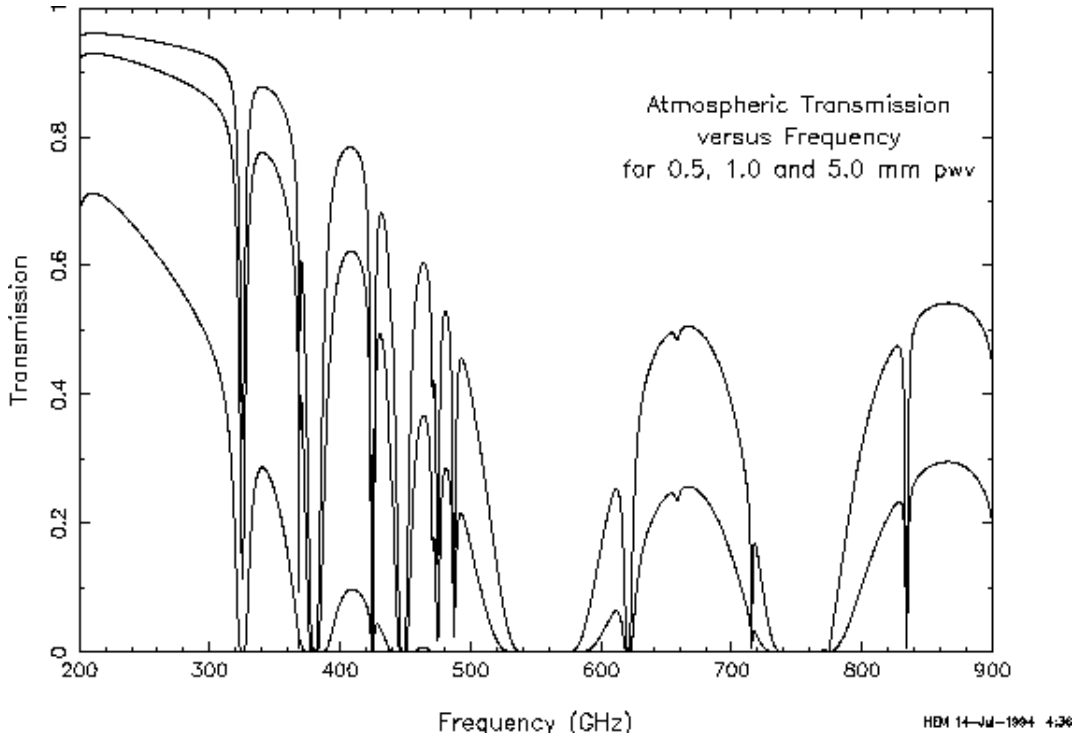

Figure 2.3: Atmospheric transmission calculated as a function of frequency in the submillimetre window for three different water vapour pressures (1mm, 0.5mm and 5mm pwv) (Matthews, 2003).

polarimetry with spectroscopy will be possible but with additional hardware being required.

At the time of writing, SCUBA - 2 is being commissioned with its full complement of arrays and expected to be operational in spring 2011. Some trial science observations have already been carried out. The SCUBA - 2 science programme includes a number of legacy surveys, including galactic star formation surveys: The SCUBA - 2 All Sky Survey (SASSy) which follows on from the IRAS all sky survey, The SCUBA - 2 Cosmology Legacy Survey (S2CLS) which aims to provide the first large samples of extragalactic sources in the 450 and 850 μm wavebands and The Gould Belt Survey (GBS) which aims to survey nearby star - forming regions. These surveys, along with four others make up the JCMT Legacy Survey (JLS).

2.6 *Spitzer* Space Telescope

The *Spitzer* Space Telescope (SST) was built as NASA's great observatory for infrared astronomy. It was launched in August 2003 and observed at 3 – 180 μm with an 0.85 m mirror. The focal plane was cooled to 5.5 K and consisted of three instruments: the Infrared Array Camera, IRAC (Fazio et al., 2004), the Infrared Spectrograph, IRS (Houck et al., 2004) and the Multiband Imaging Photometer, MIPS (Rieke et al., 2004). IRAC is an infrared camera which operates simultaneously at four wavelengths, 3.6 μm, 4.5 μm, 5.8 μm and 8 μm. IRS is an infrared spectrometer with four sub - modules which operate at the wavelengths 5.3 – 14 μm (low spectral resolution $\lambda/\triangle\lambda = 80 - 128$), 10 – 19.5 μm (high spectral resolution $\lambda/\triangle\lambda = 600$), 14 – 40 μm (low spectral resolution $\lambda/\triangle\lambda = 80 - 128$), and 19 – 37 μm (high spectral resolution $\lambda/\triangle\lambda = 600$). MIPS is an imaging photometer

and has three detector arrays in the far - infrared, 128×128 detectors at $24\,\mu$m, 32×32 detectors at $70\,\mu$m and 2×20 detectors at $160\,\mu$m. Data from MIPS are used in Chapter 3.

Two surveys of the galactic plane have been undertaken by *Spitzer*, GLIMPSE and MIPSGAL. GLIMPSE, the Galactic Legacy Infrared Mid - Plane Survey Extraordinaire, is a survey spanning $300\,^\circ$ of the inner Milky Way galaxy. It consists of approximately 444,000 images taken at four separate wavelengths using IRAC. MIPSGAL is a similar survey covering $278\,^\circ$ of the galactic disk at longer wavelengths. Together these surveys have provided the largest and most detailed infrared view of the Milky Way.

In 2004 *Spitzer* found the youngest known star, L1014 (Young et al., 2004), which could not be detected by its predecessor ISO or ground based telescopes. Since 2006, *Spitzer* has also participated in the Gould Belt survey (Evans et al., 2009), observing the Gould Belt in multiple wavelengths. During these observations the discovery of Serpens South was made (Gutermuth et al., 2008a), this is a cluster of 50 young stars in the Serpens constellation. *Spitzer* also had its own legacy surveys including the c2d Spitzer Legacy project which obtained images and photometry with both IRAC and MIPS instruments for five large, nearby molecular clouds (Kirk, Ward-Thompson, & André, 2007; Allen & Gould's Belt Team, 2006; Evans et al., 2009).

Spitzer had much more advanced and sensitive instruments than any previous FIR mission, but the telescope was still not much bigger then its predecessors, For more advances to be made in far - infrared and submillimetre astronomy, larger apertures were needed, this was fulfilled by BLAST and *Herschel*.

2.7 BLAST

The Balloon - borne Large Aperture Submillimetre Telescope (BLAST) was a balloon - borne survey experiment designed to study the evolutionary history and processes of star formation in local galaxies, and galaxies at cosmological distances (Pascale et al., 2008). It contained a continuum camera, with 270 bolometers distributed between three arrays which observed simultaneously at 250, 350, and 500 μm, a gondola, a cryostat, the primary mirror, two star pointer cameras and a stratospheric balloon. Figure 2.4 shows a cutaway model of the cryostat containing the optics box and Figure 2.5 shows the gondola (Truch, 2007). BLAST was designed as a scientific and technical precursor for *Herschel* - SPIRE, and the focal plane design is a direct copy of the SPIRE camera, with many identical or near - identical elements. BLAST had a 1.8 m Cassegrain telescope which provided a nearly diffraction - limited resolution of 36, 42, and 60 $''$ at 250, 350, and 500 μm, respectively.

2.7.1 BLAST flights

BLAST had two successful science flights. The first was a 100 hour flight in June 2005 (BLAST05) (Truch et al., 2007), launched from ESRANGE (Kiruna), Sweden and landing on Victoria Island, Northern Canada. During this flight BLAST conducted large - area surveys of Galactic fields undergoing active star formation (Chapin et al., 2008), nine bright, individual point - like sources (Pallas, CRL 2688, IRAS 20126+4104, IRAS 21078+5211, IRAS 21307+5049, IRAS 22134+5834, IRAS 23011+6126, Mrk 231 and Arp 220) and the compact low - mass protostar L1014-IRS. The second science flight took off on the 21st December 2006

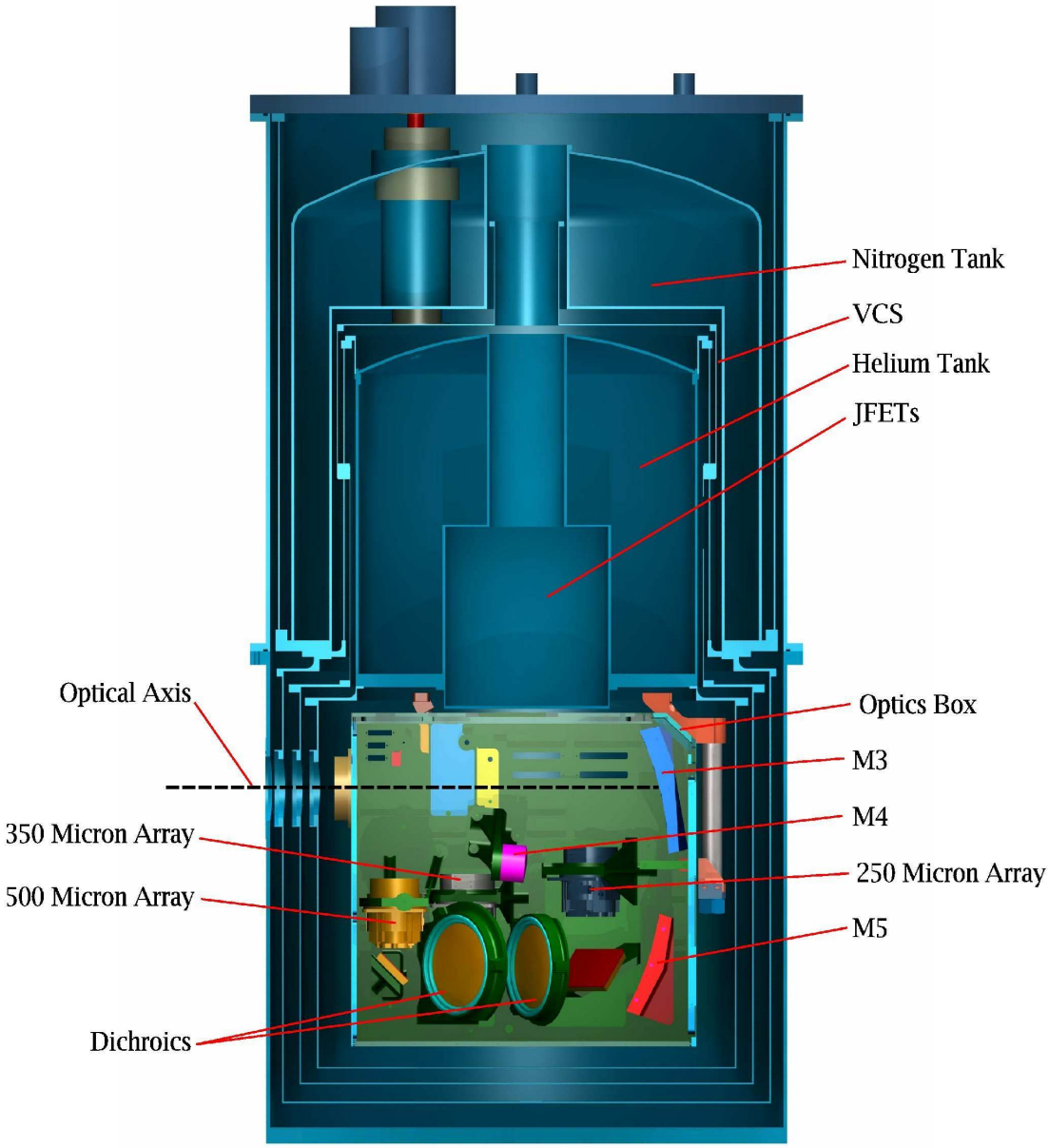

Figure 2.4: Cutaway model of the BLAST receiver showing the optics box (Pascale et al., 2008).

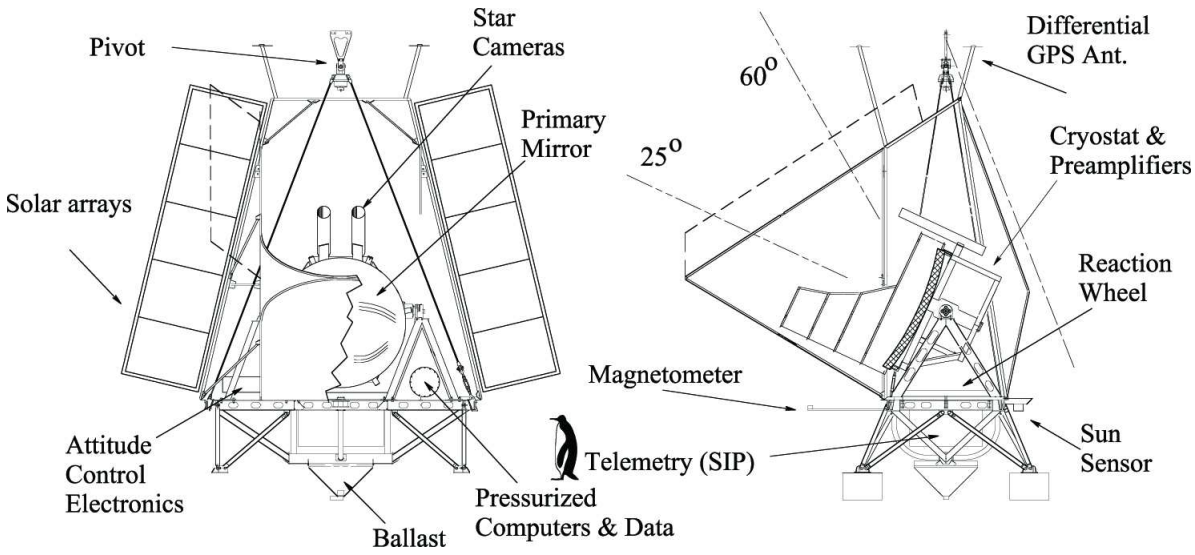

Figure 2.5: Front and side schematic drawings of the BLAST gondola. A 1 m tall Emperor penguin is shown for scale. The inner frame, which can be pointed in elevation, consists of the two star cameras, the telescope and its light baffle, the receiver cryostat and associated electronics. The solar panels and transmitting antennae are suspended below the structure shown here. The lines marked 25 degree and 60 degree show the useful range of orientation of the optic axis. The dot-dashed line at the right originating above the pivot shows a 20 degree avoidance zone required to avoid accidental contact at launch. The dashed parallelogram at the top in the right hand diagram, and to the left in the left hand diagram shows the shape of an extension to the Sun shields added for the Antarctic flight to allow observations to be made further from the anti-sun direction (Pascale et al., 2008).

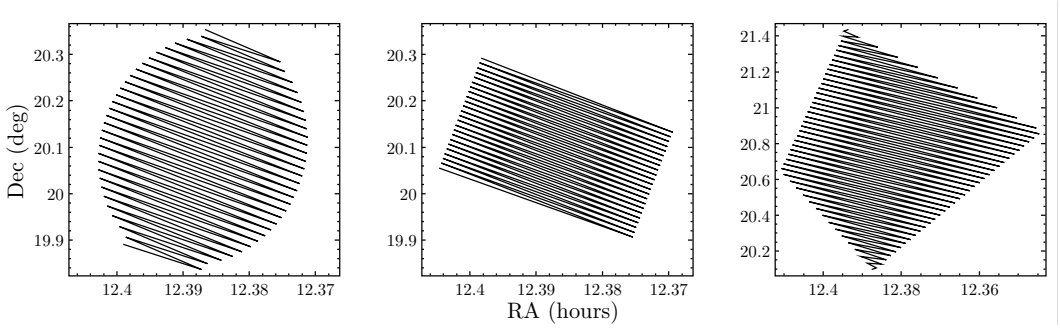

Figure 2.6: Idealised representations of BLAST's three scan modes: from left to right a 'cap', a 'box' and a 'quad' (Truch et al., 2007).

(BLAST06) from McMurdo station in Antarctica. BLAST flew for 250 hours, landing on the 2nd January 2007 on the Antarctic Plateau. It had an average altitude of 38.6 km throughout the flight. During this flight BLAST mapped many Galactic and extra - Galactic sources including the star forming regions Vela (Netterfield et al., 2009) and Carina, the supernova remnant Cassiopeia A (Sibthorpe et al., 2009) and the GOODS - South region (Dunlop et al., 2009). The Carina data are presented in Chapter 3.

2.7.2 Observing mode

BLAST had three primary scan modes, these were: 'cap', a circle centred on a target RA/Dec; 'box', a rectangle in azimuth and elevation centred on a target RA/Dec; and 'quad', an arbitrary quadrilateral specified by its four corners in RA and Dec. These are shown in Figure 2.6. The telescope scanned at a speed of $0.1\,^{o}s^{-1}$, but could scan at $0.2\,^{o}s^{-1}$ on small area maps (less than $0.3\,^{o}$ wide). Full spatial sampling was achieved by using steps of $40-100\,''$ in adjacent azimuth scans.

2.7.3 Calibration

The flux calibration during the second science flight was determined from regular observations of the evolved star VY CMa as it was the only isolated and well known object available throughout the flight. VY CMa is a red hypergiant star which is isolated, point - like, very bright, and is one of the most intrinsically luminous stars known. VY CMa is located in the Galactic Plane at RA = $7^{\,\mathrm{hr}}\,22^{\,\mathrm{min}}\,58.3^{\,\mathrm{sec}}$ and Dec = $23^{\,\circ}\,46'\,3.2''$. Errors in the VY CMa spectral energy distribution produce highly correlated absolute uncertainties of 10 %, 12 % and 13 % at 250, 350, and 500 μm respectively (Truch et al., 2009).

A far infrared spectral energy distribution (SED) of VY CMa was used to calibrate BLAST06. This is shown in Figure 2.7. The data consisted of measurements from IRAS at 12, 25, 60 and 100 μm, SCUBA on JCMT at 850 μm, SHARC - II on CSO at 350 μm, Bolocam on CSO at 1.1 mm and UKT14 on JCMT at 450 and 800 μm. The majority of these instruments were all calibrated to the same Uranus SED (Griffin & Orton, 1993), so all measurements are assumed to have a fully correlated error of 10 %.

2.8 *Herschel*

Herschel is ESA's new far - infrared and submillimetre space observatory. The telescope is named after William Herschel who first discovered infrared radiation. It was launched in May 2009, and is in orbit around the second Lagrange (L2) point of the Sun - Earth system. At this point the Earth blocks most of the thermal radiation from the Sun and the telescope stays in the same orientation with respect

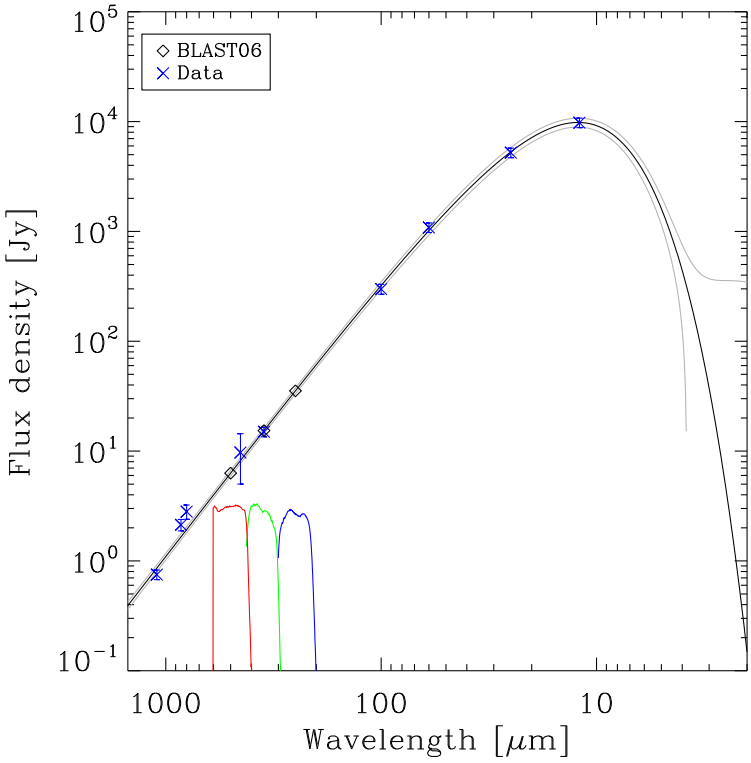

Figure 2.7: Spectral Energy Distribution (SED) of VY CMa, the absolute flux calibrator for BLAST06. The best-fit model (black solid-line) is constrained using the published data (blue crosses), excluding BLAST06 measurements. The grey-lines show the 68% confidence interval, estimated from 100 Monte-Carlo simulations, about the best-fit model. Black diamonds indicate model predictions for BLAST06 at 250, 350, and 500 um. The 1-σ uncertainties associated with these predictions are 8.1 %, 7.1 %, and 7.8 % in each band, respectively, which are highly correlated. For reference, the three BLAST passbands are shown (normalized to an arbitrary amplitude on the plot (Truch et al., 2007)).

to the Earth making shielding much simpler. *Herschel* has the largest single mirror ever built for a space telescope, at 3.5 m diameter, and is the only space observatory to cover a spectral range from the far - infrared to the submillimetre (Pilbratt et al., 2010).

2.8.1 Background and design

Herschel consists of a large superfluid helium cryostat, the primary mirror, a secondary mirror, a sun shield and three instruments: the Spectral and Photometric Imaging Receiver, SPIRE (Griffin et al., 2010), the Photodetector Array Camera and Spectrometer, PACS (Poglitsch et al., 2010) and the Heterodyne Instrument for the Far Infrared, HIFI (De Graauw et al., 2005). These instruments cover the wavelengths $55-672\,\mu$m. The telescope is shown in Figure 2.8. The satellite is expected to have a lifetime of 3.8 years before the superfluid helium is exhausted. *Herschel* has a modular design made up of the payload module (PLM) and the service module (SVM). The PLM contains the cryostat vacuum vessel (CVV) from which the superfluid helium tank is suspended and the optical bench with the three science instruments. The SVM contains the 'warm' payload electronics, the telescope's power, the altitude and orbit controls, on board data handling, the communications unit and safety monitoring.

The cooling concept for the *Herschel* instruments is based on the proven principle used for the ISO mission. The temperature required in the instrument focal plane is provided down to 1.7 K by being connected directly with the superfluid helium dewar, as shown in Figure 2.9. Further cooling down to 0.3 K, required for the PACS and SPIRE bolometers, is achieved by dedicated ^{3}He sorption coolers that are part of the respective instrument focal plane unit. The heat load on the

tank will evaporate the helium over the mission time at an estimated rate of about 200 grams per day. The enthalpy of the gas is used efficiently to cool parts of the instruments that do not require the low temperature of the tank (two temperature levels, at around 4 K and around 10 K). After leaving the instruments the evaporated gas is further used to cool the three thermal shields of the cryostat.

The spacecraft attitude is controlled by means of two components: the star trackers (STR) and gyroscopes (GYR). The STR, starting from an image of the sky, extracts the attitude information measured with respect to the J2000 inertial reference system. Gyroscopes (GYR) are devices that use a rapidly spinning mass to sense and respond to changes in the inertial orientation of its spin axis. Gyroscopes provide high - precision measures of the the spacecraft angular rate. The *Herschel* Altitude Control and Measurement System (ACMS) is provided with four gyroscopes mounted in a tetrahedral configuration. The four gyroscopes are hot - redundant, and each of the four can replace any of the others. The fourth gyroscope is not used for control, but serves to detect any inconsistencies in the output of the other three. The STRs provide an absolute reference, but with limited accuracy. On the other hand, GYRs are very accurate, but only on short temporal and spatial scales. Therefore, the GYR attitude must be re - calibrated using the STR information.

The *Herschel* pointing modes are based either on stare pointings (fine pointing mode) or moving pointings at a constant rate (line scan mode). Raster maps are 'grids' of stare pointings at regular spacings; in the position switching and nodding modes, the boresight switches repeatedly between two positions in the sky. Scan maps are sequences of line scans at regular spacing. Allowed angular speed ranges from 0.1 arcsec/sec to 1 arcmin/sec. In addition, the *Herschel* spacecraft can track moving Solar System targets at rates up to 10 arcsec/min.

All *Herschel* telemetry and auxiliary data is automatically processed at the *Herschel* Science Centre (HSC) with the Standard Product Generation software (SPG), to produce the observational data products, stored in the *Herschel* Science Archive (HSA). The following four levels of *Herschel* data products are defined:

- Level - 0 data product: Raw telemetry data, as measured by the instrument, minimally manipulated and ingested as Data Frames into the mission data base/archive.
- Level - 1 data product: Detector readouts calibrated and converted to physical units, in principle instrument and observatory independent.
- Level - 2 data product: Level - 1 data further processed to such a level that scientific analysis can be performed (e.g., maps or calibrated spectra). These data products are at a publishable quality level.
- Level - 3 data product: These are the publishable science products where level - 2 data products are used as input. These products are not only from the specific instrument, but are usually combined with theoretical models, other observations, laboratory data, catalogues, etc.

2.9 SPIRE

SPIRE, the Spectral and Photometric Imaging Receiver, (Griffin et al., 2010) consists of a three band imaging photometer operating at 250 (PSW), 350 (PMW) and 500 μm (PLW) and an imaging Fourier Transform Spectrometer (FTS) which covers simultaneously its whole operating range of 194 – 671 μm (194 – 313 μm (SSW) and 303 – 671 μm (SLW)) (Swinyard et al., 2003).

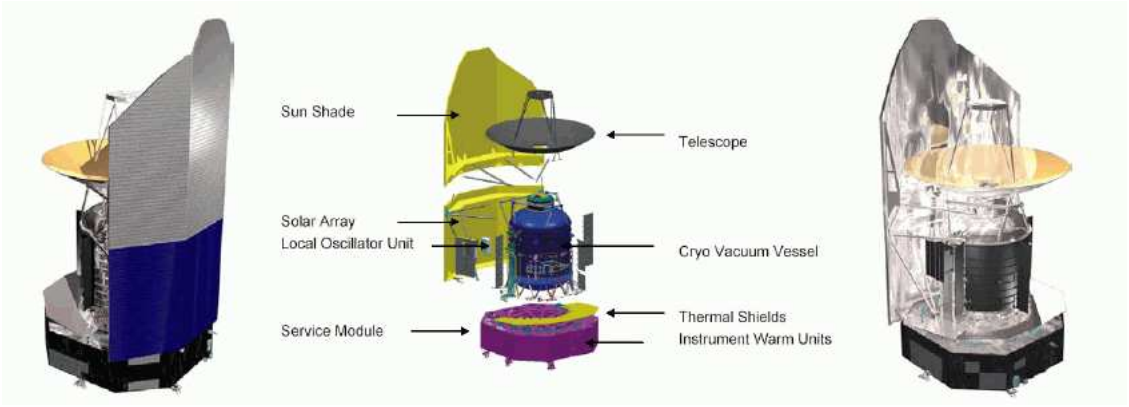

Figure 2.8: The *Herschel* spacecraft has a modular design. On the left, facing the "warm" side and on the right, facing the "cold" side of the spacecraft, the middle image names the major components (Pedro et al., 2003).

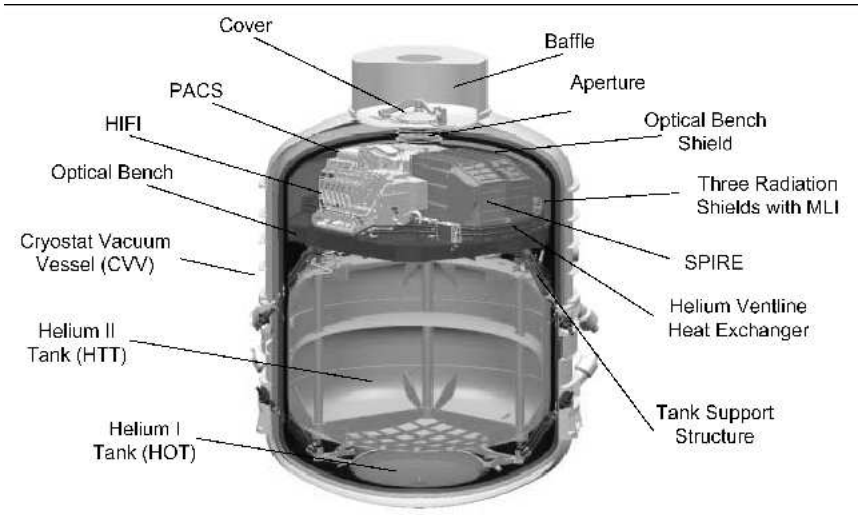

Figure 2.9: The *Herschel* cryostat (Pedro et al., 2003).

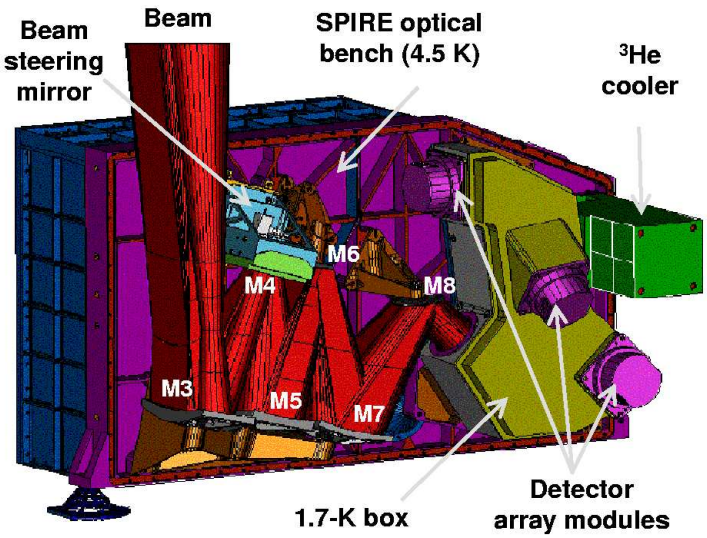

Figure 2.10: Cutaway model of the SPIRE receiver showing the optics box (Griffin et al., 2010).

The detectors are arrays of feedhorn - coupled bolometers cooled to 0.3 K. The arrays have 139 bolometers at 250 μm, 88 at 350 μm and 43 at 500 μm (Chattopadhyay et al., 2003). For the FTS there are 37 bolometers for SSW and 19 for SLW. The photometer has a field of view of $4' \times 8'$ observed simultaneously in the three spectral bands and the spectrometer has an approximately circular field of view with a diameter of $2.6'$. The layout of the photometer side of the instrument is shown in Figure 2.10.

2.9.1 Observing modes

The photometer has three observing modes, point source photometry, small area scan map and large area scan map mode (Griffin et al., 2010). The scan map mode is the optimum mode for most observations. In the scan map mode the telescope is scanned across the sky at 30 or $60''$/s. The scan angle is chosen to give the

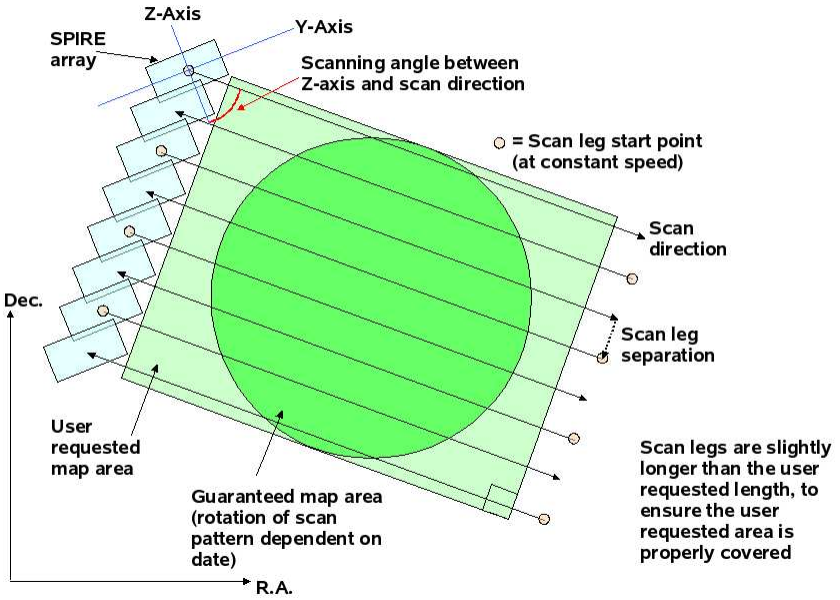

Figure 2.11: SPIRE scan map mode (Dowell et al., 2003).

beam overlap needed for a full spatial sampling, this is shown in Figure 2.11. For one complete map, two scans are normally made in orthogonal directions and then overlapped to provide data redundancy and cross-linking. The FTS takes data by scanning across the mirror at a constant speed (0.5 mm/s) with the telescope at a fixed pointing. For point source observations with the FTS, the source is positioned at the overlapping SSW and SLW detectors, at the array centres; but data are acquired for all of the detectors, providing at the same time a sparsely-sampled map of the emission from the region around the source.

The SPIRE large map and small map data processing pipeline (Dowell et al., 2003) takes as input individual scan lines in the form of timeline data. However, for the purposes of efficient processing, all scan lines for a given observation (including the end of scan turnarounds) are concatenated into a single timeline. After the processing has been completed this single timeline is then dissected into the individual scan lines for map making. All bolometers have a delay in responding

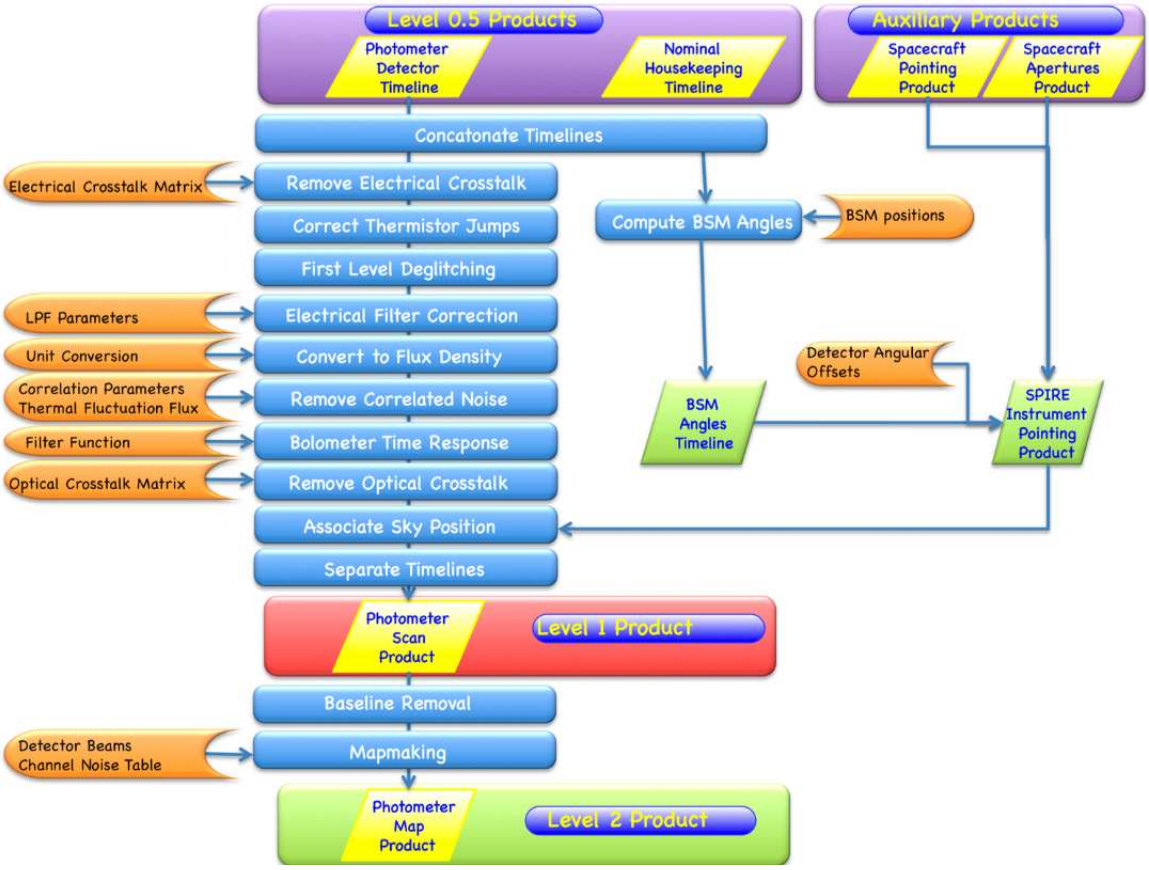

Figure 2.12: The SPIRE pipeline (Dowell et al., 2003).

to incoming radiation. For SPIRE the time constant is around 6 ms, the overall time response of the photometric detector channels is dominated by a 5 Hz low pass filter in the on board analogue electronics chain. These time constants are corrected for in the pipeline. The standard processing pipeline for large/small map mode is shown in Figure 2.12.

2.9.2 Sensitivity

The photometer sensitivity in scan map mode has been estimated from repeated scan maps of dark regions of extragalactic sky. A single map repeat is constituted

by two orthogonal scans. Multiple repeats produce a map dominated by the fixed-pattern sky confusion noise, with the instrument noise having integrated down to a negligible value. This sky map can then be subtracted from individual repeats to estimate the instrument noise. The sky confusion noise is the standard deviation of the flux density in the map in the limit of zero instrument noise. Instrument noise integrates down in proportion to the square root of the number of equal-time repetitions. The achieved instrument noise levels are comparable to the pre-launch estimates which were 9.6, 13.2, 11.2 mJy in beam at 250, 350, and 500 μm, very similar for the 250 and 500 μm bands and better for the 350 μm band (Nguyen et al., 2010).

2.9.3 Calibration

SPIRE has two internal calibration sources, the PCAL source, used in the establishment of the non-linearity correction and the SCAL source, used as a stable thermal source for calibration of the spectrometer and to balance the power from the telescope (Swinyard et al., 2010).

The photometric calibration involves the conversion from bolometer voltage to flux density, based on accurate characterisation of small degree of bolometer non-linearity and the use of Neptune as an absolute standard.

The SPIRE beam profiles are taken to be Gaussian, with the average beam sizes for three arrays (250, 350 and 500 μm) being 18.1, 25.2 and 36.6 $''$ with a 5 % uncertainty and beam areas of 501, 944 and 1924 arcsec^2.

For the wavelength calibration, the central wavelengths for the three photometer bands are derived from pre-flight measurements of the passbands of the

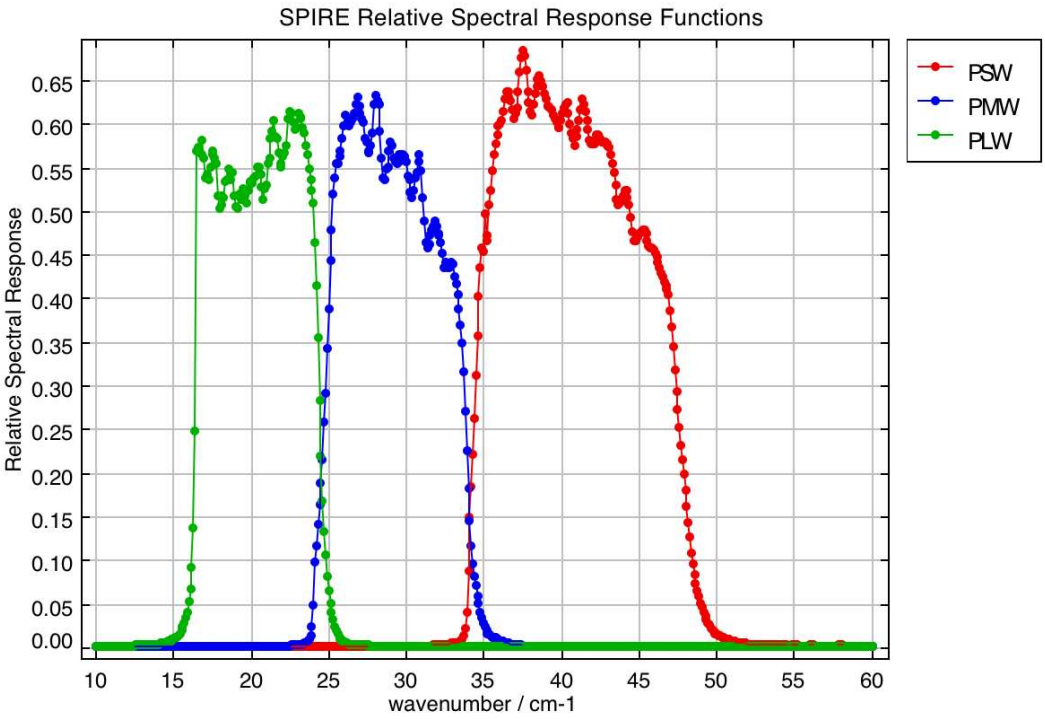

Figure 2.13: The SPIRE spectral response (Dowell et al., 2003).

detectors and their instrument optical filter chain, these are integrated over the waveband assuming a flat spectrum to give band centres at 250, 350 and 500 μm. The spectral responses are shown in Figure 2.13.

2.10 PACS

PACS, the Photodetector Array Camera and Spectrometer, (Poglitsch et al., 2010) consists of a three band photometer covering $60-210\,\mu$m and a spectrometer. PACS has two Ge:Ga photoconductor arrays with 16×25 detectors each and two silicon bolometer arrays with 16×32 and 32×64 detectors (Kraft et al., 2001).

The three bands of the photometer are designated red, blue and green. The long wave red band covers $130-210\,\mu$m and uses the 16×32 detector array with

pixel sizes of $6.4'' \times 6.4''$, the blue short wave band covers $60-85\,\mu$m and uses the larger 32×64 detector array with the smaller $3.2'' \times 3.2''$ pixels, and the green band covers $85-130\,\mu$m and also uses the 32×64 detector array (Agnese et al., 2003).

2.10.1 Observing modes

PACS can operate in either photometry mode or spectroscopy mode. In photometry mode PACS simultaneously images in two bands, either $60-85\,\mu$m or $85-130\,\mu$m and $125-210\,\mu$m with a field of view of $1.75' \times 3.5'$. In spectroscopy mode it has an instantaneous spectral coverage of 1500 km/s, a spectral resolution of 175 km/s and a field of view of $47'' \times 47''$.

When in photometer mode PACS has three observing modes, point source photometry, scan map and parallel mode. Scan map is the default mode for large areas, and is also recommended for small fields and point sources. Scan mapping is performed by slewing the spacecraft at a constant speed along parallel lines, as shown in Figure 2.14. The speeds available are 10, 20 and $60''\ s^{-1}$ in PACS prime mode and 20 or $60''\ s^{-1}$ in PACS/SPIRE parallel mode. PACS performs dual band photometry where it can observe in the red and either the blue or green band. SPIRE and PACS can be used in a parallel mode with data taken in all three of the SPIRE bands and two of the PACS bands simultaneously.

The spectrometer has three observing modes, chopped line spectroscopy, chopped range spectroscopy and wavelength switching mode. Chopped line spectroscopy mode can contain up to ten spectral line scans across different bands. Chopped range spectroscopy mode allows one or several spectral ranges to be observed.

This mode provides two spectral sampling depths, a deep sampling and a coarser Nyquist sampling depth. The deep sampling is used to measure broadened lines or ranges with several lines. The Nyquist sampling depth is used to provide a sampling of at least one sample in every half resolution element by one of the spectral pixels. Wavelength switching mode is an alternative to chopping mode for when the off position cannot be on an emission free area, for example in a crowded region. In this mode the line is scanned with the same grating step as in chopped line spectroscopy, at every step the signal is modulated by moving the line over about half of the FWHM. This allows the differential line profile to be measured, canceling out the background.

2.10.2 Sensitivity

The photometer sensitivity is driven by the foreground thermal noise emission, mostly from the telescope and the electrical noise of the readout electronics. To first order the sensitivity in all modes scales with the inverse of the square root of the on - source observation time.

The in - orbit performance depends critically on the effects of cosmic rays, in particular, high - energy protons. Analysis of in - orbit data as well as proton irradiation tests on ground indicate a permanently changing detector responsivity: cosmic ray hits lead to instantaneous increase in responsivity, followed by a curing process due to the thermal IR background radiation (Fischer et al., 2004).

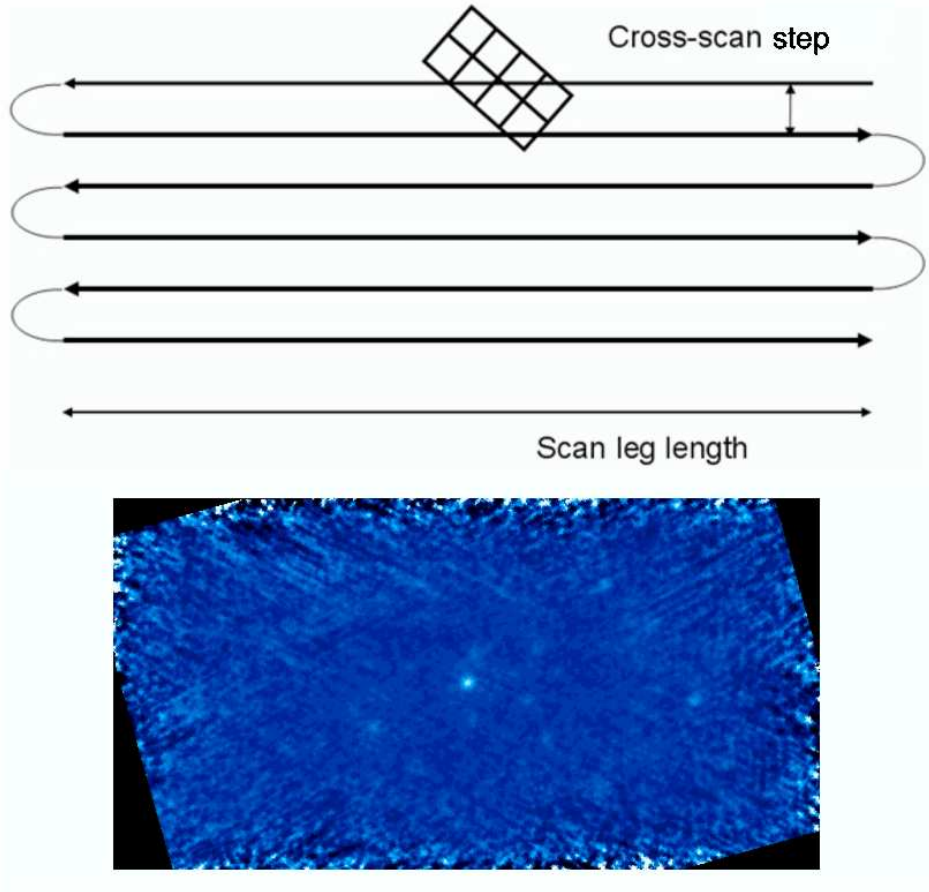

Figure 2.14: PACS scan mode path and a sample scan map (Poglitsch et al., 2010).

2.10.3 Calibration

The photometer is calibrated using an absolute flux calibration based on models of fiducial stars (α Cet, α Tau, α CMa, α Boo, γ Dra and β Peg) (Dehaes et al., 2009) and more than ten asteroids. Together they cover a flux range from 100 mJy up to 300 Jy. All the sources agreed very well in all three PACS bands and the established absolute flux calibration is consistent within 5 %, with a 10 % absolute calibration accuracy. Neptune and Uranus which have flux densities of several hundred Janskys are close to the saturation point, but have been used for flux validation. The calibration itself comprises: (i) flat - fielding, (ii) responsivity correction – conversion of engineering units (volts to Jy/pixel), and (iii) gain drift correction to account to small drifts in gain with time.

The flux calibration of the PACS photometer assumes that the detectors are linear in the full dynamic flux range observable by PACS. A set of celestial flux calibrators allow either colour - correction of the measured spectral densities or computation of the expected measured spectral densities. There is no indication of any near infrared or mid infrared filter leakage. PACS reference wavelengths were identified using the photometer filter transmission curves and bolometer responses as 70, 100 and 160 μm. The spectral responses are shown in Figure 2.15. The colour corrections were determined from the photometer filter transmission curves and bolometer responses and were found to be very small (Müller & Lagerros, 2002).

2.10.4 SPIRE and PACS Parallel Mode

Herschel offers a Parallel Mode, using SPIRE and PACS (Poglitsch et al., 2010).

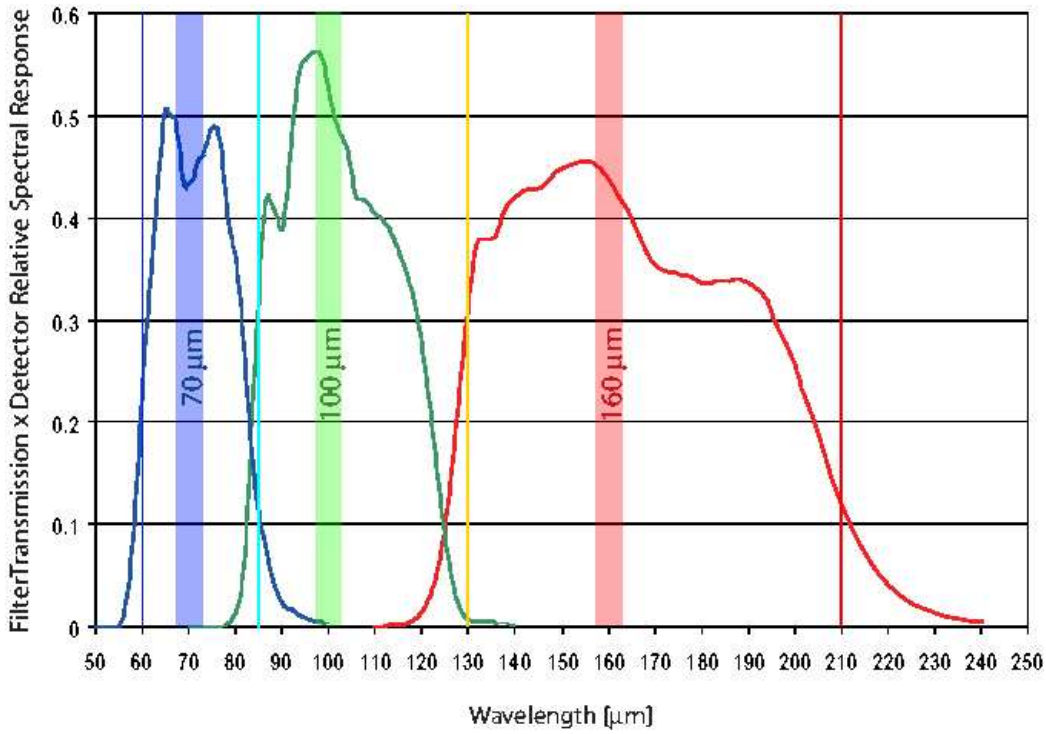

Figure 2.15: PACS spectral response (Poglitsch et al., 2010).

This is used to carry out large-scale mapping programmes with a wide range of wavelength coverage. The parallel mode sky coverage maps are driven by a fixed $21'$ separation between the PACS and SPIRE footprints. This mode is intended to make ambitious, multi-band, large area mapping programmes more efficient than carrying them out individually with each instrument in turn. In this mode SPIRE is the prime instrument and thus the driver in defining observations. While the SPIRE integration gets to a depth which is fairly close to the confusion limit (at a scan rate of $20'' s^{-1}$), the depth of exposure is relatively less for PACS. There are many advantages to using the parallel mode. Operating SPIRE and PACS together increases the load on the helium tank of *Herschel* by much less than a factor of two, because the total load is largely from the cryostat parasitics. Parallel operation is thus very favourable in terms of science per litre of helium, increasing the overall productivity of the observatory. Moreover, observations made in Parallel Mode will

have more accurate relative PACS/SPIRE astrometry, because the relative angular offsets between the two arrays are fixed and accurately known and the pointing error will be the same for the two instruments throughout the observation. The efficiency of scientific mission planning is also increased because the scheduling of PACS and SPIRE observations of the same sky area can be done within a single block. This reduces the total telescope slew time over the mission lifetime in favour of science time. This parallel mode uses the same pipeline as the SPIRE large and small scan map. Observations made with the parallel mode are used in Chapter 4.

2.11 HIFI

HIFI is the Heterodyne Instrument for the Far Infrared (De Graauw et al., 2005). It is designed to provide spectroscopy at high to very high resolution over a frequency range of approximately 480 – 1250 and 1410 – 1910 GHz (625 – 240 and 213 – 157 μm). This frequency range is covered by 7 'mixer' bands, with dual horizontal and vertical polarizations, which can be used one pair at a time.

There are four spectrometers on board HIFI, two Wide - Band acousto - optical Spectrometers (WBS) and two High Resolution autocorrelation Spectrometers (HRS). One of each spectrometer type is available for each polarization. They can be used either individually or in parallel. The WBS cover the full intermediate frequency bandwidth of 2.4 GHz in the highest frequency bands (bands 6 and 7) and 4 GHz in all other bands. The HRS have variable resolution with sub - bands sampling up to half the 4 GHz intermediate frequency range.

Line radiation is much more difficult to detect than submillimetre continuum radiation (as detected by SPIRE and PACS). There are no amplifiers available to

amplify the weak sky signals at submillimetre wavelengths, but for lower frequencies there are. Heterodyne techniques can be used in which the sky signal is mixed with another signal (Local Oscillator) very close to the frequency of interest. The resulting signal is of much lower frequency, while still having all the spectral detail of the original sky - signal. This signal can then be amplified and analysed (Pearson et al., 2000).

The WBS is based on two (vertical and horizontal polarization) four channel Acousto - Optical Spectrometers (AOS). For redundancy reasons both spectrometers are fully independent. Each spectrometer receives a pre - amplified and filtered signal (4 – 8 GHz). After further amplification in the WBS electronics, the signal is split into four channels which provide the input frequency bands for the WBS optics.

The HRS is an Auto - Correlator Spectrometer (ACS) that can process simultaneously the two signals coming from each polarization of the Focal Plane Unit, FPU (shown in Figure 2.16). The HRS provides capability to analyse four sub - bands per polarization, placed anywhere in the 2.4 or 4 GHz input bands coming from the FPU. The two units of the HRS can be used to process the same four sub - band frequency ranges in each of the two polarizations provided by the FPU, thereby reducing the integration time and providing redundancy.

HIFI's very high spectral resolution coupled with its ability to observe thousands of molecular, atomic and ionic lines at submillimetre wavelengths make it the instrument of choice to address many of the key questions in modern astrophysics related to the cyclic interaction of stars and the interstellar medium. A wide range of chemical and dynamical studies are possible using HIFI.

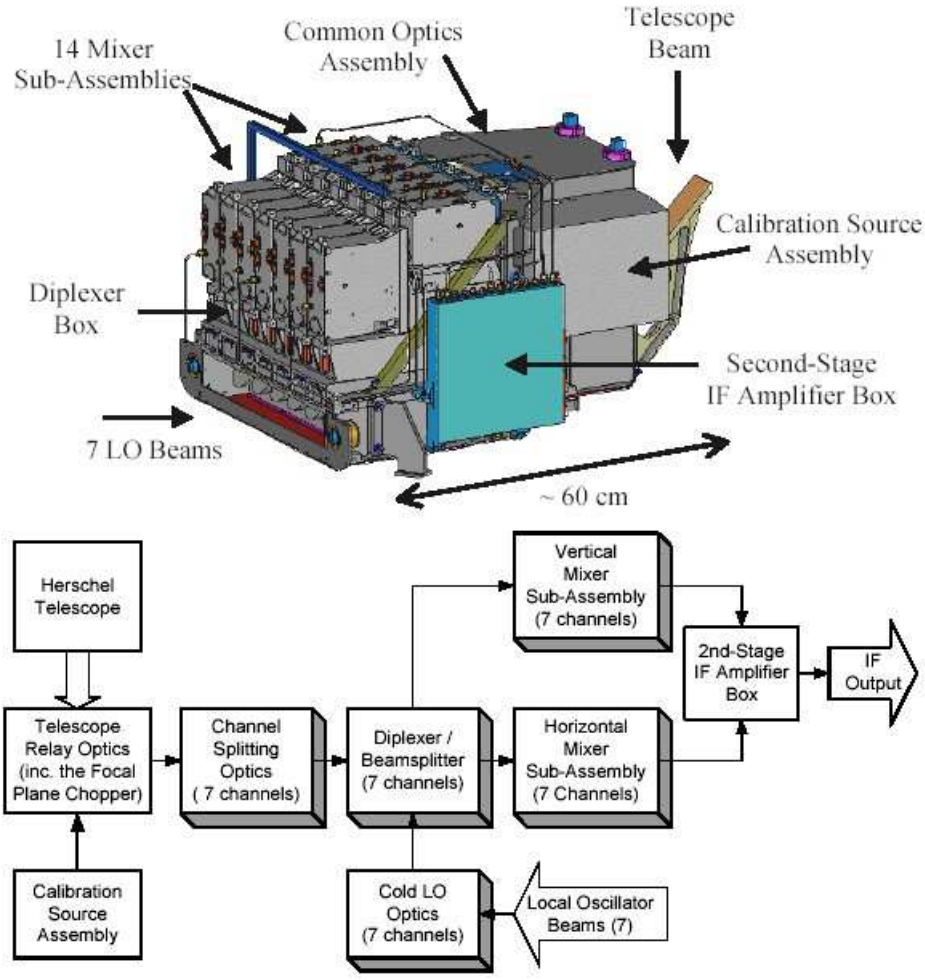

Figure 2.16: The HIFI Focal Plane Unit (FPU) (De Graauw et al., 2005).

2.12 Summary

In this chapter, I have reviewed the past infrared and submillimetre observatories and their scientific achievements. I have introduced the instruments used to obtain the data which are described in the following chapters. The different modes of data acquisition were described, the sensitivity of the instruments was discussed and the calibration methods were outlined.

Chapter 3

BLAST Observations of the Carina Nebula

3.1 Introduction

In this chapter, I present observations of the Carina Nebula, which was mapped at 250, 350 and 500 μm with BLAST in December 2006. In Section 3.2 I give a description of the high mass star formation region, Carina. The BLAST observations, data reduction and map - making is outlined in Section 3.3. The BLAST data have been analysed in conjunction with archival *Spitzer* maps which is discussed in Section 3.4. The source extraction methods are described in Section 3.5. The results are presented in Section 3.6, where I discuss the source sizes, masses, temperatures and luminosities. These are further discussed in Chapter 5.

3.2 The Carina Nebula

The Carina Nebula, NGC 3372, is an extremely bright nebula containing some of the most massive stars in our Galaxy, including the stars Eta Carina (Feast, Thackeray, & Wesselink, 1960) and HD 931294 (Walborn, 1995; Gomez et al., 2009). The nebula lies in the galactic plane, centred at RA $= 10^{\,\mathrm{hr}}\,45^{\,\mathrm{m}}\,08^{\,\mathrm{s}}$ and Dec $= -59^{\circ}\,52'\,04''$ (Dreyer, 1888) and is at a distance of $\sim 2.3\,\mathrm{kpc}$ (Tovmassian, 1995; Smith & Brooks, 2008). An optical image taken by the Hubble Space Station (HST) is shown in Figure 3.1 with several of the key features highlighted. It has a size of approx. $10 \times 10\,\mathrm{pc}$ (Gardner et al., 1970) and contains a dense central region with filaments stretching out towards the dusty pillars, labeled as (c) on Figure 3.1 (Smith et al., 2000a).

Within the Carina Nebula there is the much smaller Keyhole Nebula, labeled as (a) on Figure 3.1 (Lopez & Meaburn, 1984), this is a darker cloud of cold dust containing bright filaments of hot fluorescing gas silhouetted against the much brighter background nebula, and has a size of $2 \times 5\,\mathrm{pc}$. The nebula also contains two open OB star clusters, Tr14 and Tr16, marked as (b) on Figure 3.1 (The, Bakker, & Antalova, 1980).

The massive star Eta Car has been extensively studied at many wavelengths. In 1843 the star underwent a large eruption spilling large quantities of dust into the surrounding nebula, helping to kick start a new wave of star formation in the region (Megeath et al., 1996; Smith et al., 2010a).

We know that regions such as the Carina Nebula are high mass star formation regions for a few reasons, first there is already evidence that high mass star formation has taken place, in Carina this is the presence of Eta Carina. These are also

much larger then most of the closer low mass star formation regions meaning that there is more material available to produce a higher quantity of protostars which increases the likelihood of higher mass stars forming here. Finally the presence of stellar clusters provides the ideal conditions to produce high mass protostars (see Chapter 1 for more details on the formation of high mass protostars).

3.3 BLAST observations, data reduction and map - making

The data used for this analysis were taken during the BLAST06 science flight in December 2006 as described in Chapter 2. The total duration of the observation was one hour, and comprised two scans in orthogonal directions. The scan mode used to take the data was the 'cap' scan mode (discussed in Section 2.7.2). The total area mapped was approximately 3 $\times$ 3 degrees. The raw data were reduced using a common pipeline and made into maps using the routine SANEPIC, Signal And Noise Estimation Procedure Including Correlations (Patanchon et al., 2008).

SANEPIC uses time ordered data pre - processing which takes several steps to process the data before map - making, each step is designed to remove an artefact. The first step identifies events in the data which are localised in time, such as cosmic ray hits. The corrupted samples are removed and replaced by the average value of the samples in the vicinity. The data are then corrected in the Fourier domain for the effect of the low - pass filter in the BLAST on - board electronics. Approximately 2 % of the data samples are removed due to cosmic ray events, most of which affect a single detector. The second step filters out very low frequency drifts due to detector and telescope thermal variations. This is done by fitting a

Figure 3.1: Optical image of the Carina Nebula taken using the HST a) Eta Car b) Key hole nebula c) dusty pillars and d) open OB star clusters (Smith et al., 2007)

5 th order polynomial to the data and then removing it from each data segment (these segments can vary from 30 minutes to a few hours in length). The third step involves correcting for the time - varying calibration using measurements of an internal calibration lamp. Finally the data are put though a high - pass filter ($5 \times 10^{-3} Hz$). The high - pass filter removes residual low - frequency noise. This affects the fidelity of the maps on large angular scales of 20^o, but has little effect on the final maps as the data that are cut in this way are not expected to contribute significantly to the signal.

The data were taken in multiple scanning directions and then cross - linked during the map - making procedure, this gives a number of additional constraints. Large scale structure in the map are much better recovered in directions parallel to scans as the noise is smaller. Residual noise at low spatial frequency in the maps is significantly reduced in cross - linked maps. In timelines that include a bright object, such as Eta Car, some pixels become saturated and this causes striping across the map. To reduce this a mask is put over the effected pixels during the map - making process, so these pixels are effectively ignored and then the mask is removed in the final map. The final maps are shown in Figure 3.2.

SANEPIC is designed to deal efficiently with multi - detector data in the presence of correlated noise between detectors. It works based on an iterative algorithm that converges on the maximum likelihood maps, based on a conjugate gradient with pre - conditioner. The method works by a weighted variance of the difference between two map vectors, the first an inverse pixel - pixel covariance matrix times the current estimate of the map and the second, a map constructed by co - adding pre - whitened data. These then converge to the max likelihood map. The filtered data samples are then added to the pixels to make the final map.

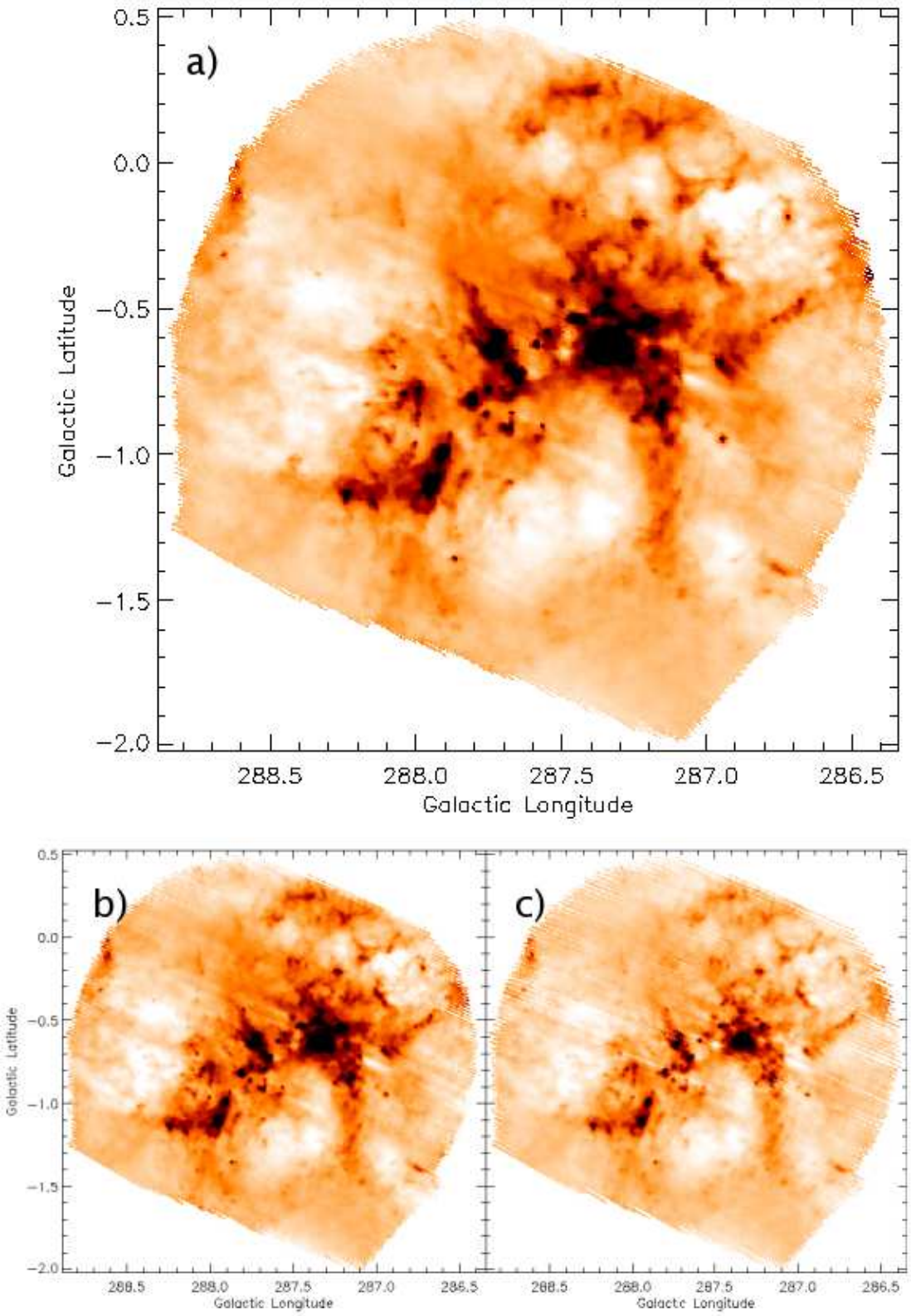

Figure 3.2: The Carina Nebula at the three BLAST wavelengths, a) 250, b) 350 and c) 500 μm

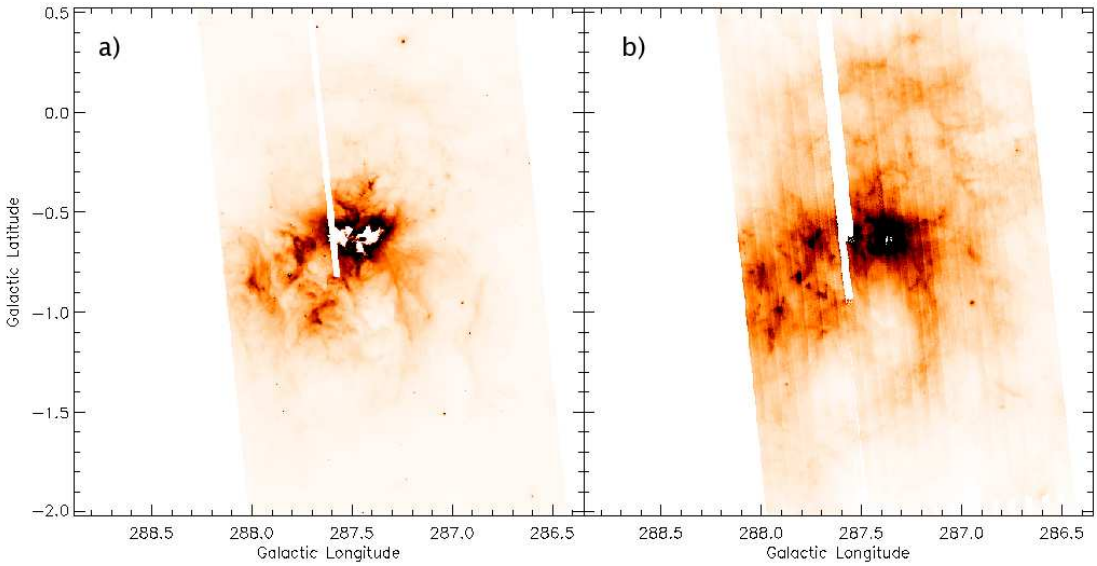

Figure 3.3: The *Spitzer* MIPS maps at a) 24 μm and b) 70 μm. The blank pixels are where the MIPS detectors became saturated due to Eta Car and Tr 14.

3.4 *Spitzer* observations

Along with the BLAST data I have also used archived 24 and 70 μm *Spitzer* MIPS data shown in Figure 3.3. The 160 μm data were also available but highly saturated so provided no useful contribution to the analysis. These data cover a smaller area compared to the BLAST data and are saturated in some regions due to Eta Car and Tr 14. The Basic Calibrated Data (BCD) was retrieved using the Spitzer Science Center (SSC) leopard software and mosaiced together using MOPEX (MOsaicker and Point source EXtractor). The archival MIPS data have been calibrated using primary (asteroids) and secondary (red extragalactic sources) calibrators. The maps are centered on 19:10:25.559 -00:45:06.16 with a pixel size of 15″ and have dimensions of $152.5 \times 152.5'$. The 24 μm data are used to provide upper limits for the Spectral Energy Distributions (SEDs) as the emission is mainly from a hotter dust component.

3.5 Source extraction

Before the advent of large - scale submillimetre mapping observations, source extraction could be conducted by eye, but as larger data sets became more available an automated version was required. The first routine to be developed was Gauss-clumps (Stutzki & Guesten, 1990) which fitted the data with a sum of triaxial Gaussians. A number of algorithms followed including Clumpfind (Williams, de Geus, & Blitz, 1994), a method based on the "by - eye" method of drawing contours and then locating emission peaks and SExtractor (Bertin & Arnouts, 1996) which uses a thresholding method that extracts eight contiguous pixels from a template frame. The specific algorithm I have used on my data was the Cardiff Source finding AlgoRithm, CSAR, developed by J. Kirk (Kirk, 2010). CSAR is a contour based algorithm. In this method a source is defined as a region that has a size for a set of contiguous pixels defined through a well - defined contouring process, and with the requirement that it does not contain more than one sub - region that also satisfy the same constraints. A detailed analysis of extraction methods can be found in Chapter 4.

First the rms for the whole map is estimated and then contours are constructed at integer multiples of the rms value, all the way up to the maximum pixel value in the map (although in cases where a single bright feature dominates the map we take the highest contour to be at a slightly lower level). Starting at the highest pixel level a binary mask is created where pixels above the contour are given the value 'true', and all other pixels are 'false'. Then all contiguous regions of 'true' pixel are found and a catalogue of candidate 'sources' is constructed for that contour level. A source will first appear at some high contour level, but as the contour level decreases, the contiguous pixel zone will grow in area. The growth is tracked

from one contour level n to the next lowest level $(n-1)$ until the point where one source in the $(n-1)$ th level overlaps two or more sources at the n th level. This is where growth is terminated, and the area of the source is determined by counting pixels at the n th level. Two additional restrictions are imposed before a source is added to the catalogue. The first is that a source must have a contrast level greater than some threshold (e.g., 3 or $5\,\sigma$) between its maximum and minimum pixel values to distinguish between a source and noise. The second is that a source must be larger than the beam area, which acts to filter out noise spikes.

CSAR has three user selectable parameters, these are, the pixel size of the map, the value of sigma and the number of sigma needed for a source to be believed. CSAR has been extensively tested as part of the *Herschel* SAG3 source extracting trials which is discussed further in Chapter 4.

For each map, the rms value was obtained by drawing sky apertures over three dark areas in the map and taking the average value. This yielded rms values of 28, 28.1 and 7.64 mJy for 250, 350 and 500 μm respectively. The contours were defined at 1/20th sigma slices to help constrain the extent of each source and 15 $''$ pixel size for each map has been used. The contours for the 250 μm map are shown in Figure 3.4 with the locations of the identified sources marked on. The source extraction was performed at 250 μm and then a mask was used to extract the flux densities from the other wavelengths, including 24 and 70 μm *Spitzer* data (shown in Figure 3.3). A selection of extracted sources is shown in Figure 3.5, in which each source is shown at 250, 350 and 500 μm. The total flux densities were calculated by summing all the flux for each source out to its largest contour as illustrated in the cartoon in Figure 3.6. Background subtraction was performed by measuring the flux in an aperture around each source and then subtracting the average value from the flux of that source. The same aperture size was used at every wavelength. All of

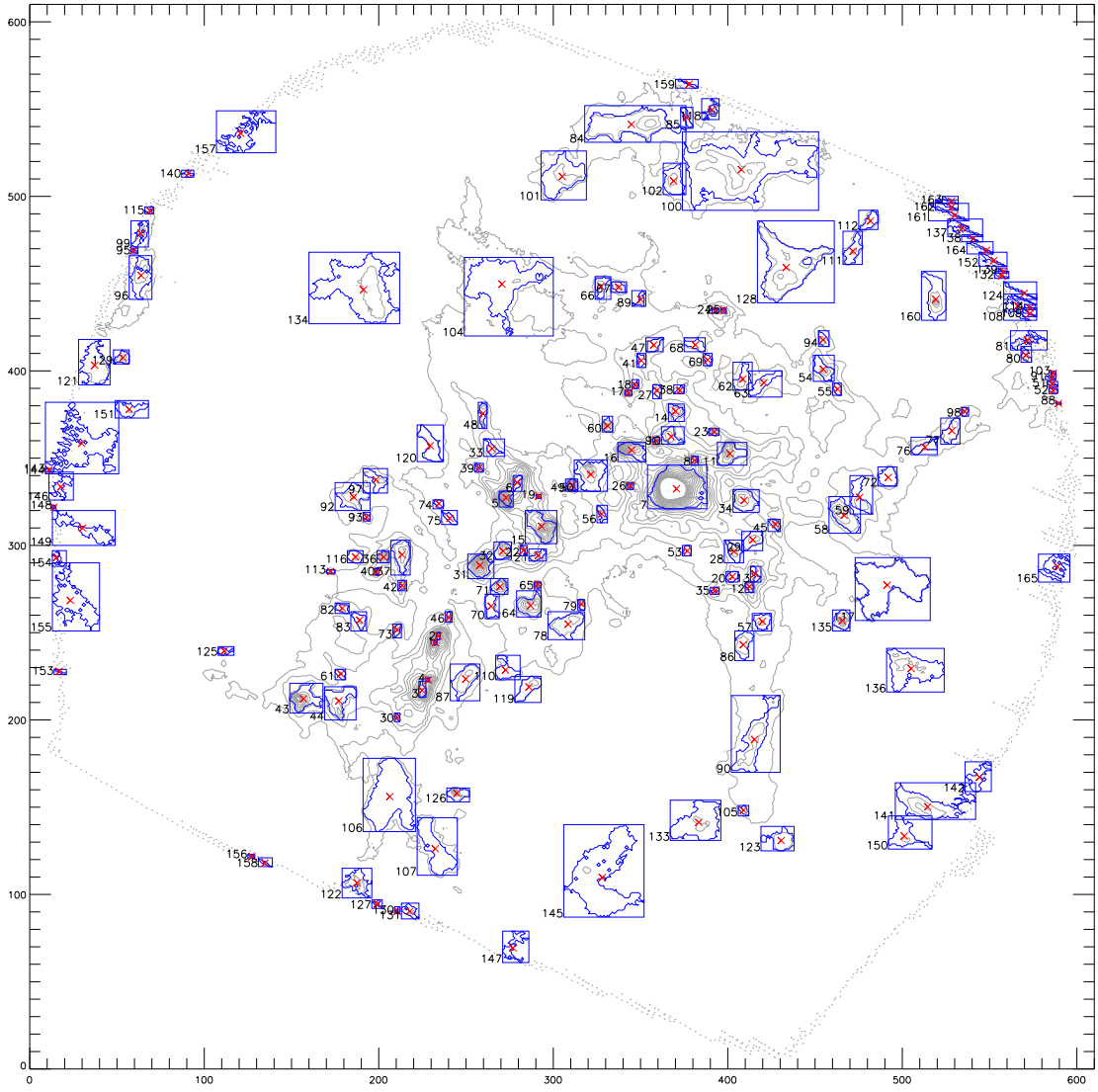

Figure 3.4: The $5\,\sigma$ slice of the $250\,\mu$m data. The blue boxes show the extent of each of the sources and the crosses show their peak. (The contours start at $3\,\sigma$ and increase by $5\,\sigma$ intervals)

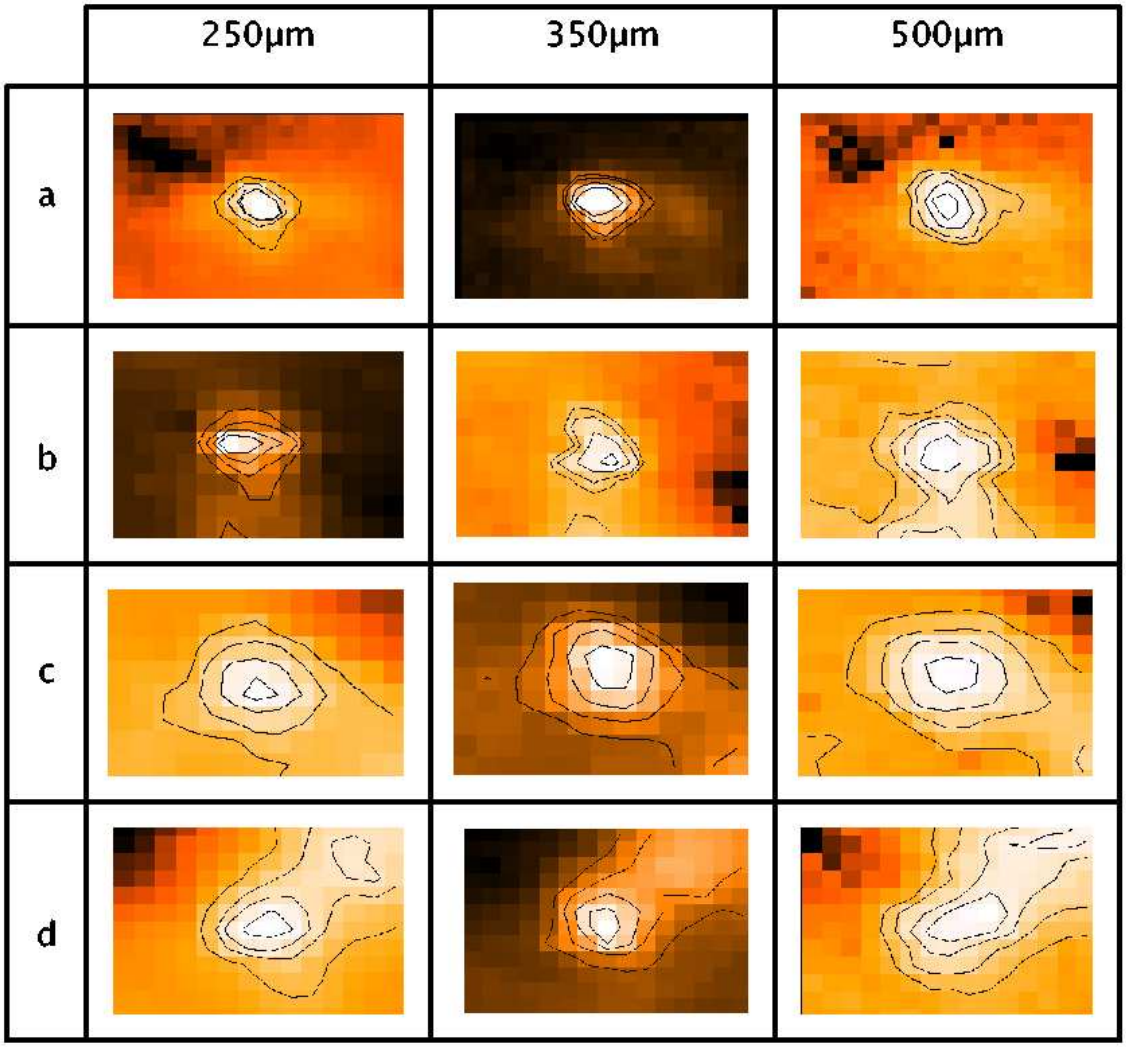

Figure 3.5: A selection of sources shown at 250 300 and 500 μm. The sources are a) BLAST 104417-602703 b) BLAST 104445-595519 c) BLAST 104352-591548 and d) BLAST 104522-592111

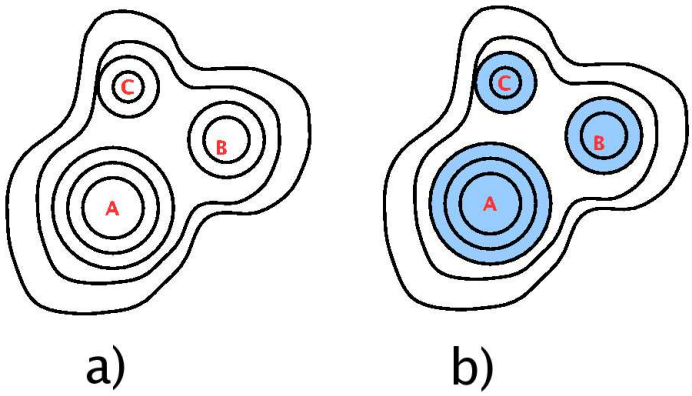

Figure 3.6: A cartoon showing the source extraction method. a) shows a sample contour map b) shows the sources (A, B and C) found by CSAR, the shaded areas show the extent of each source used to find its flux density.

the maps were convolved to the lowest resolution after the mask was created, in this case that was the resolution of the 500 μm map. Altogether, 172 sources were extracted from the maps using this method. The sources positions and total flux densities can be found in Table A.1. 30 % of the sources were not found at either of the MIPS wavelengths, all were found at 250 and 350 μm and 4 % were not found at 500 μm.

To test the completeness limit of CSAR a series of tests were carried out. This involved placing guassian sources of known size and flux density, in a 10 x 10 grid over the Carina and NGC 7538 maps and seeing how many CSAR could extract. This was carried out multiple times, each time reducing the size of the sources, starting with sources with a 8 pc diameter which was then reduced by 0.1 pc each time. Csar performed well in the less densely populated regions of the maps, the outer regions of Carina and the small filaments and surrounding areas in

NGC 7538. However in the more dense regions CSAR failed to locate the smaller sources as they became confused with other sources present in the data and the background cloud. For the Carina region the limit at which CSAR could locate all the inputted sources is a diameter of 0.6 pc which corresponds to a mass of approximately 2.5 $M_{\odot}$. Since this is a study of high mass star formation, not being able to locate the lower mass sources will not affect our results.

3.6 Results

In the following section I discuss the SED fits for the data, the source sizes and morphologies, source luminosities, temperatures and masses. For each I describe how the values were calculated and outline the results. These are discussed further in Chapter 5.

3.6.1 SEDs

For each source I fit a modified blackbody SED, using a IDL routine written by J. Kirk and outlined in Kirk, Ward-Thompson, & Andre (2005), to the three BLAST flux densities and two MIPS flux densities, where available. Fitting the equation:

$$S_{\nu} = \Omega \, f \, B(T, \nu) \, (1 - e^{-(\nu/\nu_c)^{\beta}}), \tag{3.1}$$

where S_{ν} is the flux density at frequency ν, $B(T, \nu)$ is the blackbody function at temperature T and frequency ν, ν_c is the frequency at which the optical depth is unity, Ω is the solid angle of the aperture, f is the filling factor of the source within the aperture and β is the dust emissivity index. For my SEDs I have used a fixed

value of $\beta = 2$. The fit is achieved via a simple chi - squared minimisation between the data and the greybody. The fits use the coldest temperature consistent with the data. From this I have calculated the luminosity and temperature for each source.

The errors on the SEDs consists of the errors from the instrument which in the case of blast are coherent in all wavebands, the errors in the flux densities, and the errors in the photometry. Instrumental errors arise from noise from the warm elements of the instrument and contamination from cosmic rays. The errors from these can be reduced in the data reduction stage as contaminations can be removed from the data. For more detailed discussion on the instrument calibration please see Chapter 2. Errors in the flux densities can occur during the map making process these are caused by using filters on the data and baseline subtractions. Errors in photometry are caused by the sources not having a distinct edge and contamination from the parent cloud. This is partly dealt with by background subtraction which uses the the flux density surrounding the source to act as a baseline, however if the source is in a crowded region where sources are touching then the flux from that source can cause the baseline to be higher then it should be. But most of the flux will be contained centrally so this does not have a large effect on the final flux density of the source.

For each source I have calculated two different SEDs, one using the fit with all the available data points, and the other using the fit with only the three BLAST data points. The SED using all the data points gives an upper limit for the luminosity and temperature as BLAST and *Spitzer* together are sensitive to both the cold and hot dust. The SED using only the BLAST data points gives a lower limit as we are only seeing the cold dust. This cold component of the SEDs will mainly consist of the dusty envelopes surrounding the protostars and not the hotter

embedded protostar itself, but in the early stages of star formation the majority of the mass is contained within the envelope so we will only be missing a small quantity of the overall mass and luminosity by not atempting to fit a more complex two part SED which we do not have enough data points to do reliably. A sample of SEDs is shown in Figure 3.7. The solid line shows the SED calculated using all available wavelengths and the dotted line shows the SED calculated using the BLAST wavelengths only.

3.6.2 Source sizes and morphologies

To measure the radius of each source I took the first unique contour (i.e. an enclosed contour containing only one source) and measured the area within the contour. As the sources are reasonably Gaussian, I then calculated the diameter of a circle with the same area. There is a characteristic source radius of typically $50-80''$ which corresponds to $0.7-1.0\,\mathrm{pc}$ at the distance of the Carina Nebula, and a range of $0.3-3.2\,\mathrm{pc}$ as shown in Figure 3.8. The BLAST angular resolution at $250\,\mu\mathrm{m}$ is $36''$, which is less than the $50''$ lower limit on the source radius, so this limit is not due to resolution effects. The source radii can be found in column 2 of Table A.2.

Figure 3.9 shows a selection of sources and their mean x and y profiles, from these profiles we can see the the sources are reasonably Gaussian. However a small percentage of the sources are more extended in the x direction then in the y. This would suggest that at least some of the sources are resolved. These extended sources, such as BLAST 104445-595519 are treated the same as the Gaussian sources as even though the peak is extended, when we find the largest contour of these tend to be quite spherical.

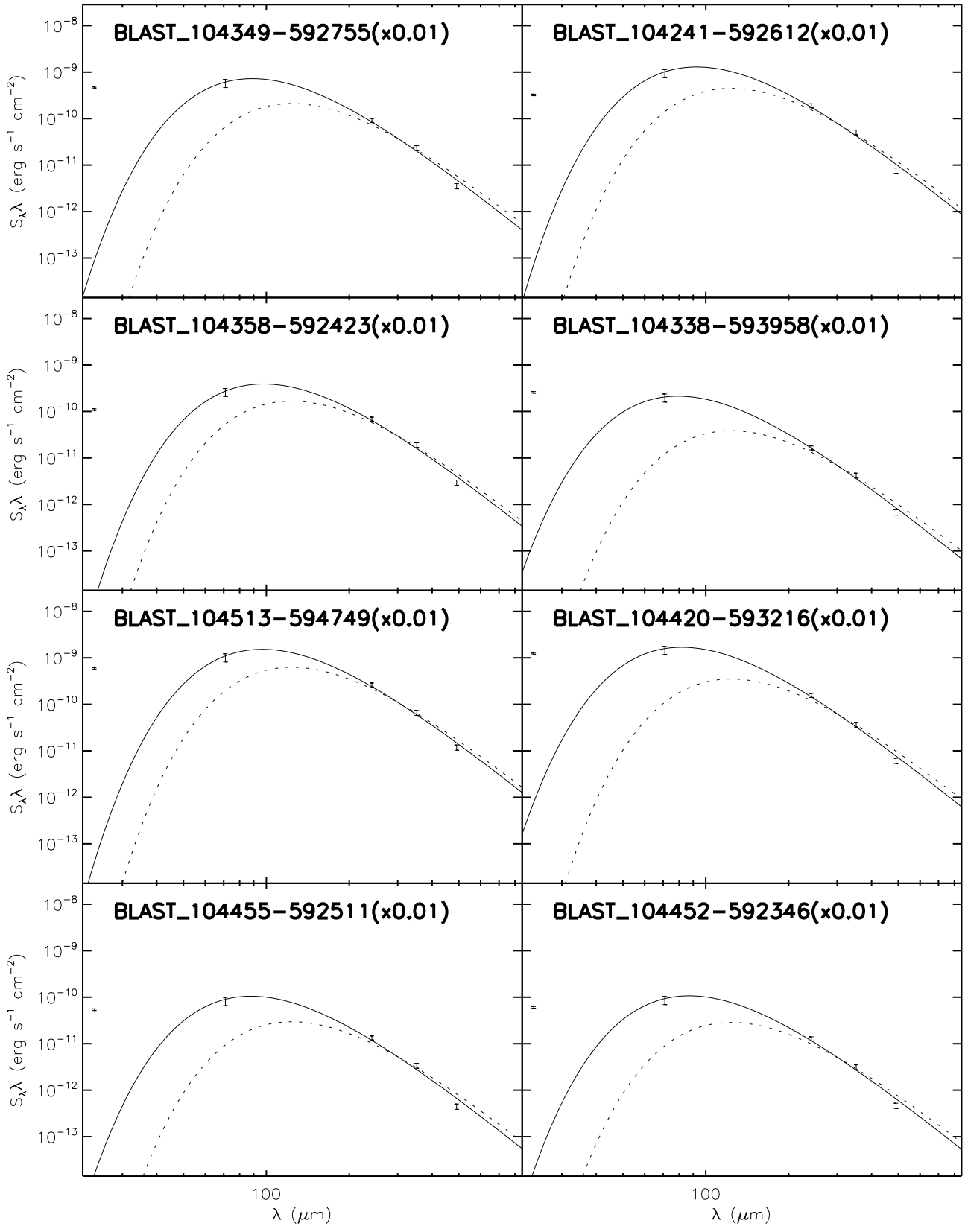

Figure 3.7: A sample of the SED's, the solid line shows the SED calculated using all available wavelengths and the dotted line shows the SED calculated using the BLAST wavelengths only.

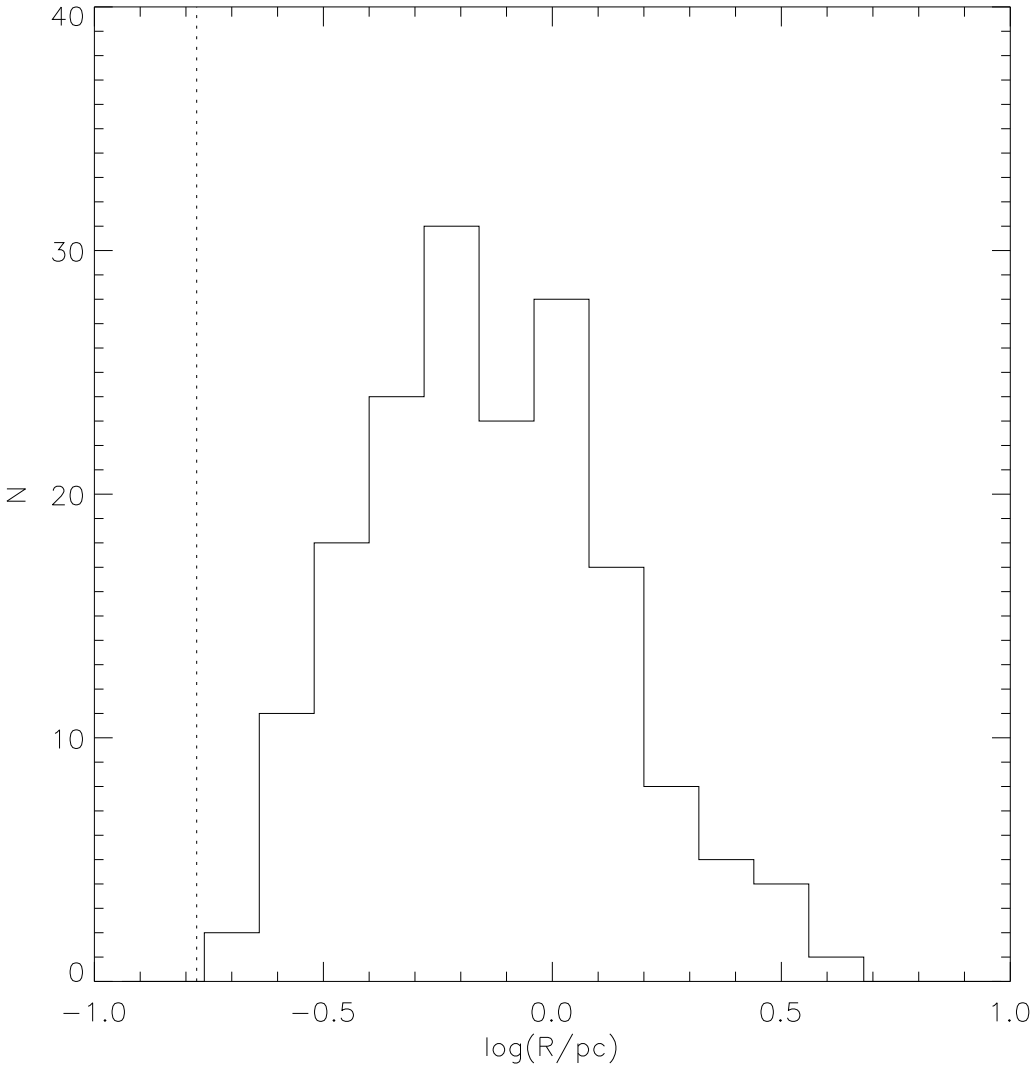

Figure 3.8: A histogram showing the source radii, the dotted line shows the angular resolution of BLAST. (These sizes have been corrected for the beam size)

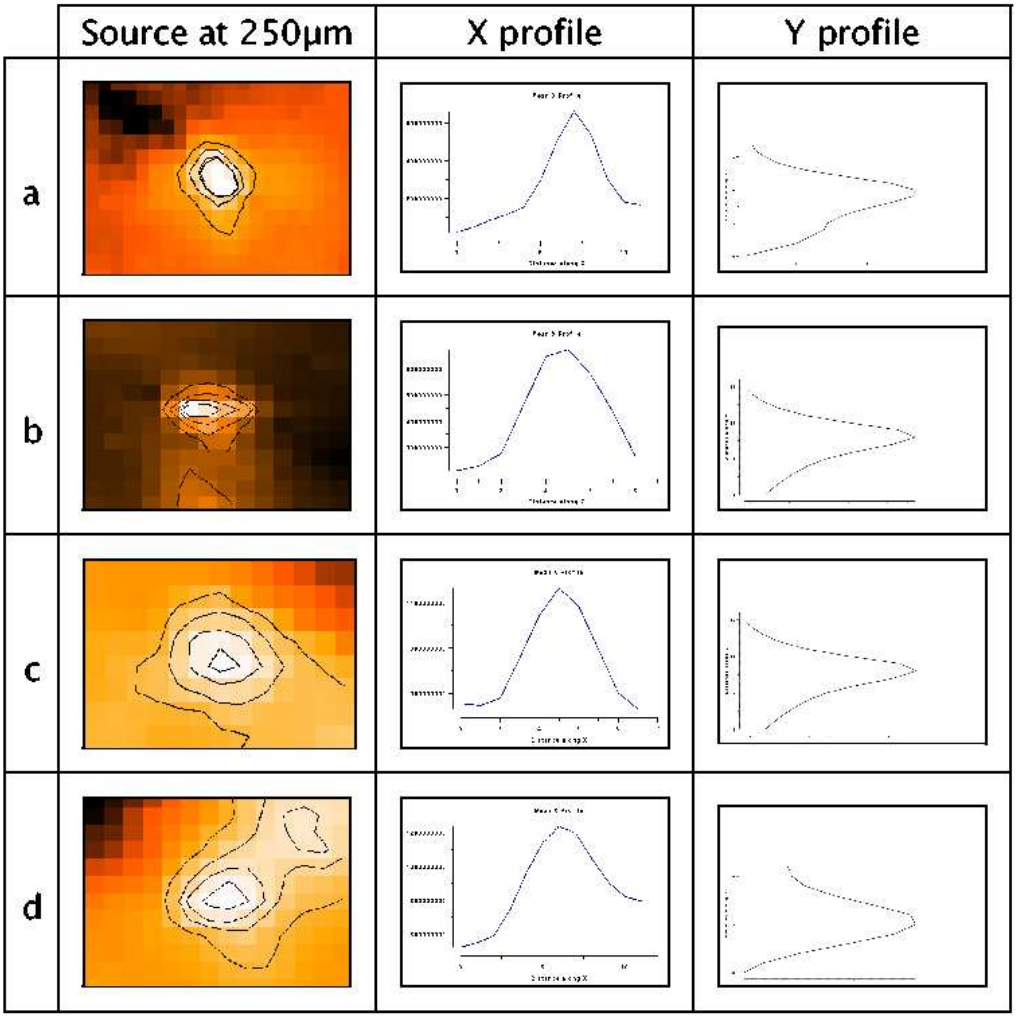

Figure 3.9: A selection of sources shown at 250 μm and their mean x and Y profiles. The sources are a) BLAST 104417-602703 b) BLAST 104445-595519 c) BLAST 104352-591548 and d) BLAST 104522-592111

3.6.3 Luminosities

The bolometric luminosities, $L_{\rm bol}$, of the sources were estimated by integrating directly under each source's SED fit using a simple trapezoidal method. The trapezoidal method involves approximating the area under the curve as a number of trapezoids. The areas of the trapezoids are then summed to give an approximate total area. The distance to each source was taken as 2.3 kpc.

The sources have differing photometric coverage depending on MIPS and BLAST detections, with approximately 30 % of the sources not having MIPS detections. Therefore, I have also calculated the more homogeneous $L_{\rm BLAST}$, which is the luminosity integrated under the fit using the three BLAST wavelengths, 250 – 500 μm. Both of these distributions are shown in Figure 3.10, the $L_{\rm bol}$ distribution peaks at a higher luminosity than $L_{\rm BLAST}$ and also has a higher luminosity tail which is absent in the $L_{\rm BLAST}$ distribution. $L_{\rm bol}$ shows a steep increase with a peak at $\sim 3000\,L_{\odot}$ and then a tail at the higher luminosity end. The completeness limit was calculated using the minimum $5\,\sigma$ detection limit set by CSAR, and gave a cut off of 94 $L_{\odot}$. The source luminosities can be found in column 3 of Table A.2. From the size and luminosities of these sources (see Section 3.6.3) we would expect most to form multiple stars.

3.6.4 Temperatures

Source temperatures derived from the modified blackbody SEDs are in the range 18 – 26 K, and have a reasonably symmetric distribution with a mean of approximately 23 K. The temperature distribution is shown in Figure 3.11, the solid line shows the temperatures calculated using all available data and the dotted line

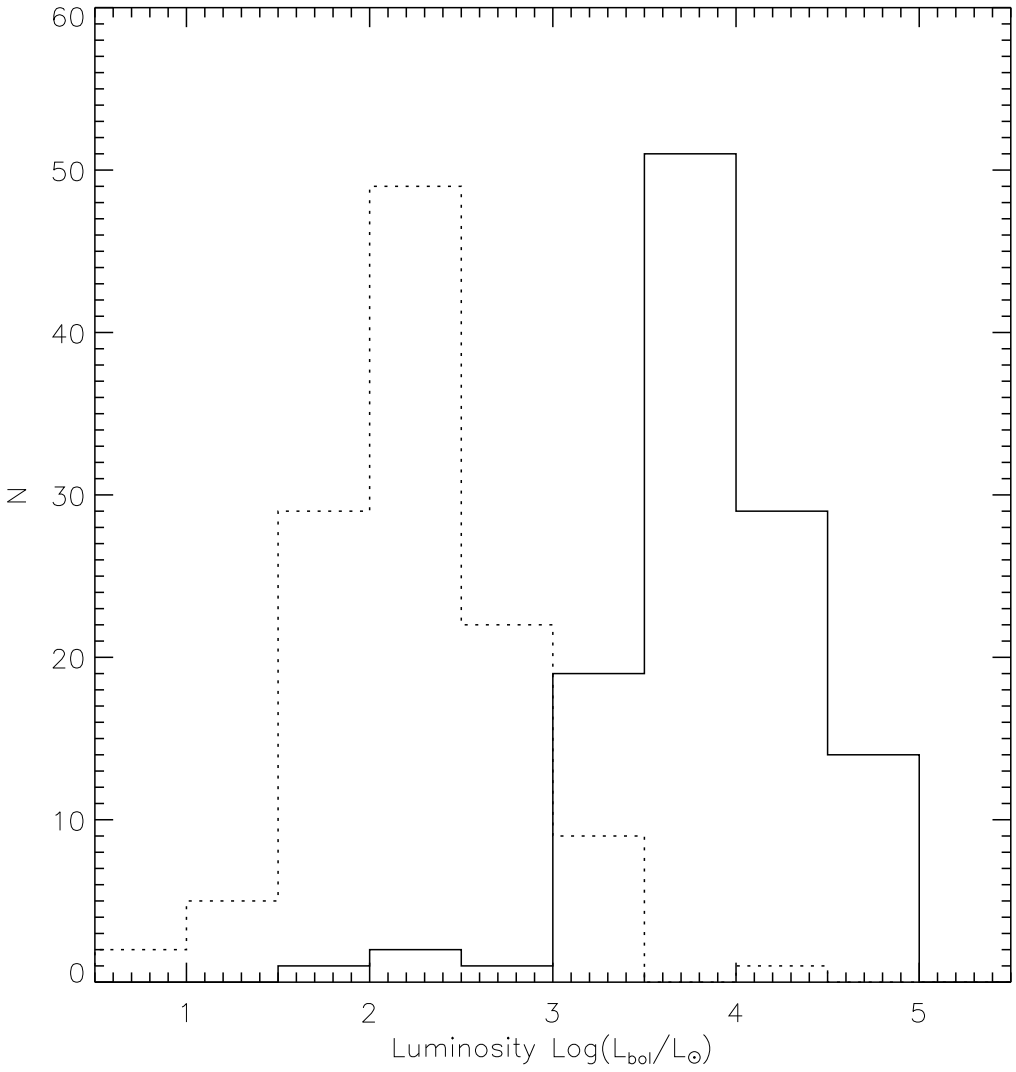

Figure 3.10: A histogram showing the source luminosities. The solid line shows the luminosities calculated using the BLAST and *Spitzer* SEDs and the dotted line shows the luminosities calculated using the BLAST only SEDs.

shows the temperatures calculated using only the BLAST wavelengths. Using the three BLAST points I can only estimate the temperatures for the colder sources ($\leq 20\,\mathrm{K}$). For the warmer objects I can only give a lower limit. The completeness limit for source temperatures is 14 K, which was derived using the same method as with luminosity. The source temperatures can be found in column 4 of Table A.2. To demonstrate the small range of temperatures found in the data Figure 3.12 shows a three colour image of the region. From this image it is clear that there is little change in the thermal emission in the three bands. The temperature dependence is discussed further in Chapter 5.

3.6.5 Masses

I assume that the 250 μm emission is optically thin and source masses are calculated using the following standard equation (discussed in Section 1.2.3) from Hildebrand (1983):

$$M = \frac{S_{250} D^2}{\kappa_{250} B_{250,T}}, \tag{3.2}$$

where,

$$\kappa_{250} = \left(\frac{4/3\, a}{Q_{250}} \right) \rho, \tag{3.3}$$

where S_{250} is the 250 μm flux density, D is the distance to the source, $B_{250,T}$ is the Planck function at the source temperature, T, κ_{250} is the mass opacity of the gas and dust, taken to be $0.16\,\mathrm{cm^2 g^{-1}}$ which was derived by Netterfield et al. (2009), a is the radius of a dust grain, Q_{250} is the emissivity at 250 μm and ρ is the density. The value of κ that we use is very uncertain, with estimates at 250 μm varying

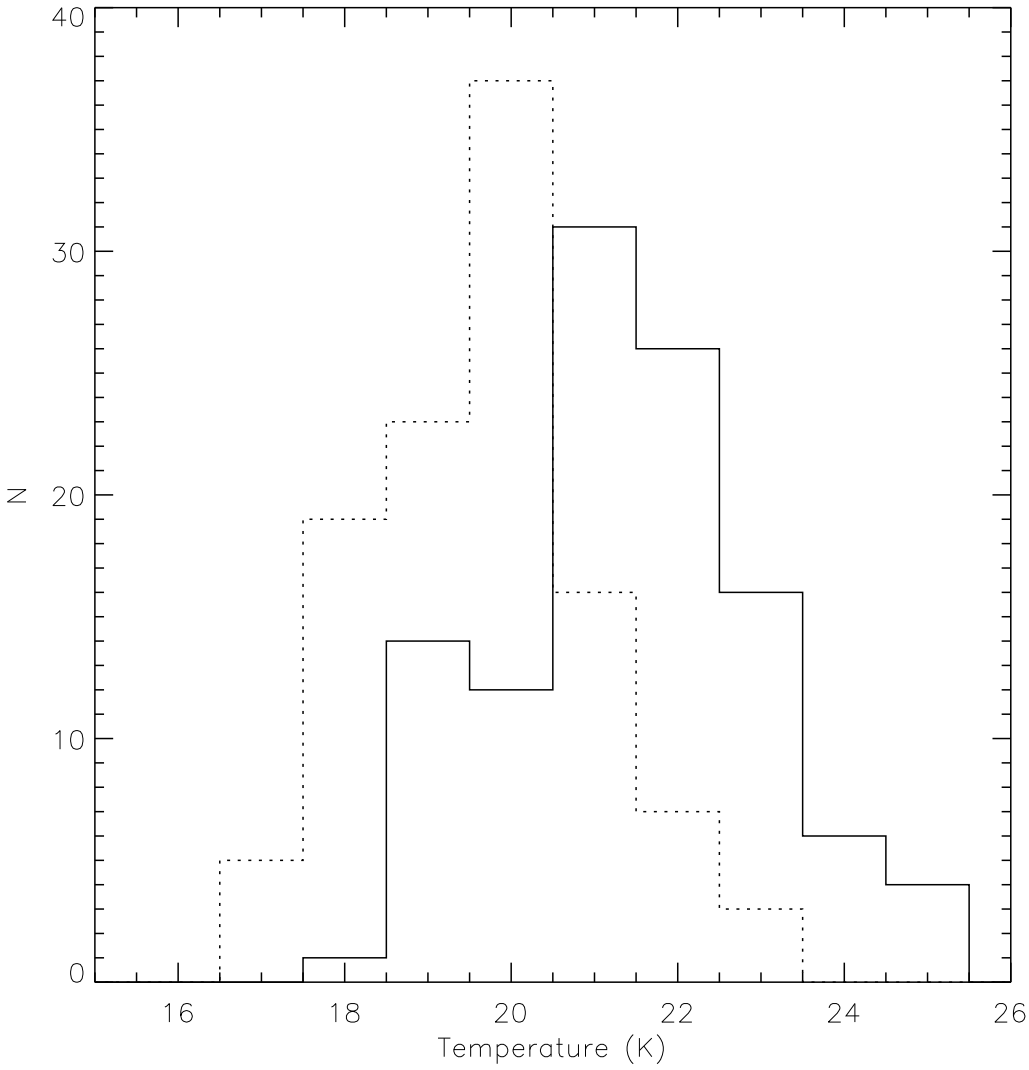

Figure 3.11: A histogram showing the source temperatures. The solid line shows the temperatures calculated using the BLAST and *Spitzer* SEDs and the dotted line shows the temperatures calculated using the BLAST only SEDs.

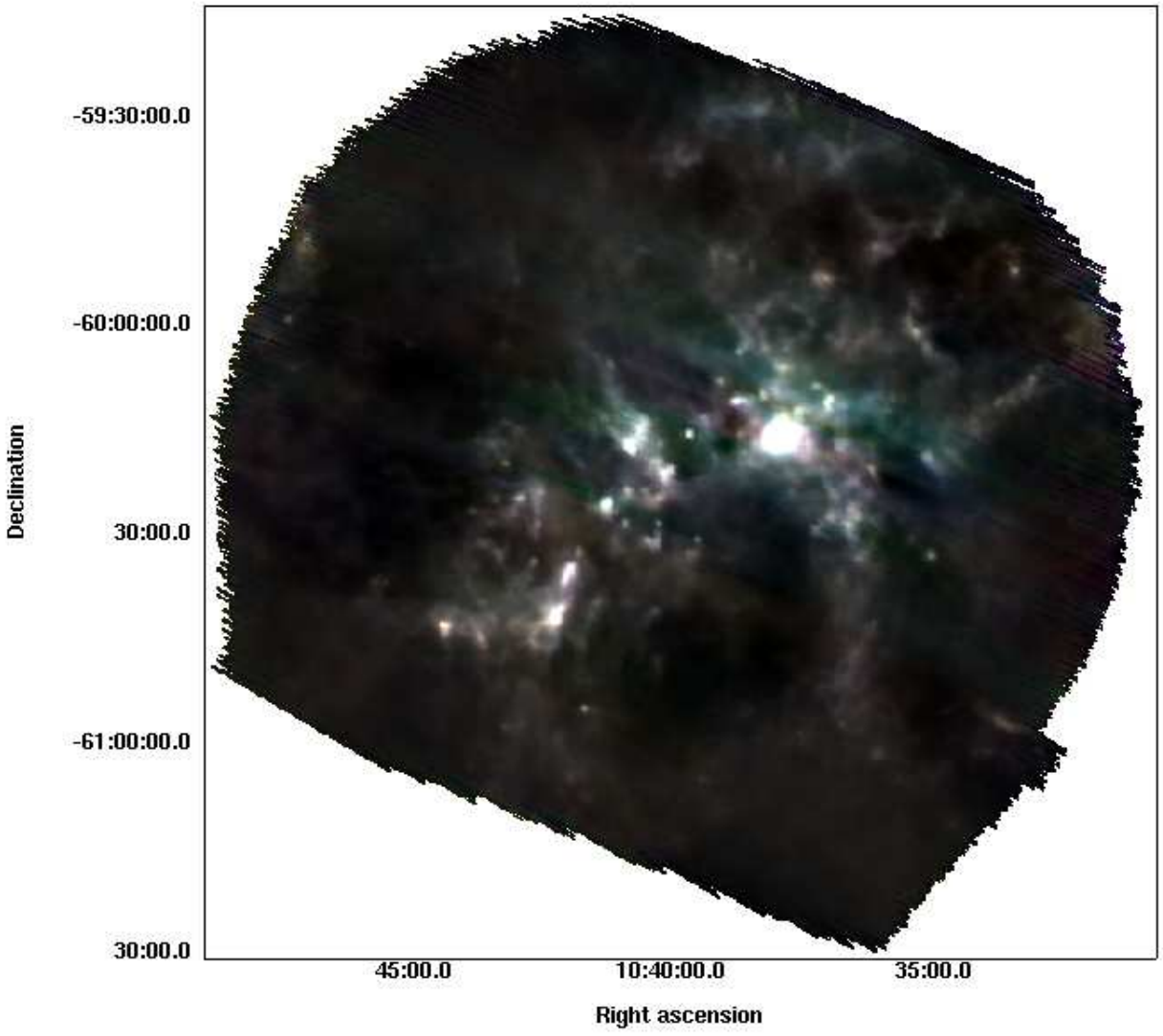

Figure 3.12: A three colour image of the Carina Nebula data. Red is 500 μm, green is 350 μm and blue is 500 μm.

from 0.024 (Draine & Li, 2007) to $0.2\,\mathrm{cm^2 g^{-1}}$ (Ossenkopf & Henning, 1994), the value we have used is quite close to the Hildebrand (1983) value of $0.1\,\mathrm{cm^2 g^{-1}}$.

The masses range from 20 to $10^4 M_\odot$ with a distribution as shown in Figure 3.13. We would expect to find more lower mass sources then we have because of the IMF (see Chapter 1) but this is likely to be due to our source extraction method not finding the lower mass sources. With such high masses, most sources are likely to be associated with cluster which are likely to form multiple stars. Most of these large clusters are likely to form at least one high mass star (a protostar with a mass of $8\,M_\odot$ or more) as well as low mass stars. The source masses can be found in column 5 of Table A.2.

3.7 Summary

In this chapter, I have analysed BLAST observations of the Carina Nebula. Using CSAR to extract sources, I have identified 172 sources. 30 % of which are not present in the MIPS data, and 4 % are not present at 500 μm. Masses of the sources range from 20 to $10^4\,M_\odot$, which indicates that most of the sources will be clusters. The source luminosities range from 10^2 to $10^5\,L_\odot$, which again suggests that the sources are high mass star clusters. I find a very small range of temperatures, 16 to 28 K which is discussed further in Chapter 5. I find source radii that has a range of 0.3 to 3.2 pc. The analysis of the results obtained in this chapter are discussed further in Chapter 5. The masses we have found in Carina are similar to those found by other surveys in this region such as Povich et al. (2011) who used the Two-Micron All Sky Survey to catalogue all the YSO's in the Great Carina nebula which covers a larger area then our maps, and **?** who used *Spitzer* IRAC to studie

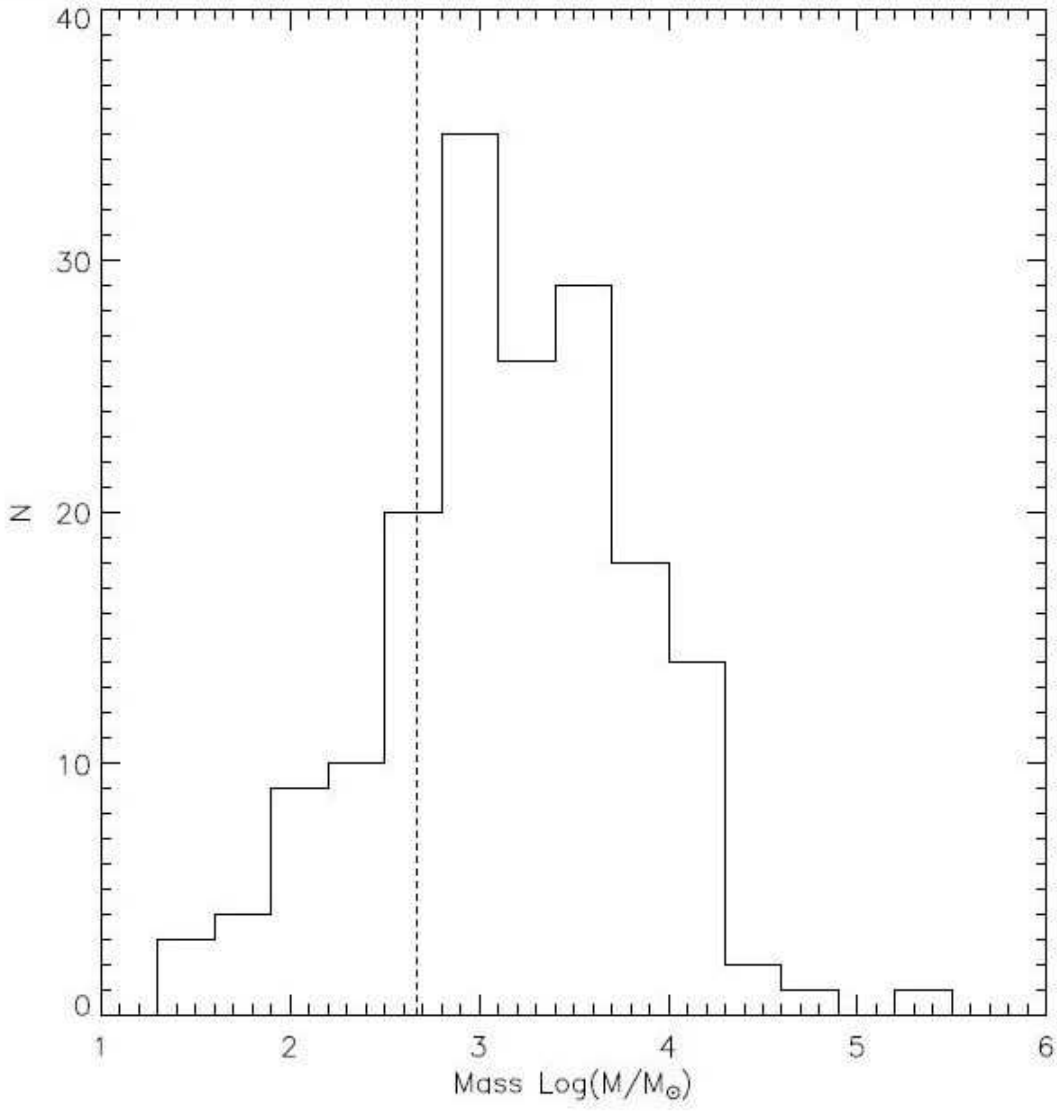

Figure 3.13: A histogram showing the source masses.The dotted line shows the completeness limit.

the properties of YSOs in this region. Since both these studies use the shorter wavelengths they both find a higher average temperature as they are finding the hotter sources.

Chapter 4

Herschel Observations of NGC 7538

4.1 Introduction

In this chapter, I present data for NGC 7538, which has been mapped at 70, 160, 250, 350 and 500 μm by PACS and SPIRE on *Herschel*, using parallel mode, as described in Section 2.10.4. In Section 4.2, I review the nearby region of high mass star formation, NGC 7538. The observations, data reduction and map making are discussed in Section 4.3, and in Section 4.4 the source extraction method is outlined. A comparison between the source extraction routines CSAR and GETSOURCES is discussed in Section 4.5. The results are presented in Section 4.6 which includes source sizes, masses, temperatures and luminosities. The analysis of the results from this chapter is presented in Chapter 5.

4.2 NGC 7538

NGC 7538 is a reflection nebula in the Perseus spiral arm. It is located in the constellation of Cepheus near the Bubble Nebula at RA = $23^{\,\mathrm{hr}}\,13^{\,\mathrm{m}}\,45.7^{\,\mathrm{s}}$ and Dec = $61^\circ\,28'\,21''$. The nebula is at a distance of 2.8 kpc (Reid & Wilson, 2005a) and is one of the nearest and youngest high mass star formation regions. This makes it an ideal location to study the early stages of high mass star formation (Beetz et al., 1976; Campbell & Thompson, 1984). NGC 7538 is made up of the well studied main cloud labeled as c) in Figure 4.1, and the surrounding diffuse emission which contains a possible ring of triggered star formation labeled as a) and two possible UCHII regions labeled as b), these are discussed further in Section 4.3.1. Figure 4.2 shows a zoomed - in IRAM 850 μm image of the main cloud with contours starting at 0.5 Jy/beam and increase in steps of 0.5 Jy/beam and the beam size of $8''$ is shown. The main cloud is made up of four spatially separate regions. The largest of these regions contains three close compact HII regions (NGC 7538 – IRS1, IRS2 and IRS3), another contains NGC7538S which is a very young accreting massive protostar all of which are labeled on the figure, and IRS11 which is a maser (not labeled). The other two regions contain single compact HII regions, labelled IRS4 and IRS9. All of the regions in Figure 4.2 contain several stars of spectral types O and B which have formed together (Thronson & Harper, 1979; Woody et al., 1989; Hackwell, Grasdalen, & Gehrz, 1982). With this study I reveal the emission surrounding the main cloud. Figure 4.1 shows a three colour image of the region (red is 500 μm, green is 250 μm and blue is 70 μm) with some key features marked on. The blue regions show the hottest emission and the red the coolest.

There are two main theories as to how star formation has occurred in NGC 7538.

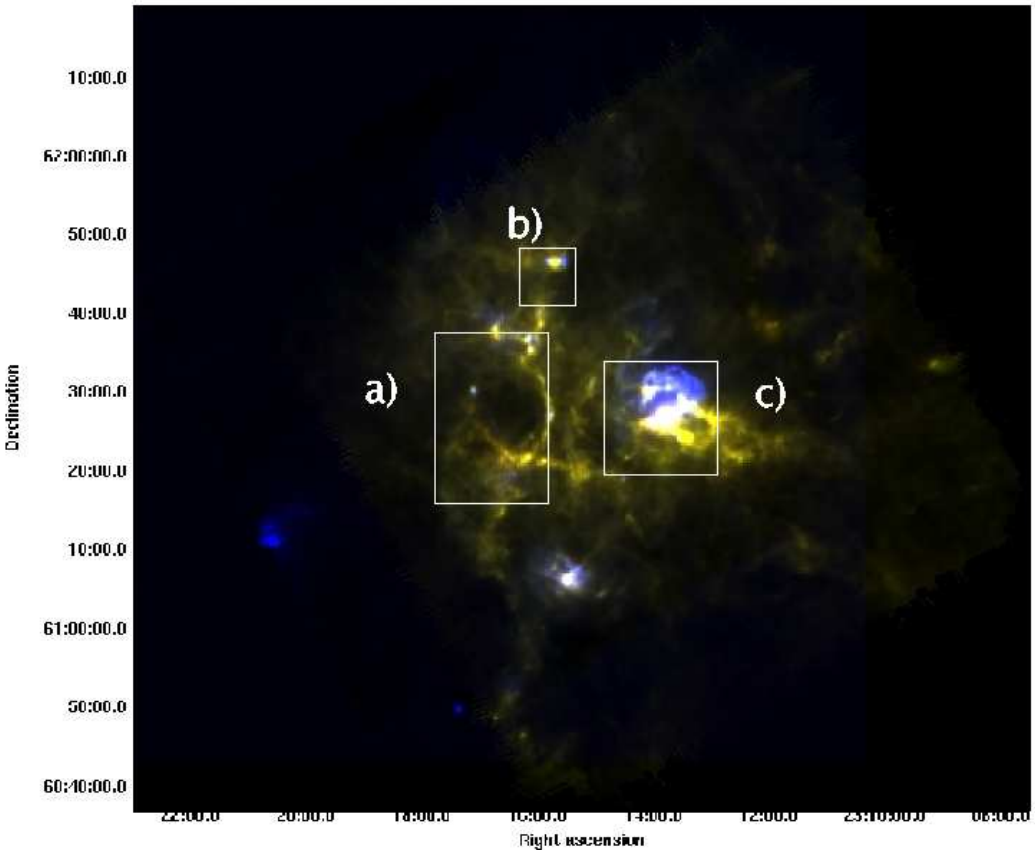

Figure 4.1: A three colour image of NGC 7538. Red is 500 μm, green is 250 μm and blue is 70 μm. The boxed marked a) shows a ring of triggered star formation and b) shows two possible UCHII regions, both of these features are discussed in Section 4.3.1, c) shows the location of the main cloud.

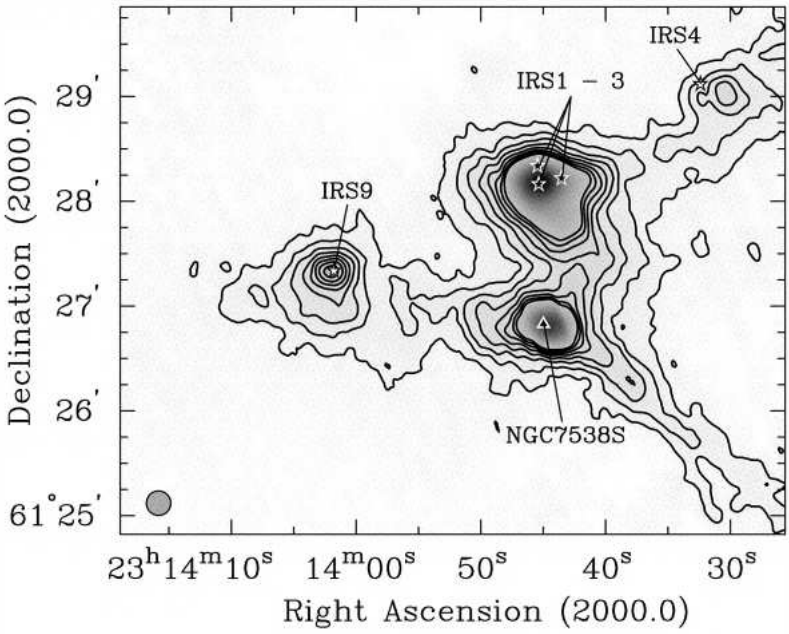

Figure 4.2: Image of the main cloud of NGC 7538 taken with IRAM at 850 μm with the locations of IRS1, 2, 3, 4 and 9 marked on. Contours start at 0.5 Jy/beam and increase in steps of 0.5 Jy/beam. The beam size of 8″ is shown (Sandell & Sievers, 2004).

Werner et al. (1979a) theorised a sequential process of star formation going from NW to SE, starting at the visible HII region. Dickel, Dickel, & Wilson (1981) suggested that varying densities within the cloud may have led to differing collapse times and thus various stages of evolution being observed in different parts of the cloud. In Chapter 5, I will look at both of these theories and see which fits our observational data best.

4.3 Observations, data reduction and map - making

The data used for this analysis were taken in December 2009 in the PACS/SPIRE parallel mode as described in Section 2.10.4. The observation, which had a total duration of approximately three hours, comprised multiple scans in orthogonal

directions which were then cross-linked. The scan mode used to take the data was the large scan map mode. The data were taken as part of the HOBYS (Motte et al., 2010) survey (Herschel imaging survey of OB Young Stellar objects), which observes regions of OB-type stars at distances of 3kpc and covers a total area of 22 $\deg^2$. The total area mapped for NGC 7538 was approximately 1.6 $\times$ 1.6 degrees.

The PACS raw data were reduced by Martin Hennemann at CEA using the HIPE 3.0.455 software with standard steps of the default pipeline. The baseline was subtracted by high-pass filtering with a $\sim 1^o$ median filter width. Multi-resolution median transform deglitching and second order deglitching were applied, and final maps were computed by the HIPE's MADmap (Cantalupo et al., 2010) method. The SPIRE parallel-mode data were reduced with HIPE 2.0 using pipeline scripts delivered with that version, modified to include data that were taken during the telescope's turnaround at the scan-ends. A median baseline was applied to the maps on individual scan legs and MADmap was used to create images.

The pixel sizes for each map are: 3.2″ for PACS 70 and 6.4″ for 160 μm, 6″ for SPIRE 250 μm, 10″ for SPIRE 350 μm and 14″ for SPIRE 500 μm. The maps are all approximately 1.6×1.6 degrees in size.

The PACS 70 and 160 μm maps are shown in Figures 4.3 and 4.4 and SPIRE 250, 350 and 500 μm maps are shown in Figures 4.5, 4.6 and 4.7 respectively. The 250 μm contour map is shown in Figure 4.8 with the locations of IRS1, 2, 3, 4 and 9 marked on.

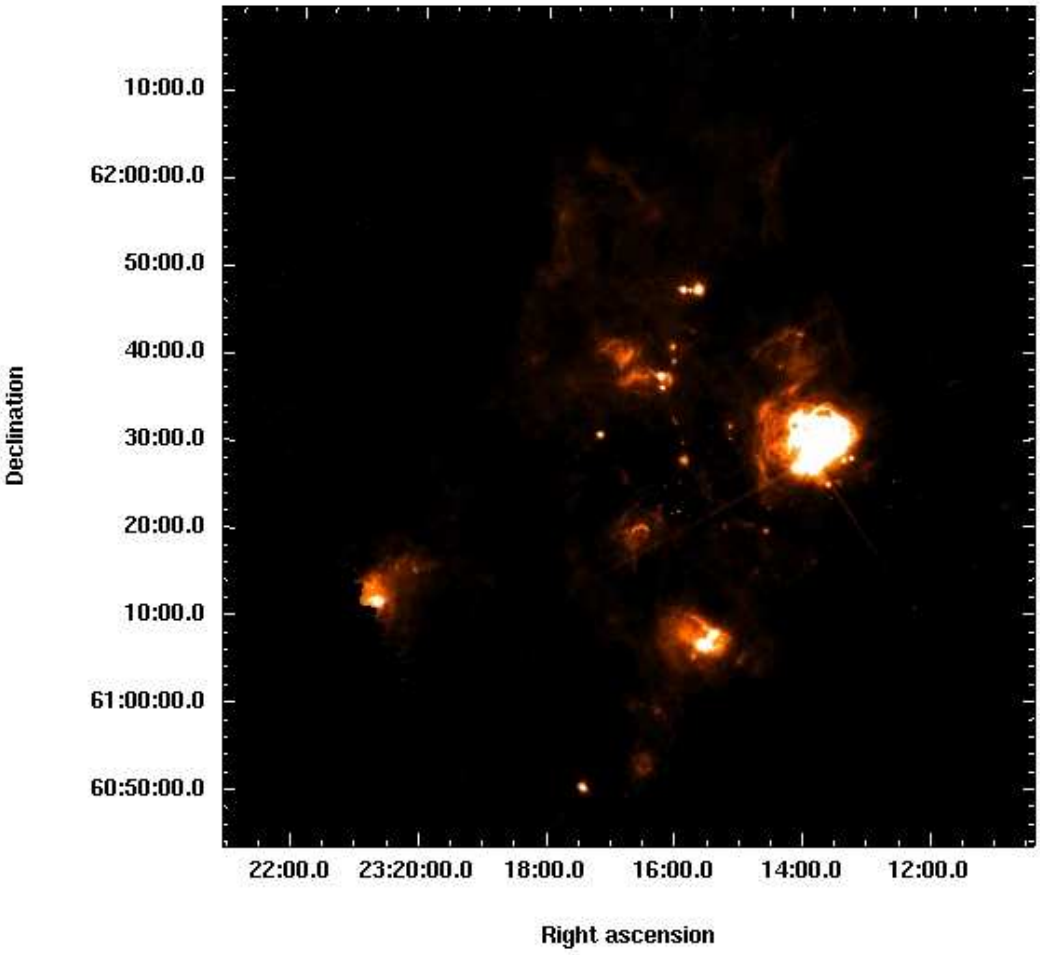

Figure 4.3: NGC 7538 PACS 70 μm.

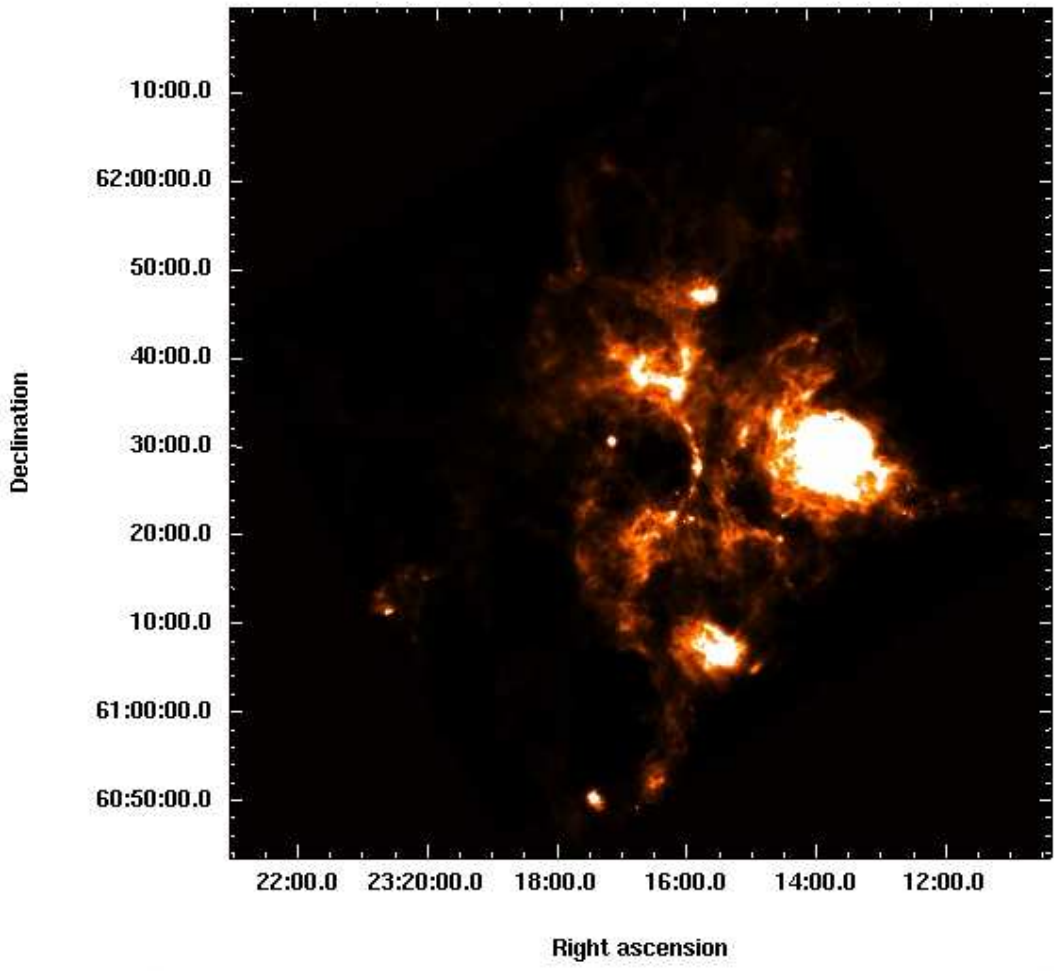

Figure 4.4: NGC 7538 PACS 160 μm.

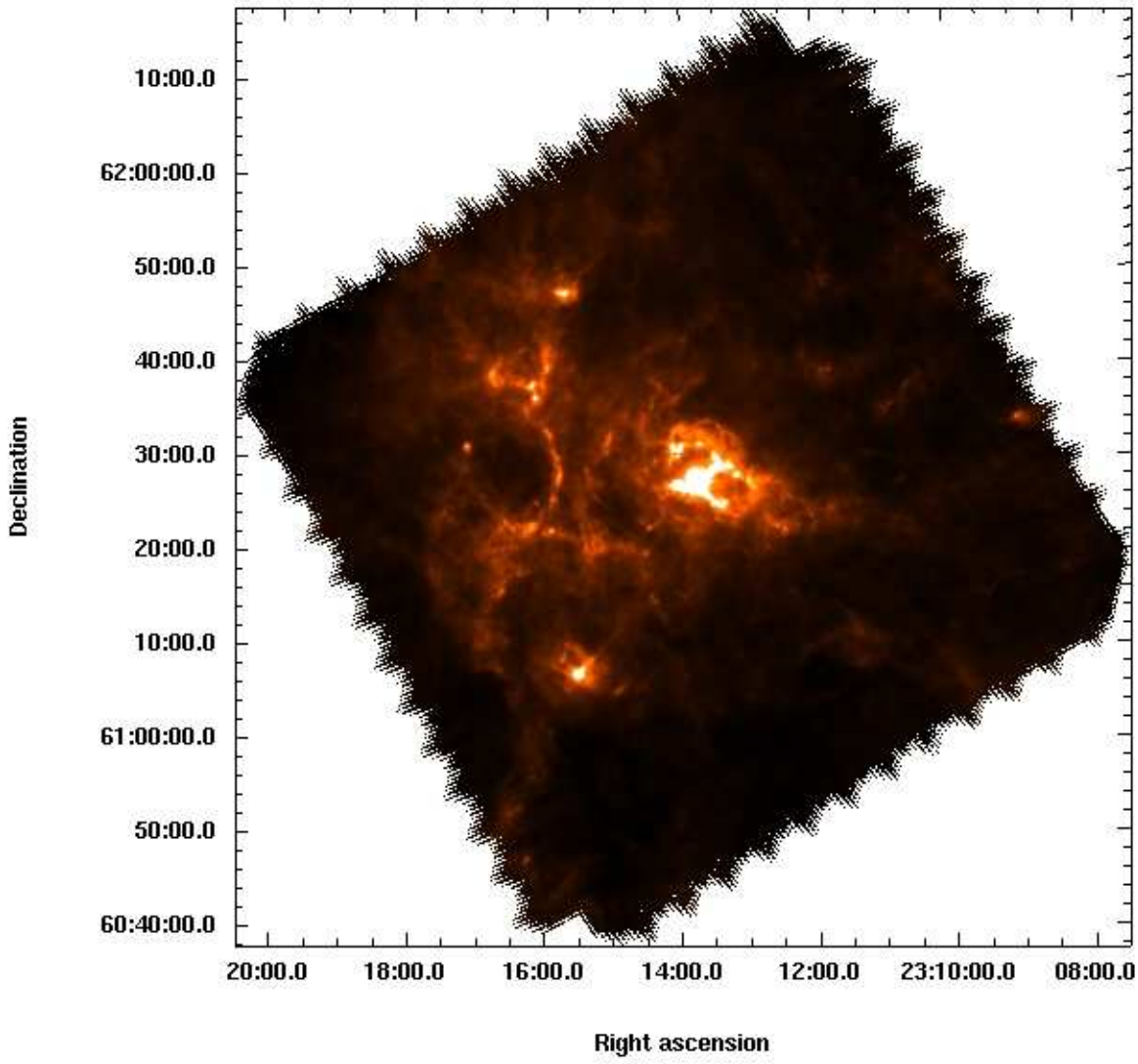

Figure 4.5: NGC 7538 SPIRE 250 μm.

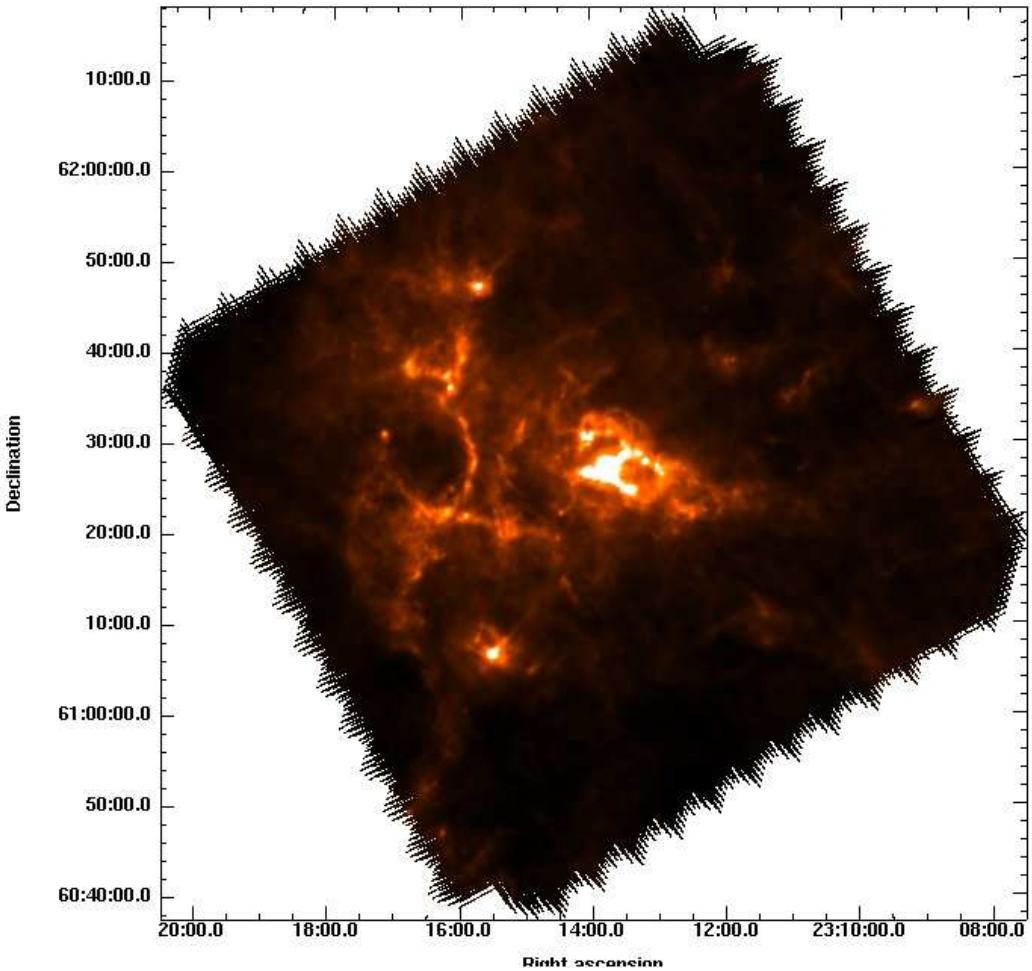

Figure 4.6: NGC 7538 SPIRE 350 μm.

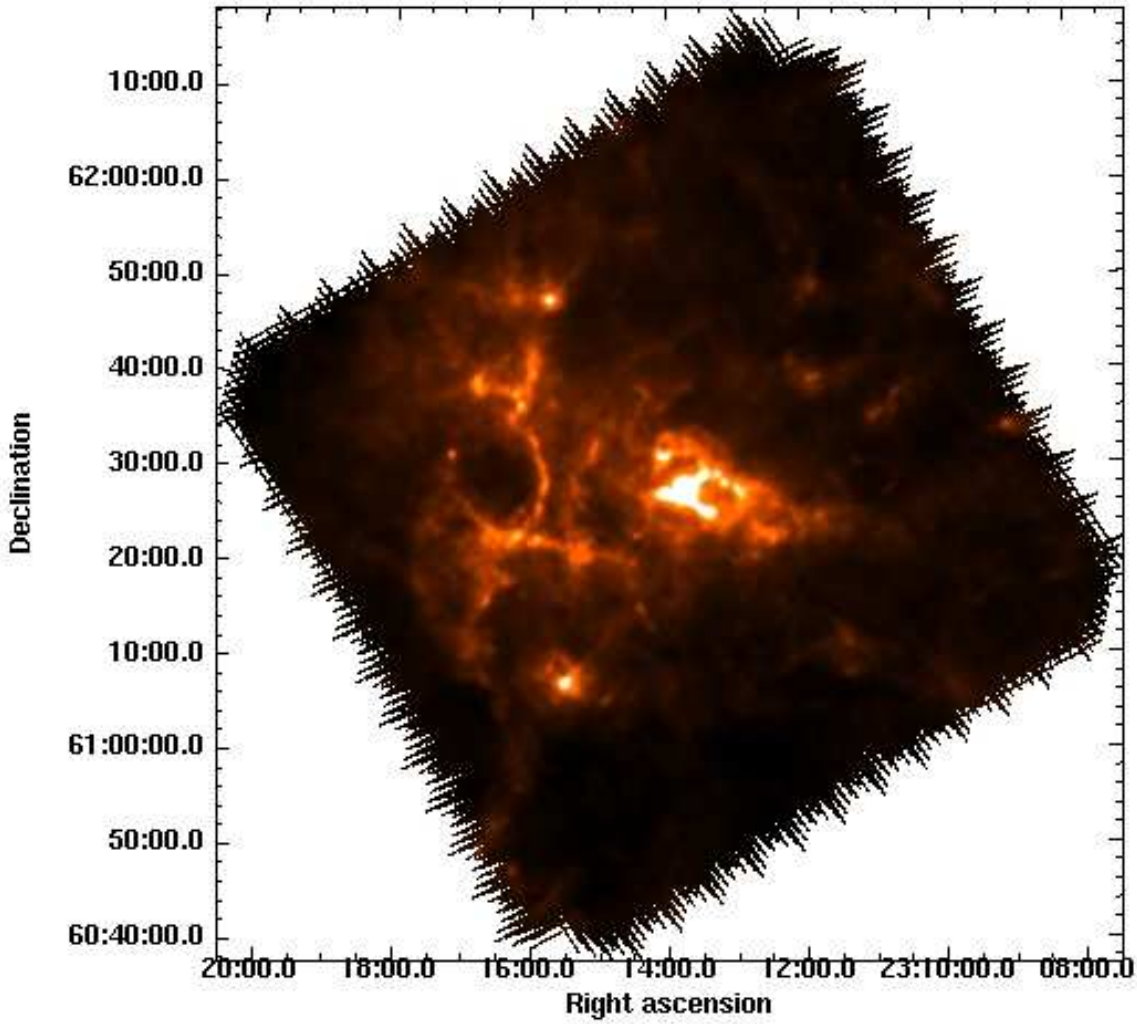

Figure 4.7: NGC 7538 SPIRE 500 μm.

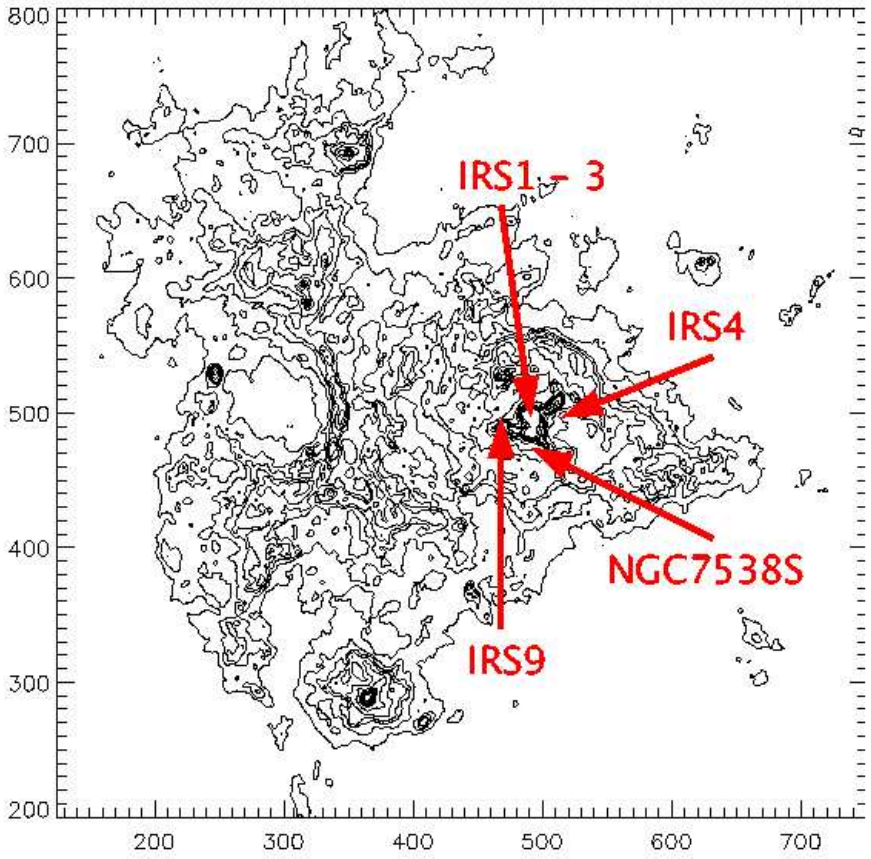

Figure 4.8: locations of IRS1, 2, 3 and 4 marked on the 250 μm contour map.

4.3.1 Interesting features

Having maps of a region spanning a range of wavelengths from 70 to 500 μm can provide a great deal of information on the structure of the clouds. The 70 μm map shows the hotter, more evolved cores. In this map there are numerous stars in the filaments, and less in the main cloud. The 500 μm map shows the younger colder cores and the areas of current star formation, with less sources in the filaments and more in the main cloud.

The main cloud of NGC 7538 has been extensively studied but there are several interesting features in the wider nebula. One of these is an apparent ring of triggered star formation (Reid et al., 2011) to the left of the main cloud. This is shown in Figure 4.9 at A) 70, B) 160, C) 350 and D) 500 μm and is highlighted as a) in Figure 4.1. The ring has the approximate dimensions of 10×7 pc. It might be expected, if this was a ring, for there to be an evolved object at the centre, but there is no recorded detection in this area. It is possible that it is just a chance alignment of two curved filaments which cause it to appear to be a bubble.

There are also two possible UCHII regions to the north of the main cloud, shown in Figure 4.10 at A) 70, B) 160, C) 350 and D) 500 μm and highlighted as b) in Figure 4.1. A three colour image shown in Figure 4.11 (where red is 500 μm, green is 250 μm and blue is 70 μm) shows three sources, two that are hot with no cold component, (as they disappear at 500 μm), and one which is colder. The two hotter sources are more likely to be UCHII regions and the colder source may be a younger core that happens to align with them. The three sources going from left to right have diameters of 1.1, 1.5 and 1.6 pc, temperatures of 30, 14 and 60 K and masses of 689, 209 and 517 $M_{\odot}$. If these were observed in radio wavelengths then we could determine their evolutionary status.

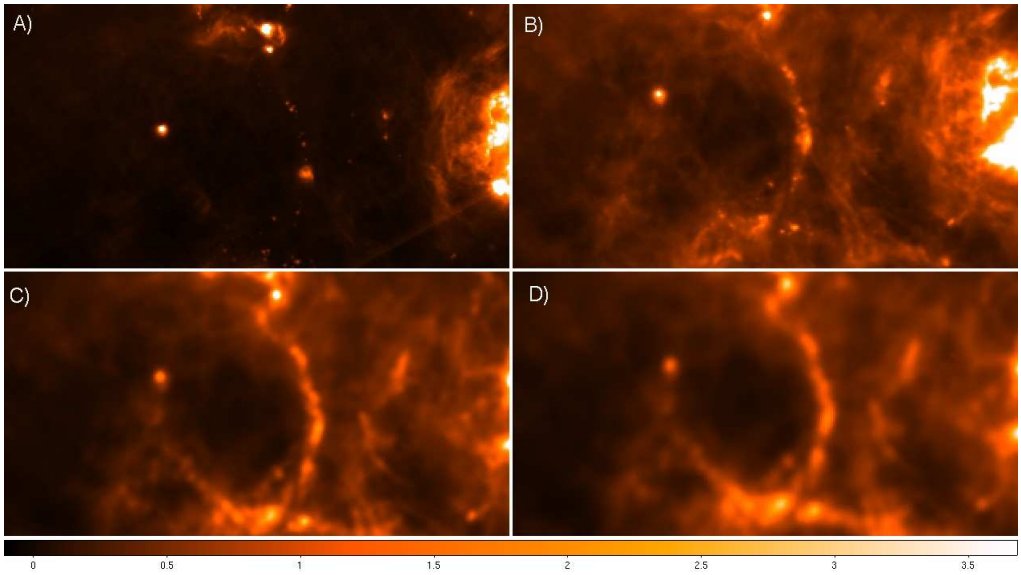

Figure 4.9: The 'ring' shown at A) 70, B) 160, C) 350 and D) 500 μm.

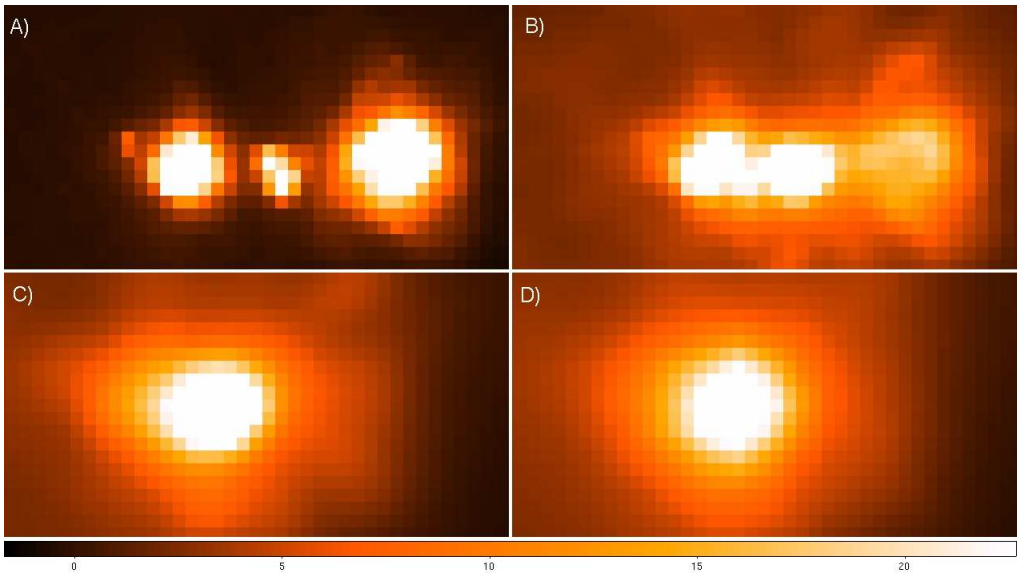

Figure 4.10: Two possible UCHII regions shown at A) 70, B) 160, C) 350 and D) 500 μm.

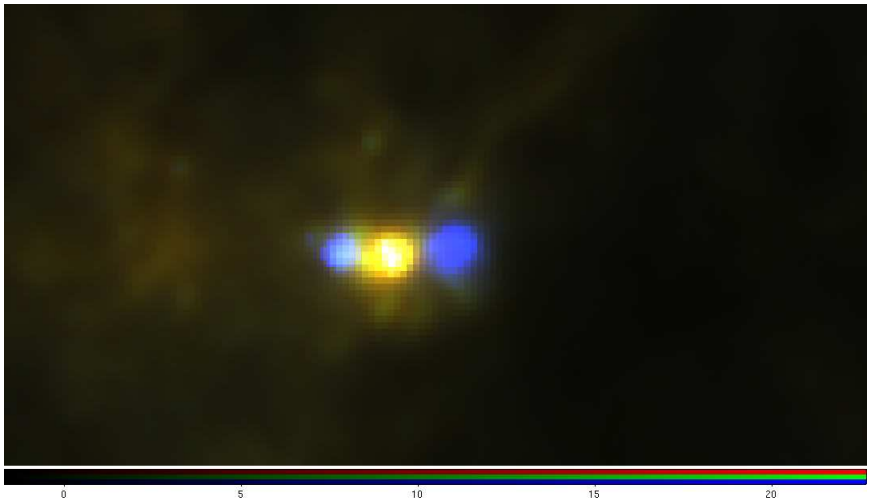

Figure 4.11: A three colour image of the UCHII region where red is 500 μm, green is 250 μm and blue is 70 μm.

4.4 Source extraction using CSAR

Sources were extracted from the data using the same method as that used for the Carina Nebula data in Chapter 3. The PACS maps are shown in surface brightness (Jy/pixel), but the SPIRE maps are shown in flux density per beam (Jy/beam). For each map, the rms value was obtained, yielding 0.05 and 0.1 Jy/pixel for 70 and 160 μm respectively and 0.46, 0.49 and 0.53 Jy/beam for 250, 350 and 500 μm respectively. The values obtained for 250, 350 and 500 μm were converted into units of surface brightness using the value for the beam areas supplied in the SPIRE Observers' Manual (see section 2.9.3). The contours were defined at 1/20th sigma slices to help constrain the extent of each source and a 14 $''$ pixel size for the PACS and SPIRE maps was used. The contour map for the 250 μm data is shown in Figure 4.13 with the locations of the identified sources marked, and a blow up of the crowded main cloud is also shown. The source extraction was performed at 250 μm and then a mask was used to extract the flux densities from the other wavelengths as before. Some extracted sources are shown in Figure 3.5, with each

source shown at 70, 160, 250, 350 and 500 μm. A total of 94 sources were extracted from the data using this method. The sources' positions and total flux densities can be found in Table A.3. The sources all appear at 250 and 350 μm, 30 % do not appear at 70 or 160 μm and 4 % do not appear at 500 μm.

4.5 Comparison of source extracting routines

With surveys becoming larger, such as those carried out by *Herschel*, and producing large multi - wavelength maps, extracting sources from the data is becoming very challenging. The traditional method of finding sources 'by eye' is no longer practical, and quicker, repeatable methods are needed. Complex, confused and crowded regions make it difficult for automated source extraction routines to pick out the sources from the background emission. This is a developing field which has had many groups working on it over the past decade (discussed in Chapter 3). This includes the *Herschel* - SPIRE SAG3 group. This group is the Galactic star formation key program team. The SAG3 group is currently working on three very different source extracting routines, after a long process of eliminating many more. Currently no one method works perfectly, with some more able to find point sources but not extended objects, and others better at finding the larger sources but unable to pick out compact ones. To make sure that all the sources we are using for now are credible, and hence that our results are valid, we choose to take a conservative approach. In this section I compare two of the source extraction routines currently used by SAG3: CSAR (described in Chapter 3) and GETSOURCES.

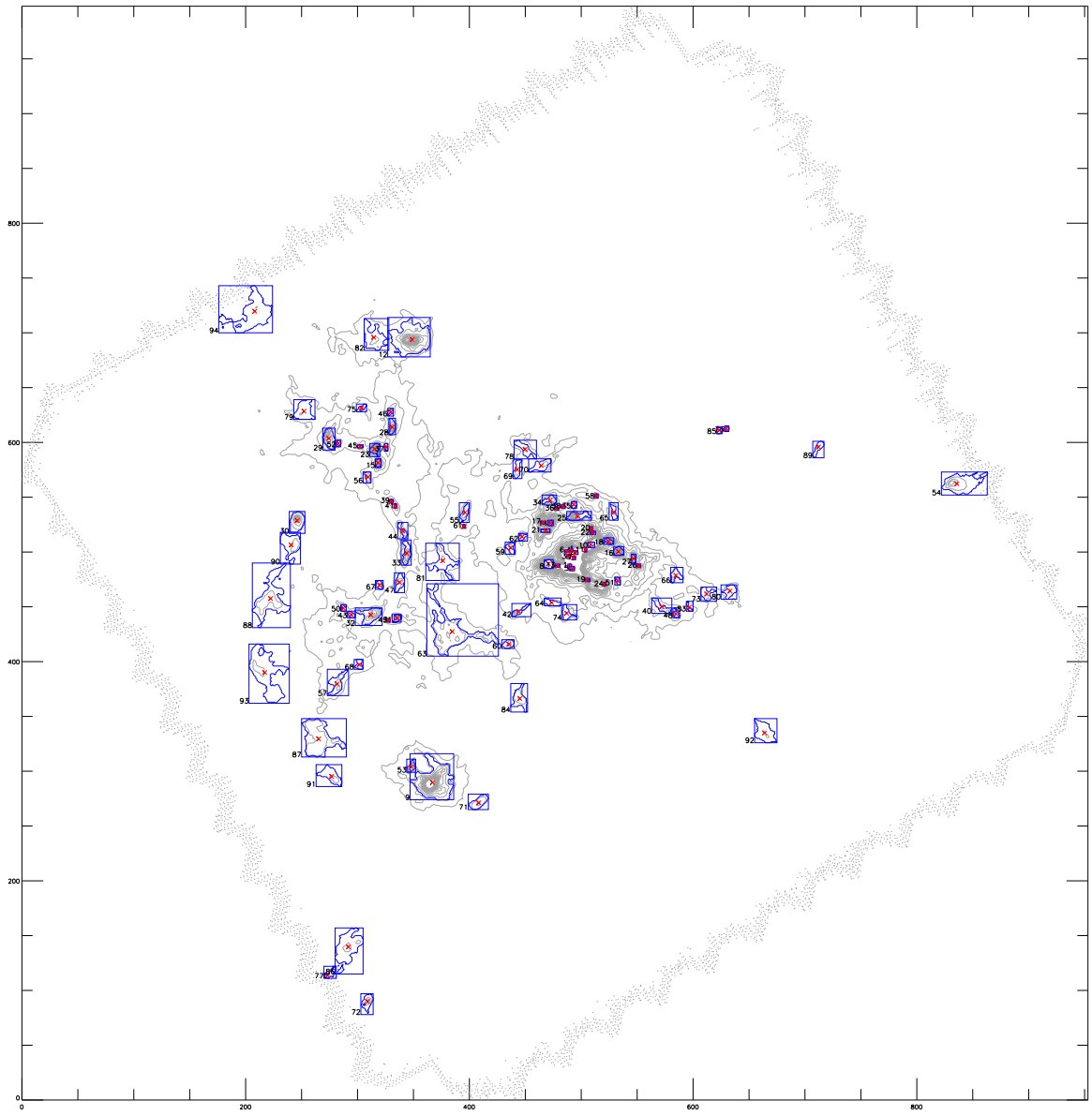

Figure 4.12: The $5\,\sigma$ slice of the $250\,\mu$m data. The blue boxes show the extent of each of the sources and the crosses show their peaks.

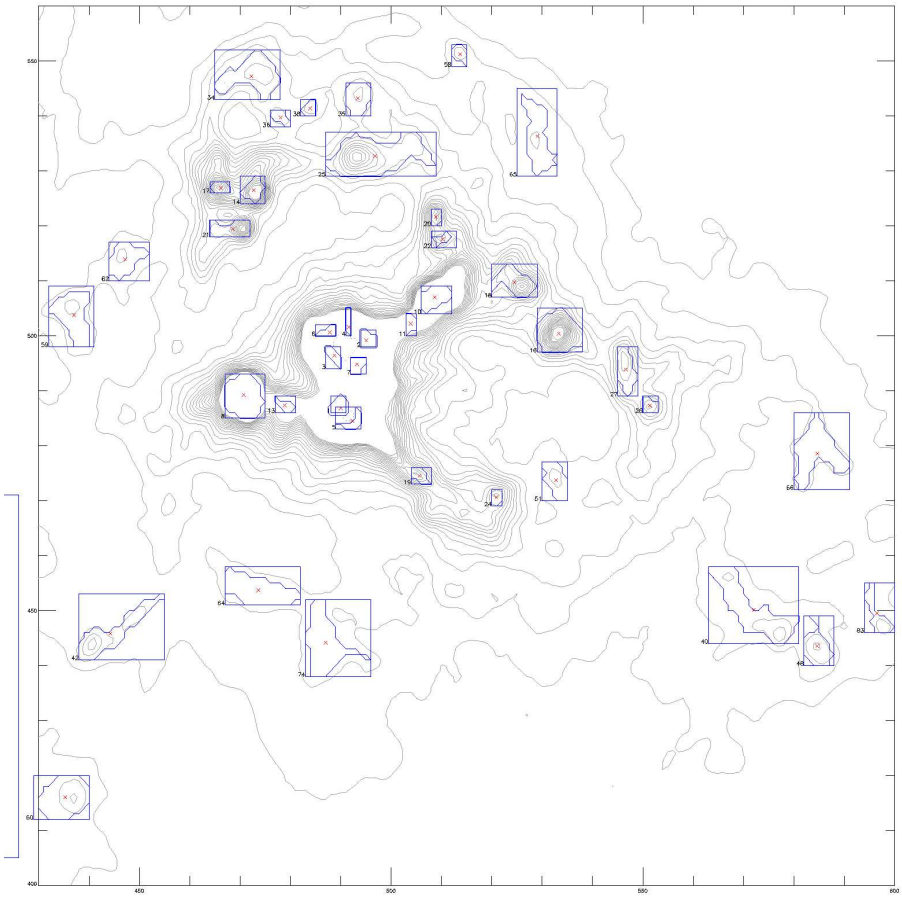

Figure 4.13: A zoomed in image of the main cloud showning the $5\,\sigma$ slice of the $250\,\mu$m data. The blue boxes show the extent of each of the sources and the crosses show their peaks.

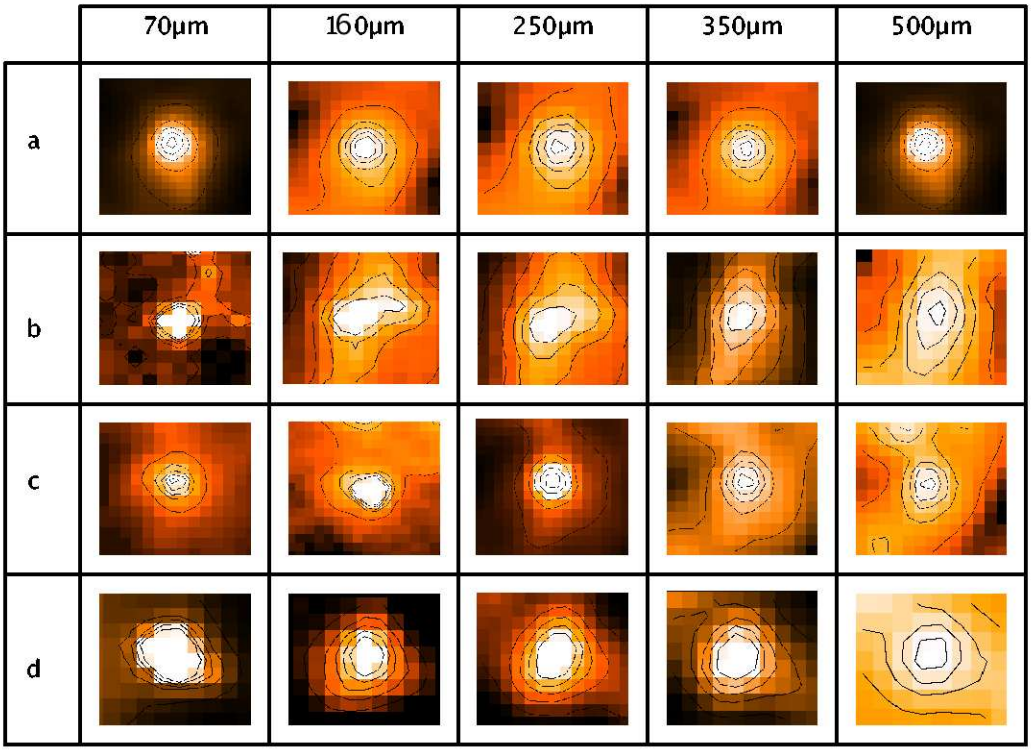

Figure 4.14: A selection of sources shown at 70, 160, 250 300 and 500 μm. The sources are a) HOBYS 231710+613124 b) HOBYS 231554+612533 c) HOBYS 231609+613631 and d) HOBYS 231310+612824.

4.5.1 GETSOURCES

GETSOURCES (Men'shchikov & et al., 2010) is a multi-scale, multi-wavelength source extraction algorithm that has been developed and extensively tested at CEA Saclay. The main idea of this method is to analyse decompositions of original images (at each wavelength) across a wide range of spatial scales. Each spatial scale is separated by only a small amount (typically $\sim 5\%$). Each of those 'single scales' is cleaned of noise and background by using an appropriate cut-off level, then re-normalized and summed up over all wavelengths in a combined single-scale detection image. The main advantage of this algorithm is in its multi-wavelength design: the same combined detection image across all wavelengths simultaneously eliminates the need for matching multiple catalogues obtained with different angular resolutions and reduces associated measurement errors. In addition, fine spatial decomposition improves the detection of even the faintest objects and aids in better deblending in crowded regions.

To separate the signals of objects from the noise and background contributions, GETSOURCES uses a 5σ cut-off level in each of the images. The standard deviation, σ, is computed outside the objects and all pixels with intensities below that level are zero-ed out, producing clean images. An advantage of this single-scale cleaning is that the noise contribution depends very significantly on the scale, at large scales the small-scale noise is diluted, whereas large objects are best visible. Objects in the combined detection image are identified by tracking their appearance and 'evolution' from small to large scales, and their footprints are determined. The objects are background-subtracted and deblended, and their sizes and fluxes are measured in the original observed images at each wavelength.

GETSOURCES has two tiers of user-selectable parameters, user and expert.

These are listed below with the default value in brackets next to it. The user parameters are:

- perform single-scale decomposition of detection images (y)
- perform cleaning single scales (y)
- combine single-scale images over all wavelengths (y)
- detect objects (y)
- measure properties of objects (y)
- visualize objects with ellipses/dots on top of images (y)
- accelerate I/O for FITS images by using a RAM disk (n)
- largest spatial scale (″) until which new objects may appear (120)
- minimum significance of reliable objects in extraction catalogues (7)
- minimum significance of tentative objects in extraction catalogues (5)
- minimum signal-to-noise ratio for objects in extraction catalogues (1.0)
- required minimum number of wavelengths for source detection (2)
- maximum relative difference of footprint area for convergence (0.001)
- verbosity level for the screen and log file output (0)

The expert parameters are:

- first (smallest) scale (″) to begin decomposition with (0)
- number of spatial scales an image must be decomposed in (99)
- scale factor by which single scales should be separated (0)
- combine scales this factor smaller than the observational beam (0.0)
- last (largest) scale as a fraction of an (average) image size (1.0)
- faintest-scale fraction of maximum intensity over single scales (0.067)
- initial number of sigma for finding cut-offs in single scales (5)

- lower limit of skewmax for defining cut - offs in single scales (0.25)
- tuning factor to slightly adjust the single - scale cleaning depth (1.0)
- minimum value of the exponent for preserving higher resolution (6.0)
- required minimum intensity contrast to identify noise peaks (2.5)
- accept lower significance of tentatives within this factor (1.0)
- make TIFF or JPG illustrations for images (n)

4.5.2 Comparison between CSAR and GETSOURCES

CSAR and GETSOURCES are very different routines. GETSOURCES finds sources at all wavelengths, whereas we use CSAR only on the 250 μm map. CSAR is a contour based algorithm and GETSOURCES is a multi - scale, multi - wavelength algorithm. GETSOURCES requires a lot of input from the user whereas CSAR is more basic to run. As part of the SAG3 evaluation GETSOURCES was run on the same NGC 7538 maps by M. Reid, but a smaller pixel size of 3″ was used. A minimum of 5 σ was required for a detection. GETSOURCES found a total of 621 'reliable' sources (reliable sources are those found a significance of 7 σ or higher) which makes up the complete catalogue. This is almost seven times as many sources as are found by CSAR (94 sources - see section 4.4). The locations of the GETSOURCES and CSAR sources are shown in Figure 4.15, plotted over a grey scale image of the 250 μm SPIRE map with contours starting at 3 σ and increasing in 2 σ steps. The blue crosses show the GETSOURCES sources and the red crosses show the CSAR sources.

Of the 621 sources found by GETSOURCES, 26% are found in the PACS maps only. These objects will be the hotter sources which may not be associated with the cloud but may be more evolved objects. For this work we want to analyse

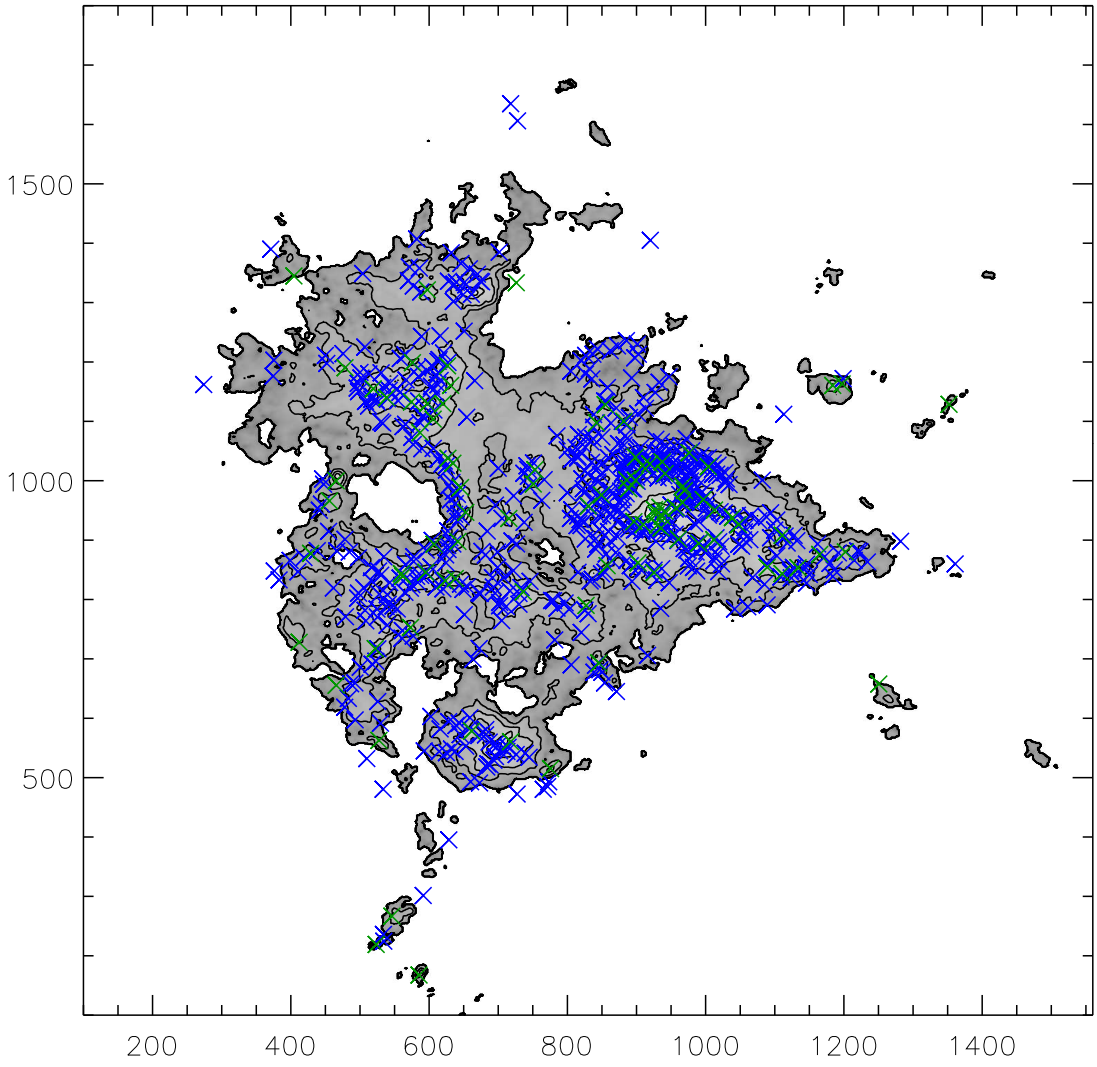

Figure 4.15: Contour plot of NGC 7538 with a greyscale image of the 250 μm map. Contours start at 3 σ and increase in 2 σ steps. Blue crosses show the locations of sources identified using GETSOURCES and green crosses show the location of sources identified using CSAR.

the physical properties (temperature, luminosity and mass) of the sources in this region, and to do this we need to construct SEDs which cover the range $70-500\,\mu$m. The flux densities which are extracted from the $70\,\mu$m map show hotter objects that do not necessarily make a major contribution to the SEDs. Figure 4.16 shows the locations of the sources from the complete GETSOURCE catalogue, plotted on a grey scale image of the $70\,\mu$m PACS map with contours starting at $3\,\sigma$ and increasing at $2\,\sigma$ intervals. From this plot it is clear that the sources follow the contours well, however there are several regions where the sources do not appear to be associated with any features of the $70\,\mu$m map.

GETSOURCES is able to extract faint compact objects at $70\,\mu$m which lie against the diffuse emission. These objects do not always show up at the longer wavelengths, which suggests that some may not be real and could just be noise. As an illustration, a section of diffuse emission is shown in Figure 4.17, at 70, 250 and $500\,\mu$m, with contours starting at $1\,\sigma$ and increasing in $1\,\sigma$ intervals. The locations of the GETSOURCES objects are marked as crosses. These objects are easily identified in the $70\,\mu$m map but are less apparent at the longer wavelengths. However, many of these sources are only seen at one or two σ above the background and are consistent with the fluctuations in the region. Because GETSOURCES finds more sources at $70\,\mu$m which are not all present at the longer wavelengths, an SED does not necessarily represent just one object. It could represent one object plus the emission surrounding it. This means we cannot rely on the physical properties that are derived from such SEDs, so any sources which appear at only $70\,\mu$m are omitted from our analysis.

The GETSOURCES catalogue can be made more reliable by filtering it to remove sources which are only present at one or two wavelengths. Note that the resultant catalogue contains sources which can be seen at a variety of combinations

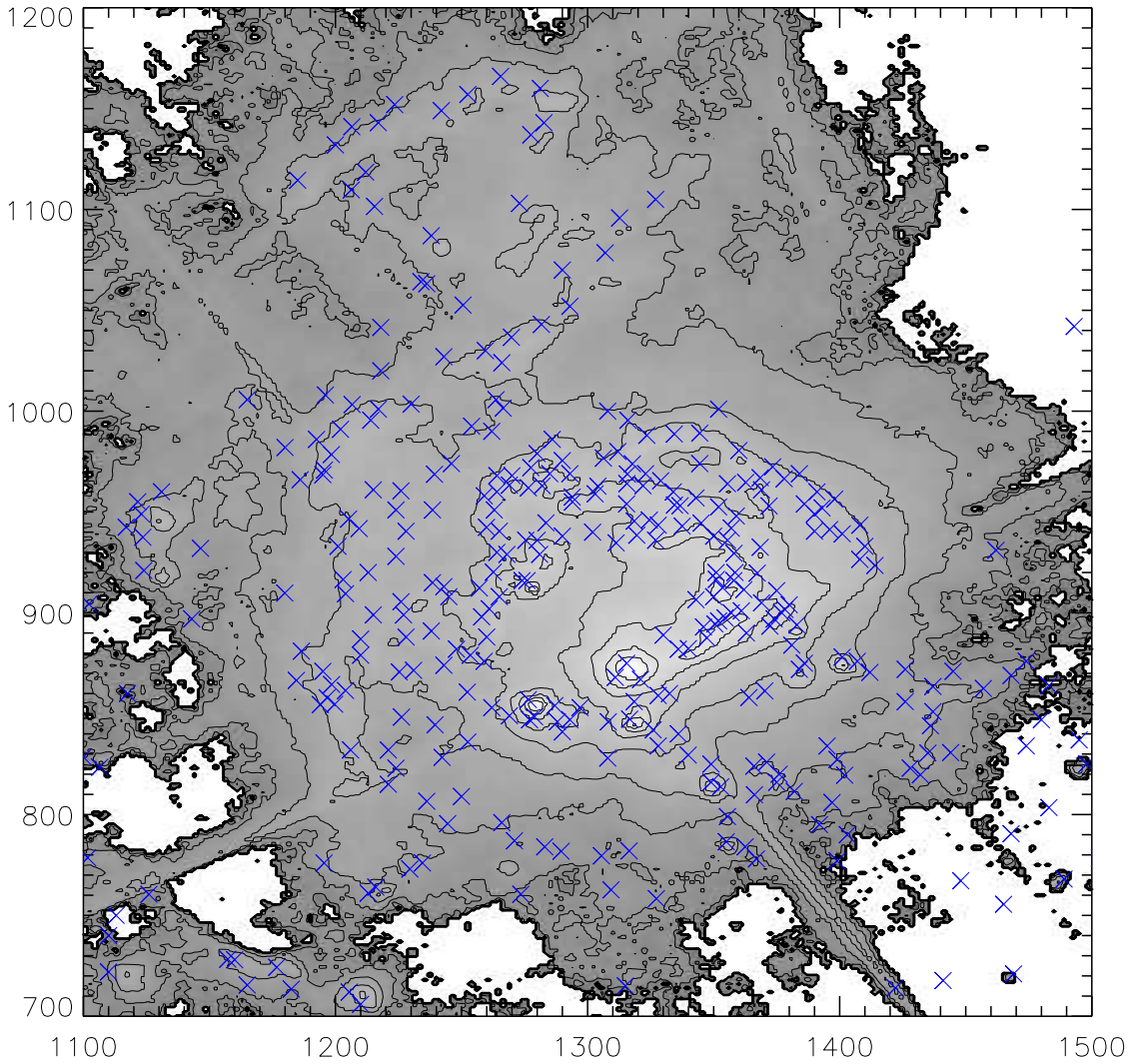

Figure 4.16: Contour plot of the main cloud region with a greyscale image of the 70 μm map. Contours start at 3 σ and increase in 2 σ steps. Blue crosses show the locations of sources identified using GETSOURCES.

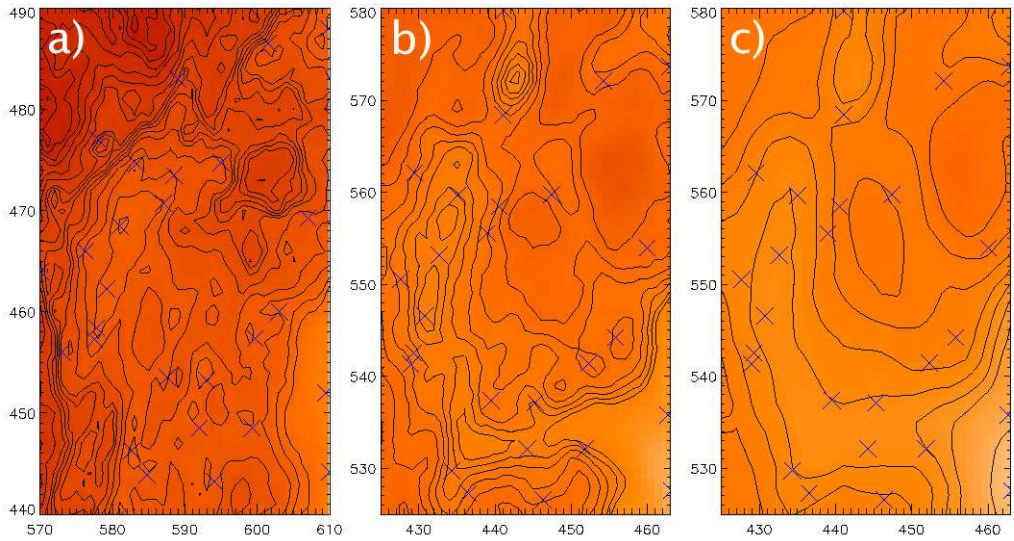

Figure 4.17: Contour plot of a section of diffuse emmision at a) 70, b) 250 and c) 500 μm. Contours start at 1 σ and increase in 1 σ steps. Blue crosses show the locations of sources identified using GETSOURCES.

of wavelengths, some for instance are seen at 70, 160 and 250 μm, others are seen at 160, 350 and 500 μm and some even at 70, 160 and 500 μm. This reduces the catalogue to 337 objects and removes all of the objects only present at 70 μm. This filtered catalogue is more compatible with the CSAR catalogue in the less dense regions of NGC 7538. An example of this is shown in Figure 4.18, which shows a small area of the diffuse emission of the cloud in the 250 μm map. The red crosses show the CSAR sources and the blue crosses show the GETSOURCES sources. Contours start at 6 σ and increase by 2 σ steps. The slight offset of the two catalogues is probably due to the differing pixel sizes used during the source extraction process. Image a) shows the CSAR sources compared with sources from the complete GETSOURCES catalogue, and image b) shows it compared to sources from the filtered GETSOURCES catalogue. In both images there are more GETSOURCES sources than CSAR ones. In image a) the source marked (i) does not appear to match any emission at this wavelength; however this source

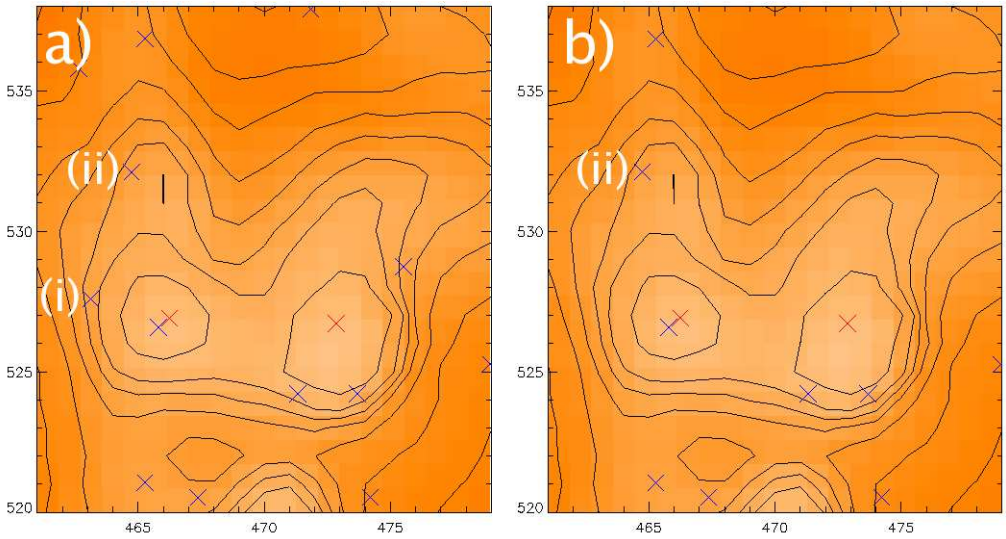

Figure 4.18: Contour plot of a section of diffuse emission at 250 μm. Contours start at 6 σ and increase in 2 σ steps. In image a) Blue crosses show the locations of the sources from the complete GETSOURCES catalogue and red crosses show the location of sources identified using CSAR. In image b) Blue crosses show the locations of the sources from the filtered GETSOURCES catalogue and red crosses show the location of sources identified using CSAR

disappears in image b). The extended emission surrounding the object marked (ii) would indicate that the source is real but possibly unresolved at 250 μm. In the diffuse emission the ratio of CSAR sources to the filtered GETSOURCES catalogue is 1.13 which shows that they have a good correspondence level.

The comparison of the filtered GETSOURCES catalogue and the CSAR catalogue for the denser region of the main cloud is demonstrated in Figures 4.19 and 4.20. Figure 4.19 shows the sources from the filtered GETSOURCES catalogue (blue crosses) plotted with the CSAR sources (red crosses) on a contour plot of the 250 μm SPIRE map, contours start at 3 σ and increase in 2 σ steps. Figure 4.20 shows the same except that the 70 μm PACS map is used. There are a lot less GETSOURCES sources now present in this dense region compared to Figure 4.16.

There is now good agreement between the two catalogues [1]. In the more dense regions of NGC 7538, the CSAR catalogue and the filtered GETSOURCES catalogue do not match up as well. In these dense regions the ratio of CSAR sources to the filtered GETSOURCES sources is 0.83, with GETSOURCES now detecting more rather than fewer objects, which shows that they do not match up quite so well.

In the densest region of the map, the central area in Figures 4.19 and 4.20, there are some sources which show up in the CSAR catalogue but are not present in the filtered GETSOURCES catalogue. These are very bright sources which show up clearly at every wavelength, as shown in Figure 4.21. GETSOURCES finds an object here at 70 μm and 250 μm but not at the other wavelengths. It is unclear as to the reason that GETSOURCES does not find these objects reliably at the other wavelengths and this is something that would need further investigation. CSAR finds multiple sources here – probably due to the saturated pixels in the 250 μm map. It is clear from Figure 4.20 there are only two objects here, so to correct for this, CSAR was run at 350 μm instead for this region, it then successfully detected the two sources that are clearly apparent. The 250 μm data point on the SED for these sources is neglected. This reduces the CSAR catalogue to 89 sources.

4.5.3 Comparison with SCUBA maps of NGC 7538

The CSAR catalogue can also be compared with another submillimetre survey conducted in this region. Reid & Wilson (2005b) surveyed a smaller part of the cloud and found 77 clumps at 850 μm and 67 at 450 μm. Their data were obtained

[1] although note that as before the slight offset between the two catalogues is probably due to differing pixel sizes used during the source extraction which causes some small uncertainties on the scale of approximately one pixel

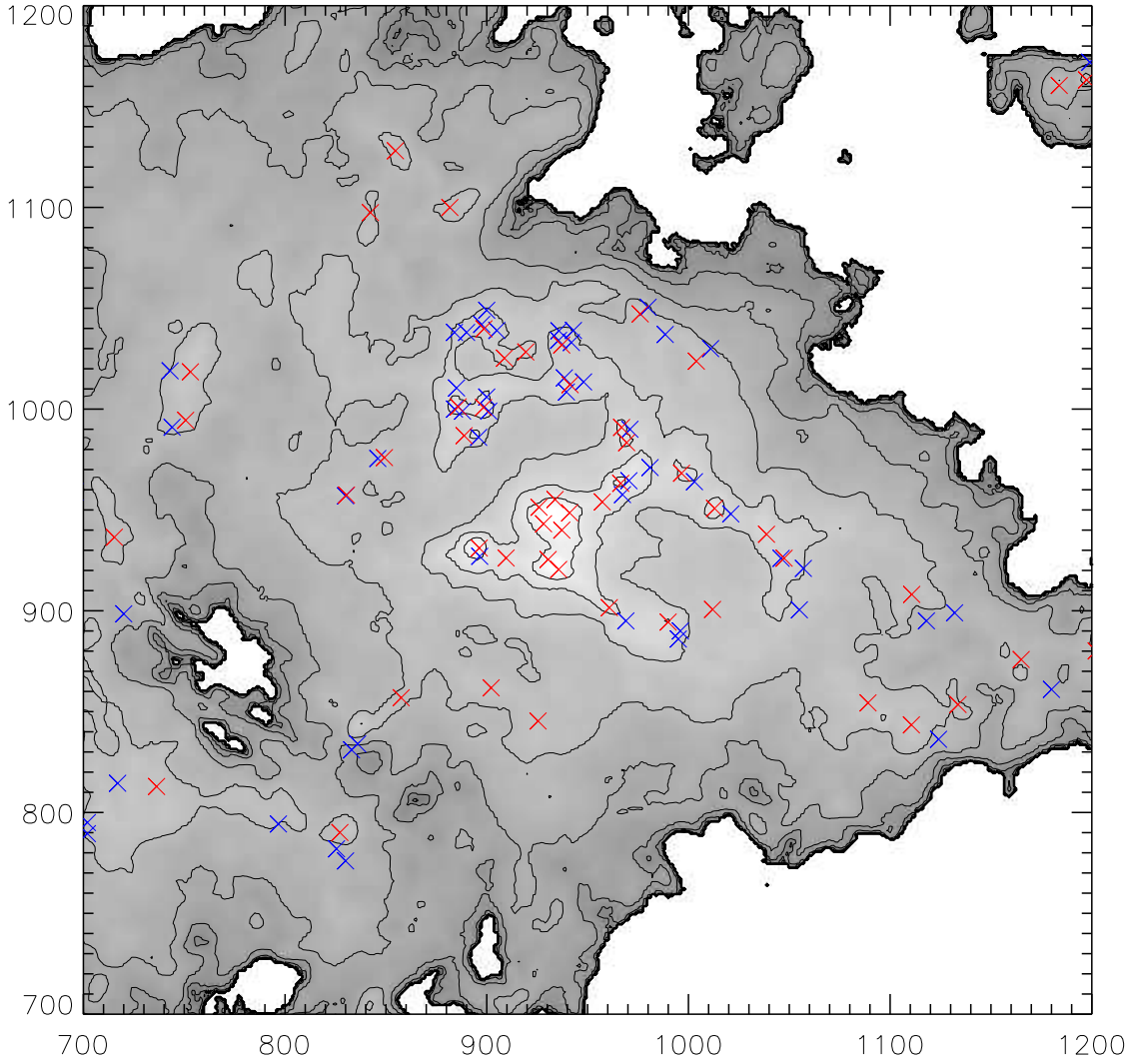

Figure 4.19: Contour plot of the main cloud with a greyscale image of the 250 μm map. Contours start at 3 σ and increase in 2 σ steps. Blue crosses show the locations of the sources from the filtered GETSOURCES catalogue and red crosses show the location of sources identified using CSAR.

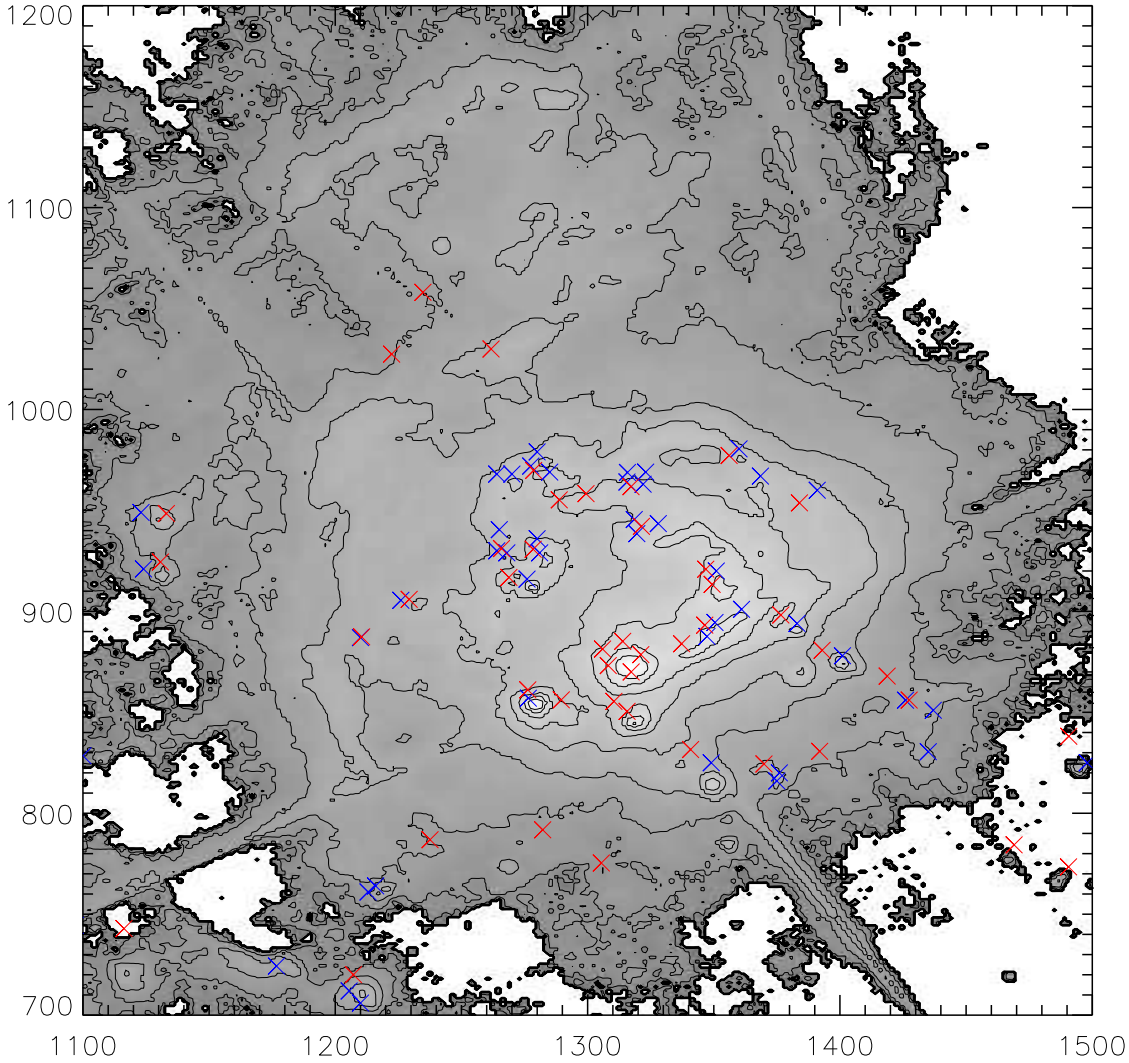

Figure 4.20: Contour plot of the main cloud with a greyscale image of the 70 μm map. Contours start at 3 σ and increase in 2 σ steps. Blue crosses show the locations of the sources from the filtered GETSOURCES catalogue and red crosses show the location of sources identified using CSAR.

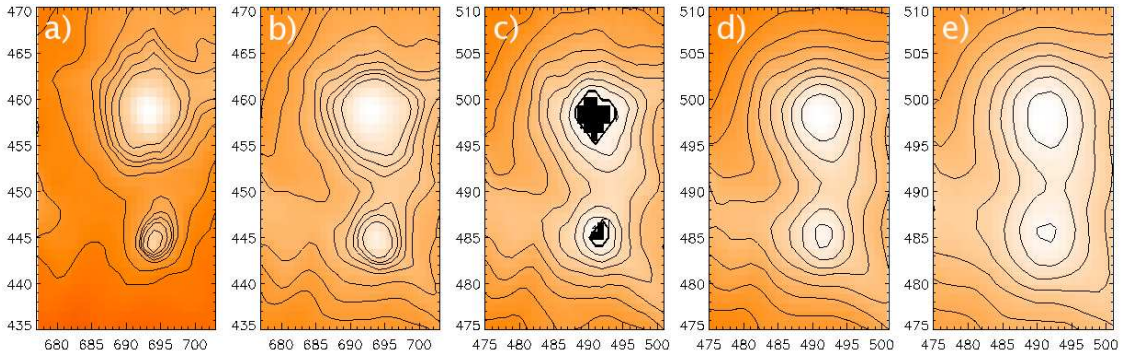

Figure 4.21: Image a) shows the bright, dense region at 70 μm, b) at 160 μm, c) 250 μm, d) 350 μm and e) 500 μm. In each the contours start at 15 σ and increase in 3 σ intervals.

using SCUBA on the JCMT (see Chapter 2) in scan - mapping mode. The clumps were extracted using clfind2d (Williams et al., 1994). The positions of the extracted sources are shown in Figure 4.22 at: A) 450 μm and B) 850 μm. Contours start at 3 σ and increase by 2 σ. Symbols indicate the peak positions of identified clumps which do (stars) and do not (triangles) show coincidence with a 2MASS point source within their 0.5 $S_{\rm peak}$ contour. Circled symbols in the 850 μm image indicate 'cold' clumps. A circled triangle indicates a possible cold, starless clump; the four such clumps are labeled.

The positions of the SCUBA sources are plotted on the 250 μm contour plot as red crosses in Figure 4.23, with the CSAR sources also shown as blue crosses. There is a good agreement between the two catalogues with every CSAR source having a SCUBA counterpart. This would support the validity of the CSAR sources and indicates that a believable far infrared - submillimetre SED can be derived for these objects. The SCUBA sources that are coincident with CSAR sources can be used to add an extra point on the SED to help constrain it. Some of the SCUBA objects do not show up in the CSAR catalogue, which is probably due to them being too cold to show up at 250 μm.

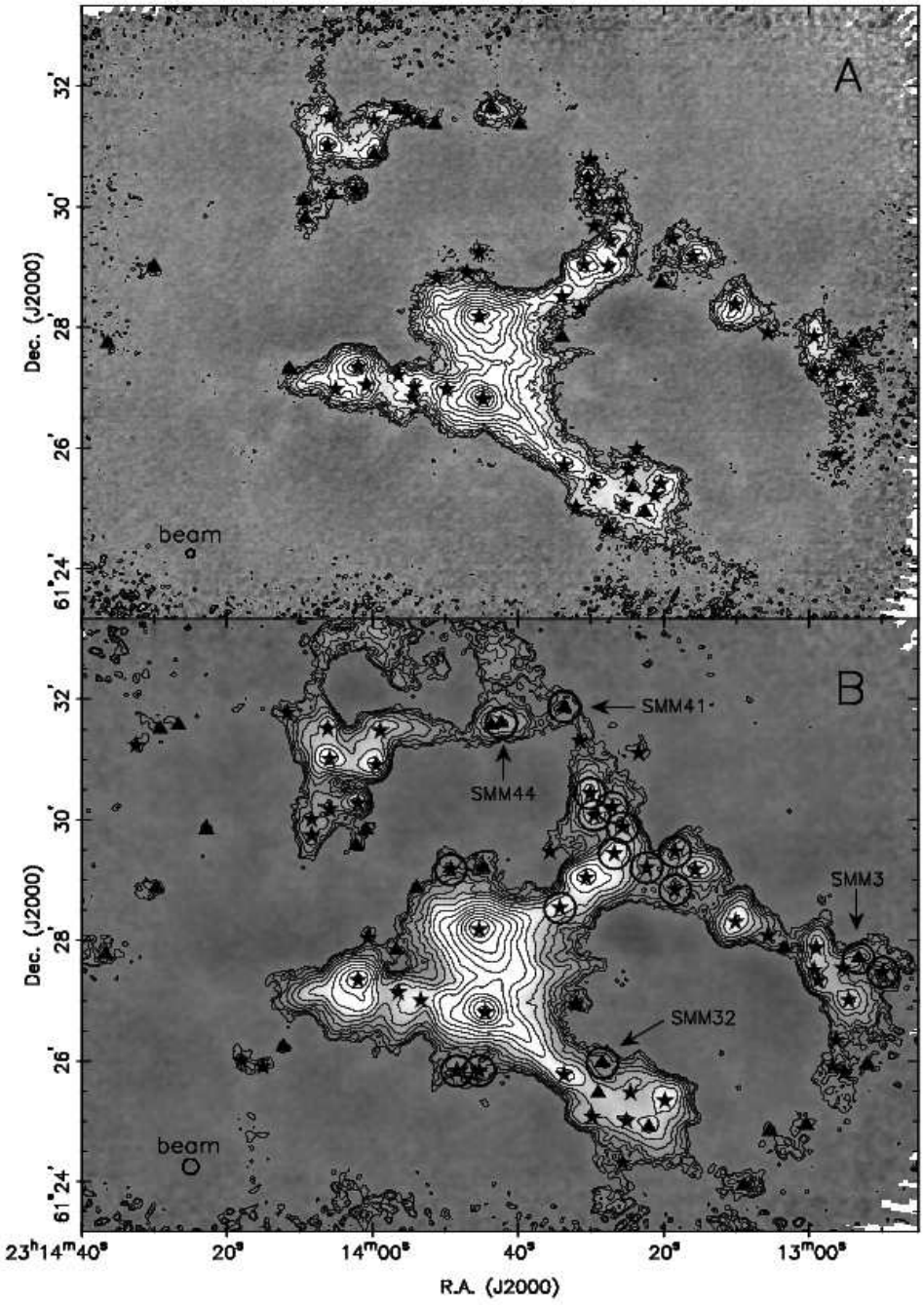

Figure 4.22: The positions of detected clumps in NGC 7538 at A) 450 μm and B) 850 μm. Contours start at $3\,\sigma$ and increase by $2\,\sigma$. Symbols indicate the peak positions of identified clumps which do (stars) and do not (triangles) show coincidence with a 2MASS point source within their $0.5\,S_{\rm peak}$ contour. Circled symbols in the 850 μm image indicate 'cold' clumps (i.e. those with estimated dust temperatures, $T_{\rm dust} \leq 30$ K). Thus, a circled triangle indicates a possible cold, starless clump; the four such clumps are labeled(Reid & Wilson, 2005b).

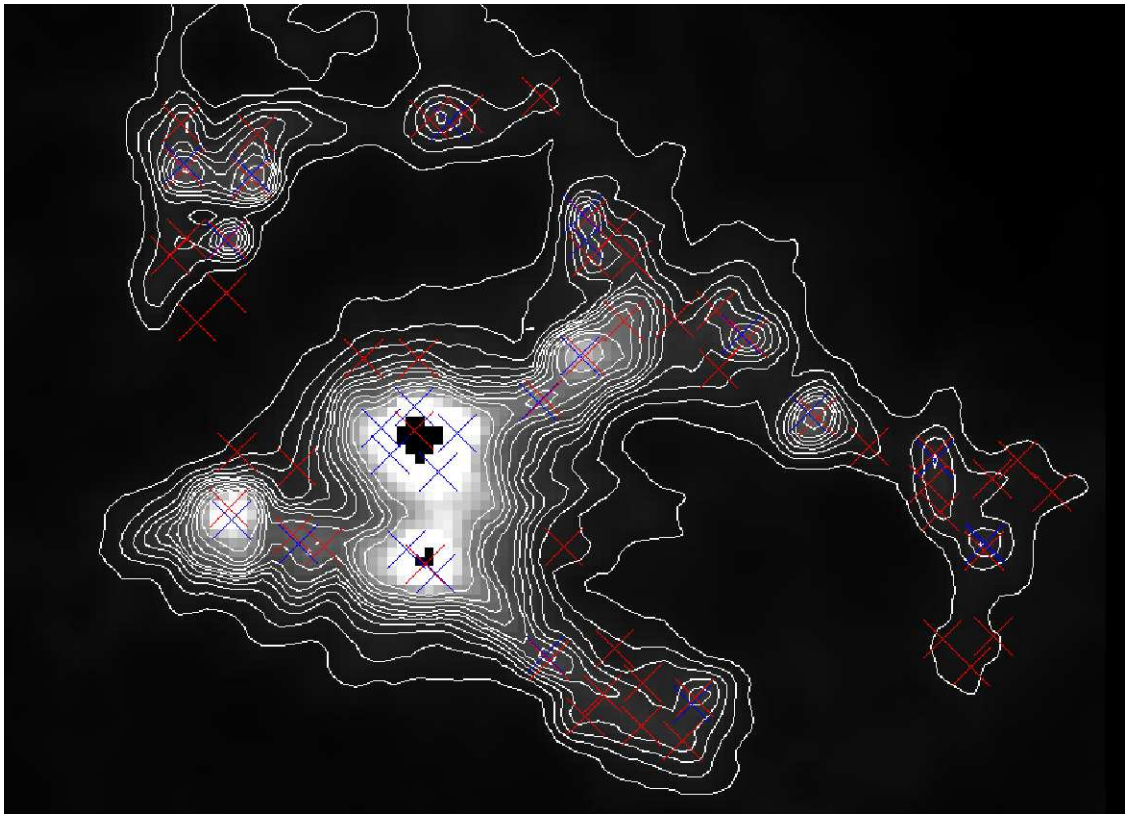

Figure 4.23: Contour plot of the main cloud region with a greyscale image of the 250 μm map. Contours start at 3 σ and increase in 2 σ steps. Blue crosses show the locations of sources identified using CSAR and red crosses show the location of the SCUBA sources.

4.5.4 Conclusions

CSAR is a very conservative source extracting routine whereas GETSOURCES is more liberal, as demonstrated by the large difference in the number of sources the two methods find. The complete GETSOURCES catalogue finds many of its sources in the 70 μm map only, which can give us some false results when we construct SEDs. When the GETSOURCES catalogue is filtered to include only objects which appear at three or more wavelengths we find a better correlation between it and the CSAR catalogue. CSAR objects tend to be also found by both SCUBA and the filtered GETSOURCES, suggesting that they can be trusted. It is clear that the CSAR catalogue is missing many sources in the data, especially in the denser regions, but those it does find can be taken as reliable. For the rest of this work I will use an amended CSAR catalogue which contains sources that are defined by the SAG3 group as robust. A robust source is one which is found by at least two source extraction routines. This reduces the catalogue to 75 sources. In Chapter 5, I will discuss the analysis of the physical properties derived for sources in this region and for the Carina Nebula.

4.6 Results

In this section I will describe how the physical properties of the sources (luminosities, temperatures and mass) were obtained from the amended CSAR catalogue and discuss the results. The analysis of the results is given in Chapter 5.

4.6.1 SEDs

The SEDs for all sources were fitted using the same method as in Chapter 3 using the 70, 160, 250, 350 and 500 μm data points. A sample of typical SEDs is shown in Figure 4.24. From the SEDs I have calculated the luminosities and temperatures of the sources using the same methods as in Chapter 3. The source sizes, masses, luminosities and temperatures can all be found in Table A.4. Due to the availability of the 160 μm data point, the peak of the SED is much better constrained compared to the Carina Nebula SEDs, and this gives more accurate values for the luminosities and temperatures. For a discussion on the errors please see Chapter 3.

4.6.2 Source sizes and morphologies

To measure the radius of each source I used the same method as in Chapter 3. Figure 4.25 shows a histogram of the size distribution of the sources in NGC 7538. It shows that there is a characteristic source radius of typically 0.5 pc at the distance of NGC 7538, and a range of 0.1 – 2 pc. This is a similar range to Carina but the peak of the distribution is at a much smaller size. The Herschel angular resolution at 250 μm is 18″, which is comparable to the 20″ lower limit on the source radius, so this limit may be due to resolution effects. The source sizes can be found in column 2 of Table A.4.

Figure 4.26 shows a selection of sources and their mean x and y profiles. The majority of sources appear to be Gaussian which means they are probably unresolved. This is supported by the angular resolution being close to the lower size limit of the sources. All the sources have been treated as being Gaussian.

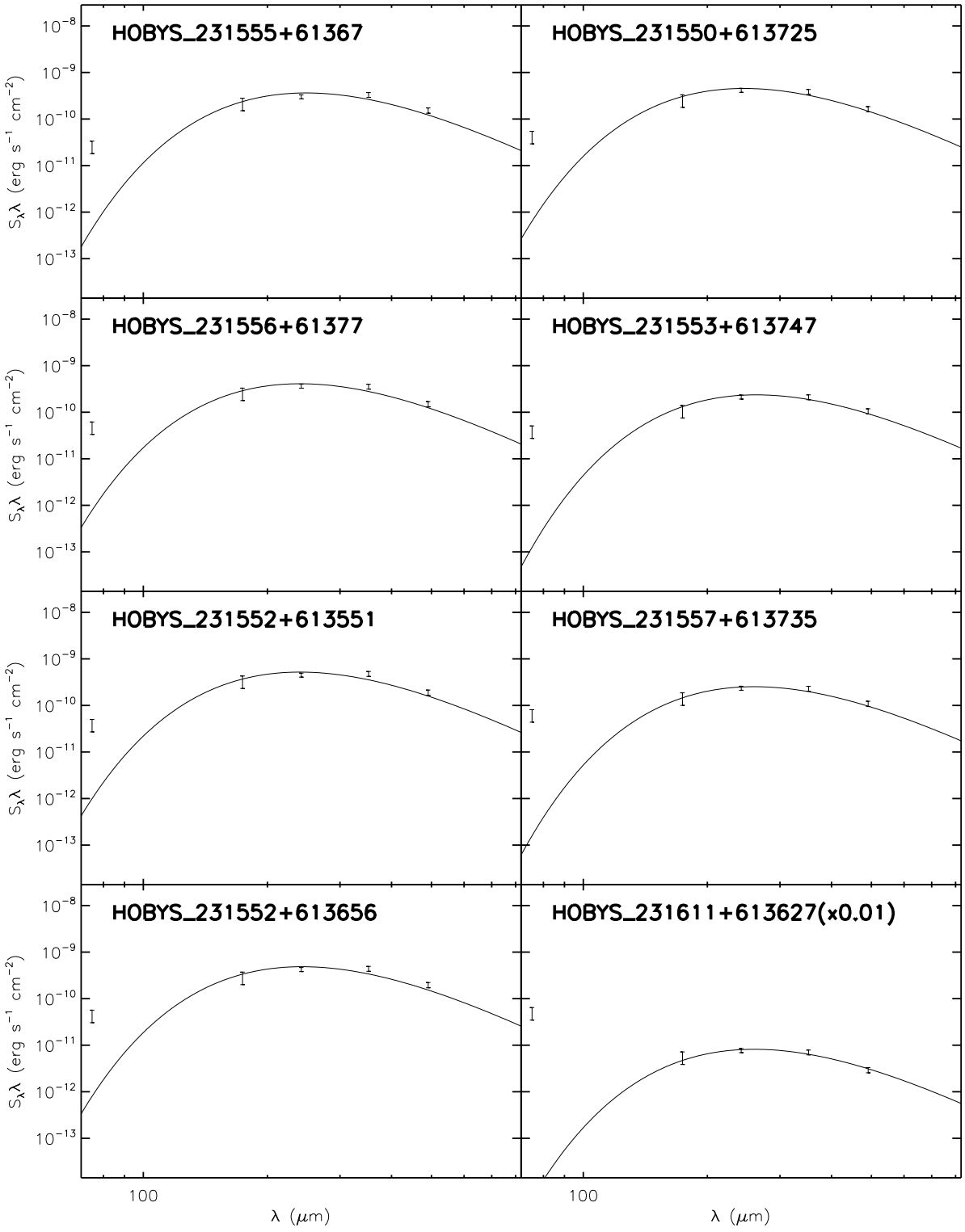

Figure 4.24: A sample of SEDs using the 70, 160, 250, 350 and 500 μm data points.

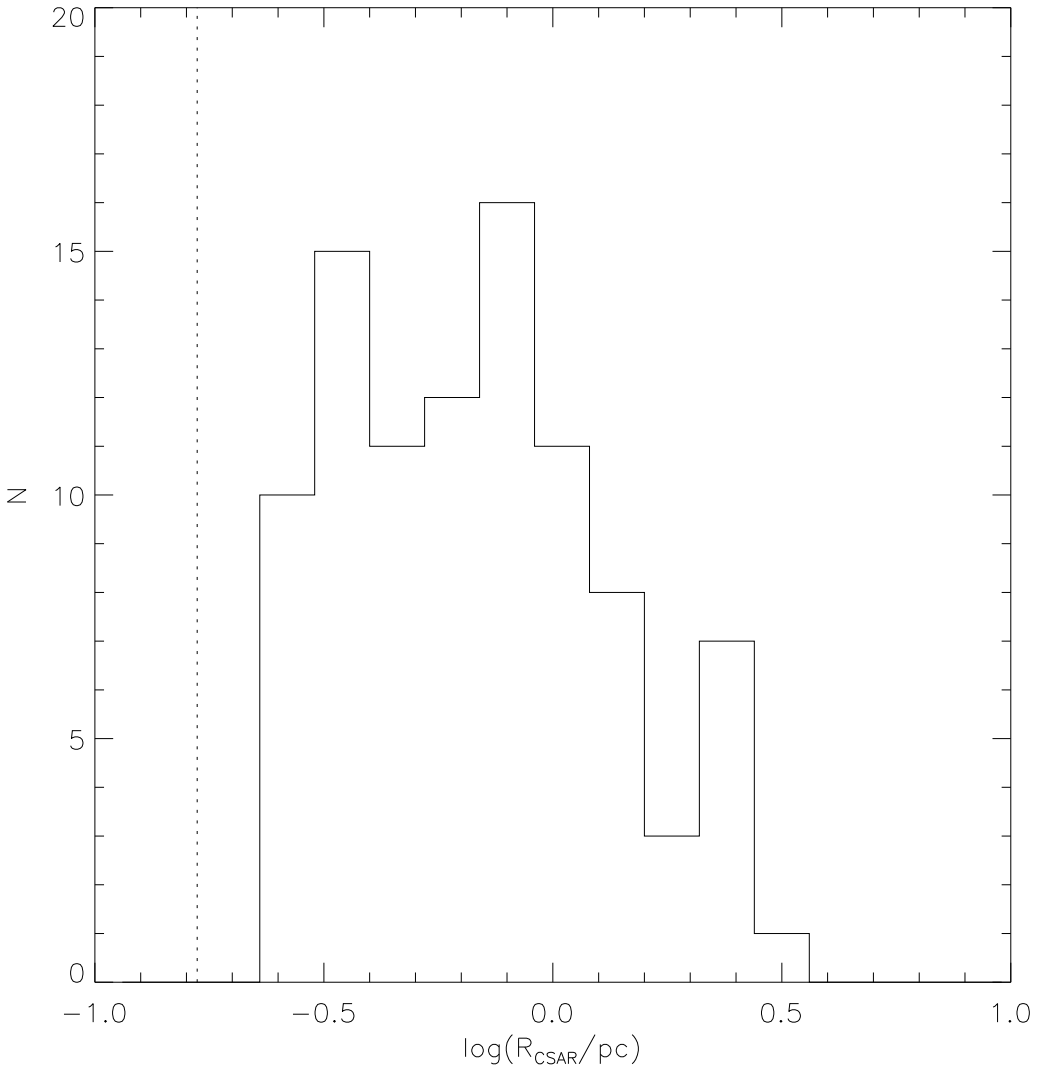

Figure 4.25: A histogram showing the size distribution of the sources in NGC 7538 extracted using CSAR. The dotted line shows the angular resolution.

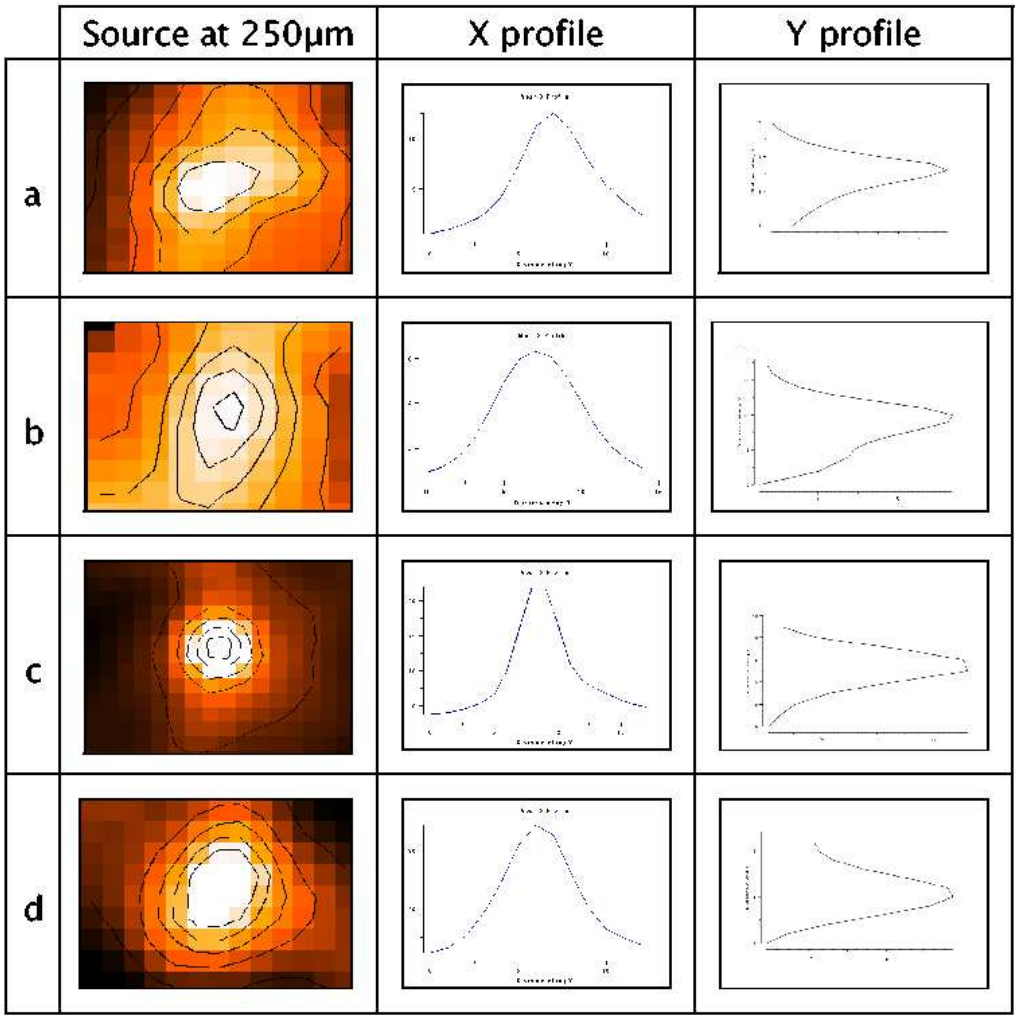

Figure 4.26: A selection of sources shown at 250 μm and their mean x and y profiles. The sources are a) HOBYS 231710+613124 b) HOBYS 231554+612533 c) HOBYS 231611+613627 and d) HOBYS 231310+612824.

4.6.3 Luminosities

The source luminosity distribution is shown in Figure 4.27, which shows a peak at $60\,L_{\odot}$, with a range from $5-10^3\,L_{\odot}$. The distribution shows a steep increase towards the peak and then a tail at the higher luminosity end. The completeness limit was calculated using the minimum $5\,\sigma$ detection limit set by CSAR, and gave a cut off of $4\,L_{\odot}$, this suggests the data are sensitivity limited. This cut off is shown as a dotted line on Figure 4.27. The source luminosities can be found in column 3 of Table A.4. These sources are smaller then those found in Carina, with on average a lower luminosity. This could suggest that most of the sources are either individual high mass cores or small clusters.

4.6.4 Temperatures

The source temperatures were derived from the modified blackbody SEDs using both PACS and SPIRE data and are in the range $\sim 10-40\,\mathrm{K}$, as shown in Figure 4.28. The temperature distribution is asymmetric with a mean of approximately 15 K. NGC 7538 has a much larger range of temperatures compared to Carina but the average temperature is lower. This small range of temperatures seems common in high mass star forming regions observed with *Herschel* as it is found in other regions such as Vela C (Hill et al., 2011). The completeness limit for source temperatures is 10 K. This was derived using the same method as for the luminosity. This may mean the sources are sensitivity limited. The source temperatures can be found in column 4 of Table A.4. Figure 4.29 shows a temperature map for NGC 7538. This was created by fitting an SED to every pixel and extracting a temperature. From this we can see the possible UCHII regions are hot, along with a few sources in the triggered ring of star formation. The four spatially separate

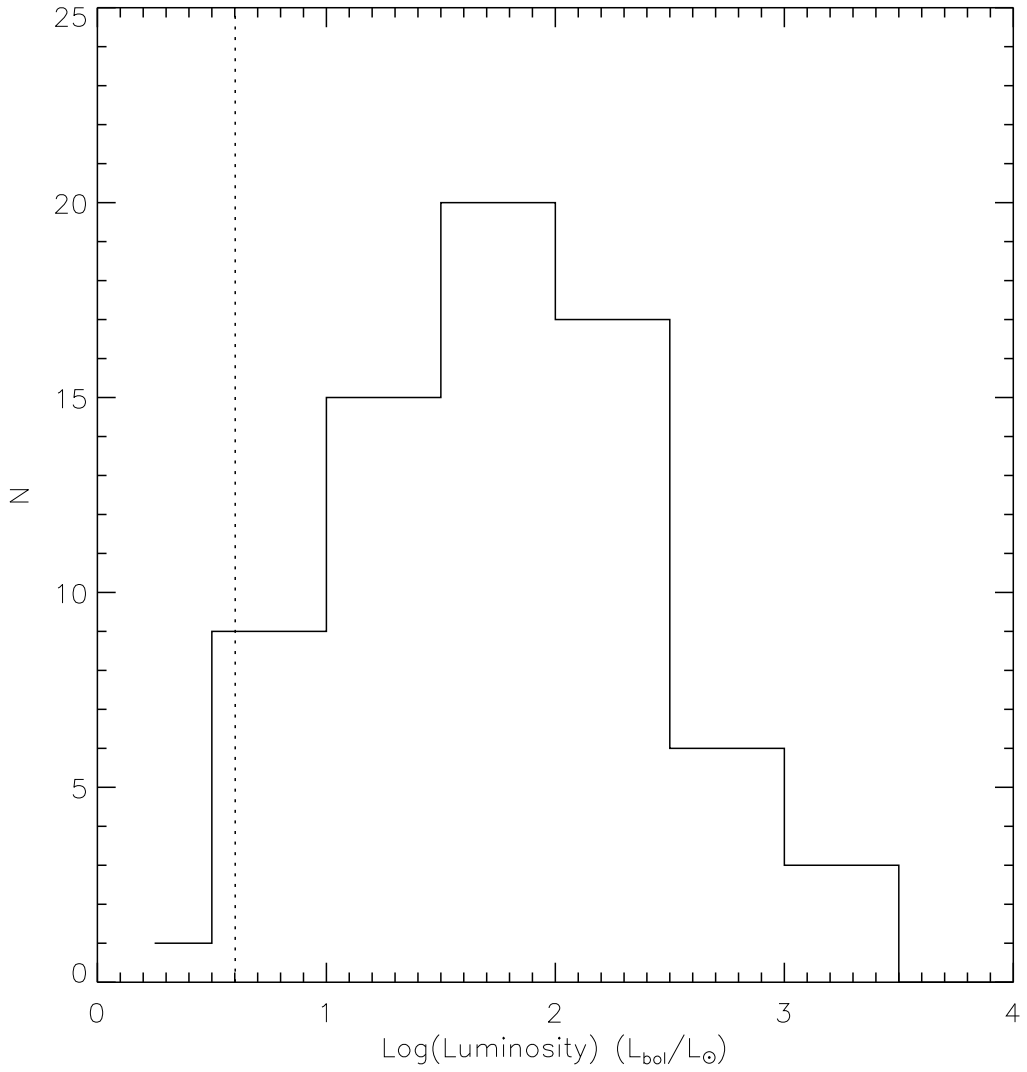

Figure 4.27: A histogram showing the luminosity distribution of the sources in NGC 7538 extracted using CSAR. The dotted line shows the completeness limit.

regions in the main cloud also appear to be very hot as expected. There is a large diffuse arc of dust which rises from the main cloud. This would suggest that there are one or more heating sources within it. These differing amounts of thermal emission throughout the cloud are in contrast to Carina, where the thermal emission was roughly constant throughout the nebula.

4.6.5 Masses

Figure 4.30 shows a histogram of the mass distribution. The source masses peak at around $80 M_{\odot}$ with a range from $5 - 10^{3} M_{\odot}$. The average mass of sources in NGC 7538 is much lower then the average source mass in Carina. The source sizes, luminosities and temperatures make it quite probable that a proportion of these sources are individual high mass cores or small clusters rather than the large high mass clusters found in Carina. The source masses can be found in column 5 of Table A.4. The dotted line shows the completeness limit for this region, like with Carina, we are probably missing many of the smaller mass sources, but as we are mainly interested in the high mass star formation this will not affect our results. We know that this region contains many high mass stars, as it is a much larger region then the closer low mass regions such as Taurus and Orion. The presence of HII regions is a signpost that high mass star formation is taking place here and the OB star associations show that high mass star formation has already taken place.

4.7 Summary

In this chapter, I have analysed *Herschel* observations of NGC 7538. I have identified 94 sources. The sources all appear at 250 and 350 μm; 30 % do not appear at

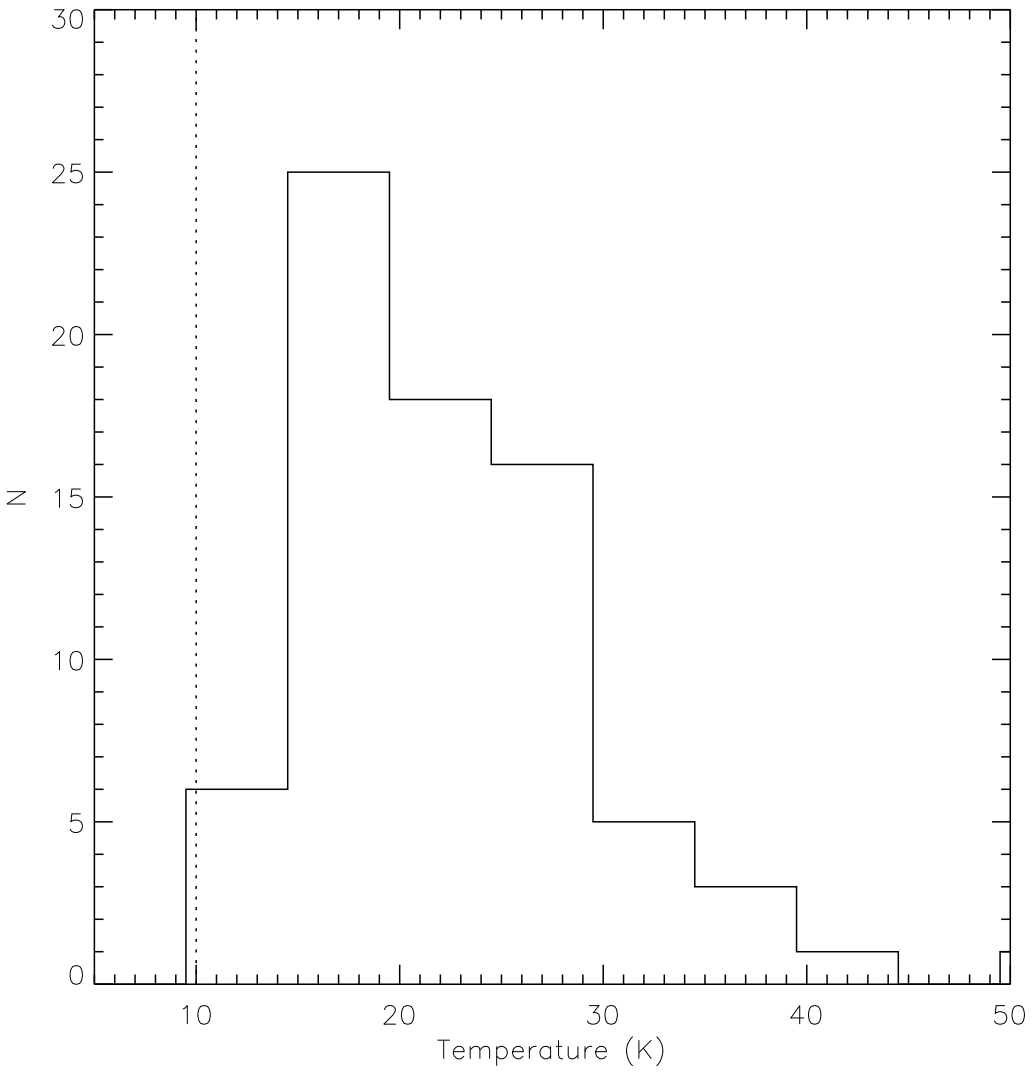

Figure 4.28: A histogram showing the temperature distribution of the sources in NGC 7538 extracted using CSAR. The dotted line shows the completeness limit.

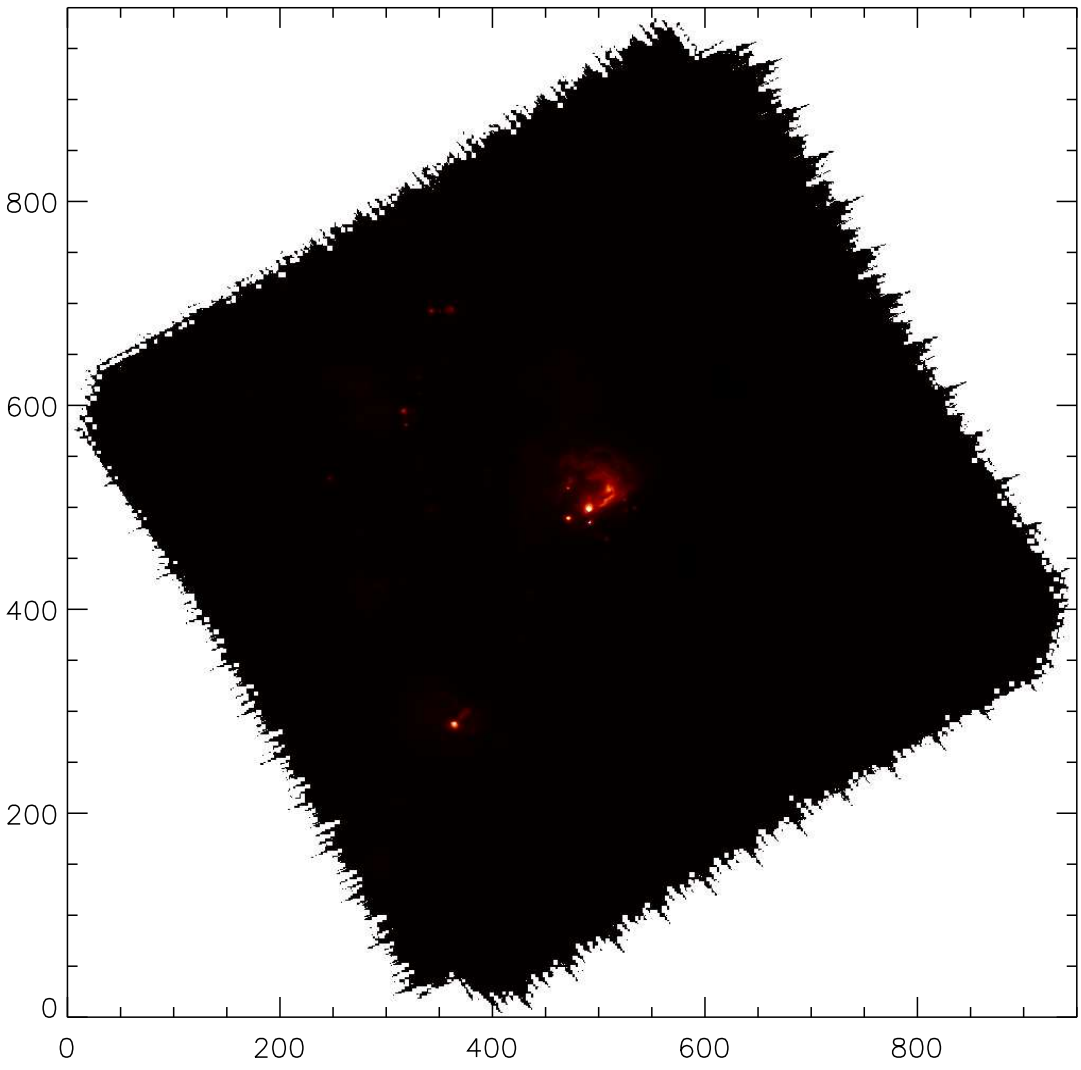

Figure 4.29: A temperature map of NGC 7538.

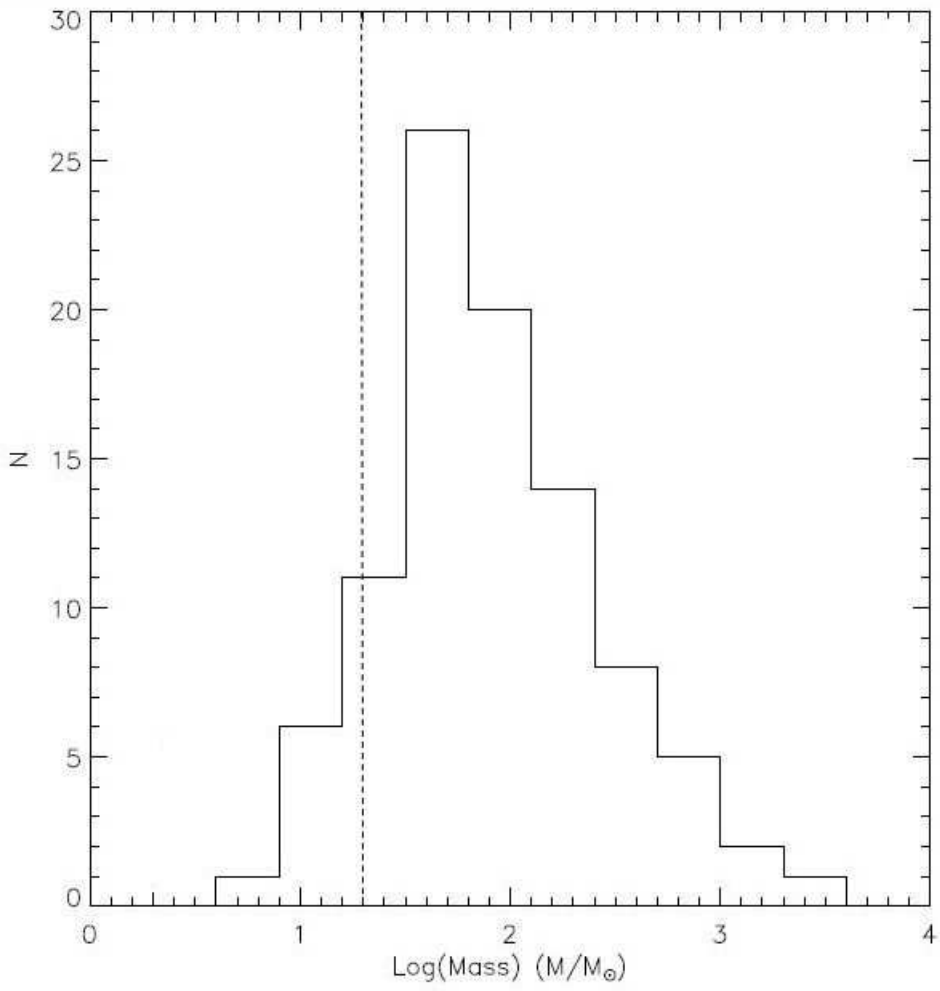

Figure 4.30: A histogram showing the mass distribution of the sources in NGC 7538. The dotted line shows the completeness limit.

70 or 160 μm; and 4 % do not appear at 500 μm. The masses of the sources range from 5 to $10^3\,M_\odot$, with an average source mass of $80\,M_\odot$. This is much smaller then the masses in Carina and indicates that the sources are likely to be individual cores or small clusters. Source luminosities range from 5 to $10^3\,L_\odot$ with a peak luminosity of $60\,L_\odot$. There is a temperature range of 10 to 40 K with an average temperature of 15 K, the temperature dependence is discussed further in Chapter 5. Source radii lie in the range of 0.1 to 2 pc. I have also compared my results with those obtained using a second source extraction algorithm, GETSOURCES. This found a total of 621 sources. After filtering the GETSOURCES catalogue I find a better correlation with the CSAR catalogue. Since there have been no other studies which cover the extented emission in NGC 7538 we cannot directly compare our results, however surveys carried out on the dense cental regions, such as Werner et al. (1979b) and Reid & Wilson (2005b), have found similar masses and temperatures.

Chapter 5

Data Analysis and Discussion

5.1 Introduction

In this chapter, I present the analysis and discussion of the results from the Carina Nebula and NGC 7538 observations described in Chapters 3 and 4. In section 5.2, I discuss the mass - radius relation derived for both regions and then compare the two. In Section 5.3, I look at the temperature dependence for both the Carina Nebula and NGC 7538 and discuss the similarities and differences between the two. In Section 5.4, I review the relation between luminosity and mass for both regions. In Sections 5.5 and 5.6, I summerise the global properties for both Carina and NGC 7538. Noting that none of these parameters alone allows us to characterise the evolutionary status of the sources, I then introduce the use of luminosity per unit volume as a potential evolutionary discriminator in Section 5.7, and consider the Carina and NGC 7538 results using this parameter.

5.2 Mass - radius relation

To find out more about the sources in a region we can analyse their physical properties. These can tell us how evolved the sources are and give us insight into how star formation has progressed. One of the properties we can analyse is the mass - radius relation. We would expect to see a linear trend with small, low mass sources and large, high mass sources.

In this Section, I will show the mass - radius for the Carina Nebula in 5.2.1 using the results from Chapter 3 and for NGC 7538 in 5.2.2 using the amended catalogue found in Chapter 4. I will then discuss the analysis and compare the results in 5.2.3.

5.2.1 Carina Nebula

Using the masses and radii calculated in Chapter 3, I can find the mass - radius relation for the sources in the Carina Nebula. This is shown in Figure 5.1. It is clear that there is a correlation between the two properties. I used the IDL function LINFIT to find the relation between the mass and radius. It fits a linear model to the data by minimising the chi - squared error statistic and returns the error on the parameters. Using this function, I find a relation following $M \propto R^{1.8 \pm 0.3}$ (plotted as a solid line in Figure 5.1). The correlation coefficient for this fit is 0.5. This is consistent with the Larson relation of $M \propto R^2$ (discussed in Chapter 1), which is plotted on Figure 5.1 as a red line. This means that these sources roughly follow the same mass - radius relation as most other objects in a molecular cloud, including the cloud itself which means that this relation is independent of scale. For the Carina Nebula there is a mass range of $10^2 - 10^4\,M_\odot$ and a range of radii

of 0.2 – 3.2 pc. From the figure we can see that the data points are very spread out with around an order of magnitude spread of masses for every value of radius and vice versa for mass. For example, for a radius of 1 pc there is a range of masses of $10^3 - 10^4\,M_\odot$. This could be due to the diverse populations of sources present in the sample, including large high mass clusters. As noted by Larson it could also be because some of the sources are undergoing gravitational collapse and so are not in virial balance, and the spread could also be partly caused by inaccuracies in measuring the sizes of the sources.

5.2.2 NGC 7538

As above I can use the results from Chapter 4 to find the mass - radius relation for NGC 7538. This is shown in Figure 5.2. If the three outliers in the upper right hand corner of the plot are ignored, then there is no clear correlation between the source mass and radius. The routine LINFIT was unable to converge on a fit, with the correlation coefficient for this fit being 0.09. Again there is a large range of masses for every value of radius, for example for a radius of 0.3 pc there is a spread of values of masses ranging from $10 - 100 M_\odot$ and the same is true for mass. From this figure it is clear that there are many sources with small radii (around 0.16 pc). This could be due to a bias caused by sources being a similar size to the beam or smaller. However even if we only look at sources starting at slightly above the beam size there is still no relation between the mass and radius. This is probably not significant as many sources were removed from the catalogue when making it robust. For this region there is a mass range of $10 - 10^3\,M_\odot$ and a radius range of 0.1 – 2.0 pc. This large spread in values and lack of a relation between the mass and radius could tell us that the sources are at a range of evolutionary states

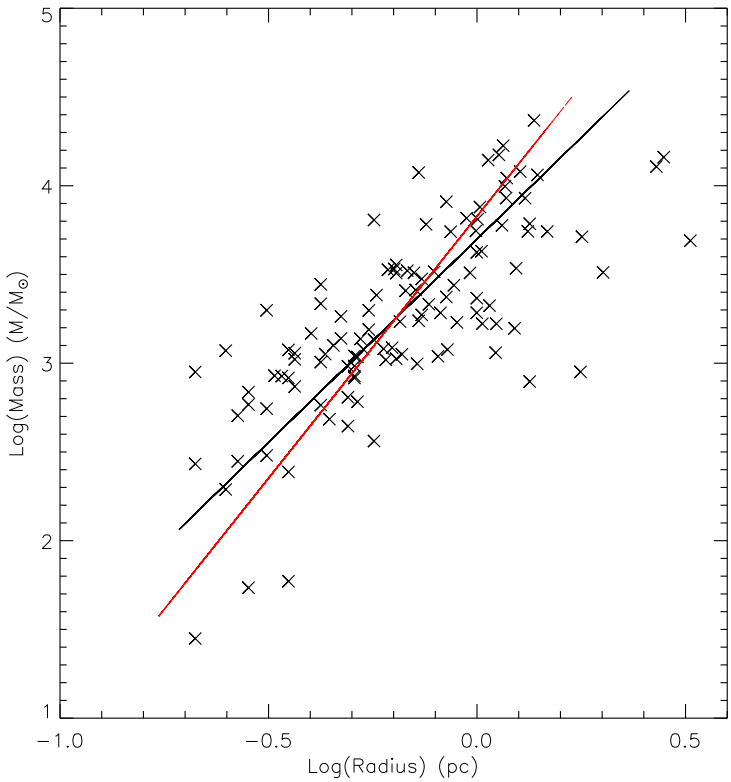

Figure 5.1: Mass against radius for the Carina Nebula. The solid line shows the trend calculated by LINFIT, $M \propto R^{1.8}$. The red line shows the Larson relation of $M \propto R^2$.

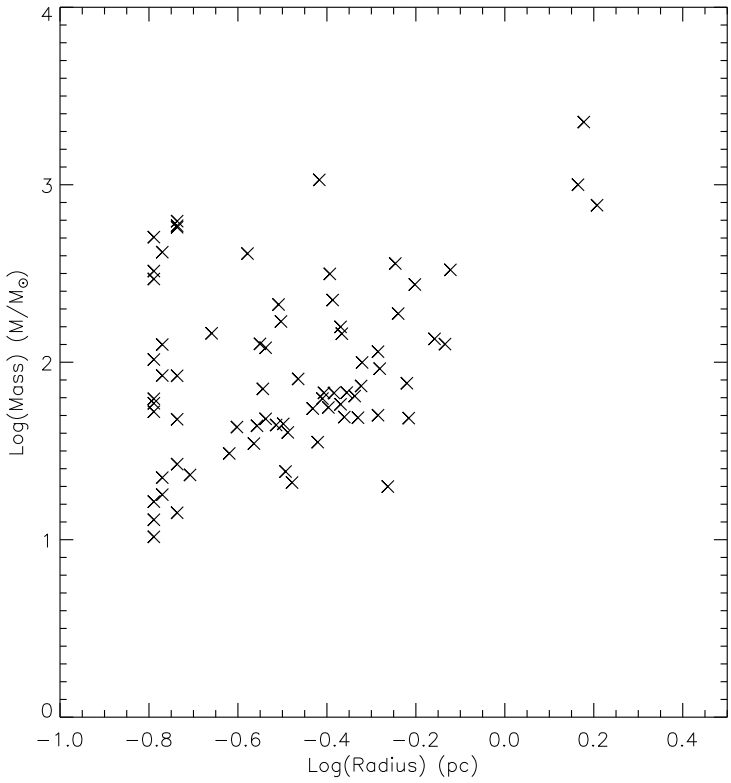

Figure 5.2: Mass against radius for NGC 7538.

with some in free fall collapse or undergoing gravitational contraction. From the figure there is a group of what appear to be outliers with radii of approximately 1.9 pc and masses of around $10^3 M_\odot$. These three sources are located in the dense filament directly above the ring of triggered star formation. They are large with high masses but mid range luminosities and temperatures, but do not otherwise show any unusual features. It is worth noting that these three sources only appear exceptional when using the robust catalogue which contains sources found by both CSAR and GETSOURCES. A number of the larger radius sources present in the original CSAR catalogue were not found by GETSOURCES so were removed. This means that the gap between these sources and the rest of the sample could be artificial.

5.2.3 Discussion

In the Carina Nebula I find a relation following $M \propto R^{1.8 \pm 0.3}$ whereas the results from NGC 7538 show no correlation with the routine LINFIT being unable to converge on a fit. This shows that there must be some key differences between the two regions. *Herschel* has a better angular resolution than BLAST so the lower radius limit for NGC 7538 is slightly lower than that for Carina. NGC 7538 also appears to have smaller sources overall. The Carina Nebula contains higher mass sources with a mass range of $10^2 - 10^4\, M_\odot$ and NGC 7538 has significantly lower mass sources with a mass range of $10 - 10^3\, M_\odot$. There is a difference in distance between the two regions with Carina being at a distance of 2.3 kpc and NGC 7538 at a distance of 2.8 kpc, however the difference in masses in the two nebulae is not a distance selection effect as SPIRE is more sensitive then BLAST. For both regions there is a wide spread of masses for every radius. This wide spread could be due to

the diverse populations present in each region, with sources at differing stages of evolution. As star - forming cores evolve they get smaller, so for any given radius, there could be sources of varying masses which happen to be at the same radius at the time they were observed, e.g., an old massive source and a younger less massive source could have similar sizes. These sources could also be undergoing gravitational collapse so their radius will be decreasing even though their mass will be constant. Neither region shows a tight correlation of around half an order of magnitude as was predicted by Larson for sources of this size. This could show that his relation may not be completely valid for high mass clusters. This may be due to the nature of clusters which have complex internal structures which will be constantly changing as the cores within move and evolve. So for sources of this type, the Larson relation may just be an indicator of what to expect.

5.3 Temperature - luminosity and temperature - mass relation

We can investigate the relation between temperature and other source properties as a possible way of distinguishing the evolutionary status of the sources in a region. This is done by plotting the source temperature against luminosity or mass. From the theory (discussed in Chapter 1) we would expect more evolved star - forming cores to be hotter and more luminous then less evolved star - forming cores.

In this Section, I will show the temperature relations for the Carina Nebula in 5.3.1 using the results from Chapter 3 and for NGC 7538 in 5.3.2 using the robust catalogue found in Chapter 4. I will then discuss the analysis in 5.3.3.

5.3.1 Carina Nebula

Using the calculated temperatures, luminosities and masses from Chapter 3, I can search for any temperature dependence present in this region. Figures 5.3 and 5.4 show the source luminosity against temperature, and the source mass against temperature respectively. Neither of these properties shows a relation with temperature. The correlation coefficient for Figure 5.3 is 0.05 and for Figure 5.4 is 0.07. In each plot there is a small range of temperatures but a large spread of values for the other properties (about an order of magnitude). The lack of any relation between temperature and mass or luminosity means that for this region we can not use temperature to tell us about the evolutionary status of the sources. This lack of any dependence could be due to the sources being in clusters, so the calculated temperature is an average for all the stars in the cluster. The small spread of temperatures may also be due to how the region was observed. BLAST was only sensitive to a specific range of temperatures due to its limited wavelength coverage, so because of this we may be missing some of the less massive, hotter sources from our catalogue.

5.3.2 NGC 7538

As for the Carina Nebula I can use the calculated temperatures, luminosities and masses from Chapter 4 to show any temperature dependence for NGC 7538. Figure 5.5 shows the source luminosity against temperature and Figure 5.6 shows the source mass against temperature. From Figure 5.5 there is a weak relation between the source temperature and luminosity following $T \propto L^{0.25 \pm 0.08}$ with the hotter sources being slightly more luminous, the correlation coefficient for this fit is 0.3. Although there is a spread of values spanning two orders of magnitude it does

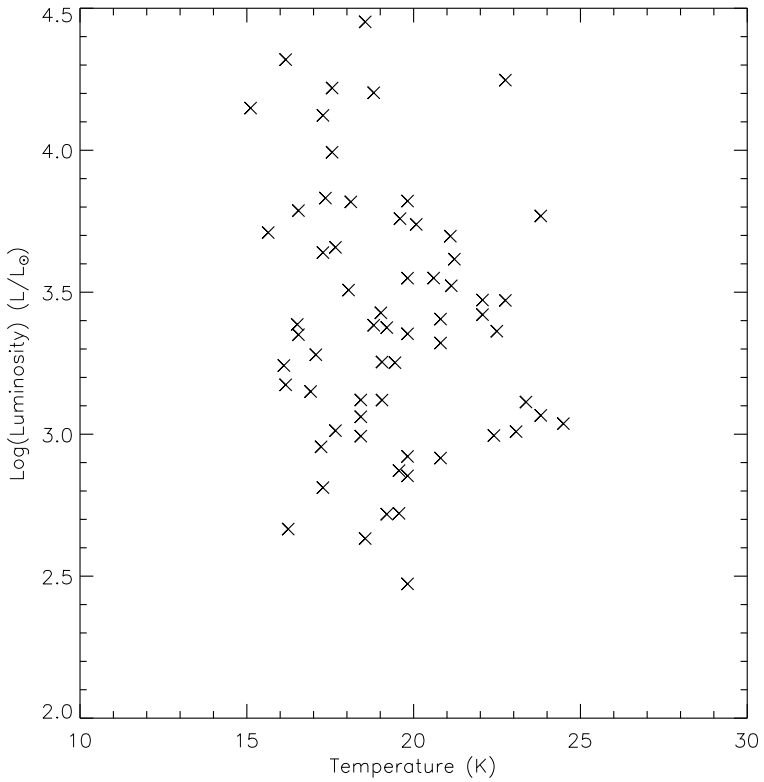

Figure 5.3: Luminosity against temperature for the Carina Nebula.

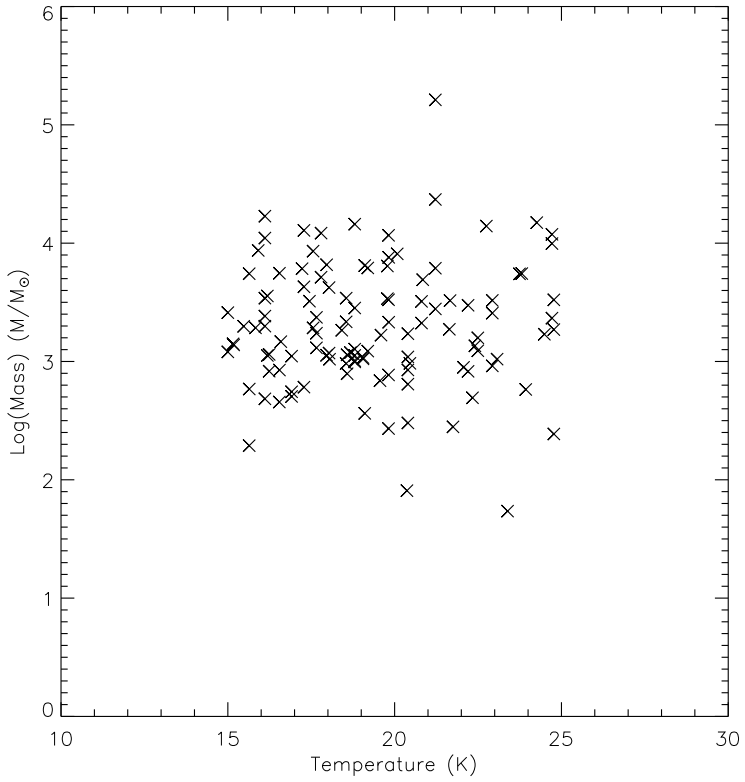

Figure 5.4: Mass against temperature for the Carina Nebula.

appear to be real, if any outliers are removed the relation remains unchanged. From Figure 5.6 there is no dependence of temperature on source mass with LINFIT being unable to converge on a fit. The correlation coefficient in this case is 0.08. This lack of a correlation could be due to the differing populations present in the region, with some sources being part of clusters so the temperature of each individual source within the cluster is being averaged over the entire cluster. In both plots there appears to be an outlier. This source has a high temperature and luminosity but a mid range mass. It is possible that this particular source is at a more advance stage of evolution compared to the other sources in the region.

5.3.3 Discussion

In this section I have plotted the source temperature against luminosity and the source mass against temperature for both the Carina Nebula and NGC 7538. In the Carina Nebula I find no relation between temperature and either luminosity or mass. In NGC 7538 I find a weak relation between temperature and luminosity following $T \propto L^{0.25 \pm 0.08}$ but no relation between temperature and mass. The lack of any relation between temperature and the source luminosity or mass is surprising as we would expect there to be a connection between the two. Because there is not a correlation this means that we can not use temperature as a way of distinguishing the sources or to get any information about their evolutionary status. NGC 7538 shows a larger temperature range then in Carina, this may be one of the key differences between the two regions and why we see a relation between temperature and luminosity in NGC 7538 but not in Carina. The Carina Nebula contains more higher mass sources, these are likely to be massive protoclusters so any property is not related to just one star - forming core. The fact that the

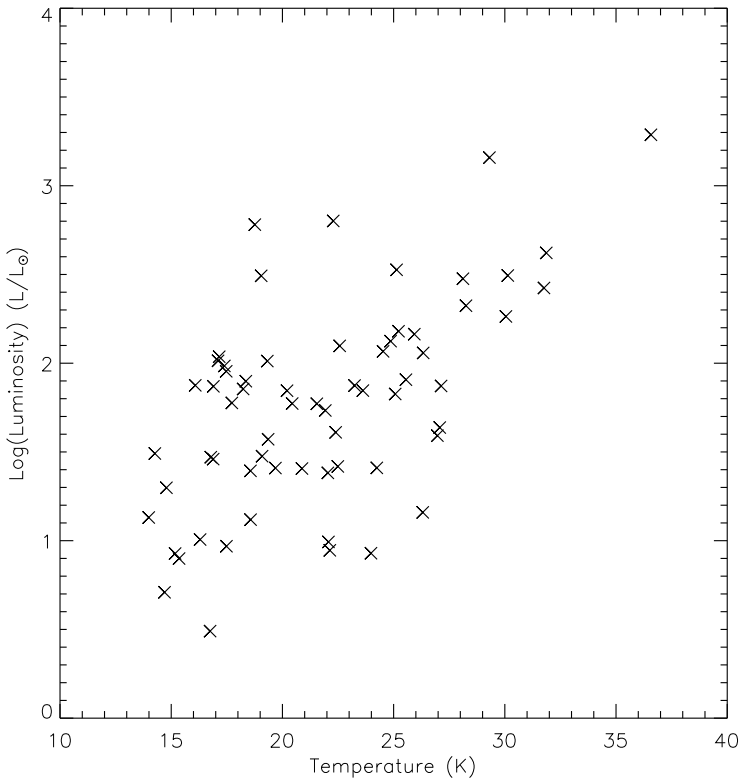

Figure 5.5: Luminosity against temperature for NGC 7538.

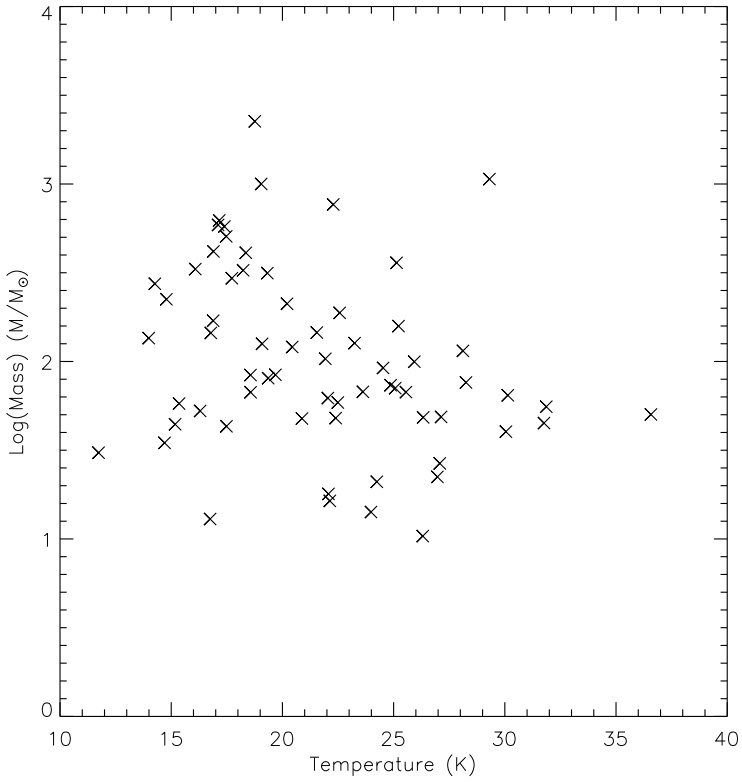

Figure 5.6: Mass against temperature for NGC 7538.

temperature is not linked to the evolutionary state of the sources means that the material we are seeing is never being dominated by warm dust around the YSOs, even in highly evolved regions such as Carina. So the material responsible for the 70 μm sources is not really important for the overall energy output, most of which goes to heating larger quantities of cooler dust.

5.4 Luminosity - mass relation

A source's luminosity is inevitably closely related to its mass due to how these properties are interlinked at a fundamental level. By plotting luminosity against source mass we expect to see a tight correlation. In this section, I show the relation between luminosity and mass for both the Carina Nebula in 5.4.1 and NGC 7538 in 5.4.2, I then discuss the results and their implications in 5.4.3.

5.4.1 Carina Nebula

I can use the luminosities and masses calculated for the Carina Nebula in Chapter 3 to plot the luminosity - mass relation. This is plotted in Figure 5.7. We can see that there is a clear correlation between the two, following $L \propto M^{1 \pm 0.09}$, plotted as a solid line on the figure. This fit has a high correlation coefficient of 0.9. This is exactly as we would expect, however even though there is a very clear correlation with the high mass and high luminosity sources, at the smaller mass and luminosity range there is a deviation from the best fit line of around one order of magnitude. There appears to be one source which is an outlier with a mass around $10^{3.5} M_{\odot}$ and a luminosity of $10^{4} L_{\odot}$. This source, shown in Figure 5.9(A), is BLAST 104348-592824 and lies in the confused and dense central region

of the nebula which means that it may represent more than one cluster, or be contaminated from the surrounding dust. This source does not affect the fit to the data.

5.4.2 NGC 7538

As for the Carina Nebula I have used the calculated luminosities and masses for NGC 7538 to see the luminosity - mass relation. This is shown in Figure 5.8. I have calculated a best fit line using the routine LINFIT and found the relation $L \propto M^{1 \pm 0.2}$. This is a weak relation with a large spread of values for the mass at any given luminosity and the same the other way round. The correlation coefficient for this fit is 0.4. Again there is a clear outlier present in the plot. This source was identified in the previous section as being hot and luminous but only having a mid range mass. The source, shown in Figure 5.9(B), is HOBYS 231610+613626 and is located in the triggered ring of star formation to the left of the main cloud and is possibly at a more evolved state compared to the other sources in the nebula.

5.4.3 Discussion

In Carina I find a tight correlation following $L \propto M^{1 \pm 0.09}$ and in NGC 7538 I find a weaker relation following $L \propto M^{1 \pm 0.2}$. In both regions there is a spread of luminosities for a given mass. In Carina this spread is almost an order of magnitude at the lower luminosity and mass end which decreases to around a quarter of an order of magnitude at the higher luminosity and mass end. This spread is much greater in NGC 7538, with the luminosities spreading over an order of magnitude for the whole mass range. The two graphs are combined in Figure 5.10. It is clear

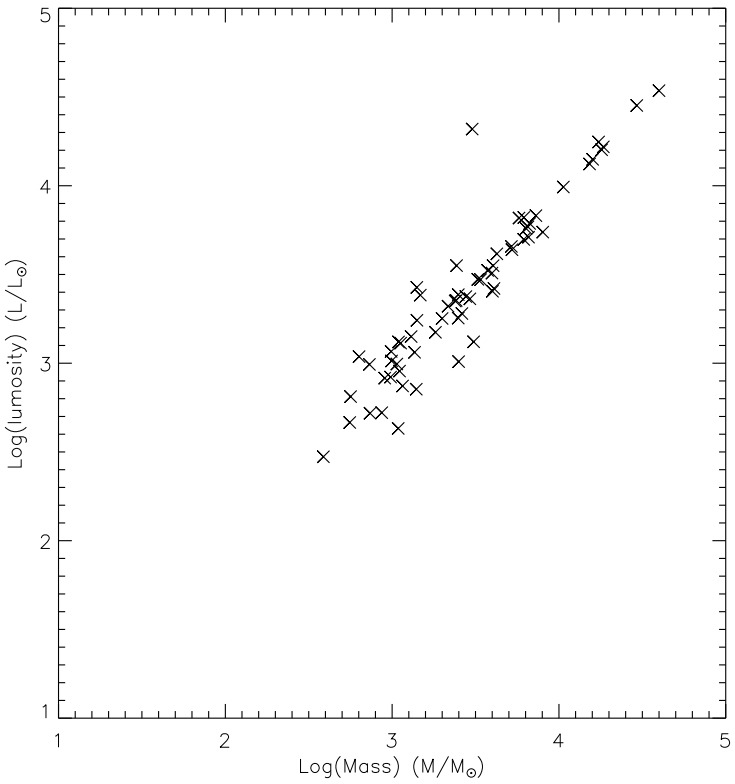

Figure 5.7: Luminosity against mass for the Carina Nebula. The solid line shows the relation $L \propto M$.

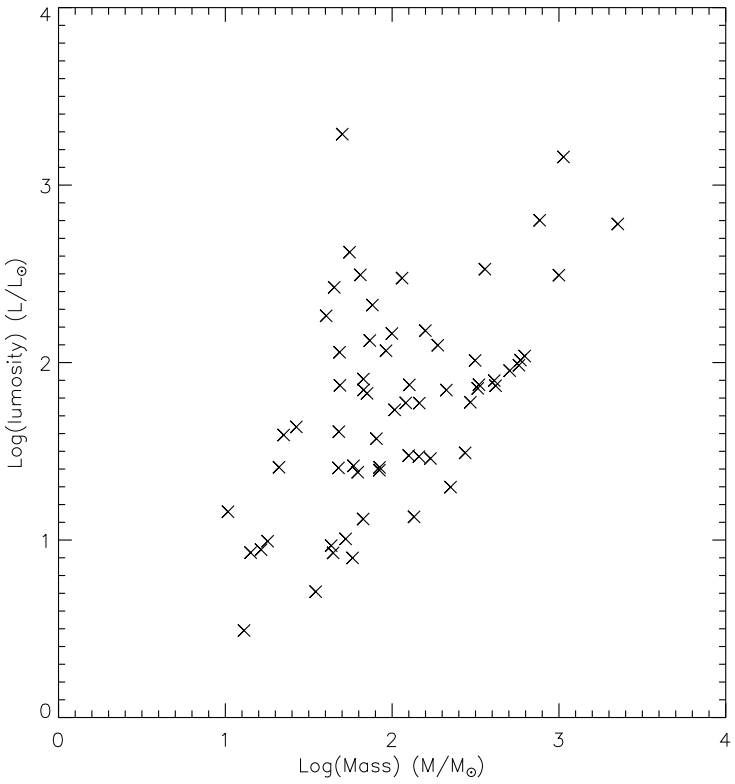

Figure 5.8: Luminosity against mass for NGC 7538.

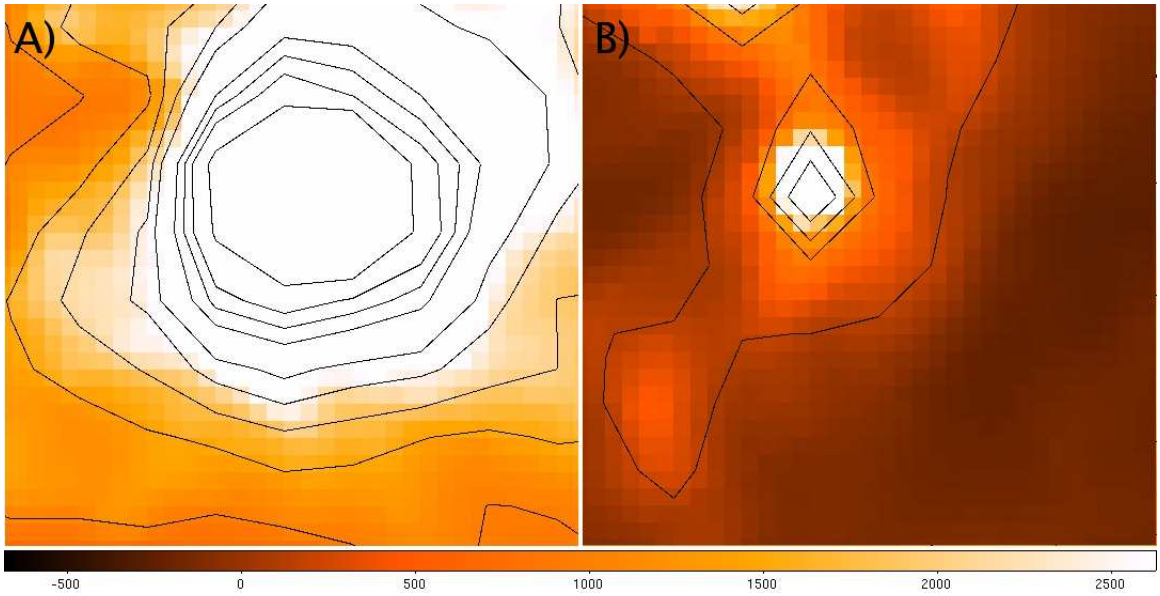

Figure 5.9: A) BLAST 104348-592824 B) HOBYS 231610+613626

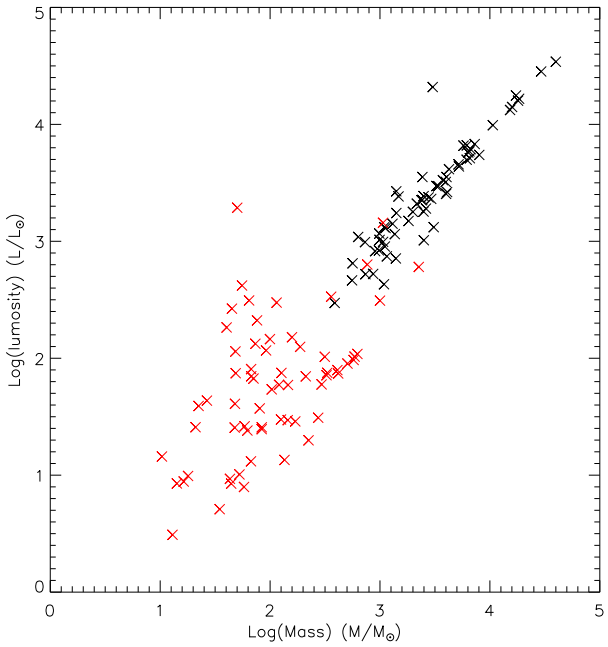

Figure 5.10: Luminosity against mass for NGC 7538 (red crosses) and the Carina Nebula (black crosses)

that they both follow the same slope of $L \propto M$ but there is a large spread at the low mass and low luminosity range that becomes much smaller as the mass and luminosity increases. The larger range of temperatures present in NGC 7538 may account for the larger spread of values seen on the plot. This relation is as we expected, as the masses are calculated from the submillimetre flux densities and if there is a small range of temperatures the mass and luminosity should be related in a consistent way.

5.5 Global properties of the Carina Nebula

In Chapter 3, I analysed BLAST scan map observations of the Carina Nebula at 250, 350 and 500 μm. From these I identified 172 sources using the source extraction algorithm CSAR, and shown that there is high mass star formation taking place throughout the nebula. In this region I found a very small range of temperatures, $16-28$ K. Source masses are in the range, $10-10^5\,M_\odot$, and the source radii lie in the range of $0.3-3.2$ pc with a characteristic source size of 1 pc. The source luminosities range from $10^2-10^5\,L_\odot$. The high luminosities and masses in this region and the source radii, suggest that many of the sources are clusters of high mass protostars.

In this chapter, I have looked at the physical properties of the sources in the Carina Nebula and analysed them to see if any property could tell us more about the evolutionary state of the sources. I find that there is a mass - radius relation of $M \propto R^{1.8\pm0.3}$ which is within a $1\,\sigma$ error of the Larson relation of $M \propto R^2$. This means that these sources roughly follow the same mass - radius relation as most other objects in a molecular cloud, including the cloud itself which means that

this relation is independent of scale. However there is a large spread of values for both mass and radius. I have also looked into the relations between temperature and other properties and found that there is no correlation between the source temperature and mass or luminosity in this region. This means that temperature cannot be used to distinguish the sources. I find a tight correlation between source luminosity and mass which is as expected, this relation follows $L \propto M^{1\pm0.09}$, although there is still a spread of values around one order of magnitude. The results from this region would suggest that the global properties of these sources cannot be used to tell us any information on the evolutionary state of the sources, this is most likely due the diversity of the sources present in the region.

5.6 Global properties of NGC 7538

I have analysed *Herschel* observations of NGC 7538 in Chapter 4, at 70, 160, 250, 350 and 500 μm and from these I have identified 94 sources using CSAR. This was then reduced to 75 sources using the SAG3 'robust' definition. From these sources I have shown that there is massive star formation taking place within the main cloud and in the filaments surrounding it. In this region I have found a range of temperatures of 10 – 60 K, with an average temperature of 15 K. The hottest sources are in the ring of triggered star formation, the possible UCHII regions and in the main cloud. Masses of the sources range from $5-10^3\,M_\odot$, indicating that the nebula contains some cluster - forming sources and some individual high mass sources. Source radii lie in the range of 0.1 – 2 pc and source luminosities range from $5-10^3\,L_\odot$ with a peak luminosity of $60\,L_\odot$.

In this chapter, I have analysed the global properties of the sources in NGC 7538,

and from these I have found no relation between mass and radius. From this plot there is a wide dispersion of values of both mass and radius which could be due to the nebula containing a wide variety of sources at differing stages of evolution. I have found a weak correlation between the temperature and luminosity following $L \propto T^{0.25 \pm 0.08}$, with hotter sources being more luminous. However, as in the Carina Nebula, there is no relation between temperature and the mass of the sources. From this it is clear that we can not use temperature as an evolutionary discriminator. I find a weak relation between mass and luminosity, which follows $L \propto M^{1 \pm 0.2}$ which is surprising as we would expect a tight correlation, however this large spread is probably due to the larger range of temperatures present in the region. Again like in Carina from this analysis I can conclude that none of the physical properties of the sources in this region can be used to identify the evolutionary status of the sources.

5.7 Luminosity per unit volume

To find out more about the two regions we need to look further then just the basic properties of the sources. These properties are very useful to get a general idea of what is happening in the cloud but do not tell us a lot about the evolutionary status of the sources. To understand how star formation has progressed in a region we need to know at what evolutionary stage the sources are. In the following section I discuss the property, luminosity per unit volume, and show the values for sources in both the Carina Nebula and NGC 7538. I then go on to discuss the theory behind this property and then take it a step further to see how these sources are distributed throughout the nebulae.

By calculating the luminosity per unit volume we can see the differences between our sources. As a protostar or protocluster evolves, we might expect this parameter to increase as the source contracts. So if they give us a range of values then this could tell us more about the types of sources that are present in the nebulae and their evolutionary sate. I define the luminosity per unit volume as,

$$\mathcal{L} = \frac{L}{\frac{4}{3}\,\pi\,R^3}, \tag{5.1}$$

where R is the radius in parsec, derived by CSAR (see section 3.5), as the largest contiguous contour containing only one source.

I have used the values of luminosity and radius listed in table A.3 and equation 5.1 to calculate the luminosity per unit volume for all the sources in the Carina Nebula. These values are shown in Figure 5.11, plotted against source diameter. It is clear that there is a trend with sources that have a large diameter having a low value of luminosity per unit volume and those with a small diameter having a large luminosity per unit volume. There is a concentration of sources around the low diameter and low luminosity region of the plot, which could be due to a resolution effect.

As above we can calculate the luminosity per unit volume for the sources found in NGC 7538. This is shown plotted against diameter in Figure 5.12. From this plot we can see a similar trend as in Carina, despite the big difference in source masses and luminosities between the two regions. In Figure 5.12 there is a gap with no sources in the middle of the diameter range (between approximately $1.5-2.9\,\mathrm{pc}$) but we note that some sources in this region were removed when making the final robust catalogue. There is one point which does not seem to fit the trend as it has quite a large diameter but also a large luminosity per unit volume. This source is

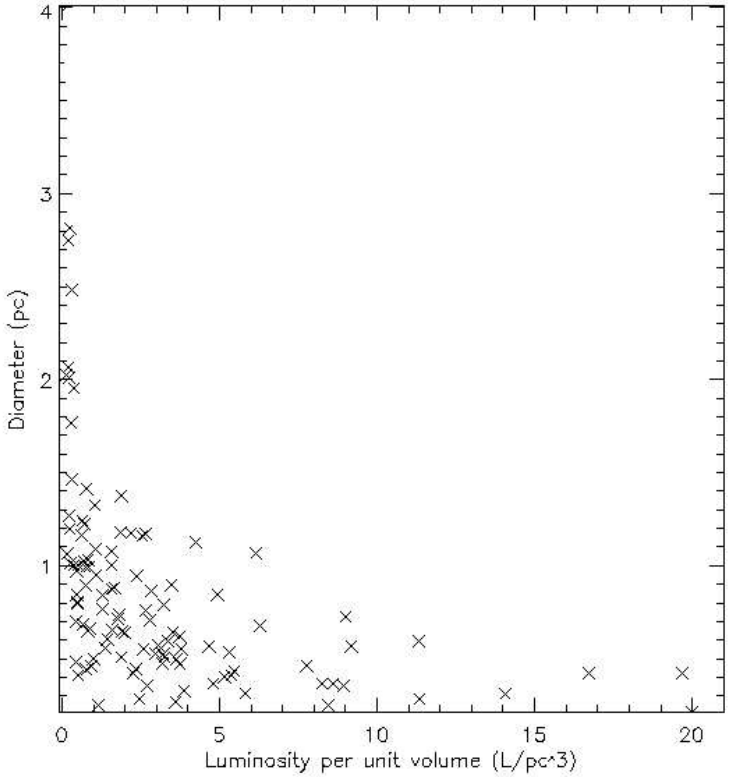

Figure 5.11: Luminosity per unit volume against diameter for the Carina Nebula

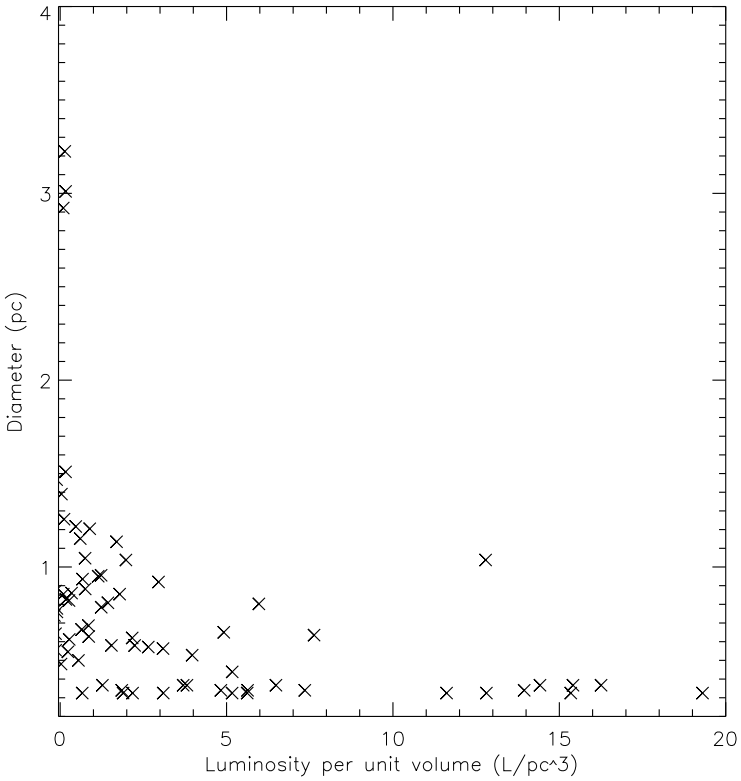

Figure 5.12: Luminosity per unit volume against diameter for NGC 7538

HOBYS 231610+613626 which has stood out as abnormal in previous graphs with a high luminosity and high temperature. This graph emphasises that this source is different to the rest.

5.7.1 Discussion

For both the Carina Nebula and NGC 7538 we see a trend where the larger sources have a lower value of luminosity per unit volume and the smaller sources have a larger value for luminosity per unit volume. The plots in Figure 5.11 and 5.12 are remarkably similar. This would suggest that we have a range of evolutionary stages present in both samples. Even though both regions are very different we find a very similar trend in both, this could suggest that this is a universal property that does not rely on other environmental factors. It is possible that this property can be used as an evolutionary indicator, with a large young source having a low luminosity per unit volume then as it evolves its diameter decreases but its luminosity per unit volume increases. So as a source evolves it moves from the left of the graph to the right. Typical errors in diameter are around two pixels (0.33 pc for Carina and 0.16 pc for NGC 7538) and typical errors in luminosity per unit volume are around $0.6\,\mathrm{L}_\odot\,\mathrm{pc}^{-3}$ for Carina and $0.37\,\mathrm{L}_\odot\,\mathrm{pc}^{-3}$ for NGC 7538.

5.7.2 Theory

To calculate the luminosity per unit volume, $\mathcal{L}$, of a source we must first start with the number of dust grains per unit volume, n_d. This is given by the density of the cloud, ρ_c, divided by the mass of a dust grain (assuming spherical dust grains (Hildebrand, 1983)).

$$n_d = \frac{\rho_c}{\frac{4}{3}\pi\, a^3 \rho_d}, \tag{5.2}$$

where a is the radius of a dust grain and ρ_d is the density of the dust grain. The luminosity per unit volume is then given by the number of dust grains per unit volume multiplied by the surface area of the dust grain, A, multiplied by the dust emission (i.e., emitted power per unit surface area). We assume the source emits as a black body so the emission is given by $\sigma_{SB}\, T^4$, where σ_{SB} is the Stefan-Boltzmann constant and T is the temperature. We finally have to multiply by an emissivity function, $Q(T)$. If the source is a perfect black body then this would be equal to 1. This gives:

$$\mathcal{L} = n_d\, A\, \sigma_{SB}\, T^4\, Q(T), \tag{5.3}$$

where the surface area of a dust grain is given by:

$$A = 4\,\pi\, a^2. \tag{5.4}$$

Substituting equations 5.2 and 5.4 into equation 5.3 gives:

$$\mathcal{L} = \frac{\rho_c}{\frac{4}{3}\,\pi\, a^3\, \rho_d}\, 4\,\pi\, a^2\, \sigma_{SB}\, T^4\, Q(T), \tag{5.5}$$

which can be simplified to:

$$\mathcal{L} = \frac{3\, Q(T)}{a\, \rho_d}\, \rho_c\, \sigma_{SB}\, T^4. \tag{5.6}$$

The mean dust mass opacity, $\bar{\kappa}_p(T)$, assuming the dust is optically thin, can be expressed as (Hildebrand, 1983):

$$\bar{\kappa}(T) = \frac{3\,Q(T)}{4\,a\,\rho_d}, \tag{5.7}$$

substituting this into equation 5.6 gives:

$$\mathcal{L} = 4\,\bar{\kappa}(T)\,\rho_c\,\sigma_{SB}\,T^4, \tag{5.8}$$

which gives us the luminosity per unit volume of an optically thin source. For the source to collapse its density must be greater than a critical density. This density, derived from the Jeans instability (see Chapter 1), can be expressed as:

$$\rho_c \approx \frac{k_B\,T}{G\,\bar{m}\,R_J^2}, \tag{5.9}$$

where k_B is the Boltzmann constant, G is the gravitational constant, R_J is the Jeans radius, and $\bar{m}$ is the mean mass of a gas particle. This can then be substituted into equation 5.8, giving the luminosity per unit volume of a Jeans stable source $\mathcal{L}_{\rm J}$:

$$\mathcal{L}_{\rm J} \approx 4\,\bar{\kappa}(T)\,\frac{k_B\,T}{G\bar{m}\,R_J^2}\,\sigma_{SB}\,T^4, \tag{5.10}$$

which can be rearranged to give:

$$\mathcal{L}_{\rm J}\,R_J^2 \approx \frac{4\,k_B\,\bar{\kappa}(T)\,\sigma_{SB}\,T^5}{G\bar{m}}. \tag{5.11}$$

To calculate the value of $\bar{\kappa}(T)$ we need to assume $\bar{\kappa} \approx \kappa_{\lambda_{peak}}$. We know that $\kappa_{\lambda_{peak}} \propto \lambda_{peak}^{-\beta}$, and from Weins law, $\lambda_{peak} = \frac{const}{T}$, so $\lambda_{peak} \propto T^{-1}$. Therefore $\kappa_{\lambda_{peak}} \propto \lambda_{peak}^{-\beta} \propto (T^{-1})^{-\beta} \propto T^{\beta}$. So to find the value of $\bar{\kappa}$ at 20 K (150 μm) we can say $\bar{\kappa}(T) = \kappa_{\lambda_{peak}}(T) = \kappa\,(20\,K)\left(\frac{T}{20\,K}\right)^{\beta}$. Using $\bar{\kappa}_{250\,\mu m} = 0.016\,\mathrm{m^2\,kg^{-1}}$ and $\beta = 2$ (as used in Chapters 3 and 4), we find a value of $\bar{\kappa}(20\,K) \approx 0.04\,\mathrm{m^2\,kg^{-1}}$.

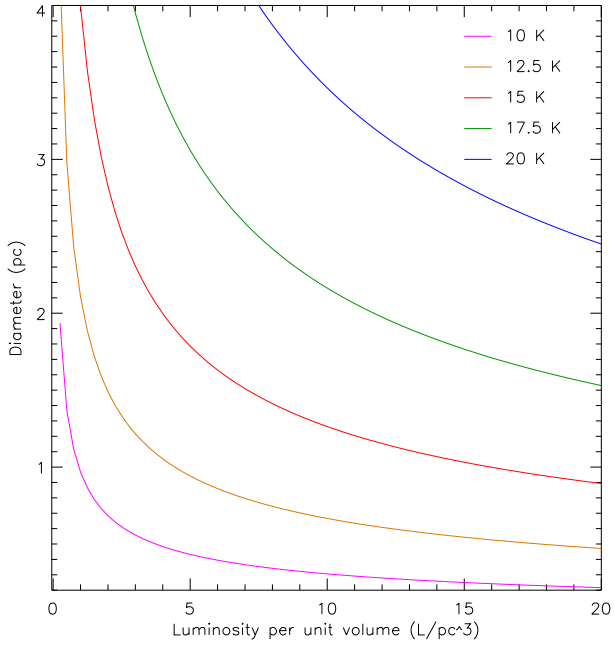

Figure 5.13: Luminosity per unit volume of an approximately Jeans stable source calculated with varying values of T. Pink, $T = 10\,\mathrm{K}$, orange, $T = 12.5\,\mathrm{K}$, Red, $T = 15\,\mathrm{K}$, green, $T = 17.5\,\mathrm{K}$ and blue, $T = 20\,\mathrm{K}$.

We can substitute values in for $\bar{\kappa}(T = 20\,K) \approx 0.04\,\mathrm{m^2\,kg^{-1}}\left(\frac{\mathrm{T}}{20\,\mathrm{K}}\right)^{\beta}$, $k_B = 1.38 \times 10^{-23}\,\mathrm{kg\,m^2\,s^{-2}\,K^{-1}}$, $\sigma_{SB} = 5.67 \times 10^{-8}\,\mathrm{W\,m^{-2}\,K^{-4}}$, $G = 6.67 \times 10^{-11}\,\mathrm{m^3\,kg^{-1}\,s^{-2}}$, $\bar{m} = 4 \times 10^{-26}\,\mathrm{kg}$ (assuming the gas is made up of 80% molecular hydrogen and 20% helium), $L_{\odot} = 3.84 \times 10^{26}\,\mathrm{kg\,m^2\,s^{-2}}$ and $1\,pc = 3.09 \times 10^{16}\,\mathrm{m}$, which gives us:

$$\left(\frac{\mathcal{L}_{\mathrm{J}}\,R_J^2}{L_{\odot}\,pc^{-3}\,pc^2}\right) \approx 120\left(\frac{T}{20\,K}\right)^{5}\left(\frac{T}{20\,K}\right)^{\beta}, \tag{5.12}$$

which can be rearranged to give:

$$\left(\frac{\mathcal{L}_{\mathrm{J}}}{L_{\odot}\,pc^{-3}}\right)\left(\frac{R_J}{pc}\right)^{2} \approx 120\left(\frac{T}{20K}\right)^{(5+\beta)}. \tag{5.13}$$

This now gives us an estimate for the boundary of the luminosity per unit volume of an approximately Jeans stable source. This boundary is heavily dependent on the value for the temperature as it increases by a power of $(5 + \beta)$, because

of this it can vary significantly. This is shown in Figure 5.13, where the pink line shows $T = 10\,\mathrm{K}$, the orange line shows $T = 12.5\,\mathrm{K}$, the red line shows $T = 15\,\mathrm{K}$, the green line shows $T = 17.5\,\mathrm{K}$, and the blue line shows $T = 20\,\mathrm{K}$. For each line I have assumed a value of the dust emissivity power law index, $\beta = 2$. Since $L \propto M$ (as shown in Section 5.4) this means that the luminosity per unit volume is also a measure of the density of the sources. This means that from Figure 5.13, for a source to be larger and denser it also needs to be hotter in order to be stable. For a source to be in equilibrium, its radius, density and temperature must all be balanced, change any one of these and keep the other two constant and the source will either begin to collapse or will disperse. The boundarys can now be plotted on the graphs for each region, Figure 5.14 for Carina and Figure 5.15 for NGC 7538. For each region I have plotted the boundary related to the regions lowest temperature and the boundary for its average temperature. In Carina I have taken the lowest temperature to be 15 K, which is plotted with a red line on Figure 5.3 and an average value of 20 K, plotted as a blue line. In NGC 7538, I have taken the lowest temperature to be 15 K, plotted as a red line on Figure 5.5 and an average temperature of 23 K, which is plotted as a blue line (note that this line is in the upper right hand corner of the plot). In both regions the sources all lie below the lower temperature boundary. To investigate this further I have plotted the ratio of the theoretical luminosity per unit volume with the observed luminosity per unit volume for each source. This is shown in Figure 5.16 for Carina and Figure 5.17 for NGC 7538. In both plots all the sources lie below the solid line which represents a ratio of 1. I interpret this as meaning all the sources are in the process of collapsing. If the sources were in equilibrium then they would have an observed luminosity per unit volume which is equal to their theoretical one. This would agree with the large spread present in the mass - radius plots in Section 5.2.

This analysis we have conducted is similar to, and based upon, a Virial theorem analysis. The Virial theorem provides a direct way of analysing the energy balance of a bounded region (Chandrasekhar & Fermi, 1953). It can be used to say if a core is in equilibrium (bounded) or not (unbounded). The virial theorem relates the kinetic energy (K) to the potential gravitational energy (U),

$$K = -\frac{1}{2}U. \tag{5.14}$$

If we consider a spherical core, If $2K + U = 0$, then the core is in equilibrium and is therefore gravitationally bound. So for the core to collapse the the kinetic energy must be less then the potential gravitational energy,

$$K < -\frac{1}{2}U, \tag{5.15}$$

so $2K + U > 0$. Our analysis builds upon this method to use directly measurable physical properties to suggest if a core is bound or not.

To investigate what our results means for each region I can split up the graph into three sub regions, each has been given a different colour and symbol. For both plots the symbols show, blue triangle: $\mathcal{L} \leq 1\,\mathrm{L_\odot pc^{-3}}$; red square: $1 \leq \mathcal{L} \leq 3.5\,\mathrm{L_\odot pc^{-3}}$ and green circle: $\mathcal{L} \geq 3.5\,\mathrm{L_\odot pc^{-3}}$.

5.7.3 Mass - radius

We can use the sub - samples outlined above to identify different populations of sources within the regions. I can plot these symbols on a mass - radius plot for each region, these are shown in Figure 5.18 for Carina and 5.19 for NGC 7538. The red squares have been removed to make the separation of the two sub - samples

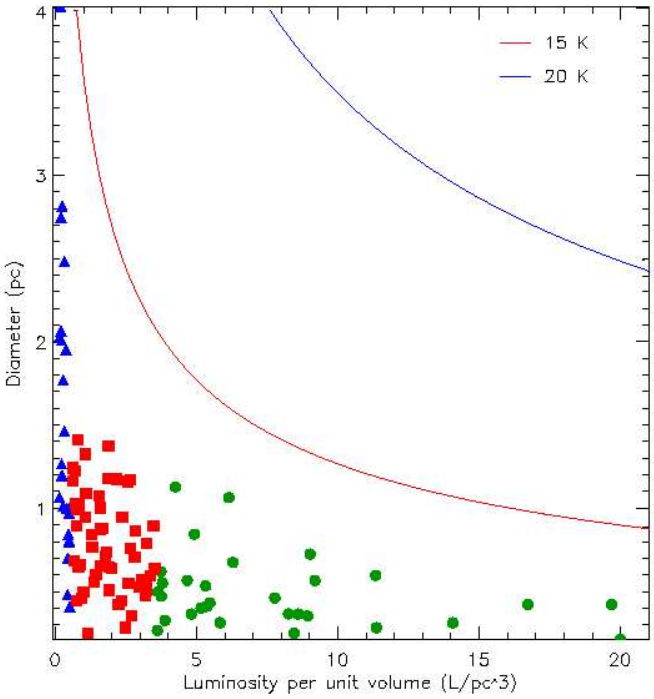

Figure 5.14: Luminosity per unit volume against diameter for the Carina Nebula. The symbols show: blue triangle: $\mathcal{L} \leq 1\,\mathrm{L}_{\odot}\mathrm{pc}^{-3}$; red square: $1 \leq \mathcal{L} \leq 3.5\,\mathrm{L}_{\odot}\mathrm{pc}^{-3}$ and green circle: $\mathcal{L} \geq 3.5\,\mathrm{L}_{\odot}\mathrm{pc}^{-3}$. The red line shows the calculated boundary for the lowest temperature (15 K) in the region and the blue line shows the boundary for the average temperature (23 K).

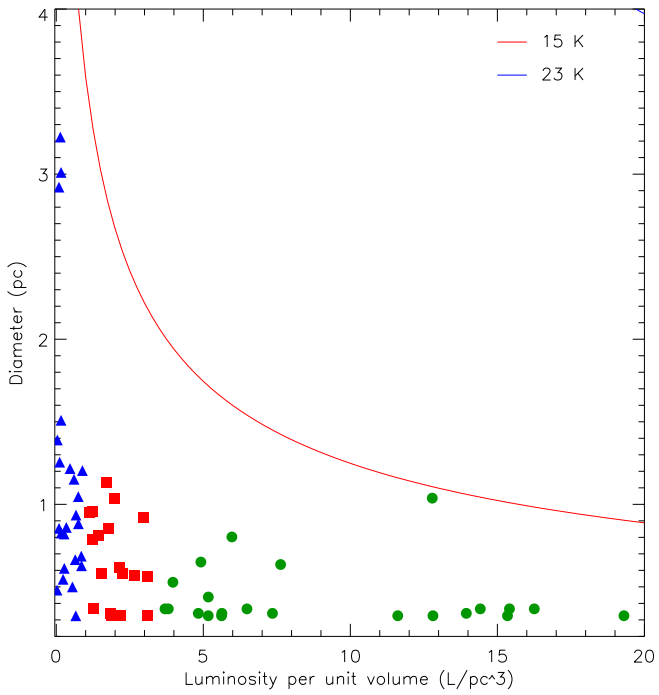

Figure 5.15: Luminosity per unit volume against diameter for NGC 7538. The symbols show: blue triangle: $\mathcal{L} \leq 1\,\mathrm{L}_{\odot}\mathrm{pc}^{-3}$; red square: $1 \leq \mathcal{L} \leq 3.5\,\mathrm{L}_{\odot}\mathrm{pc}^{-3}$ and green circle: $\mathcal{L} \geq 3.5\,\mathrm{L}_{\odot}\mathrm{pc}^{-3}$. The red line shows the calculated boundary for the lowest temperature (15 K) in the region and the blue line shows the boundary for the average temperature (23 K).

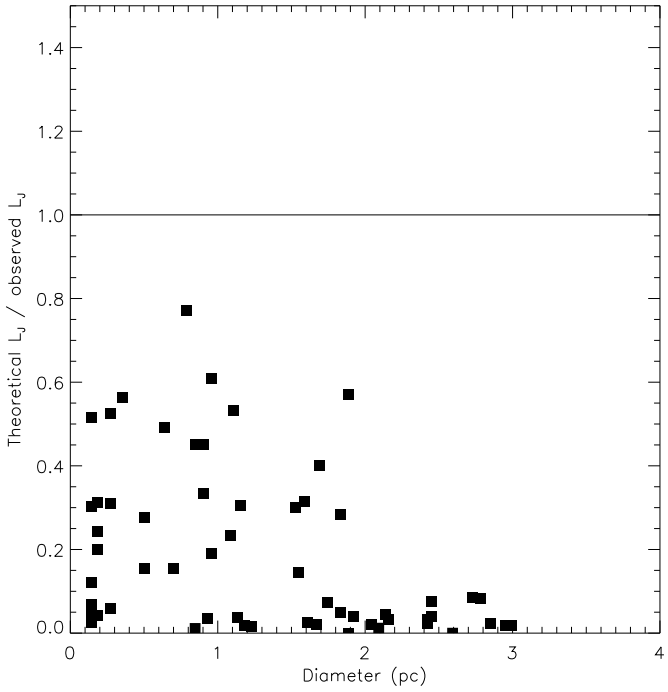

Figure 5.16: The ratio of the theorectical luminosity per unit volume with the observed luminosity per unit volume for each source in the Carina Nebula. The solid line shows a ratio of 1.

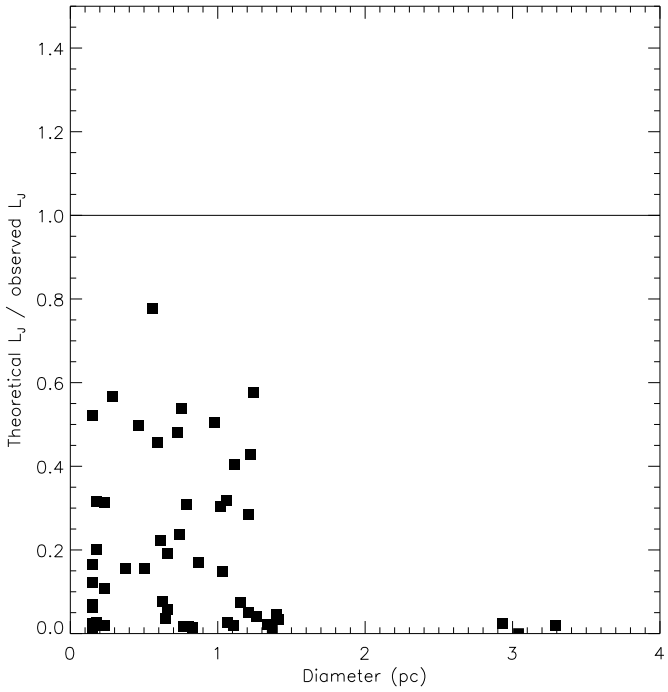

Figure 5.17: The ratio of the theorectical luminosity per unit volume with the observed luminosity per unit volume for each source in NGC 7538. The solid line shows a ratio of 1.

clearer. In Carina it is very clear there are two different populations of sources from the plot. The sources with a low luminosity per unit volume lie in a band at the lower end, and sources with a high luminosity per unit volume lie in the upper part of the plot. I fit two separate straight lines to the two samples. Both have approximately the same slope of $M \propto R^2$. From Figure 5.19 there is no clear separation in the two sub - samples in NGC 7538. This could be due to the small number of sources in the sample, the sources with a high luminosity per unit volume not being resolved, or maybe simply there not being a large difference in ambient gas pressure. The differences in the two populations in Carina could be explained by the differences in pressure. The pressure balance can be shown by the following equation (derived in Chapter 1) which assumes that the source is an isothermal sphere,

$$P \approx \frac{3\,GM^2}{4\pi\,R^4}, \tag{5.16}$$

this means that the inward force of gravity in a source is balanced with the gas pressure. A higher pressure means that a source can have a higher mass. From Figure 5.18 there is a difference of around an order of magnitude in mass between the two populations in Carina (one with a high luminosity per unit volume and one with a low luminosity per unit volume). This could mean there is a difference in pressure. In this picture the sources represented by the green circles are the sources with a higher pressure which are likely to be forming in a higher pressure environment. These are therefore more likely to be able to form more higher mass cores. The sources represented by the blue triangles are the sources with a lower pressure which are therefore probably forming in a lower pressure environment, these are less likely to form higher mass stars.

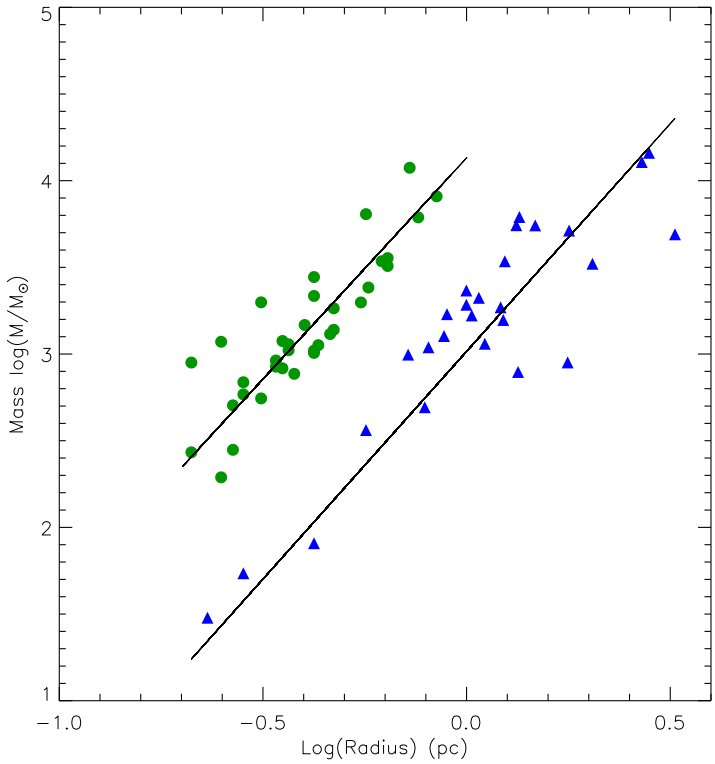

Figure 5.18: Mass against radius for the Carina Nebula. The symbols show: blue triangle: $\mathcal{L} \leq 1\,\mathrm{L}_{\odot}\mathrm{pc}^{-3}$; and green circle: $\mathcal{L} \geq 3.5\,\mathrm{L}_{\odot}\mathrm{pc}^{-3}$. The two solid lines show the trends.

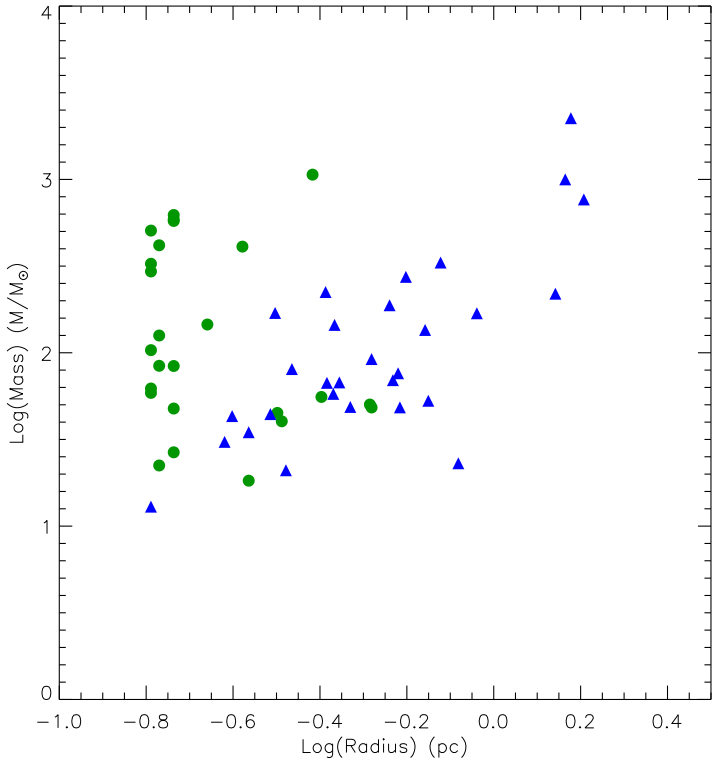

Figure 5.19: Mass against radius for NGC 7538. The symbols show: blue triangle: $\mathcal{L} \leq 1\,\mathrm{L}_{\odot}\mathrm{pc}^{-3}$; and green circle: $\mathcal{L} \geq 3.5\,\mathrm{L}_{\odot}\mathrm{pc}^{-3}$.

5.7.4 Distribution of the sources within the nebula

Since there is a pressure difference between the two populations in Carina, identified in Figure 5.18, we can also look to see if there is a difference in the way the sources are distributed spatially in each nebula. Using the same sub - samples as before we can plot the sources on contour plots of each region.

5.7.5 Carina Nebula

The distribution of the luminosity per unit volume sub - samples for Carina is shown in Figure 5.20 plotted on a contour plot of the 250 μm map. On this plot the sources with a high luminosity per unit volume lie in the central dense region of the cloud and those with a low luminosity per unit volume lie in the outer less dense regions. Since we know there is a difference in the pressure surrounding the two sub - samples, this distribution of sources implies that a higher external pressure exists in the centre of the nebula, which could mean that higher mass stars are more likely to form there. Hence the most massive star formation is occurring in the centre of the nebula.

I can also look to see how the sources are distributed throughout the nebula in relation to their other physical properties, temperature, luminosity, mass and radius. Figure 5.21 shows the distribution of source temperatures, the blue triangles show sources with $T \leq 20\,\mathrm{K}$ and green circles show sources with $T \geq 25\,\mathrm{K}$. The distribution of the sources is quite random, with the colder sources scattered throughout the nebula and the slightly hotter ones in small clumps distributed throughout the region.

Figure 5.22 shows the distribution of luminosities in the nebula. The blue triangles show sources with $L \leq 10^{1.5}\mathrm{L}_{\odot}$ and the green circles show sources with $L \geq 10^{2}\mathrm{L}_{\odot}$. The sources with a higher luminosity, shown by the green circles, are quite evenly distributed in the cloud, however the lower luminosity sources, shown by the blue triangles, tend to be in the denser regions only.

Figure 5.23 shows distribution of masses in Carina. The blue triangles show sources with $M \leq 10^{1.5}\mathrm{M}_{\odot}$ and the green circles show sources with $M \geq 10^{2}\mathrm{M}_{\odot}$. In this figure the lower mass objects are scattered throughout Carina with no preference to density but the higher mass objects tend to be in the denser regions. This is what we would expect to find as we have already shown that there is a higher pressure present in the central regions which should help the formation of higher mass sources.

In Figure 5.24 the distribution of source radii is shown. The blue triangles show sources with $R \leq 0.8\,\mathrm{pc}$ and the green circles show sources with $R \geq 1.2\,\mathrm{pc}$. Both the large radius and smaller radius sources are distributed evenly throughout the nebula with no strong preference for either.

From these plots it is clear that the only source property that has a clear pattern to its spatial distribution in the nebula is the luminosity per unit volume. Sources forming in the centre of the nebula are more likely to contain a larger number of high mass star - forming cores due to the higher ambient gas pressure present there, and these are more likely to be the most evolved sources. This would suggest that the luminosity per unit volume is tracing the source evolution in the nebula, with the higher mass and hence more evolved star - forming cores in the central dense regions and the less evolved low mass star - forming cores in the outer regions. Star formation could have started at a similar time throughout the

nebula, but progressed quicker in the central regions due to the higher mass cores. So the rate of evolution in the region is being influenced by the gas pressures in the cloud.

5.7.6 NGC 7538

We can repeat the same analysis with the sources in NGC 7538. I have used the same sub - samples and again have removed the mid range sample (red squares) for clarity. The distribution of luminosity per unit volume is shown in Figure 5.25. In NGC 7538 the sources with a high luminosity per unit volume (green circles) are in the dense regions of the main cloud and in the denser parts of the filaments. This is the same spatial distribution as we saw in Carina even through we do not see the same change in gas pressure. The sources with a low luminosity per unit volume (blue triangles) are in the less dense parts of the filaments. Following on from what we saw in Carina this would suggest that high mass core forming sources are evolving in the dense regions and lower mass forming sources in the less dense regions. The lower mass sources forming in the filaments would support the results from the Gould Belt survey (André et al., 2010) who have used *Herschel* observations of Aquila and Polaris to show that complex networks of long, thin filaments form first within molecular clouds, and then the densest filaments fragment into a number of prestellar cores via gravitational instability.

As for Carina, I can also look at the distribution of the other physical properties of the sources in the region. Figure 5.26 shows the distribution of temperatures in the region. The blue triangles show the distribution of sources with $T \leq 18\,\mathrm{K}$ and the green circles show sources with $T \geq 22\,\mathrm{K}$. There is a concentration of hotter sources in the dense region but also some in less dense regions. The colder

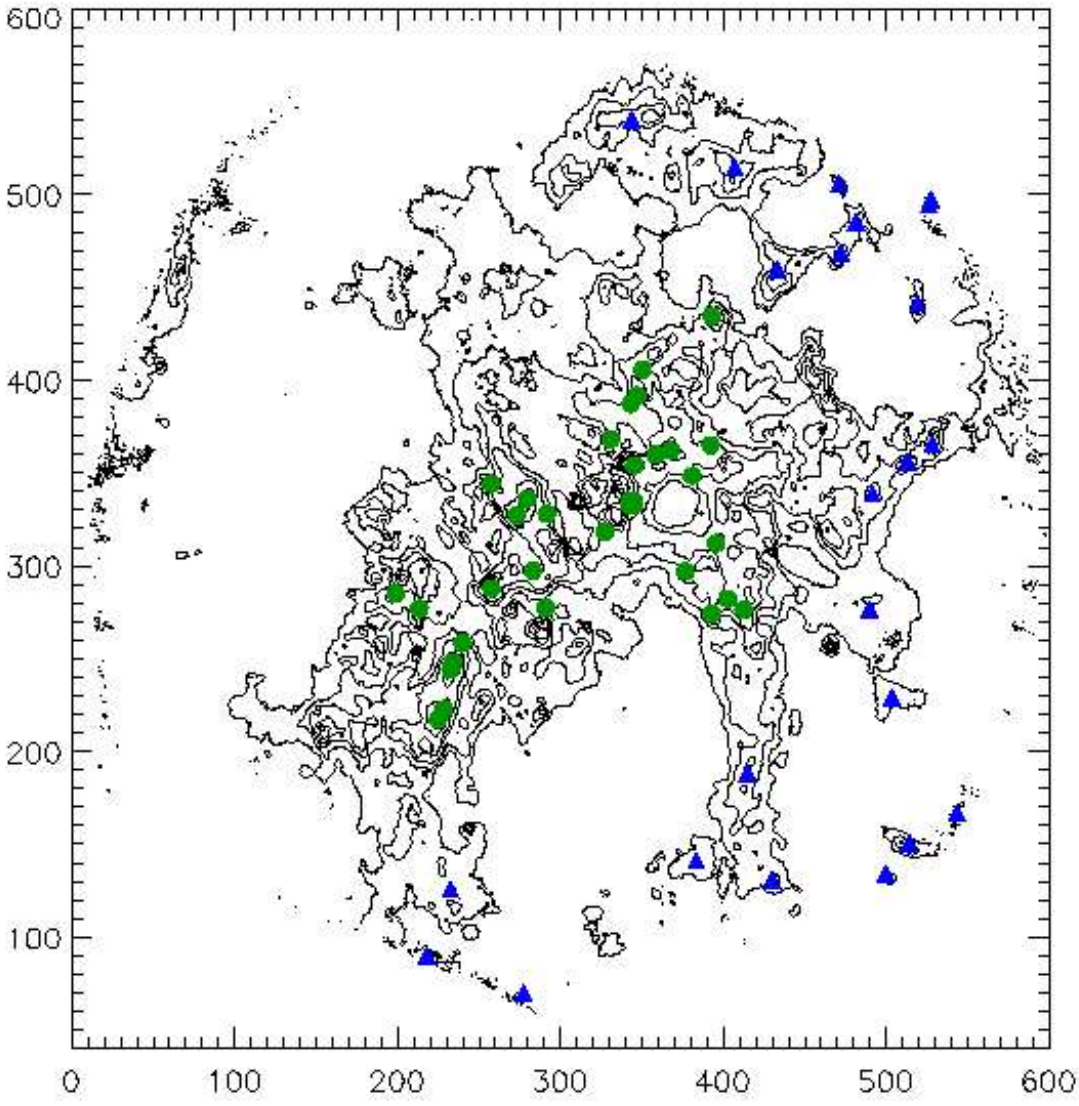

Figure 5.20: The distribution of luminosity per unit volume of sources in the Carina Nebula within the region. Blue triangles show sources with: $\mathcal{L} \leq 1\,\mathrm{L}_{\odot}\mathrm{pc}^{-3}$ and green circles show sources with: $\mathcal{L} \geq 3.5\,\mathrm{L}_{\odot}\mathrm{pc}^{-3}$

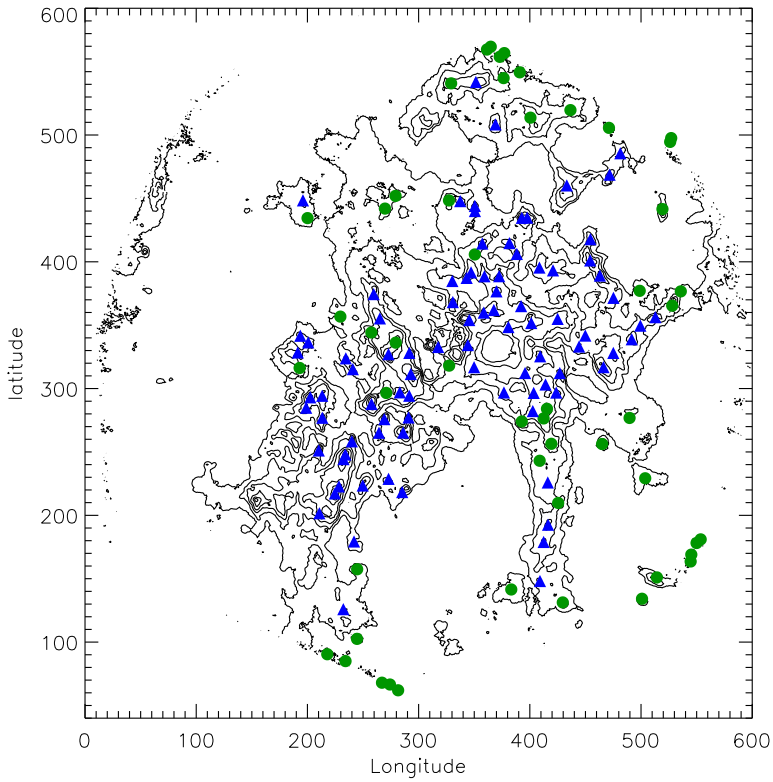

Figure 5.21: Distribution of temperatures of sources in the Carina Nebula with temperature, $\leq 20\,K$ (blue triangle) and $\geq 25\,K$ (green circle)

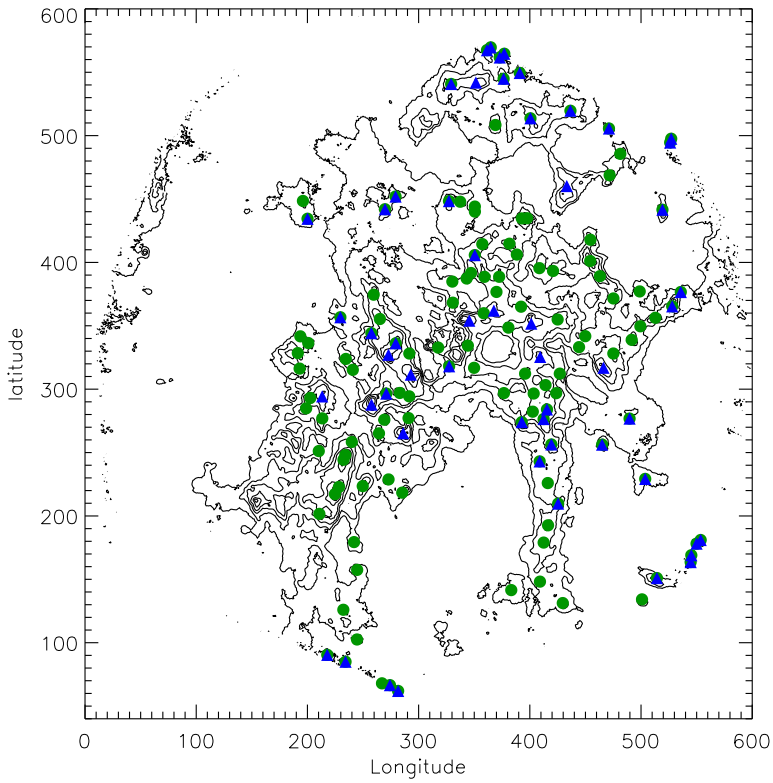

Figure 5.22: Distribution of luminosities of sources in the Carina Nebula with luminosities $\leq 32\,L_{\odot}$ (blue triangle) and $\geq 100\,L_{\odot}$ (green circle)

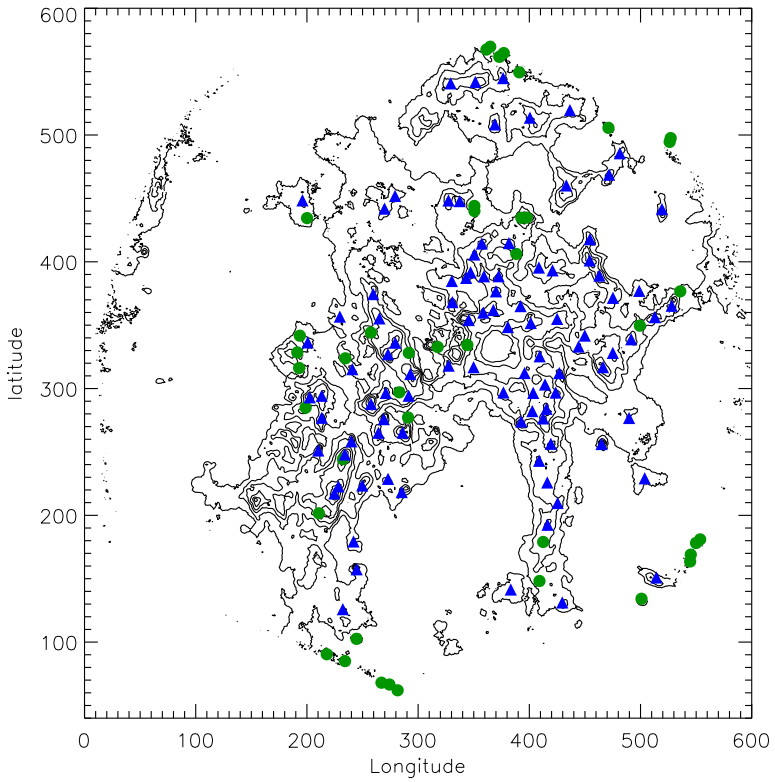

Figure 5.23: Distribution of masses of sources in the Carina Nebula with masses $\leq 32\,M_{\odot}$ (blue triangle) and $\geq 100\,M_{\odot}$ (green circle)

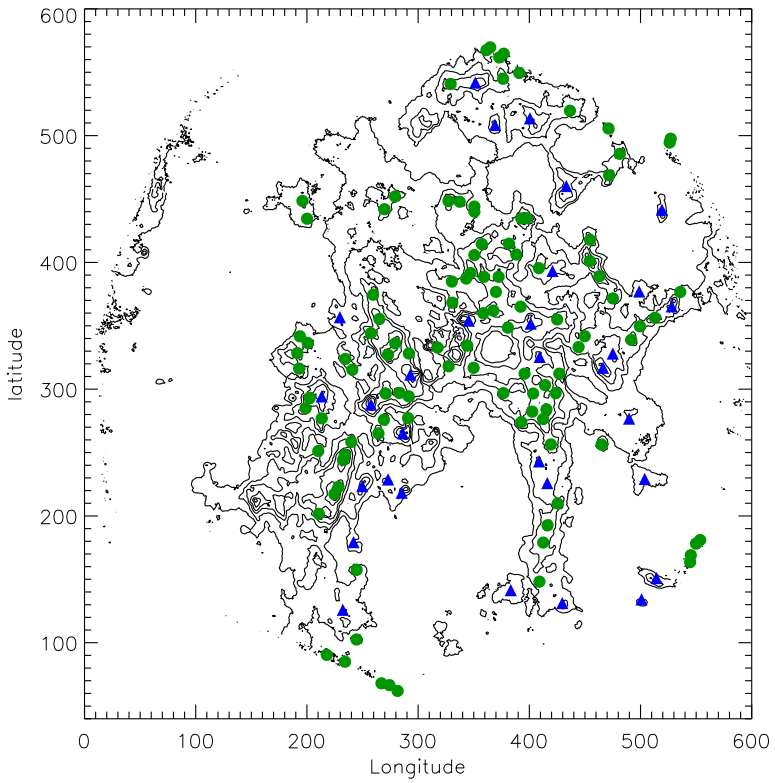

Figure 5.24: Distribution of radii of sources in the Carina Nebula with radius $\leq 0.8\,pc$ (blue triangle) and $\geq 1.2\,pc$ (green circle)

sources tend to be in the filaments but some are present in the dense main cloud.

Figure 5.27 shows the distribution of luminosity in NGC 7538. The distribution of sources with $L \leq 63\mathrm{L}_{\odot}$ is shown by the blue triangles and sources with $L \geq 158\mathrm{L}_{\odot}$ is shown by the green circles. The distribution of the luminosities appears completely random, with both high and low luminosity sources in the dense and less dense regions of the nebula.

The distribution of source mass is shown in Figure 5.28. The blue triangles show the sources with $M \leq 20\mathrm{M}_{\odot}$ and the green circles show sources with $M \geq 63\mathrm{M}_{\odot}$. The distribution of both these sub - samples is quite random. However there is a small concentration of higher mass objects in the dense main cloud region which is as we would expect but there are also lower mass objects present.

Figure 5.29 shows the distribution of source radii. Sources with $R \leq 0.5\,\mathrm{pc}$ are shown by a blue triangle and sources with $R \geq 0.7\,\mathrm{pc}$ are shown by a green circle. Most of the smaller sources tend to be in the dense region, which would be expected as these are also the most crowded regions, but there are some larger sources present in these regions.

As in the Carina Nebula, the luminosity per unit volume seems to be a unique property as it shows a preference to how the sources are distributed in the region which no other physical property does. Since the sources with a higher luminosity per unit volume, which are most likely to contain the higher mass and hence more evolved cores, tend to be in the densest regions of the nebula, this would agree with the findings of Dickel et al. (1981), discussed in Chapter 4, in that star formation has occurred in NGC 7538 at the same time throughout the region and progressed at differing rates depending on density, with the sources in the densest regions

evolving faster.

5.7.7 Discussion

Both the Carina Nebula and NGC 7538 show a pattern to the distribution of sources with a high or low luminosity per unit volume. Sources with a high luminosity per unit volume are only found in the dense regions of the nebula and those with a low luminosity per unit volume are only found in the less dense regions. In Carina this separation is probably being caused by the increase in gas pressure in the denser regions of the nebula, however from Figure 5.19 there does not appear to be any change in gas pressure in NGC 7538. This means that either there is a higher gas pressure in the denser regions which is not evident in the plots or there is another factor causing the spatial separation. Neither region shows any strong separation for any other physical property. Since we know that the sources containing the higher mass cores are more likely to be in the higher density regions, this could mean that the luminosity per unit volume could be used as a indicator of evolution status of the sources in a region. Luminosity per unit volume can thus indicate where the high mass sources are forming in a region and it could be used to see how star formation has progressed. In the Carina Nebula we can see that the sources with a high luminosity per unit volume are in the centre of the nebula. This means that the more evolved sources lie in the centre and the less evolved around the edges. Combined with the higher pressure present in the centre, this possibly means that star formation has started simultaneously throughout the nebula but progressed quicker in the centre due to the clusters of higher mass cores. In NGC 7538 the sources with a high luminosity per unit volume are located in the dense regions which suggests that star formation has taken place throughout the

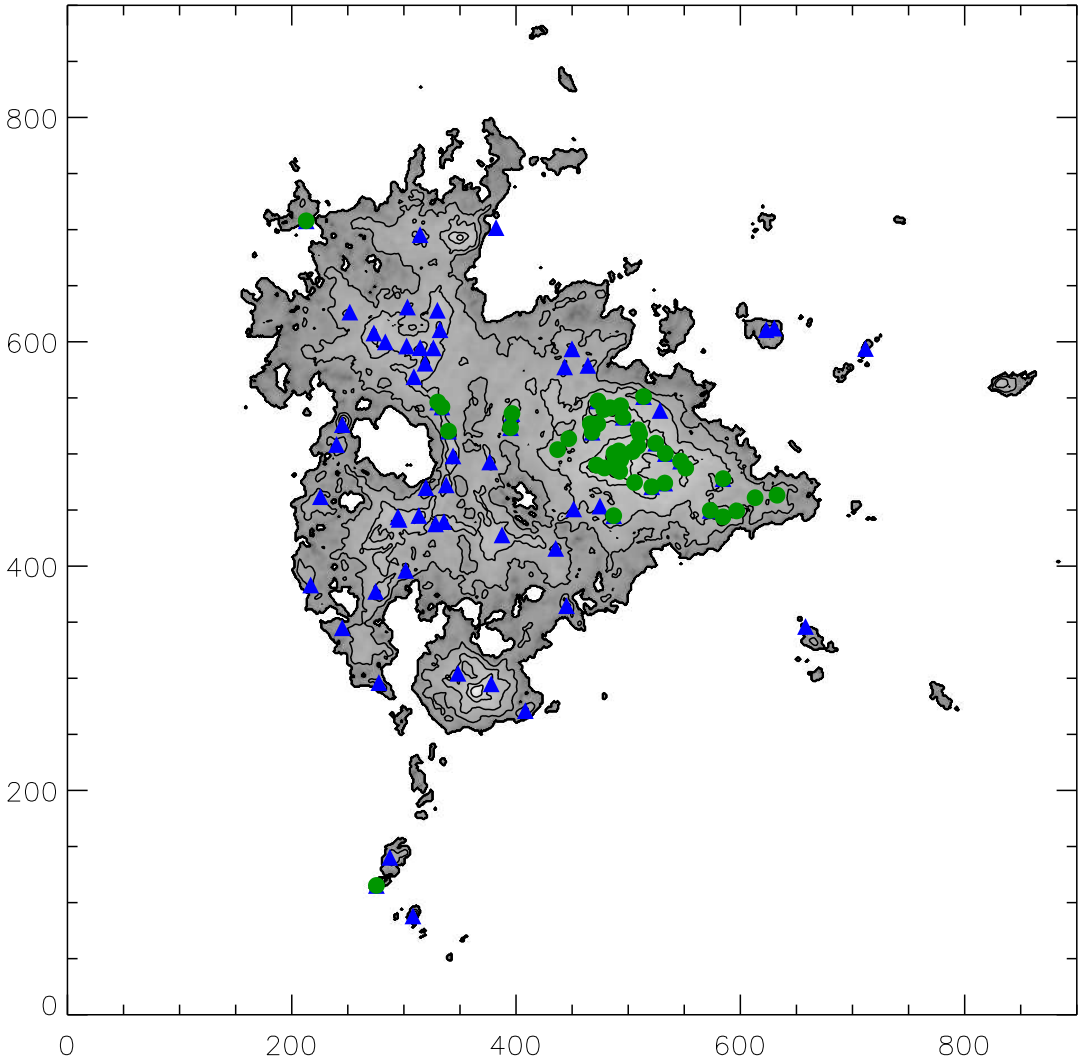

Figure 5.25: Distribution of luminosity per unit volume of sources within NGC 7538, blue triangles show sources with $\mathcal{L} \leq 1\,\mathrm{L}_{\odot}\mathrm{pc}^{-3}$ and green circles show sources with $\mathcal{L} \geq 3.5\,\mathrm{L}_{\odot}\mathrm{pc}^{-3}$

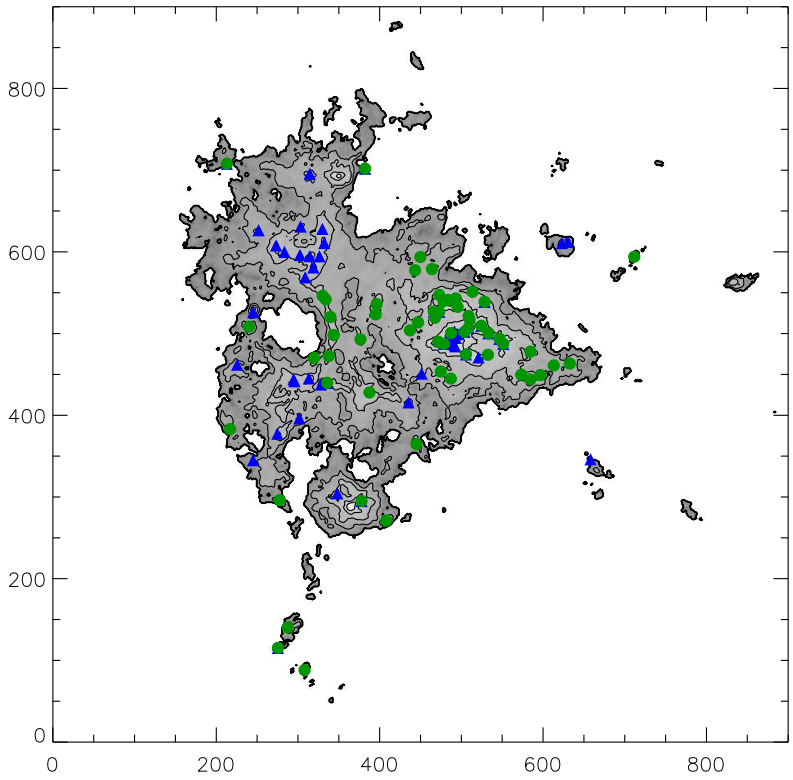

Figure 5.26: Distribution of temperatures of sources in NGC 7538 with temperature $\leq 18\,\mathrm{K}$ (blue triangle) and $\geq 22\,\mathrm{K}$ (green circle)

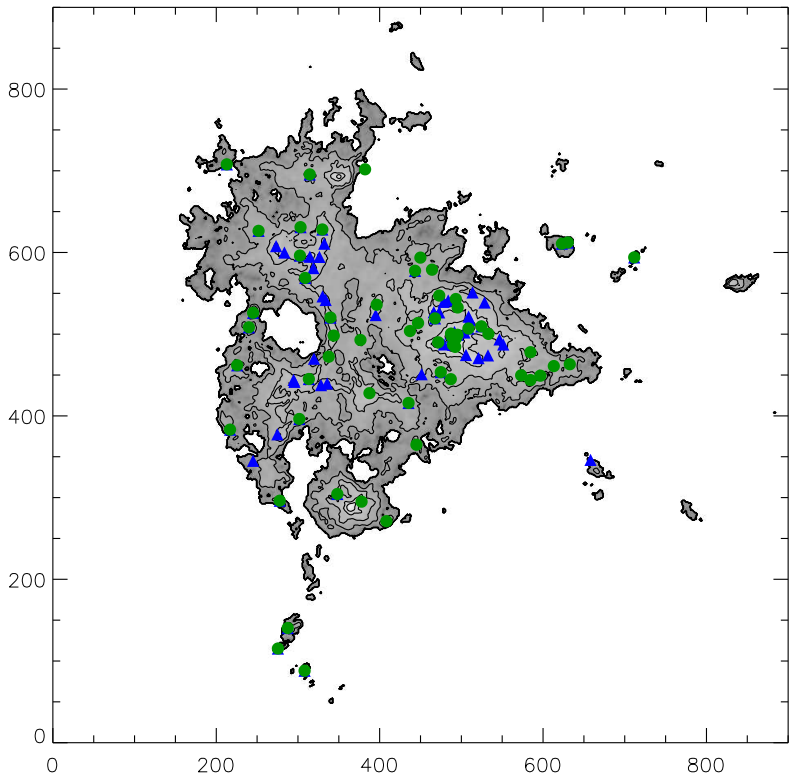

Figure 5.27: Distribution of luminosities of sources in NGC 7538 with luminosities $\leq 63\mathrm{L}_{\odot}$ (blue triangle) and $\geq 158\mathrm{L}_{\odot}$ (green circle)

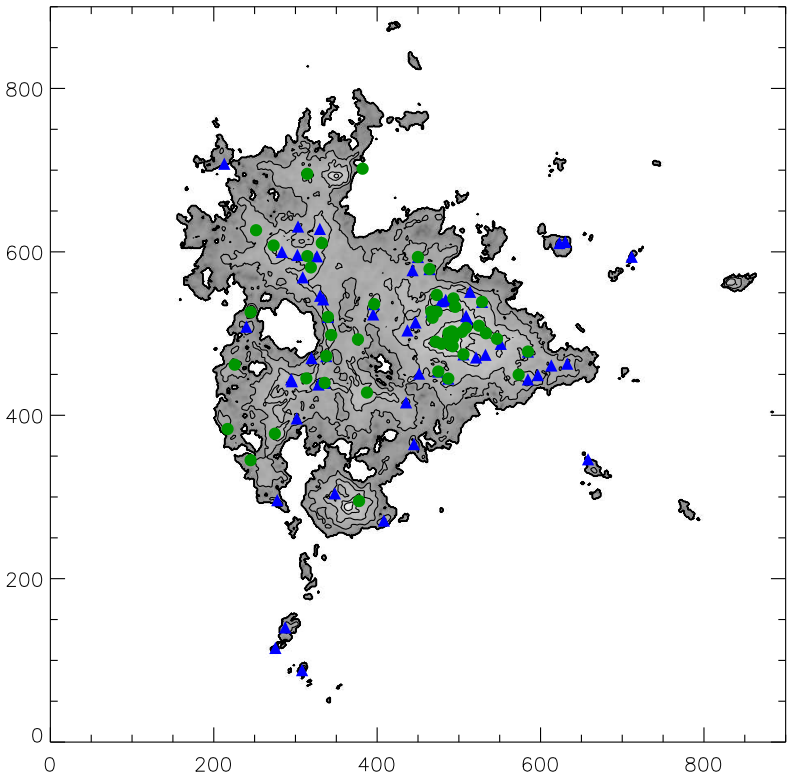

Figure 5.28: Distribution of masses of sources in NGC 7538 with masses $\leq 20 M_{\odot}$ (blue triangle) and $\geq 63 M_{\odot}$ (green circle)

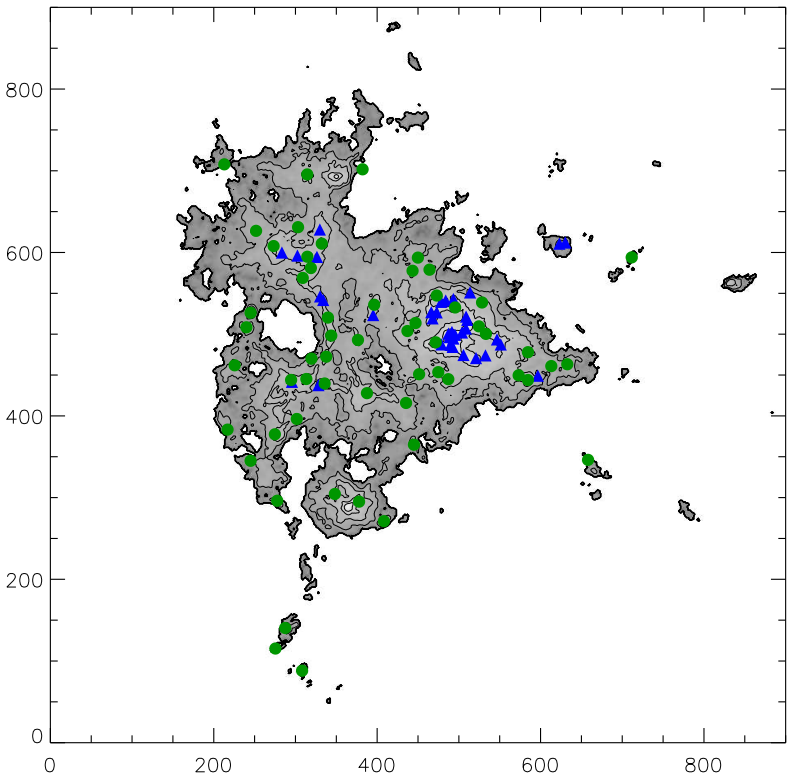

Figure 5.29: Distribution of radii of sources in NGC 7538 with radius ≤ 0.5 pc (blue triangle) and ≥ 0.7 pc (green circle)

region but has progressed at differing speeds depending on the density.

5.8 Summary

In this chapter I have analysed the physical properties for the Carina Nebula and NGC 7538. Both are regions of high mass star formation, but they are very different nebulae. Carina consists of one large cloud, whereas NGC 7538 is made up of several small filaments, two possible UCHII regions and a dense main cloud. The Carina Nebula contains larger, higher mass sources on average compared to NGC 7538 which contains many small, less massive sources.

From analysing the physical properties I find that Carina shows a mass - radius relation of $M \propto R^{1.8 \pm 0.3}$ which is comparable to the $M \propto R^2$ relation found by Larson (1981). NGC 7538 however does not show a relation between mass and source radius. Both nebulae show a spread of between one and two orders of magnitude in mass for any value of radius and vice versa. This could be due to the star - forming cores undergoing gravitational collapse, inaccuracies in measuring the radius (in confused regions) and the diverse populations present in each region. Neither region shows any dependence on temperature or mass. However, NGC 7538 shows a relation of $T \propto L^{0.25 \pm 0.08}$ between temperature and luminosity. This is probably due to the small range of temperatures found in each region. This means that we cannot use the source temperatures to derive the evolutionary status of the sources and that the material we are seeing is never being dominated by warm dust around the young stellar objects. The source luminosity when plotted against the mass gives a constant slope for both regions, in Carina the relation is $L \propto M^{1 \pm 0.09}$ and in NGC 7538 it is $L \propto M^{1 \pm 0.2}$ as expected. However for NGC 7538 there is a

Relations	Carina Nebula	NGC 7538
Mass - Radius	$M \propto R^{1.8 \pm 0.3}$	–
Temperature - Luminosity	–	$T \propto L^{0.25 \pm 0.08}$
Luminosity - Mass	$L \propto M^{1 \pm 0.09}$	$L \propto M^{1 \pm 0.2}$

Table 5.1: Property relations

wide spread of masses for a given luminosity. When the luminosities and masses for both regions are combined on the same graph we see that both have the same slope of $L \propto M$. This is due to the masses being calculated from the submillimetre flux densities and the small range of temperatures. There is a large spread around the fit for NGC 7538 (low luminosity and mass) but the deviation decreases as the mass and luminosity increases (Carina). A summary of all the relations between source properties is given in Table 5.1.

The basic physical properties in both regions give interesting results and highlight some of the differences between them, but they do not tell us anything about the evolutionary status of the sources. By looking at the luminosity per unit volume we find out more. By plotting this parameter against diameter we find that each region follows the same pattern with large sources having a low luminosity per unit volume and the smaller sources having a higher luminosity per unit volume. Both graphs look very similar even though the regions are very different, which could mean that the luminosity per unit volume may not be strongly influenced by other environmental factors. By splitting the plot into three sub - samples I have investigated the properties of sources with a low luminosity per unit volume and those with a high value. Plotting the mass against radius using two of the three sub - samples (the central sample was removed for clarity) I find a clear difference in ambient gas pressure of approximately two orders of magnitude present

in Carina with the sources with a high luminosity per unit volume also having a higher ambient gas pressure, which means that they are more likely to be higher mass star - forming cores and so more evolved. This difference in gas pressure is not clear in NGC 7538, which could be due to the small sample size, or perhaps there may not be a large difference in the gas pressure as most of the region is made up of small filaments. Using the two sub - samples we see a clear separation in geographical location for low luminosity per unit volume and high luminosity per unit volume sources for both regions. The sources with a high luminosity per unit volume are preferentially in the dense regions and the sources with a low luminosity per unit volume in the less dense regions. This implies that in Carina the sources with a high luminosity per unit volume also have a higher gas pressure so are also more likely to form higher mass stars, so the higher mass sources must be in the denser areas of the regions. Since higher mass objects evolve faster than lower mass sources it must also follow that sources with a higher luminosity per unit volume are more evolved. This geographical separation of the high and low luminosity per unit volume appears to be unique as no other physical property shows any preference to its location within the nebulae.

From this analysis I have shown that the property of luminosity per unit volume could be used to identify the evolutionary status of sources in a region. Sources should move from left to right on the plot as they evolve, starting off as large low luminosity sources with a low luminosity per unit volume, then as they evolve they contract into smaller high luminosity sources with a high luminosity per unit volume.

Chapter 6

Summary and Conclusions

6.1 Thesis summary

Star formation is an extremely important process in the universe and has many consequences for other aspects of astronomy. With the advent of new observatories working in the far - infrared and submillimetre, some of the poorly understood processes involved in high - mass star formation can now be investigated. In this thesis I have presented an observational study of high mass star formation in two regions, the Carina Nebula and NGC 7538. Below is a brief summary of each chapter.

In Chapter 1, I discussed our current understanding of the process of high mass star formation. I reviewed the environments that stars are born in and how we can measure their properties. I gave an overview of the two current theories that attempt to explain how and why high mass stars and clusters form with the properties that we observe and the possible stages that the stars go through. I

reviewed why far - infrared and submillimetre observations are important to star formation and the problems and observational needs associated with observing in these wavelengths.

In Chapter 2, I introduced the infrared and submillimetre observatories of the past and present that have advanced our understanding of star formation. I reviewed the balloon - borne telescope, BLAST and the *Herschel* Space Observatory, which were used to obtain the data presented in Chapters 3 and 4 of this thesis. I discussed observing modes, calibration, sensitivity and the data reduction process for each.

In Chapter 3, I presented data for the Carina Nebula taken with the balloon - borne telescope BLAST. I reviewed the current observations of Carina and our understanding of the region. I described the BLAST scan - map observations, the data reduction methods used and the map - making process. I used these data to identify 172 sources with the source extracting routine CSAR and calculated the mass, luminosity, temperature and size of each source. Masses of the sources range from 20 to $10^4\,M_\odot$, luminosities range from 10^2 to $10^5\,L_\odot$, temperatures range from 16 to 28 K and source radii lie in the range of 0.3 to 3.2 pc.

In Chapter 4, I presented data for NGC 7538. I described the scan - map observations of this region taken with SPIRE and PACS on *Herschel*, the data reduction methods used and the map - making process. I used CSAR to identify 94 sources. I compared the results from another source extraction routine, GETSOURCES. This routine involves a more complex method and uses multi - wavelength data, and found a much larger number of sources. I compared the results from both routines and found when the GETSOURCES catalogue was filtered to remove sources which are only found at one or two wavelengths, then there is a good agreement

between the two, and with SCUBA observations of part of the same region. From this I created a robust catalogue, containing 75 sources which are found in both catalogues. For each source I measured the mass, luminosity, temperature and size. Masses of the sources range from 5 to $10^3\,M_\odot$, luminosities range from 5 to $10^3\,L_\odot$, temperatures range from 10 to 40 K and source radii lie in the range of 0.1 to 2 pc.

In Chapter 5, I presented an analysis of the results for Carina and NGC 7538. For the Carina Nebula I found a mass - radius relation of $M \propto R^{1.8\pm0.3}$ which is similar to the Larson relation of $M \propto R^2$. For NGC 7538 I found no clear relation. For Carina I found no relation between any source property and temperature whereas for NGC 7538 I found a relation between temperature and luminosity following $L \propto T^{0.25\pm0.08}$ but again no relation between temperature and mass. In each region there is an expected relation between mass and luminosity following $L \propto M$. For each cloud I found a relation between the property luminosity per unit volume and size, with the smaller sources having a larger luminosity per unit volume and the larger sources having a smaller luminosity per unit volume. Sources with a high value of this parameter tend to lie in the denser regions of the clouds and those with a lower value lie in the outer less dense regions. I discussed the similarities and differences between these two regions.

6.2 Key conclusions

The two regions studied in this work have a number of similarities and some key differences. In NGC 7538 the majority of the star formation occurring in the nebula is within the filaments, but in Carina most of the star formation is happening in

the dense central region. From the masses, luminosites and sizes of the sources in each region, Carina contains larger, higher mass sources, which are likely to be high mass cluster forming sources. NGC 7538 contains sources which are a combination of small cluster forming sources and individual high mass protostars. Carina is possibly an older region compared to NGC 7538.

The Carina Nebula shows a relation between mass and radius similar to the one found by Larson, whereas there is no clear relation present in the NGC 7538 data. This could be because the sources in NGC 7538 are undergoing gravitational collapse and have a wider range of evolutionary conditions, so that a smaller more evolved source and a larger less evolved source could have the same mass. Carina shows no relation between any source property and temperature whereas NGC 7538 shows a weak relation between temperature and luminosity. This effect could be due to BLAST data, with a narrower wavelength coverage, being sensitive to a smaller range of temperatures. Source temperature is not a useful discriminator for sources in either region.

By plotting the luminosity per unit volume against diameter for both the Carina Nebula and NGC 7538 I have found that smaller sources tend to have a larger luminosity per unit volume and larger sources have a lower luminosity per unit volume. By studying the distribution of sources with a high and low luminosity per unit volume within the nebulae, I have found that sources with a high luminosity per unit volume tend to lie in the denser regions of the clouds (the centre regions in Carina and the dense parts of the filaments in NGC 7538) and those with a lower luminosity per unit volume lie in the less dense regions. Bearing in mind the higher ambient gas pressure present in the denser regions, the sources with a high luminosity per unit volume are probably the more evolved sources. This would suggest that as a core evolves, contracting in size, it moves from left

to right on the plot. This means that luminosity per unit volume could be used as an indicator of how evolved a high mass source is compared to other sources in the same region.

There are still many unanswered questions associated with high mass star formation, but with the large quantities of data coming from observatories such as *Herschel*, there will be plenty to keep astronomers busy for many years to come.

6.3 Consequences of this work

In this thesis I have built upon previous studies as well as introducing a new method of analysis. Our survey of the high mass star formation region, Carina, agrees with previous surveys (Povich et al., 2011; Smith et al., 2010b), finding similar high mass objects throughout the nebula. Our results agree with Smith et al. (2000b), who theorised that the more evolved YSOs inhabit the central regions whereas the younger objects were near the outskirts. However we disagree that this was caused by sequential star formation, with the evolved central sources kick starting a wave of star formation moving from the centre to the edge of the nebula, but rather that the star formation could of occurred at the same time throughout the nebula, but the sources evolved at differing rates depending on the environmental factors.

For NGC 7538, we have shown the emission surrounding the main nebula and identified interesting objects, such as a ring of star formation and two possible UCHII regions which have not been studied before. For the central region our results agree with Werner et al. (1979b) and Reid & Wilson (2005b) who have conduced similar surveys. Our results also agree with Dickel et al. (1981) who theorised that the differing evolutionary stages of YSOs present in this region was

due to environmental factors, opposed to Werner et al. (1979a) who suggested a sequential process of star formation going from NW to SE, starting at the visible HII region.

In the second half of this work I introduced a new large scale method of analysing the evolutionary state of sources in a region. This provides an easy method of identifying if the sources in a region are bound or unbound using their physical properties. This analysis can also be used as an observational method to find the density of a source. Similar analysis have been carried out with Virial analysis (Gutermuth et al., 2008b; Beuther & Henning, 2009; Tachihara et al., 2002). These analysis tend to be used for individual YSO's or single clusters, whereas our method gives an overall picture of the evolutionary state of all the objects in a region which allows to quickly identify different populations. This then allows for more in depth studies of particular groups of objects such as their graphical locations within a nebula which could be used to trace how star formation has progressed in different regions.

6.4 Future work

Source extraction has turned out to be a very difficult issue for *Herschel* Galactic observations, and one that can have a major influence on the interpretation of the data. At present, the *Herschel* Gould Belt survey team is following a conservative approach similar to the one adopted in this work. With more experience, and with the addition of data from other wavelengths, it will become easier to obtain more reliable information from *Herschel* maps.

The property luminosity per unit volume of the sources has been shown to be a

potentially useful parameter in tracing the evolutionary status of individual objects and of regions within a cloud. This should be followed up by similar analysis of many other regions mapped by *Herschel*.

With further improvements in *Herschel* data reduction and in the treatment of extended emission, it will be possible to deconvolve the beam profile for regions observed with high signal to noise. This will allow better effective angular resolution, which will be very helpful especially for the longer wavelength data.

To counteract the fundamental problem that *Herschel* has with angular resolution, follow up of *Herschel* maps with observations from the ground (e.g., SCUBA-2 and ALMA) will be very useful.

Appendix A

Source tables

Table A.1: Source Positions and Flux Densities for the Carina Nebula

Source ID	l	b	α_{2000}	δ_{2000}	$S_{250\mu m}$ [Jy]	$S_{350\mu m}$ [Jy]	$S_{500\mu m}$ [Jy]
BLAST 103813-585717	286.481	-0.405	$10^h38^m13.0^s$-58°57′17″		373 ± 2.0	189 ± 2.0	86.7 ± 0.5
BLAST 103842-585338	286.507	-0.321	$10^h38^m42.3^s$-58°53′38″		190 ± 1.0	90.7 ± 1.3	36.9 ± 0.4
BLAST 103857-585223	286.525	-0.287	$10^h38^m57.5^s$-58°52′23″		99.5 ± 1.0	47.6 ± 1.0	20.2 ± 0.3
BLAST 103936-584943	286.577	-0.208	$10^h39^m36.6^s$-58°49′43″		69.7 ± 1.9	54.7 ± 1.9	32.5 ± 0.5
BLAST 103909-590413	286.644	-0.447	$10^h39^m09.7^s$-59°04′13″		62.3 ± 1.1	39.6 ± 1.1	07.4 ± 0.3
BLAST 103915-590730	286.681	-0.489	$10^h39^m15.2^s$-59°07′30″		159 ± 1.0	111 ± 1.0	29.4 ± 0.4
BLAST 104036-585337	286.722	-0.202	$10^h40^m36.4^s$-58°53′37″		173 ± 2.0	107 ± 2.0	48.6 ± 0.6
BLAST 103927-591113	286.734	-0.530	$10^h39^m27.5^s$-59°11′13″		34.0 ± 0.8	23.1 ± 0.8	08.4 ± 0.2
BLAST 103614-595645	286.750	-1.392	$10^h36^m14.0^s$-59°56′45″		315 ± 3.0	152 ± 3.0	64.7 ± 0.9
BLAST 103938-591237	286.766	-0.539	$10^h39^m38.5^s$-59°12′37″		45.3 ± 0.8	26.0 ± 0.8	10.1 ± 0.2
BLAST 103614-600209	286.795	-1.470	$10^h36^m14.5^s$-60°02′09″		10.1 ± 1.0	03.2 ± 0.9	···
BLAST 103949-591459	286.805	-0.563	$10^h39^m49.1^s$-59°14′59″		21.8 ± 0.7	10.1 ± 0.7	05.5 ± 0.1
BLAST 103952-591808	286.836	-0.605	$10^h39^m52.5^s$-59°18′08″		146 ± 2.0	70.5 ± 1.5	33.9 ± 0.4
BLAST 104124-590049	286.869	-0.258	$10^h41^m24.1^s$-59°00′49″		03.1 ± 0.7	04.2 ± 0.7	02.1 ± 0.1
BLAST 104226-584708	286.878	0.006	$10^h42^m26.5^s$-58°47′08″		30.0 ± 1.2	16.6 ± 1.2	07.9 ± 0.3
BLAST 104012-592202	286.906	-0.642	$10^h40^m12.9^s$-59°22′02″		346 ± 2.0	143 ± 2.0	60.7 ± 0.6
BLAST 104051-591322	286.908	-0.475	$10^h40^m51.6^s$-59°13′22″		55.5 ± 1.4	25.8 ± 1.4	11.2 ± 0.4
BLAST 104226-585207	286.917	-0.067	$10^h42^m26.3^s$-58°52′07″		24.4 ± 0.6	14.6 ± 0.6	05.9 ± 0.1
BLAST 104224-585332	286.926	-0.090	$10^h42^m24.7^s$-58°53′32″		16.0 ± 0.4	09.4 ± 0.4	03.7 ± 0.1
BLAST 103918-593920	286.945	-0.949	$10^h39^m18.8^s$-59°39′20″		36.3 ± 0.7	15.2 ± 0.7	03.4 ± 0.2
BLAST 104018-592549	286.946	-0.691	$10^h40^m18.4^s$-59°25′49″		487 ± 2.0	198 ± 2.0	79.5 ± 0.5
BLAST 104129-591030	286.957	-0.394	$10^h41^m29.7^s$-59°10′30″		94.0 ± 0.9	50.6 ± 0.9	17.0 ± 0.2
BLAST 104150-590910	286.986	-0.353	$10^h41^m50.7^s$-59°09′10″		119 ± 1.0	67.3 ± 0.8	21.4 ± 0.2
BLAST 104210-590515	286.991	-0.276	$10^h42^m10.2^s$-59°05′15″		104 ± 1.0	51.4 ± 1.2	18.9 ± 0.3
BLAST 104202-590832	287.003	-0.332	$10^h42^m02.4^s$-59°08′32″		50.7 ± 0.6	26.1 ± 0.6	08.3 ± 0.1
BLAST 104107-592232	287.011	-0.593	$10^h41^m07.3^s$-59°22′32″		41.4 ± 0.9	16.5 ± 0.9	07.5 ± 0.2
BLAST 104110-592517	287.038	-0.631	$10^h41^m10.1^s$-59°25′17″		78.0 ± 1.2	33.1 ± 1.2	16.3 ± 0.3
BLAST 104137-592015	287.048	-0.530	$10^h41^m37.0^s$-59°20′15″		15.4 ± 0.4	08.1 ± 0.4	03.5 ± 0.1
BLAST 104413-584412	287.060	0.159	$10^h44^m13.7^s$-58°44′12″		222 ± 2.0	74.2 ± 2.0	18.5 ± 0.6
BLAST 104135-592211	287.061	-0.559	$10^h41^m35.9^s$-59°22′11″		17.6 ± 0.4	08.1 ± 0.4	03.4 ± 0.1
BLAST 104324-585902	287.083	-0.109	$10^h43^m24.6^s$-58°59′02″		1174 ± 5.0	499 ± 5.0	219 ± 1.0
BLAST 103816-601106	287.088	-1.475	$10^h38^m16.0^s$-60°11′06″		30.4 ± 1.3	13.5 ± 1.3	05.2 ± 0.3
BLAST 103940-595319	287.098	-1.131	$10^h39^m40.7^s$-59°53′19″		10.1 ± 0.4	05.7 ± 0.4	02.1 ± 0.1
BLAST 104236-591244	287.101	-0.359	$10^h42^m36.8^s$-59°12′44″		37.6 ± 0.7	21.1 ± 0.7	09.1 ± 0.1
BLAST 104118-593141	287.104	-0.716	$10^h41^m18.1^s$-59°31′41″		90.9 ± 0.7	45.1 ± 0.7	18.7 ± 0.2
BLAST 104202-592247	287.116	-0.541	$10^h42^m02.5^s$-59°22′47″		212 ± 1.0	79.6 ± 1.0	32.9 ± 0.3
BLAST 104037-594507	287.137	-0.954	$10^h40^m37.7^s$-59°45′07″		170 ± 1.0	59.5 ± 1.3	18.5 ± 0.4
BLAST 104248-591550	287.148	-0.392	$10^h42^m48.9^s$-59°15′50″		149 ± 1.0	74.5 ± 1.3	38.1 ± 0.3

Continued on Next Page...

Table A.1 – Continued

Source ID	l	b	α_{2000}	δ_{2000}	$S_{250\mu m}$ [Jy]	$S_{350\mu m}$ [Jy]	$S_{500\mu m}$ [Jy]
BLAST 103942-600018	287.157	-1.231	$10^h39^m42.0^s$	-60°00′ 18″	895 ± 4.0	366 ± 4.0	134 ± 1.0
BLAST 104115-593900	287.158	-0.826	$10^h41^m15.5^s$	-59°39′ 00″	145 ± 1.0	57.5 ± 0.8	22.2 ± 0.2
BLAST 104109-594058	287.162	-0.861	$10^h41^m09.3^s$	-59°40′ 58″	283 ± 1.0	119 ± 1.0	45.5 ± 0.3
BLAST 104133-593528	287.162	-0.756	$10^h41^m33.2^s$	-59°35′ 28″	230 ± 1.0	85.5 ± 1.1	35.5 ± 0.3
BLAST 104206-593027	287.183	-0.650	$10^h42^m06.1^s$	-59°30′ 27″	647 ± 1.0	244 ± 1.0	112 ± 0.0
BLAST 103914-600948	287.183	-1.398	$10^h39^m14.4^s$	-60°09′ 48″	13.5 ± 0.6	06.6 ± 0.6	02.3 ± 0.1
BLAST 104043-594941	287.184	-1.015	$10^h40^m43.2^s$	-59°49′ 41″	142 ± 2.0	54.6 ± 1.8	17.0 ± 0.5
BLAST 104308-591609	287.187	-0.377	$10^h43^m08.5^s$	-59°16′ 09″	210 ± 1.0	101 ± 1.0	51.6 ± 0.4
BLAST 104225-592759	287.200	-0.594	$10^h42^m25.7^s$	-59°27′ 59″	159 ± 1.0	61.9 ± 0.7	26.1 ± 0.2
BLAST 104132-594113	287.206	-0.842	$10^h41^m32.1^s$	-59°41′ 13″	241 ± 1.0	94.7 ± 1.1	36.2 ± 0.3
BLAST 104148-593751	287.209	-0.776	$10^h41^m48.5^s$	-59°37′ 51″	246 ± 1.0	87.3 ± 1.1	31.9 ± 0.3
BLAST 104509-585050	287.218	0.117	$10^h45^m09.4^s$	-58°50′ 50″	1389 ± 4.0	569 ± 4.0	232 ± 1.0
BLAST 104244-592621	287.222	-0.551	$10^h42^m44.2^s$	-59°26′ 21″	532 ± 1.0	236 ± 1.0	97.9 ± 0.3
BLAST 104402-590822	287.227	-0.209	$10^h44^m02.3^s$	-59°08′ 22″	65.7 ± 0.6	36.2 ± 0.6	12.7 ± 0.2
BLAST 104212-593525	287.235	-0.716	$10^h42^m12.8^s$	-59°35′ 25″	60.8 ± 0.5	21.8 ± 0.5	09.3 ± 0.1
BLAST 104410-590854	287.247	-0.208	$10^h44^m10.8^s$	-59°08′ 54″	58.4 ± 0.6	28.5 ± 0.6	09.8 ± 0.1
BLAST 104142-594421	287.250	-0.877	$10^h41^m42.6^s$	-59°44′ 21″	57.0 ± 0.7	23.0 ± 0.7	06.0 ± 0.1
BLAST 104308-592425	287.252	-0.499	$10^h43^m08.5^s$	-59°24′ 25″	163 ± 1.0	79.0 ± 0.9	36.4 ± 0.2
BLAST 104556-581039	287.254	0.264	$10^h45^m56.0^s$	-58°44′ 03″	75.1 ± 1.8	27.8 ± 1.8	06.6 ± 0.5
BLAST 104434-590531	287.265	-0.134	$10^h44^m34.3^s$	-59°05′ 31″	22.0 ± 0.8	06.8 ± 0.8	01.5 ± 0.2
BLAST 104352-591553	287.268	-0.329	$10^h43^m52.7^s$	-59°15′ 53″	54.9 ± 0.8	22.8 ± 0.8	10.6 ± 0.2
BLAST 104229-593701	287.278	-0.723	$10^h42^m29.0^s$	-59°37′ 01″	43.3 ± 0.4	16.5 ± 0.4	06.5 ± 0.1
BLAST 104353-591826	287.290	-0.365	$10^h43^m53.8^s$	-59°18′ 26″	41.7 ± 0.7	17.9 ± 0.7	08.3 ± 0.2
BLAST 104411-591416	287.291	-0.286	$10^h44^m11.9^s$	-59°14′ 16″	136 ± 1.0	58.3 ± 1.5	23.9 ± 0.4
BLAST 103955-601418	287.294	-1.422	$10^h39^m55.1^s$	-60°14′ 18″	02.5 ± 0.4	<0.998	<0.344
BLAST 104314-592923	287.303	-0.565	$10^h43^m14.9^s$	-59°29′ 23″	218 ± 1.0	85.0 ± 0.6	32.7 ± 0.2
BLAST 104617-584639	287.314	0.246	$10^h46^m17.0^s$	-58°46′ 39″	16.1 ± 0.4	08.6 ± 0.4	03.0 ± 0.1
BLAST 104232-594056	287.315	-0.777	$10^h42^m32.6^s$	-59°40′ 56″	31.3 ± 0.5	10.3 ± 0.5	03.2 ± 0.1
BLAST 104625-584543	287.323	0.268	$10^h46^m25.2^s$	-58°45′ 43″	17.6 ± 0.5	09.3 ± 0.5	03.1 ± 0.1
BLAST 104406-592005	287.327	-0.376	$10^h44^m06.9^s$	-59°20′ 05″	50.0 ± 0.6	21.9 ± 0.6	10.1 ± 0.2
BLAST 104404-592126	287.333	-0.399	$10^h44^m04.5^s$	-59°21′ 26″	91.1 ± 0.7	40.9 ± 0.7	18.8 ± 0.2
BLAST 104317-593353	287.344	-0.628	$10^h43^m17.9^s$	-59°33′ 53″	11974 ± 3.0	4555 ± 3.0	1849 ± 1.0
BLAST 104358-592424	287.345	-0.449	$10^h43^m58.1^s$	-59°24′ 24″	366 ± 1.0	165 ± 1.0	73.2 ± 0.3
BLAST 104559-585530	287.349	0.098	$10^h45^m59.3^s$	-58°55′ 30″	211 ± 2.0	82.8 ± 1.9	34.9 ± 0.5
BLAST 104348-592824	287.357	-0.517	$10^h43^m48.2^s$	-59°28′ 24″	315 ± 1.0	124 ± 1.0	52.7 ± 0.2
BLAST 104521-590728	287.369	-0.116	$10^h45^m21.4^s$	-59°07′ 28″	04.8 ± 0.5	02.5 ± 0.5	00.6 ± 0.1
BLAST 104427-592255	287.389	-0.397	$10^h44^m27.9^s$	-59°22′ 55″	175 ± 1.0	76.4 ± 0.9	35.9 ± 0.3
BLAST 104400-592936	287.390	-0.522	$10^h44^m00.9^s$	-59°29′ 36″	336 ± 1.0	129 ± 1.0	52.4 ± 0.2
BLAST 104454-591744	287.399	-0.294	$10^h44^m54.9^s$	-59°17′ 44″	144 ± 1.0	58.3 ± 1.0	24.9 ± 0.3
BLAST 104354-593341	287.410	-0.589	$10^h43^m54.1^s$	-59°33′ 41″	95.5 ± 0.5	37.1 ± 0.5	16.1 ± 0.1
BLAST 104657-584949	287.417	0.240	$10^h46^m57.6^s$	-58°49′ 49″	485 ± 2.0	196 ± 2.0	66.9 ± 0.5
BLAST 104402-593307	287.421	-0.572	$10^h44^m02.5^s$	-59°33′ 07″	64.4 ± 0.4	22.9 ± 0.4	10.2 ± 0.1
BLAST 104532-591144	287.424	-0.168	$10^h45^m32.7^s$	-59°11′ 44″	09.3 ± 0.7	04.6 ± 0.4	01.3 ± 0.1
BLAST 104529-591241	287.425	-0.185	$10^h45^m29.5^s$	-59°12′ 41″	09.3 ± 0.7	04.5 ± 0.4	01.4 ± 0.1
BLAST 104458-592017	287.427	-0.328	$10^h44^m58.9^s$	-59°20′ 17″	114 ± 1.0	45.8 ± 0.9	20.7 ± 0.2
BLAST 104338-593948	287.428	-0.695	$10^h43^m38.2^s$	-59°39′ 48″	94.3 ± 0.5	33.6 ± 0.5	12.0 ± 0.1
BLAST 104451-592333	287.438	-0.383	$10^h44^m51.2^s$	-59°23′ 33″	83.4 ± 0.6	33.8 ± 0.6	14.9 ± 0.2
BLAST 104347-593857	287.439	-0.673	$10^h43^m47.7^s$	-59°38′ 57″	63.4 ± 0.4	23.1 ± 0.4	08.9 ± 0.1
BLAST 104421-593152	287.446	-0.536	$10^h44^m21.1^s$	-59°31′ 52″	855 ± 1.0	331 ± 1.0	134 ± 0.2
BLAST 104403-593649	287.452	-0.626	$10^h44^m03.6^s$	-59°36′ 49″	66.1 ± 0.5	26.6 ± 0.5	11.5 ± 0.1
BLAST 104454-592512	287.457	-0.404	$10^h44^m54.9^s$	-59°25′ 12″	71.5 ± 0.5	29.8 ± 0.5	10.7 ± 0.1
BLAST 104520-592116	287.475	-0.320	$10^h45^m20.8^s$	-59°21′ 16″	27.6 ± 0.5	12.3 ± 0.5	05.4 ± 0.1
BLAST 104559-591224	287.479	-0.152	$10^h45^m59.3^s$	-59°12′ 24″	83.9 ± 1.0	38.1 ± 1.0	14.1 ± 0.3
BLAST 104455-593052	287.503	-0.487	$10^h44^m55.7^s$	-59°30′ 52″	303 ± 1.0	127 ± 1.0	58.4 ± 0.3
BLAST 104736-585248	287.513	0.234	$10^h47^m36.1^s$	-58°52′ 48″	77.6 ± 0.9	30.9 ± 0.9	10.6 ± 0.2
BLAST 104550-591922	287.517	-0.263	$10^h45^m50.6^s$	-59°19′ 22″	73.0 ± 1.1	32.1 ± 1.1	16.3 ± 0.3
BLAST 104518-592718	287.518	-0.411	$10^h45^m18.8^s$	-59°27′ 18″	29.3 ± 0.5	11.4 ± 0.5	05.2 ± 0.1
BLAST 104419-594158	287.521	-0.686	$10^h44^m19.2^s$	-59°41′ 58″	80.4 ± 0.7	22.8 ± 0.7	06.3 ± 0.2
BLAST 104617-591327	287.522	-0.149	$10^h46^m17.7^s$	-59°13′ 27″	123 ± 1.0	53.2 ± 1.2	22.0 ± 0.3
BLAST 104430-593924	287.523	-0.637	$10^h44^m30.9^s$	-59°39′ 24″	27.5 ± 0.4	08.1 ± 0.4	02.7 ± 0.1
BLAST 104450-593742	287.546	-0.593	$10^h44^m50.6^s$	-59°37′ 42″	33.9 ± 0.3	10.8 ± 0.3	04.3 ± 0.1

Continued on Next Page...

Table A.1 – Continued

Source ID	l	b	α_{2000}	δ_{2000}	$S_{250\mu m}$ [Jy]	$S_{350\mu m}$ [Jy]	$S_{500\mu m}$ [Jy]
BLAST 104455-593714	287.552	-0.581	$10^h44^m55.7^s$	-59°37′ 14″	47.0 ± 0.4	16.1 ± 0.4	05.9 ± 0.1
BLAST 104118-602816	287.557	-1.544	$10^h41^m18.7^s$	-60°28′ 16″	03.8 ± 0.7	02.7 ± 0.7	<0.517
BLAST 104420-594632	287.559	-0.753	$10^h44^m20.0^s$	-59°46′ 32″	92.2 ± 1.1	31.2 ± 1.1	02.8 ± 0.3
BLAST 104348-595504	287.567	-0.909	$10^h43^m48.6^s$	-59°55′ 04″	59.6 ± 0.7	28.9 ± 0.7	10.1 ± 0.2
BLAST 104502-594041	287.591	-0.625	$10^h45^m02.1^s$	-59°40′ 41″	349 ± 1.0	138 ± 1.0	53.9 ± 0.2
BLAST 104750-590201	287.612	0.112	$10^h47^m50.9^s$	-59°02′ 01″	558 ± 3.0	138 ± 3.0	59.3 ± 0.8
BLAST 104355-595955	287.619	-0.974	$10^h43^m55.7^s$	-59°59′ 55″	904 ± 3.0	407 ± 3.0	157 ± 1.0
BLAST 104501-591039	287.639	-0.720	$10^h45^m01.2^s$	-59°47′ 03″	56.3 ± 0.3	22.5 ± 0.3	07.5 ± 0.1
BLAST 104506-594803	287.656	-0.730	$10^h45^m06.3^s$	-59°48′ 03″	272 ± 1.0	118 ± 1.0	40.1 ± 0.2
BLAST 104517-594733	287.672	-0.712	$10^h45^m17.1^s$	-59°47′ 33″	41.6 ± 0.3	17.5 ± 0.3	05.7 ± 0.1
BLAST 104443-595530	287.673	-0.861	$10^h44^m43.9^s$	-59°55′ 30″	54.5 ± 0.5	22.5 ± 0.5	06.6 ± 0.1
BLAST 104530-594430	287.674	-0.654	$10^h45^m30.6^s$	-59°44′ 30″	68.3 ± 0.5	23.4 ± 0.5	07.6 ± 0.1
BLAST 104434-595816	287.676	-0.912	$10^h44^m34.2^s$	-59°58′ 16″	91.5 ± 0.5	38.9 ± 0.5	13.5 ± 0.1
BLAST 104547-594054	287.677	-0.584	$10^h45^m47.1^s$	-59°40′ 54″	16.8 ± 0.4	05.3 ± 0.4	01.5 ± 0.1
BLAST 104500-595205	287.677	-0.795	$10^h45^m00.8^s$	-59°52′ 05″	286 ± 1.0	132 ± 1.0	48.6 ± 0.3
BLAST 104524-594718	287.685	-0.701	$10^h45^m24.9^s$	-59°47′ 18″	85.7 ± 0.5	37.1 ± 0.5	12.0 ± 0.1
BLAST 104357-600854	287.692	-1.104	$10^h43^m57.3^s$	-60°08′ 54″	155 ± 2.0	61.8 ± 1.6	17.2 ± 0.4
BLAST 104442-595852	287.697	-0.912	$10^h44^m42.9^s$	-59°58′ 52″	130 ± 1.0	53.9 ± 0.6	19.0 ± 0.2
BLAST 104518-595157	287.709	-0.776	$10^h45^m18.2^s$	-59°51′ 57″	40.0 ± 0.4	17.4 ± 0.4	05.8 ± 0.1
BLAST 104558-594357	287.721	-0.619	$10^h45^m58.3^s$	-59°43′ 57″	441 ± 1.0	164 ± 1.0	60.0 ± 0.3
BLAST 104744-591830	287.724	-0.139	$10^h47^m44.0^s$	-59°18′ 30″	31.3 ± 1.0	09.1 ± 0.9	04.0 ± 0.2
BLAST 104156-604322	287.746	-1.727	$10^h41^m56.9^s$	-60°43′ 22″	13.1 ± 0.9	09.7 ± 0.8	01.6 ± 0.3
BLAST 104601-594637	287.748	-0.655	$10^h46^m01.7^s$	-59°46′ 37″	828 ± 1.0	324 ± 1.0	111 ± 0.6
BLAST 104428-600847	287.749	-1.072	$10^h44^m28.9^s$	-60°08′ 47″	96.7 ± 1.3	42.6 ± 1.3	13.0 ± 0.4
BLAST 104459-600138	287.749	-0.937	$10^h44^m59.5^s$	-60°01′ 38″	10.7 ± 0.3	04.7 ± 0.3	01.5 ± 0.1
BLAST 104537-595344	287.757	-0.784	$10^h45^m37.0^s$	-59°53′ 44″	334 ± 1.0	137 ± 1.0	49.8 ± 0.3
BLAST 104625-594229	287.761	-0.570	$10^h46^m25.6^s$	-59°42′ 29″	33.8 ± 0.4	12.1 ± 0.4	03.3 ± 0.1
BLAST 104750-592153	287.763	-0.183	$10^h47^m50.7^s$	-59°21′ 53″	103 ± 2.0	46.6 ± 1.8	25.4 ± 0.5
BLAST 104520-595822	287.763	-0.868	$10^h45^m20.7^s$	-59°58′ 22″	273 ± 1.0	113 ± 1.0	44.0 ± 0.3
BLAST 104509-600204	287.770	-0.934	$10^h45^m09.1^s$	-60°02′ 04″	29.2 ± 0.5	13.0 ± 0.5	04.3 ± 0.1
BLAST 104641-594139	287.783	-0.543	$10^h46^m41.1^s$	-59°41′ 39″	70.6 ± 0.7	23.4 ± 0.7	07.0 ± 0.2
BLAST 104521-600113	287.787	-0.909	$10^h45^m21.6^s$	-60°01′ 13″	187 ± 1.0	82.6 ± 1.2	29.9 ± 0.3
BLAST 104711-593645	287.802	-0.441	$10^h47^m11.2^s$	-59°36′ 45″	35.9 ± 0.9	12.4 ± 0.9	07.4 ± 0.2
BLAST 104552-595701	287.811	-0.817	$10^h45^m52.6^s$	-59°57′ 01″	1305 ± 2.0	531 ± 2.0	202 ± 0.9
BLAST 104645-594437	287.813	-0.583	$10^h46^m45.1^s$	-59°44′ 37″	44.8 ± 0.5	15.4 ± 0.5	04.4 ± 0.2
BLAST 104652-594647	287.844	-0.608	$10^h46^m52.9^s$	-59°46′ 47″	44.2 ± 0.8	14.2 ± 0.8	<0.262
BLAST 104506-601228	287.846	-1.090	$10^h45^m06.4^s$	-60°12′ 28″	453 ± 2.0	192 ± 2.0	68.9 ± 0.6
BLAST 104617-595603	287.850	-0.778	$10^h46^m17.7^s$	-59°56′ 03″	47.4 ± 0.7	20.1 ± 0.7	07.1 ± 0.2
BLAST 104413-602723	287.866	-1.360	$10^h44^m13.8^s$	-60°27′ 23″	123 ± 1.0	66.0 ± 1.4	23.6 ± 0.4
BLAST 104320-603934	287.867	-1.590	$10^h43^m20.9^s$	-60°39′ 34″	38.2 ± 1.4	33.1 ± 1.4	05.8 ± 0.4
BLAST 104719-594345	287.871	-0.537	$10^h47^m19.7^s$	-59°43′ 45″	06.4 ± 0.8	...	...
BLAST 104645-595305	287.879	-0.708	$10^h46^m45.2^s$	-59°53′ 05″	85.9 ± 1.1	31.0 ± 1.1	04.9 ± 0.3
BLAST 104439-602259	287.879	-1.270	$10^h44^m39.8^s$	-60°22′ 59″	62.1 ± 1.3	32.5 ± 1.3	09.2 ± 0.4
BLAST 104827-592809	287.880	-0.240	$10^h48^m27.6^s$	-59°28′ 09″	49.1 ± 2.0	30.3 ± 2.0	11.1 ± 0.6
BLAST 104556-600537	287.885	-0.940	$10^h45^m56.7^s$	-60°05′ 37″	94.7 ± 0.7	41.8 ± 0.7	14.7 ± 0.2
BLAST 104352-603714	287.905	-1.525	$10^h43^m52.7^s$	-60°37′ 14″	147 ± 2.0	84.0 ± 1.7	21.5 ± 0.5
BLAST 104325-604351	287.908	-1.649	$10^h43^m25.1^s$	-60°43′ 51″	33.8 ± 1.3	25.5 ± 1.3	06.0 ± 0.3
BLAST 104705-595159	287.908	-0.672	$10^h47^m05.6^s$	-59°51′ 59″	39.8 ± 0.8	13.0 ± 0.8	<0.341
BLAST 104557-600832	287.910	-0.982	$10^h45^m57.6^s$	-60°08′ 32″	117 ± 0.3	47.2 ± 0.4	16.4 ± 0.1
BLAST 104556-600940	287.917	-1.000	$10^h45^m56.9^s$	-60°09′ 40″	87.7 ± 0.4	36.7 ± 0.4	12.8 ± 0.1
BLAST 104543-601449	287.932	-1.089	$10^h45^m43.1^s$	-60°14′ 49″	93.6 ± 0.4	41.8 ± 0.4	15.1 ± 0.1
BLAST 104424-603359	287.938	-1.447	$10^h44^m24.8^s$	-60°33′ 59″	98.9 ± 1.5	58.2 ± 1.5	18.3 ± 0.4
BLAST 104636-600347	287.944	-0.875	$10^h46^m36.0^s$	-60°03′ 47″	28.9 ± 0.5	14.6 ± 0.5	05.3 ± 0.1
BLAST 104544-601641	287.949	-1.115	$10^h45^m44.6^s$	-60°16′ 41″	525 ± 1.0	238 ± 1.0	92.7 ± 0.2
BLAST 104358-604443	287.975	-1.630	$10^h43^m58.5^s$	-60°44′ 43″	32.3 ± 1.1	19.3 ± 1.1	04.3 ± 0.3
BLAST 104700-600435	287.996	-0.863	$10^h47^m00.8^s$	-60°04′ 35″	93.1 ± 0.6	41.6 ± 0.6	14.9 ± 0.2
BLAST 104716-600051	287.996	-0.793	$10^h47^m16.5^s$	-60°00′ 51″	715 ± 2.0	305 ± 2.0	116 ± 0.8
BLAST 104556-602141	288.008	-1.178	$10^h45^m56.0^s$	-60°21′ 41″	62.6 ± 0.5	30.9 ± 0.5	11.6 ± 0.1
BLAST 104642-601039	288.009	-0.971	$10^h46^m42.6^s$	-60°10′ 39″	92.1 ± 0.8	44.5 ± 0.8	15.2 ± 0.2
BLAST 104536-602908	288.030	-1.307	$10^h45^m36.2^s$	-60°29′ 08″	116 ± 1.0	56.2 ± 1.3	21.3 ± 0.4
BLAST 104639-601456	288.036	-1.037	$10^h46^m39.7^s$	-60°14′ 56″	59.2 ± 0.6	25.5 ± 0.6	09.1 ± 0.2

Continued on Next Page...

Table A.1 – Continued

Source ID	l	b	α_{2000}	δ_{2000}	$S_{250\mu m}$ [Jy]	$S_{350\mu m}$ [Jy]	$S_{500\mu m}$ [Jy]
BLAST 104523-603316	288.039	-1.380	$10^h45^m23.4^s$	-60°33′ 16″	152 ± 1.0	71.7 ± 1.5	22.2 ± 0.4
BLAST 104735-600227	288.043	-0.799	$10^h47^m35.1^s$	-60°02′ 27″	278 ± 1.0	123 ± 1.0	45.2 ± 0.3
BLAST 104946-593105	288.051	-0.208	$10^h49^m46.7^s$	-59°31′ 05″	19.7 ± 0.8	12.4 ± 0.8	03.0 ± 0.2
BLAST 104817-595331	288.052	-0.627	$10^h48^m17.0^s$	-59°53′ 31″	48.9 ± 1.2	25.2 ± 1.2	03.0 ± 0.3
BLAST 104627-602009	288.054	-1.126	$10^h46^m27.3^s$	-60°20′ 09″	115 ± 1.0	52.6 ± 0.8	19.9 ± 0.2
BLAST 104733-600452	288.059	-0.836	$10^h47^m33.8^s$	-60°04′ 52″	39.2 ± 0.4	18.5 ± 0.4	06.4 ± 0.1
BLAST 104644-601717	288.064	-1.066	$10^h46^m44.8^s$	-60°17′ 17″	225 ± 1.0	98.1 ± 1.3	35.0 ± 0.3
BLAST 105007-592822	288.070	-0.148	$10^h50^m07.4^s$	-59°28′ 22″	61.3 ± 1.6	28.0 ± 1.6	05.8 ± 0.4
BLAST 104534-603547	288.079	-1.406	$10^h45^m34.9^s$	-60°35′ 47″	21.9 ± 0.6	12.1 ± 0.6	03.4 ± 0.2
BLAST 104813-595812	288.081	-0.700	$10^h48^m13.0^s$	-59°58′ 12″	38.0 ± 0.7	24.8 ± 0.7	09.1 ± 0.2
BLAST 104836-595237	288.081	-0.595	$10^h48^m36.1^s$	-59°52′ 37″	11.3 ± 0.7	04.9 ± 0.6	···
BLAST 104719-594345	288.087	-0.650	$10^h48^m26.8^s$	-59°55′ 41″	22.4 ± 0.5	08.3 ± 0.5	02.3 ± 0.1

Table A.2: Source sizes, Luminosities, Temperatures and Masses for the Carina Nebula

ID	Size arcsec	Luminosity [$L_\odot$]	Temperature [K]	Mass [$M_\odot$]
BLAST 103813-585717	18.9	1510±75	20.8±1.0	892±44
BLAST 103842-585338	28.1	3468±173	21.1±1.0	198±99
BLAST 103857-585223	50.8	6810±340	19.7±0.9	6410±320
BLAST 103936-584943	22.4	1056±52	19.0±0.9	1176±58
BLAST 103909-590413	65.0	27618±1380	21.6±1.1	11867±593
BLAST 103915-590730	50.8	13405±670	21.6±1.1	5675±283
BLAST 104036-585337	217	···	···	···
BLAST 103927-591113	37.9	11895±594	23.7±1.2	2781±139
BLAST 103614-595645	37.9	10111±505	23.9±1.2	2162±108
BLAST 103938-591237	75.7	23788±1189	21.8±1.1	8121±406
BLAST 103614-600209	103	32021±1601	21.1±1.1	16901±845
BLAST 103949-591459	44.8	36335±181	19.9±1.0	2863±143
BLAST 103952-591808	47.1	37382±186	19.9±1.0	2907±145
BLAST 104124-590049	68.2	9402±470	20.4±1.0	6139±306
BLAST 104226-584708	128	39240±1962	20.4±1.0	23393±1169
BLAST 104012-592202	95.4	59423±2971	23.1±1.2	13938±696
BLAST 104051-591322	31.7	3160±158	21.8±1.1	1189±59
BLAST 104226-585207	32.8	3371±168	22.1±1.1	1138±56
BLAST 104224-585332	25.4	2073±103	21.8±1.1	687±34
BLAST 103918-593920	55.5	7115±355	21.3±1.1	3429±171
BLAST 104018-592549	57.4	4219±210	19.7±0.9	3575±178
BLAST 104129-591030	29.3	1089±54	19.9±1.0	850±42
BLAST 104150-590910	32.8	3240±162	22.6±1.1	1051±52
BLAST 104210-590515	42.3	3160±158	20.4±1.0	1835±91
BLAST 104202-590832	23.9	551±27	19.7±0.9	505±25
BLAST 104107-592232	25.4	450±22	18.6±0.9	584±29
BLAST 104110-592517	30.5	···	···	···
BLAST 104137-592015	51.5	4651±232	20.8±1.0	2419±120
BLAST 104413-584412	77.6	14689±734	22.3±1.1	5504±275
BLAST 104135-592211	84.6	15967±798	21.8±1.1	6566±328
BLAST 104324-585902	31.7	9562±47	19.7±0.9	826±41
BLAST 103816-601106	101	49054±2452	22.9±1.1	14920±746
BLAST 103940-595319	80.3	20003±1000	21.8±1.1	6710±335
BLAST 104236-591244	63.3	7938±396	21.8±1.1	3230±161
BLAST 104118-593141	105	24308±1215	21.8±1.1	11045±552
BLAST 104202-592247	36.9	2997±149	22.1±1.1	1104±55
BLAST 104037-594507	57.4	7409±370	21.8±1.1	3219±160
BLAST 104248-591550	105	34464±1723	22.9±1.1	9974±498

Continued on Next Page...

Table A.2 – Continued

ID	Size arcsec	Luminosity [$L_\odot$]	Temperature [K]	Mass [$M_\odot$]
BLAST 103942-600018	42.3	2683±134	21.3±1.1	1379±68
BLAST 104115-593900	35.9	2660±133	22.1±1.1	972±48
BLAST 104109-594058	28.1	1437±71	22.3±1.1	554±27
BLAST 104133-593528	49.4	5070±253	22.6±1.1	1639±81
BLAST 104206-593027	41.5	6171±308	23.1±1.2	1304±65
BLAST 103914-600948	113	...	...	...
BLAST 104043-594941	118	...	...	...
BLAST 104308-591609	49.4	3462±173	20.8±1.0	1984±99
BLAST 104225-592759	38.8	3552±177	22.1±1.1	1124±56
BLAST 104132-594113	66.1	5855±292	21.3±1.1	2984±149
BLAST 104148-593751	63.9	5147±257	21.3±1.1	2587±129
BLAST 104509-585050	56.8	...	...	...
BLAST 104244-592621	132	...	...	...
BLAST 104402-590822	32.8	...	...	...
BLAST 104212-593525	34.9	...	...	...
BLAST 104410-590854	47.9	6507±325	23.9±1.2	1410±70
BLAST 104142-594421	89.2	6646±332	19.9±1.0	5569±278
BLAST 104308-592425	50.1	1901±95	19.9±1.0	1584±79
BLAST 104556-581039	53.5	19370±968	25.9±1.3	1775±88
BLAST 104434-590531	78.5	8555±427	21.6±1.1	3899±194
BLAST 104229-593701	126	17706±885	20.6±1.0	11679±583
BLAST 104353-591826	104	7676±383	20.1±1.0	6122±306
BLAST 104411-591416	60.4	15463±773	23.9±1.2	2562±128
BLAST 103955-601418	47.9	...	...	...
BLAST 104314-592923	89.2	5902±295	20.4±1.0	4182±209
BLAST 104617-584639	91.9	6074±303	20.1±1.0	4277±213
BLAST 104232-594056	101	28299±1414	22.6±1.1	8525±426
BLAST 104625-584543	32.8	1889±94	21.6±1.1	739±36
BLAST 104406-592005	75.7	6204±310	21.6±1.1	2854±142
BLAST 104404-592126	58.6	3558±177	21.3±1.1	1715±85
BLAST 104317-593353	68.8	4708±235	21.6±1.1	2147±107
BLAST 104358-592424	45.6	1988±99	21.6±1.1	963±48
BLAST 104559-585530	78.9	9119±455	22.9±1.1	2749±137
BLAST 104348-592824	70.8	12788±639	23.1±1.2	3271±163
BLAST 104521-590728	87.1	3497±174	19.5±0.9	3282±164
BLAST 104427-592255	47.1	3464±173	22.6±1.1	1109±55
BLAST 104400-592936	45.6	3422±171	23.9±1.2	825±41
BLAST 104454-591744	53.5	5752±287	23.9±1.2	1205±60
BLAST 104354-593341	75.7	2199±110	19.0±0.9	2360±118
BLAST 104657-584949	89.9	3171±158	19.0±0.9	3615±180
BLAST 104402-593307	120	...	...	...
BLAST 104532-591144	43.9	...	...	...
BLAST 104529-591241	92.3	7156±357	22.1±1.1	3034±151
BLAST 104458-592017	54.9	...	...	...
BLAST 104338-593948	84.6	...	...	...
BLAST 104451-592333	56.1	...	...	...
BLAST 104347-593857	66.1	...	...	...
BLAST 104421-593152	222	38882±1944	21.1±1.1	22322±1116
BLAST 104403-593649	58.0	1776±88	20.6±1.0	1236±61
BLAST 104454-592512	97.6	11162±558	22.9±1.1	3404±170
BLAST 104520-592116	118	19622±981	23.1±1.2	5533±276
BLAST 104559-591224	18.9	...	...	...
BLAST 104455-593052	54.2	2539±126	22.3±1.1	974±48
BLAST 104736-585248	28.1	...	...	...
BLAST 104550-591922	175	22745±1137	21.8±1.1	10240±512
BLAST 104518-592718	116	...	...	...
BLAST 104419-594158	37.9	1351±67	21.8±1.1	580±29
BLAST 104617-591327	39.7	1634±81	23.1±1.2	483±24
BLAST 104430-593924	58.0	4125±206	23.4±1.2	1078±53
BLAST 104450-593742	59.2	2051±102	21.1±1.0	1123±56
BLAST 104455-593714	28.1	...	...	...
BLAST 104118-602816	121	...	...	...
BLAST 104420-594632	39.7	531±26	19.7±0.9	437±21

Continued on Next Page...

Table A.2 – Continued

ID	Size arcsec	Luminosity [$L_\odot$]	Temperature [K]	Mass [$M_\odot$]
BLAST 104348-595504	78.5	···	···	···
BLAST 104502-594041	359	98312±4915	22.1±1.1	40575±2028
BLAST 104750-590201	169	···	···	···
BLAST 104355-595955	111	9701±485	22.6±1.1	3429±171
BLAST 104501-591039	20.7	···	···	···
BLAST 104506-594803	255	···	···	···
BLAST 104517-594733	44.8	989±49	21.8±1.0	454±22
BLAST 104443-595530	240	···	···	···
BLAST 104530-594430	158	12222±611	22.1±1.1	5073±253
BLAST 104434-595816	89.9	···	···	···
BLAST 104547-594054	35.9	···	···	···
BLAST 104500-595205	89.9	12791±639	25.9±1.3	1604±80
BLAST 104524-594718	89.9	4042±202	21.6±1.0	1935±96
BLAST 104357-600854	72.3	2027±101	21.1±1.1	1093±54
BLAST 104442-595852	31.7	···	···	···
BLAST 104518-595157	31.7	···	···	···
BLAST 104558-594357	32.8	···	···	···
BLAST 104744-591830	64.5	···	···	···
BLAST 104156-604322	246	32564±1628	22.6±1.1	10540±527
BLAST 104601-594637	61.6	1713±85	22.6±1.1	631±31
BLAST 104428-600847	96.5	15643±782	25.6±1.3	2119±105
BLAST 104459-600138	109	10338±516	25.1±1.3	1936±96
BLAST 104537-595344	148	···	···	···
BLAST 104625-594229	107	···	···	···
BLAST 104750-592153	107	3182±159	20.6±1.0	1830±91
BLAST 104520-595822	50.8	···	···	···
BLAST 104509-600204	52.9	···	···	···
BLAST 104641-594139	80.3	4364±218	22.1±1.1	1698±84
BLAST 104521-600113	34.9	···	···	···
BLAST 104711-593645	65.6	···	···	···
BLAST 104552-595701	25.4	···	···	···
BLAST 104645-594437	62.8	1218±60	22.1±1.1	481±24
BLAST 104652-594647	252	41602±2080	22.6±1.1	14514±725
BLAST 104506-601228	180	14218±710	23.9±1.2	3254±162
BLAST 104617-595603	35.9	···	···	···
BLAST 104413-602723	278	···	···	···
BLAST 104320-603934	85.1	7380±369	23.1±1.2	2014±100
BLAST 104719-594345	73.8	···	···	···
BLAST 104645-595305	36.9	···	···	···
BLAST 104439-602259	185	13639±681	23.7±1.2	3374±168
BLAST 104827-592809	37.9	···	···	···
BLAST 104556-600537	71.3	1982±99	24.8±1.2	384±19
BLAST 104352-603714	26.8	···	···	···
BLAST 104325-604351	181	8870±443	21.3±1.1	4168±208
BLAST 104705-595159	95.4	1398±69	21.3±1.1	630±31
BLAST 104557-600832	25.4	···	···	···
BLAST 104556-600940	227	···	···	···
BLAST 104543-601449	85.5	···	···	···
BLAST 104424-603359	292	···	···	···
BLAST 104424-603359	90.8	2190±109	24.5±1.2	432±21
BLAST 104636-600347	20.7	···	···	···
BLAST 104544-601641	128	···	···	···
BLAST 104358-604443	113	3598±179	24.5±1.2	738±36
BLAST 104700-600435	90.4	···	···	···
BLAST 104716-600051	52.2	···	···	···
BLAST 104556-602141	31.7	516±48	27.9±1.8	486±07
BLAST 104642-601039	51.5	···	···	···
BLAST 104536-602908	180	···	···	···
BLAST 104639-601456	26.8	···	···	···
BLAST 104523-603316	142	213±38	25.5±1.5	456±08
BLAST 104735-600227	35.9	···	···	···
BLAST 104946-593105	22.4	142±07	24.8±1.2	23±01
BLAST 104817-595331	41.5	734±36	24.8±1.2	145±07

Continued on Next Page...

Table A.2 – Continued

ID	Size arcsec	Luminosity [$L_\odot$]	Temperature [K]	Mass [$M_\odot$]
BLAST 104627-602009	131	7751±387	23.4±1.2	2192±109
BLAST 104733-600452	56.8	...	...	...
BLAST 104644-601717	43.2	391±19	22.6±1.1	121±06
BLAST 105007-592822	36.9	283±14	22.1±1.1	103±05
BLAST 104534-603547	47.1	...	...	...
BLAST 104813-595812	123	1052±15	22.7±1.1	108±04
BLAST 104836-595237	96.9	851±13	21.4±1.1	421±06
BLAST 104719-594345	110	...	...	...

Table A.3: Source Positions and Flux Densities for NGC 7538

Source ID	l	b	α_{2000}	δ_{2000}	$S_{70\mu m}$ [Jy]	$S_{160\mu m}$ [Jy]	$S_{250\mu m}$ [Jy]	$S_{350\mu m}$ [Jy]	$S_{500\mu m}$ [Jy]
HOBYS 231324+612056	111.460	0.680	$23^h13^m24.8^s$	$61^o20'56''$	···	11.63 ± 1.62	1.34 ± 0.07	3.46 ± 0.38	3.16 ± 0.63
HOBYS 231233+614718	111.528	1.125	$23^h12^m33.7^s$	$61^o47'18''$	···	···	0.33 ± 0.04	1.31 ± 0.20	1.15 ± 0.33
HOBYS 231346+613327	111.576	0.858	$23^h13^m46.3^s$	$61^o33'27''$	215.00 ± 0.53	262.12 ± 1.00	2.81 ± 0.04	6.63 ± 0.24	5.87 ± 0.40
HOBYS 231403+613315	111.607	0.842	$23^h14^m03.8^s$	$61^o33'15''$	198.00 ± 0.31	328.36 ± 1.23	2.93 ± 0.04	6.76 ± 0.24	5.99 ± 0.39
HOBYS 231418+613200	111.627	0.812	$23^h14^m18.7^s$	$61^o32'00''$	16.74 ± 0.16	43.75 ± 0.51	1.06 ± 0.02	2.44 ± 0.13	2.14 ± 0.21
HOBYS 231429+613127	111.644	0.795	$23^h14^m29.6^s$	$61^o31'27''$	22.66 ± 0.11	55.67 ± 0.68	2.62 ± 0.03	6.20 ± 0.15	5.43 ± 0.24
HOBYS 231429+613505	111.665	0.852	$23^h14^m29.3^s$	$61^o35'05''$	22.34 ± 0.12	78.44 ± 0.94	3.75 ± 0.04	8.02 ± 0.21	6.77 ± 0.35
HOBYS 231439+613204	111.666	0.798	$23^h14^m39.7^s$	$61^o32'04''$	20.74 ± 0.18	72.31 ± 1.07	6.68 ± 0.04	15.16 ± 0.22	12.9 ± 0.44
HOBYS 231347+614921	111.675	1.104	$23^h13^m47.0^s$	$61^o49'21''$	···	···	0.51 ± 0.02	1.02 ± 0.10	0.77 ± 0.17
HOBYS 231353+614912	111.686	1.097	$23^h13^m53.4^s$	$61^o49'12''$	···	···	0.66 ± 0.02	1.72 ± 0.13	1.52 ± 0.21
HOBYS 231459+613607	111.727	0.847	$23^h14^m59.1^s$	$61^o36'07''$	0.76 ± 0.02	6.35 ± 0.36	2.77 ± 0.01	5.32 ± 0.08	4.01 ± 0.14
HOBYS 231503+613647	111.738	0.854	$23^h15^m03.1^s$	$61^o36'47''$	1.66 ± 0.03	14.24 ± 0.64	7.02 ± 0.02	13.64 ± 0.10	10.20 ± 0.26
HOBYS 231515+613442	111.749	0.813	$23^h15^m15.9^s$	$61^o34'42''$	0.50 ± 0.03	14.91 ± 0.68	2.79 ± 0.02	4.99 ± 0.13	4.01 ± 0.22
HOBYS 231515+613731	111.765	0.857	$23^h15^m15.3^s$	$61^o37'31''$	2.09 ± 0.04	21.10 ± 0.85	18.30 ± 0.01	30.32 ± 0.23	20.61 ± 0.33
HOBYS 231526+613422	111.766	0.800	$23^h15^m26.3^s$	$61^o34'22''$	···	1.43 ± 0.32	3.06 ± 0.01	5.77 ± 0.08	4.35 ± 0.12
HOBYS 231523+613830	111.785	0.866	$23^h15^m23.0^s$	$61^o38'30''$	1.79 ± 0.03	15.00 ± 0.67	12.37 ± 0.02	17.03 ± 0.16	11.06 ± 0.22
HOBYS 231540+613446	111.794	0.796	$23^h15^m40.0^s$	$61^o34'46''$	0.34 ± 0.02	4.78 ± 0.36	4.88 ± 0.01	8.58 ± 0.08	5.88 ± 0.14
HOBYS 231519+614137	111.797	0.917	$23^h15^m19.3^s$	$61^o41'37''$	0.24 ± 0.04	<1.69	3.90 ± 0.03	4.48 ± 0.19	2.79 ± 0.31
HOBYS 231556+613137	111.806	0.735	$23^h15^m56.8^s$	$61^o31'37''$	2.73 ± 0.05	51.60 ± 0.94	4.28 ± 0.04	7.88 ± 0.22	6.29 ± 0.36
HOBYS 231537+613814	111.810	0.852	$23^h15^m37.2^s$	$61^o38'14''$	1.25 ± 0.03	9.63 ± 0.52	23.80 ± 0.03	29.61 ± 0.13	16.74 ± 0.26
HOBYS 231535+613921	111.814	0.871	$23^h15^m35.8^s$	$61^o39'21''$	0.99 ± 0.02	6.33 ± 0.32	3.42 ± 0.01	3.80 ± 0.08	2.53 ± 0.12
HOBYS 231541+613743	111.815	0.841	$23^h15^m41.6^s$	$61^o37'43''$	0.59 ± 0.02	5.00 ± 0.33	7.32 ± 0.01	9.09 ± 0.08	5.85 ± 0.13
HOBYS 231537+613947	111.819	0.876	$23^h15^m37.0^s$	$61^o39'47''$	0.76 ± 0.02	5.90 ± 0.32	3.62 ± 0.01	3.87 ± 0.08	2.26 ± 0.12
HOBYS 231551+613550	111.823	0.804	$23^h15^m51.8^s$	$61^o35'50''$	0.97 ± 0.02	7.17 ± 0.36	36.33 ± 0.02	56.15 ± 0.12	31.06 ± 0.11
HOBYS 231634+612304	111.825	0.575	$23^h16^m34.5^s$	$61^o23'04''$	10.64 ± 0.11	138.45 ± 1.23	3.08 ± 0.06	5.89 ± 0.33	4.69 ± 0.54
HOBYS 231707+611305	111.827	0.397	$23^h17^m07.0^s$	$61^o13'05''$	3.20 ± 0.06	43.37 ± 1.28	2.82 ± 0.05	4.17 ± 0.28	2.88 ± 0.46
HOBYS 231549+613725	111.827	0.831	$23^h15^m49.2^s$	$61^o37'25''$	1.05 ± 0.02	6.80 ± 0.36	33.57 ± 0.01	45.24 ± 0.15	26.87 ± 0.12
HOBYS 231551+613656	111.828	0.822	$23^h15^m51.1^s$	$61^o36'56''$	1.09 ± 0.02	6.61 ± 0.36	34.25 ± 0.06	51.71 ± 0.11	32.32 ± 0.16
HOBYS 231554+613607	111.829	0.807	$23^h15^m54.3^s$	$61^o36'07''$	0.65 ± 0.02	4.51 ± 0.33	24.31 ± 0.04	38.91 ± 0.12	25.13 ± 0.16
HOBYS 231532+614256	111.830	0.929	$23^h15^m32.5^s$	$61^o42'56''$	0.32 ± 0.02	2.39 ± 0.36	0.83 ± 0.02	0.88 ± 0.09	0.49 ± 0.14
HOBYS 231607+613233	111.832	0.742	$23^h16^m07.7^s$	$61^o32'33''$	1.69 ± 0.04	24.31 ± 0.97	3.93 ± 0.04	6.82 ± 0.20	5.20 ± 0.33
HOBYS 231552+613747	111.836	0.834	$23^h15^m52.6^s$	$61^o37'47''$	0.98 ± 0.02	6.25 ± 0.32	17.16 ± 0.03	24.80 ± 0.13	17.21 ± 0.16
HOBYS 231555+613707	111.837	0.822	$23^h15^m55.3^s$	$61^o37'07''$	1.19 ± 0.02	6.75 ± 0.32	29.51 ± 0.03	41.95 ± 0.10	24.60 ± 0.15
HOBYS 231556+613734	111.841	0.828	$23^h15^m56.4^s$	$61^o37'34''$	1.57 ± 0.02	8.33 ± 0.32	19.03 ± 0.01	27.02 ± 0.13	17.86 ± 0.13
HOBYS 231604+613610	111.847	0.801	$23^h16^m04.1^s$	$61^o36'10''$	2.00 ± 0.02	13.19 ± 0.36	6.03 ± 0.01	9.33 ± 0.08	6.39 ± 0.12
HOBYS 231549+614059	111.848	0.886	$23^h15^m49.0^s$	$61^o40'59''$	14.71 ± 0.15	97.14 ± 1.11	20.94 ± 0.04	27.23 ± 0.30	17.41 ± 0.40
HOBYS 231550+614205	111.858	0.902	$23^h15^m50.9^s$	$61^o42'05''$	2.80 ± 0.03	19.98 ± 0.64	4.12 ± 0.02	5.31 ± 0.13	3.53 ± 0.22

Continued on Next Page...

Table A.3 – Continued

Source ID	l	b	α_{2000}	δ_{2000}	$S_{70\mu m}$ [Jy]	$S_{160\mu m}$ [Jy]	$S_{250\mu m}$ [Jy]	$S_{350\mu m}$ [Jy]	$S_{500\mu m}$ [Jy]
HOBYS 231610+613626	111.861	0.800	$23^h16^m10.4^s$	$61^o36'26''$	124.01 ± 0.01	252.56 ± 1.02	62.06 ± 0.02	82.63 ± 0.26	48.01 ± 0.35
HOBYS 231628+613216	111.870	0.723	$23^h16^m28.7^s$	$61^o32'16''$	···	2.78 ± 0.84	3.37 ± 0.03	5.63 ± 0.20	3.95 ± 0.32
HOBYS 231559+614153	111.873	0.893	$23^h15^m59.4^s$	$61^o41'53''$	1.69 ± 0.02	12.64 ± 0.31	1.30 ± 0.01	1.61 ± 0.08	1.05 ± 0.13
HOBYS 231643+612831	111.874	0.654	$23^h16^m43.0^s$	$61^o28'31''$	···	···	2.86 ± 0.04	4.77 ± 0.20	3.61 ± 0.33
HOBYS 231834+605331	111.877	0.029	$23^h18^m34.7^s$	$60^o53'31''$	···	···	1.16 ± 0.04	2.11 ± 0.25	<1.19
HOBYS 231604+614143	111.881	0.887	$23^h16^m04.4^s$	$61^o41'43''$	2.19 ± 0.02	12.97 ± 0.44	1.55 ± 0.01	2.05 ± 0.08	1.42 ± 0.14
HOBYS 231609+614021	111.882	0.862	$23^h16^m09.3^s$	$61^o40'21''$	1.75 ± 0.02	14.50 ± 0.41	8.47 ± 0.02	10.91 ± 0.10	6.43 ± 0.17
HOBYS 231613+613934	111.886	0.847	$23^h16^m13.9^s$	$61^o39'34''$	2.63 ± 0.03	20.83 ± 0.66	7.38 ± 0.02	9.25 ± 0.13	5.76 ± 0.21
HOBYS 231734+611538	111.893	0.417	$23^h17^m34.1^s$	$61^o15'38''$	4.14 ± 0.15	131.24 ± 3.02	131.65 ± 1.06	189.23 ± 1.26	133.12 ± 1.02
HOBYS 231615+614022	111.893	0.858	$23^h16^m15.3^s$	$61^o40'22''$	0.57 ± 0.02	5.17 ± 0.33	4.89 ± 0.01	7.17 ± 0.08	4.33 ± 0.13
HOBYS 231609+614232	111.895	0.896	$23^h16^m09.2^s$	$61^o42'32''$	6.57 ± 0.04	44.17 ± 0.81	9.21 ± 0.03	11.95 ± 0.23	7.63 ± 0.32
HOBYS 231632+613858	111.917	0.824	$23^h16^m32.6^s$	$61^o38'58''$	11.71 ± 0.06	51.23 ± 0.64	2.34 ± 0.03	3.32 ± 0.15	2.33 ± 0.25
HOBYS 231641+613755	111.927	0.801	$23^h16^m41.5^s$	$61^o37'55''$	31.84 ± 0.04	103.24 ± 1.01	3.24 ± 0.03	4.95 ± 0.19	3.53 ± 0.30
HOBYS 231617+614555	111.930	0.943	$23^h16^m17.2^s$	$61^o45'55''$	10.54 ± 0.16	66.46 ± 1.20	4.43 ± 0.05	5.84 ± 0.28	3.70 ± 0.46
HOBYS 231853+605905	111.944	0.103	$23^h18^m53.2^s$	$60^o59'05''$	···	···	3.46 ± 0.09	3.93 ± 0.54	<1.67
HOBYS 231800+611637	111.948	0.414	$23^h18^m00.5^s$	$61^o16'37''$	···	···	3.19 ± 0.03	5.00 ± 0.17	3.55 ± 0.28
HOBYS 231903+605623	111.948	0.053	$23^h19^m03.5^s$	$60^o56'23''$	···	···	0.53 ± 0.03	···	···
HOBYS 231725+612948	111.961	0.644	$23^h17^m25.8^s$	$61^o29'48''$	20.14 ± 0.24	185.91 ± 3.23	44.63 ± 0.10	91.34 ± 0.73	78.21 ± 1.20
HOBYS 231630+614730	111.963	0.959	$23^h16^m30.0^s$	$61^o47'30''$	9.10 ± 0.06	63.44 ± 1.24	4.04 ± 0.05	6.98 ± 0.27	5.01 ± 0.44
HOBYS 231635+614547	111.963	0.928	$23^h16^m35.9^s$	$61^o45'47''$	4.40 ± 0.05	19.63 ± 0.90	2.83 ± 0.04	4.29 ± 0.22	2.91 ± 0.35
HOBYS 231719+613960	112.009	0.807	$23^h17^m19.2^s$	$61^o39'60''$	0.79 ± 0.02	3.92 ± 0.32	0.60 ± 0.01	0.96 ± 0.08	0.70 ± 0.12
HOBYS 231718+614120	112.015	0.829	$23^h17^m18.1^s$	$61^o41'20''$	7.53 ± 0.05	40.77 ± 0.94	5.80 ± 0.04	10.42 ± 0.26	7.88 ± 0.36
HOBYS 231735+613644	112.020	0.745	$23^h17^m35.9^s$	$61^o36'44''$	31.41 ± 0.10	133.38 ± 2.45	9.84 ± 0.07	19.33 ± 0.42	15.92 ± 0.71
HOBYS 231812+613102	112.054	0.630	$23^h18^m12.2^s$	$61^o31'02''$	1.24 ± 0.03	7.08 ± 0.67	4.69 ± 0.03	10.81 ± 0.23	8.94 ± 0.26
HOBYS 231903+611541	112.060	0.355	$23^h19^m03.0^s$	$61^o15'41''$	<0.0757	···	2.05 ± 0.06	3.24 ± 0.34	2.24 ± 0.55
HOBYS 231819+613049	112.066	0.622	$23^h18^m19.0^s$	$61^o30'49''$	···	<0.474	0.75 ± 0.01	1.52 ± 0.08	1.29 ± 0.12
HOBYS 231810+613432	112.072	0.686	$23^h18^m10.6^s$	$61^o34'32''$	5.53 ± 0.05	32.31 ± 1.01	5.35 ± 0.04	11.42 ± 0.21	9.31 ± 0.40
HOBYS 231805+613717	112.078	0.733	$23^h18^m05.3^s$	$61^o37'17''$	6.04 ± 0.06	28.23 ± 1.10	10.93 ± 0.03	19.83 ± 0.32	14.80 ± 0.41
HOBYS 231842+612623	112.083	0.537	$23^h18^m42.4^s$	$61^o26'23''$	···	···	2.06 ± 0.03	4.51 ± 0.18	3.84 ± 0.29
HOBYS 231832+613136	112.095	0.625	$23^h18^m32.3^s$	$61^o31'36''$	···	11.10 ± 1.52	19.34 ± 0.11	43.13 ± 0.31	38.14 ± 0.61
HOBYS 231809+613938	112.099	0.767	$23^h18^m09.0^s$	$61^o39'38''$	5.01 ± 0.04	18.89 ± 0.83	3.91 ± 0.03	7.42 ± 0.18	5.58 ± 0.30
HOBYS 231826+613416	112.100	0.671	$23^h18^m26.8^s$	$61^o34'16''$	0.98 ± 0.03	7.89 ± 0.65	1.22 ± 0.03	2.45 ± 0.15	1.94 ± 0.25
HOBYS 231906+612421	112.116	0.488	$23^h19^m06.2^s$	$61^o24'21''$	···	<2.42	7.88 ± 0.06	15.51 ± 0.34	12.51 ± 0.5
HOBYS 231848+613114	112.122	0.608	$23^h18^m48.0^s$	$61^o31'14''$	···	<0.0481	2.02 ± 0.02	4.46 ± 0.13	3.94 ± 0.21
HOBYS 231814+614156	112.122	0.799	$23^h18^m14.3^s$	$61^o41'56''$	0.47 ± 0.02	2.06 ± 0.33	1.04 ± 0.01	1.75 ± 0.08	1.23 ± 0.13
HOBYS 231849+613128	112.125	0.611	$23^h18^m49.0^s$	$61^o31'28''$	···	<0.619	2.58 ± 0.02	6.31 ± 0.14	5.71 ± 0.23
HOBYS 231817+614224	112.131	0.804	$23^h18^m17.8^s$	$61^o42'24''$	0.43 ± 0.02	1.80 ± 0.32	0.95 ± 0.01	1.57 ± 0.08	1.08 ± 0.12
HOBYS 231731+615901	112.144	1.095	$23^h17^m31.4^s$	$61^o59'01''$	18.55 ± 0.10	17.24 ± 2.94	58.26 ± 0.10	103.41 ± 1.01	81.77 ± 1.14

Continued on Next Page...

Table A.3 – Continued

Source ID	l	b	α_{2000}	δ_{2000}	$S_{70\mu m}$ [Jy]	$S_{160\mu m}$ [Jy]	$S_{250\mu m}$ [Jy]	$S_{350\mu m}$ [Jy]	$S_{500\mu m}$ [Jy]
HOBYS 231932+612052	112.145	0.416	$23^h19^m32.4^s$	$61°20'52''$	...	11.10 ± 2.73	12.81 ± 0.12	23.05 ± 0.63	18.63 ± 1.11
HOBYS 231821+614733	112.169	0.882	$23^h18^m21.5^s$	$61°47'33''$	0.34 ± 0.03	<0.302	2.51 ± 0.02	4.22 ± 0.12	3.12 ± 0.19
HOBYS 231816+614917	112.169	0.912	$23^h18^m16.3^s$	$61°49'17''$	0.26 ± 0.04	<2.41	8.43 ± 0.03	15.3 ± 0.2	11.5 ± 0.3

Table A.4: Source sizes, Luminosities, Temperatures and Masses For NGC 7538

ID	Size arcsec	Luminosity [$L_\odot$]	Temperature [K]	Mass [$M_\odot$]
HOBYS 231324+612056	12.51	74.08±3.70	18.64±0.48	417.00±20.85
HOBYS 231233+614718	13.51	96.54±4.83	19.75±0.49	575.91±28.80
HOBYS 231346+613327	11.98	90.01±4.50	15.98±0.50	506.83±25.34
HOBYS 231403+613315	11.98	59.73±2.99	9.20±0.46	294.47±14.72
HOBYS 231418+613200	13.51	108.83±5.44	20.98±0.50	623.48±31.17
HOBYS 231429+613127	11.98	71.55±3.58	17.31±0.47	326.25±16.31
HOBYS 231429+613505	13.51	103.18±5.16	15.86±0.49	587.79±29.39
HOBYS 231439+613204	28.20	1440.31±72.02	10.94±0.55	1065.41±53.27
HOBYS 231347+614921	110.88	603.57±30.18	25.20±0.46	2254.79±112.74
HOBYS 231353+614912	19.44	79.17±3.96	11.42±0.47	409.62±20.48
HOBYS 231459+613607	12.51	29.92±1.50	30.53±0.48	125.77±6.29
HOBYS 231503+613647	107.60	310.86±15.54	17.83±0.39	1000.49±50.02
HOBYS 231515+613442	11.98	54.15±2.71	15.53±0.48	103.55±5.18
HOBYS 231515+613731	16.15	59.10±2.95	10.33±0.52	145.55±7.28
HOBYS 231526+613422	23.12	28.82±1.44	18.30±0.41	169.74±8.49
HOBYS 231523+613830	29.78	102.85±5.14	14.99±0.45	314.58±15.73
HOBYS 231540+613446	12.51	25.66±1.28	19.53±0.48	84.10±4.21
HOBYS 231519+614137	22.84	70.00±3.50	9.64±0.48	211.40±10.57
HOBYS 231556+613137	13.51	24.75±1.24	16.69±0.43	83.89±4.19
HOBYS 231537+613814	11.98	24.09±1.20	18.94±0.55	62.21±3.11
HOBYS 231535+613921	20.74	74.89±3.74	10.69±0.53	126.82±6.34
HOBYS 231541+613743	11.98	26.20±1.31	20.57±0.53	58.70±2.93
HOBYS 231537+613947	30.21	19.87±0.99	30.50±0.02	223.99±11.20
HOBYS 231551+613550	11.98	10.15±0.51	18.02±0.40	52.65±2.63
HOBYS 231634+612304	41.80	336.05±16.80	10.94±0.55	359.96±18.00
HOBYS 231707+611305	13.51	25.50±1.28	15.79±0.44	47.67±2.38
HOBYS 231549+613725	21.36	59.24±2.96	25.69±0.43	120.70±6.04
HOBYS 231551+613656	31.68	29.55±1.48	17.92±0.40	144.81±7.24
HOBYS 231554+613607	46.24	30.99±1.55	20.50±0.02	274.08±13.70
HOBYS 231532+614256	54.04	45.61±2.28	22.50±0.02	126.52±6.33
HOBYS 231607+613233	25.28	37.26±1.86	27.02±0.40	80.53±4.03
HOBYS 231552+613747	55.59	75.04±3.75	17.57±0.38	331.59±16.58
HOBYS 231555+613707	42.42	125.24±6.26	18.99±0.45	187.92±9.40
HOBYS 231556+613734	31.48	151.35±7.57	10.94±0.55	158.25±7.91
HOBYS 231604+613610	21.05	67.08±3.35	10.81±0.54	70.74±3.54
HOBYS 231549+614059	13.51	43.41±2.17	11.19±0.56	26.65±1.33
HOBYS 231550+614205	18.41	9.30±0.47	17.66±0.38	43.13±2.16
HOBYS 231610+613626	12.51	39.06±1.95	36.72±0.59	22.38±1.12
HOBYS 231628+613216	11.98	8.82±0.44	13.20±0.46	16.38±0.82
HOBYS 231559+614153	38.21	299.21±14.96	29.10±0.45	114.72±5.74
HOBYS 231643+612831	12.51	9.84±0.49	19.20±0.46	17.94±0.90
HOBYS 231834+605331	31.48	7.93±0.40	18.69±0.43	57.91±2.90
HOBYS 231604+614143	22.55	8.46±0.42	17.06±0.35	44.28±2.21
HOBYS 231609+614021	28.89	80.76±4.04	14.31±0.47	67.22±3.36
HOBYS 231613+613934	14.44	5.67±0.28	15.50±0.02	23.17±1.16
HOBYS 231734+611538	38.55	116.61±5.83	18.99±0.45	91.97±4.60
HOBYS 231615+614022	23.40	265.41±13.27	19.31±0.47	44.98±2.25
HOBYS 231609+614232	11.98	3.09±0.15	17.83±0.39	12.95±0.65
HOBYS 231632+613858	20.10	5.12±0.26	16.44±0.32	34.80±1.74
HOBYS 231641+613755	21.36	40.77±2.04	19.42±0.47	47.96±2.40
HOBYS 231617+614555	17.69	0.38±0.02	27.50±0.02	30.62±1.53
HOBYS 231853+605905	27.26	9.51±0.48	13.50±0.02	54.82±2.74
HOBYS 231800+611637	82.50	···	16.50±0.02	120.47±6.02
HOBYS 231903+605623	35.19	145.76±7.29	19.75±0.49	99.72±4.99
HOBYS 231725+612948	28.66	6.32±0.32	25.50±0.02	62.41±3.12
HOBYS 231630+614730	51.19	13.51±0.68	17.66±0.38	135.38±6.77
HOBYS 231635+614547	13.51	8.50±0.42	11.72±0.59	14.18±0.71
HOBYS 231719+613960	29.56	418.59±20.93	11.86±0.59	55.60±2.78
HOBYS 231718+614120	32.09	12.77±0.64	18.50±0.02	49.11±2.46
HOBYS 231735+613644	11.98	14.44±0.72	20.09±0.50	10.37±0.52
HOBYS 231812+613102	23.95	183.41±9.17	11.86±0.59	40.24±2.01
HOBYS 231903+611541	118.77	633.14±31.66	15.79±0.44	766.62±38.33

Continued on Next Page...

Table A.4 – Continued

ID	Size arcsec	Luminosity [$L_\odot$]	Temperature [K]	Mass [$M_\odot$]
HOBYS 231819+613049	32.50	70.11±3.51	14.75±0.49	67.45±3.37
HOBYS 231810+613432	30.43	13.14±0.66	17.53±0.48	67.05±3.35
HOBYS 231805+613717	33.87	311.89±15.59	13.75±0.49	64.49±3.22
HOBYS 231842+612623	24.49	25.72±1.29	19.20±0.46	21.00±1.05
HOBYS 231832+613136	27.97	5.87±0.29	18.50±0.02	35.46±1.77
HOBYS 231809+613938	34.44	74.44±3.72	10.45±0.52	48.68±2.43
HOBYS 231826+613416	44.37	210.80±10.54	12.13±0.61	76.16±3.81
HOBYS 231906+612421	44.81	114.27±5.71	31.32±0.57	48.43±2.42
HOBYS 231848+613114	40.21	40.17±2.01	22.50±0.02	19.92±1.00
HOBYS 231814+614156	38.21	1936.98±96.85	10.69±0.53	50.27±2.51
HOBYS 231849+613128	35.01	133.08±6.65	19.86±0.49	73.49±3.67
HOBYS 231817+614224	23.68	5.04±0.25	21.50±0.02	24.22±1.21
HOBYS 231731+615901	16.15	3.12±0.16	14.50±0.02	8.68±0.43
HOBYS 231932+612052	28.20	···	16.50±0.02	9.16±0.46
HOBYS 231821+614733	43.18	196.35±9.82	10.57±0.53	69.49±3.47
HOBYS 231816+614917	57.55	44.09±2.20	20.50±0.02	106.99±5.35

Bibliography

Agnese P., Cigna C., Pornin J., Accomo R., Bonnin C., Colombel N., Delcourt M., Doumayrou E., Lepennec J., Martignac J., Reveret V., Rodriguez L., Vigroux L. G., 2003, in Presented at the Society of Photo-Optical Instrumentation Engineers (SPIE) Conference, Vol. 4855, T. G. Phillips & J. Zmuidzinas , ed, Society of Photo-Optical Instrumentation Engineers (SPIE) Conference Series, p. 108

Allen L., Gould's Belt Team , 2006, in Bulletin of the American Astronomical Society, Vol. 38, Bulletin of the American Astronomical Society, p. 1204

Alves J., Lombardi M., Lada C. J., The mass function of dense molecular cores and the origin of the IMF, 2007, A&A, 462, L17

André P. et al., From filamentary clouds to prestellar cores to the stellar IMF: Initial highlights from the Herschel Gould Belt Survey, 2010, A&A, 518, L102

André P., Motte F., Bacmann A., Discovery of an Extremely Young Accreting Protostar in Taurus, 1999, ApJ, 513, L57

Andre P., Ward-Thompson D., Barsony M., Submillimeter continuum observations of Rho Ophiuchi A - The candidate protostar VLA 1623 and prestellar clumps, 1993, ApJ, 406, 122

Andre P., Ward-Thompson D., Barsony M., From Prestellar Cores to Protostars: the Initial Conditions of Star Formation, 2000, Protostars and Planets IV, 59

Bacmann A., André P., Puget J., Abergel A., Bontemps S., Ward-Thompson D., An ISOCAM absorption survey of the structure of pre-stellar cloud cores, 2000, A&A, 361, 555

Balbus S. A., Enhanced Angular Momentum Transport in Accretion Disks, 2003, ARA&A, 41, 555

Balbus S. A., Hawley J. F., A powerful local shear instability in weakly magnetized disks. I - Linear analysis. II - Nonlinear evolution, 1991, ApJ, 376, 214

Ballesteros-Paredes J., Klessen R. S., Mac Low M., Vazquez-Semadeni E., Molecular Cloud Turbulence and Star Formation, 2007, Protostars and Planets V, 63

Beetz M., Elsaesser H., Weinberger R., Poulakos C., Several H II regions in the near infrared, 1976, A&A, 50, 41

Benjamin R. A., Churchwell E., Babler B. L., Bania T. M., Clemens D. P., Cohen M., Dickey J. M., Indebetouw R., Jackson J. M., Kobulnicky H. A., Lazarian A., Marston A. P., Mathis J. S., Meade M. R., Seager S., Stolovy S. R., Watson C., Whitney B. A., Wolff M. J., Wolfire M. G., GLIMPSE. I. An SIRTF Legacy Project to Map the Inner Galaxy, 2003, PASP, 115, 953

Bertin E., Arnouts S., SExtractor: Software for source extraction., 1996, A&AS, 117, 393

Beuther H., Henning T., Multiple low-turbulence starless cores associated with intermediate- to high-mass star formation, 2009, A&A, 503, 859

Binney J., Tremaine S., 1987, Galactic dynamics. Cambridge University Press

Campbell B., Thompson R. I., Star formation in the NGC 7538 molecular cloud - Near-infrared and radio spectroscopy, 1984, ApJ, 279, 650

Cantalupo C. M., Borrill J. D., Jaffe A. H., Kisner T. S., Stompor R., MADmap: A Massively Parallel Maximum Likelihood Cosmic Microwave Background Map-maker, 2010, ApJS, 187, 212

Carpenter J. M., Snell R. L., Schloerb F. P., Skrutskie M. F., Embedded star clusters associated with luminous IRAS point sources, 1993, ApJ, 407, 657

Cernicharo J., Gonzalez-Alfonso E., Lefloch B., 1997, in ESA Special Publication, Vol. 419, A. M. Heras, K. Leech, N. R. Trams, & M. Perry , ed, The first ISO workshop on Analytical Spectroscopy, p. 23

Cesaroni R., 2005, in IAU Symposium, Vol. 227, R. Cesaroni, M. Felli, E. Churchwell, & M. Walmsley , ed, Massive Star Birth: A Crossroads of Astrophysics, p. 59

Cesarsky C. J. et al., ISOCAM in flight., 1996, A&A, 315, L32

Chandrasekhar S., Fermi E., Problems of Gravitational Stability in the Presence of a Magnetic Field., 1953, ApJ, 118, 116

Chapin E. L. et al., The Balloon-borne Large Aperture Submillimeter Telescope (BLAST) 2005: A 4 deg^2 Galactic Plane Survey in Vulpecula (l = 59deg), 2008, ApJ, 681, 428

Chattopadhyay G., Glenn J., Bock J. J., Rownd B. K., Caldwell M., Griffin M. J., Feed horn coupled bolometer arrays for spire-design, simulations, and measurements, 2003, IEEE Transactions on Microwave Theory Techniques, 51, 2139

Chen H., Grenfell T. G., Myers P. C., Hughes J. D., Comparison of Star Formation in Five Nearby Molecular Clouds, 1997, ApJ, 478, 295

Chen H., Myers P. C., Ladd E. F., Wood D. O. S., Bolometric temperature and young stars in the Taurus and Ophiuchus complexes, 1995, ApJ, 445, 377

Clegg P. E. et al., The ISO Long-Wavelength Spectrometer., 1996, A&A, 315, L38

Cohen R. S., Cong H., Dame T. M., Thaddeus P., Molecular clouds and galactic spiral structure, 1980, ApJ, 239, L53

Dale J. E., Davies M. B., Collisions and close encounters involving massive main-sequence stars, 2006, MNRAS, 366, 1424

De Graauw T., Caux E., Guesten R., Helmich F., Pearson J., Phillips T. G., Schieder R., Tielens X., Saraceno P., Stutzki J., Wafelbakker C. K., Whyborn N. D., 2005, in Bulletin of the American Astronomical Society, Vol. 37, Bulletin of the American Astronomical Society, p. 1219

De Graauw T. et al., Observing with the ISO Short-Wavelength Spectrometer., 1996, A&A, 315, L49

Dehaes S., Bauwens E., Decin L., Eriksson K., Raskin G., Butler B., Dowell C. D., Ali B., Blommaert J. A. D. L., Structure of the outer layers of cool standard stars, 2009, ArXiv e-prints

Di Francesco J., Johnstone D., Kirk H., MacKenzie T., Ledwosinska E., The SCUBA Legacy Catalogues: Submillimeter-Continuum Objects Detected by SCUBA, 2008, ApJS, 175, 277

Dickel H. R., Dickel J. R., Wilson W. J., The molecular cloud associated with NGC 7538, 1981, ApJ, 250, L43

Dowell , others , 2003, Spectral and Photometric Imaging Receiver (SPIRE) Observers' Manual,
http://www.jach.hawaii.edu/JACpublic/JCMT/User_documentation/Users_guide/guide/guide.html

Draine B. T., Li A., Infrared Emission from Interstellar Dust. IV. The Silicate-Graphite-PAH Model in the Post-Spitzer Era, 2007, ApJ, 657, 810

Dreyer J., A new generation catalogue of nebulae and clusters of stars, 1888, MNRAS, 49, 1

Dunlop J. S. et al., The BLAST 250-micron selected galaxy population in GOODS-South, 2009, ArXiv e-prints

Dunne L., Eales S., Edmunds M., Ivison R., Alexander P., Clements D. L., The SCUBA Local Universe Galaxy Survey - I. First measurements of the submillimetre luminosity and dust mass functions, 2000, MNRAS, 315, 115

Egan M. P., Shipman R. F., Price S. D., Carey S. J., Clark F. O., Cohen M., A Population of Cold Cores in the Galactic Plane, 1998, ApJ, 494, L199

Evans N. J., Dunham M. M., Jørgensen J. K., Enoch M. L., Merín B., van Dishoeck E. F., Alcalá J. M., Myers P. C., Stapelfeldt K. R., Huard T. L., Allen L. E., Harvey P. M., van Kempen T., Blake G. A., Koerner D. W., Mundy L. G., Padgett D. L., Sargent A. I., The Spitzer c2d Legacy Results: Star-Formation Rates and Efficiencies; Evolution and Lifetimes, 2009, ApJS, 181, 321

Fazio G. G. et al., The Infrared Array Camera (IRAC) for the Spitzer Space Telescope, 2004, ApJS, 154, 10

Feast M. W., Thackeray A. D., Wesselink A. J., The brightest stars in the Magellanic Clouds, 1960, MNRAS, 121, 337

Fischer J., Klaassen T., Hovenier N., Jakob G., Poglitsch A., Sternberg O., Cryogenic Far-Infrared Laser Absorptivity Measurements of the Herschel Space Observatory Telescope Mirror Coatings, 2004, Appl. Opt., 43, 3765

Garay G., Faúndez S., Mardones D., Bronfman L., Chini R., Nyman L., Discovery of Four New Massive and Dense Cold Cores, 2004, ApJ, 610, 313

Gardner F. F., Milne D. K., Mezger P. G., Wilson T. L., The Carina nebula at 6 cm., 1970, A&A, 7, 349

Gardner J. P. et al., The James Webb Space Telescope, 2006, Space Sci. Rev., 123, 485

Goldsmith P. F., Langer W. D., Molecular cooling and thermal balance of dense interstellar clouds, 1978, ApJ, 222, 881

Gomez H., others , Submillimeter variability of eta carinae: Cool dust within the outer ejecta, 2009, MNRAS

Griffin M. J. et al., The Herschel-SPIRE instrument and its in-flight performance, 2010, ArXiv e-prints

Griffin M. J., Orton G. S., The near-millimeter brightness temperature spectra of Uranus and Neptune, 1993, Icarus, 105, 537

Gutermuth R. A., Bourke T. L., Allen L. E., Myers P. C., Megeath S. T., Matthews B. C., Jørgensen J. K., Di Francesco J., Ward-Thompson D., Huard T. L., Brooke T. Y., Dunham M. M., Cieza L. A., Harvey P. M., Chapman N. L., The Spitzer Gould Belt Survey of Large Nearby Interstellar Clouds: Discovery of a Dense Embedded Cluster in the Serpens-Aquila Rift, 2008a, ApJ, 673, L151

Gutermuth R. A., Myers P. C., Megeath S. T., Allen L. E., Pipher J. L., Muzerolle J., Porras A., Winston E., Fazio G., Spitzer Observations of NGC 1333: A Study of Structure and Evolution in a Nearby Embedded Cluster, 2008b, ApJ, 674, 336

Hackwell J. A., Grasdalen G. L., Gehrz R. D., 10 and 20 micron images of regions of star formation, 1982, ApJ, 252, 250

Hall J. S., Observations of the Polarized Light from Stars, 1949, Science, 109, 166

Hawley J. F., Balbus S. A., A Powerful Local Shear Instability in Weakly Magnetized Disks. II. Nonlinear Evolution, 1991, ApJ, 376, 223

Herbig G. H., Eruptive phenomena in early stellar evolution, 1977a, ApJ, 217, 693

Herbig G. H., Radial velocities and spectral types of T Tauri stars, 1977b, ApJ, 214, 747

Hildebrand R., The determination of cloud masses and dust characteristics from sub-millimeter thermal emission, 1983, QJRAS, 24, 267

Hill T., Motte F., Didelon P., Bontemps S., Minier V., Andre P., Arzoumanian D., Bernard J., Hennemann M., Nguyen-Loung Q., Peretto N., Roussel H., Schneider N., Sousbie T., Filaments and Ridges in Vela C revealed by Herschel: from low-mass to high-mass star forming sites, 2011, A & A, 109, 165

Hillenbrand L. A., On the Stellar Population and Star-Forming History of the Orion Nebula Cluster, 1997, AJ, 113, 1733

Hiltner W. A., Polarization of Light from Distant Stars by Interstellar Medium, 1949, Science, 109, 165

Hoare M. G., Kurtz S. E., Lizano S., Keto E., Hofner P., Ultracompact Hii Regions and the Early Lives of Massive Stars, 2007, Protostars and Planets V, 181

Holland W. et al., 2006, in Society of Photo-Optical Instrumentation Engineers (SPIE) Conference Series, Vol. 6275, Society of Photo-Optical Instrumentation Engineers (SPIE) Conference Series

Holland W. S., Duncan W., Kelly B. D., Irwin K. D., Walton A. J., Ade P. A. R., Robson E. I., 2003, in Society of Photo-Optical Instrumentation Engineers (SPIE) Conference Series, Vol. 4855, T. G. Phillips & J. Zmuidzinas , ed, Society of Photo-Optical Instrumentation Engineers (SPIE) Conference Series, p. 1

Holland W. S., Robson E. I., Gear W. K., Cunningham C. R., Lightfoot J. F., Jenness T., Ivison R. J., Stevens J. A., Ade P. A. R., Griffin M. J., Duncan W. D., Murphy J. A., Naylor D. A., SCUBA: a common-user submillimetre camera operating on the James Clerk Maxwell Telescope, 1999, MNRAS, 303, 659

Houck J. R. et al., The Infrared Spectrograph (IRS) on the Spitzer Space Telescope, 2004, ApJS, 154, 18

Jeans J. H., 1929, The universe around us. Cambridge University Press

Jessop N. E., Ward-Thompson D., A far-infrared survey of molecular cloud cores, 2000, MNRAS, 311, 63

Jones B. F., Herbig G. H., Proper motions of T Tauri variables and other stars associated with the Taurus-Auriga dark clouds, 1979, AJ, 84, 1872

Joy A. H., T Tauri Variable Stars., 1945, ApJ, 102, 168

Kessler M. F., Steinz J. A., Anderegg M. E., Clavel J., Drechsel G., Estaria P., Faelker J., Riedinger J. R., Robson A., Taylor B. G., Ximénez de Ferrán S., The Infrared Space Observatory (ISO) mission., 1996, A&A, 315, L27

Keto E., The Formation of Massive Stars: Accretion, Disks, and the Development of Hypercompact H II Regions, 2007, ApJ, 666, 976

Kirk J., SExtractor: Software for source extraction., 2010, A&AS, 117, 393

Kirk J., Ward-Thompson D., Andre P.., 2005, MNRAS, 360, 1506

Kirk J. M., Ward-Thompson D., André P., The initial conditions of isolated star formation - VII. Spitzer mapping of pre-stellar cores, 2007, MNRAS, 375, 843

Kraft S., Merken P., Creten Y., Putzeys J., Van Hoof C. A., Katterloher R. O., Rosenthal D., Rumitz M., Groezinger U., Hofferbert R., Beeman J. W., 2001, in Presented at the Society of Photo-Optical Instrumentation Engineers (SPIE) Conference, Vol. 4540, H. Fujisada, J. B. Lurie, & K. Weber , ed, Society of Photo-Optical Instrumentation Engineers (SPIE) Conference Series, p. 374

Kurtz S., Cesaroni R., Churchwell E., Hofner P., Walmsley C. M., Hot Molecular Cores and the Earliest Phases of High-Mass Star Formation, 2000, Protostars and Planets IV, 299

Lada C. J., Lada E. A., Embedded Clusters in Molecular Clouds, 2003, ARA&A, 41, 57

Larson R. B., Turbulence and star formation in molecular clouds, 1981, MNRAS, 194, 809

Lemke D. et al., ISOPHOT - capabilities and performance., 1996, A&A, 315, L64

Lopez J. A., Meaburn J., The Structure and Dynamics of the CARINAE-1 / Keyhole / Region in the Carina Nebula, 1984, Revista Mexicana de Astronomia y Astrofisica, 9, 119

Madden S. C., Galliano F., Jones A. P., Sauvage M., ISM properties in low-metallicity environments, 2006, A&A, 446, 877

Mathis J. S., Interstellar dust and extinction, 1990, ARA&A, 28, 37

Mathis J. S., Rumpl W., Nordsieck K. H., The size distribution of interstellar grains, 1977, ApJ, 217, 425

Matthews H., 2003, The James Clerk Maxwell Telescope: User Guide, http://www.jach.hawaii.edu/JACpublic/JCMT/User_documentation/Users_guide/guide/guide.html

McKee C. F., Ostriker E. C., Theory of Star Formation, 2007, ARA&A, 45, 565

McKee C. F., Tan J. C., The Formation of Massive Stars from Turbulent Cores, 2003, ApJ, 585, 850

Megeath S. T., Cox P., Bronfman L., Roelfsema P. R., Evidence for ongoing star formation in the Carina nebula., 1996, A&A, 305, 296

Mengel J. G., Demarque P., Sweigart A. V., Gross P. G., Stellar evolution from the zero-age main sequence, 1979, ApJS, 40, 733

Men'shchikov A., et al. , In prep, 2010, aap

Menten K. M., Pillai T., Wyrowski F., 2005, in IAU Symposium, Vol. 227, R. Cesaroni, M. Felli, E. Churchwell, & M. Walmsley , ed, Massive Star Birth: A Crossroads of Astrophysics, p. 23

Menten K. M., Reid M. J., Forbrich J., Brunthaler A., The distance to the Orion Nebula, 2007, A&A, 474, 515

Mestel L., Spitzer L., Jr., Star formation in magnetic dust clouds, 1956, MNRAS, 116, 503

Mezger P. G., Altenhoff W., Schraml J., Burke B. F., Reifenstein E. C., III, Wilson T. L., A New Class of Compact H II Regions Associated with OH Emission Sources, 1967, ApJ, 150, L157

Mortier A. M. J. et al., The SCUBA Half-Degree Extragalactic Survey - I. Survey motivation, design and data processing, 2005, MNRAS, 363, 563

Motte F. et al., Initial highlights of the HOBYS key program, the Herschel imaging survey of OB young stellar objects, 2010, A&A, 518, L77

Mouschovias T. C., Nonhomologous contraction and equilibria of self-gravitating, magnetic interstellar clouds embedded in an intercloud medium: Star formation. II - Results, 1976, ApJ, 207, 141

Muench A. A., Alves J., Lada C. J., Lada E. A., Evidence for Circumstellar Disks around Young Brown Dwarfs in the Trapezium Cluster, 2001, ApJ, 558, L51

Müller T. G., Lagerros J. S. V., Asteroids as calibration standards in the thermal infrared for space observatories, 2002, A&A, 381, 324

Murphy T., Cohen M., Ekers R. D., Green A. J., Wark R. M., Moss V., Ultra- and hyper-compact HII regions at 20 GHz, 2010, MNRAS, 405, 1560

Netterfield C. B. et al., BLAST: The Mass Function, Lifetimes, and Properties of Intermediate Mass Cores from a 50 deg^2 Submillimeter Galactic Survey in Vela (ell 265deg), 2009, ApJ, 707, 1824

Neugebauer G. et al., The Infrared Astronomical Satellite (IRAS) mission, 1984, ApJ, 278, L1

Nguyen H. T. et al., HerMES: The SPIRE confusion limit, 2010, A&A, 518, L5

Nielbock M., Chini R., Hoffmeister V. H., Scheyda C. M., Steinacker J., Nürnberger D., Siebenmorgen R., The Morphology of M17-UC1: A Disk Candidate Surrounding a Hypercompact H II Region, 2007, ApJ, 656, L81

Nyrén M., Anzeige des Todes von Otto Wilhelm Struve, 1905, Astronomische Nachrichten, 168, 77

Ossenkopf V., Henning T., Dust opacities for protostellar cores, 1994, A&A, 291, 943

Palla F., Stahler S. W., The Pre-Main-Sequence Evolution of Intermediate-Mass Stars, 1993, ApJ, 418, 414

Pascale E. et al., The Balloon-borne Large Aperture Submillimeter Telescope: BLAST, 2008, ApJ, 681, 400

Patanchon G. et al., SANEPIC: A Mapmaking Method for Time Stream Data from Large Arrays, 2008, ApJ, 681, 708

Pearson J. C., Guesten R., Klein T., Whyborn N. D., 2000, in Presented at the Society of Photo-Optical Instrumentation Engineers (SPIE) Conference, Vol. 4013, J. B. Breckinridge & P. Jakobsen , ed, Society of Photo-Optical Instrumentation Engineers (SPIE) Conference Series, p. 264

Pedro G.-L., Bruno M., Miguel S.-P., Kidger M., 2003, Herschel Observers Manual, http://herschel.esac.esa.int/Docs/Herschel/html/observatory.html

Perault M. et al., First ISOCAM images of the Milky Way., 1996, A&A, 315, L165

Pilbratt G. L., Riedinger J. R., Passvogel T., Crone G., Doyle D., Gageur U., Heras A. M., Jewell C., Metcalfe L., Ott S., Schmidt M., Herschel Space Observatory - An ESA facility for far-infrared and submillimetre astronomy, 2010, ArXiv e-prints

Poglitsch A. et al., The Photodetector Array Camera and Spectrometer (PACS) on the Herschel Space Observatory, 2010, ArXiv e-prints

Povich M. S., Smith N., Majewski S. R., Getman K. V., Townsley L. K., Babler B. L., Broos P. S., Indebetouw R., Meade M. R., Robitaille T. P., Stassun K. G., Whitney B. A., Yonekura Y., Fukui Y., A Pan-Carina Young Stellar Object Catalog: Intermediate-mass Young Stellar Objects in the Carina Nebula Identified Via Mid-infrared Excess Emission, 2011, ApJS, 194, 14

Reid C. M., Borrill J. D., Jaffe A. H., Kisner T. S., Stompor R., Herschel's First Look at the Massive Satr Formation Region NGC 7538, 2011, ApJS, 187, 212

Reid M. A., Wilson C. D., High-Mass Star Formation. I. The Mass Distribution of Submillimeter Clumps in NGC 7538, 2005a, ApJ, 625, 891

Reid M. A., Wilson C. D., High-Mass Star Formation. I. The Mass Distribution of Submillimeter Clumps in NGC 7538, 2005b, apj, 625, 891

Rieke G. H. et al., The Multiband Imaging Photometer for Spitzer (MIPS), 2004, ApJS, 154, 25

Rivera-Ingraham A. et al., The BLAST View of the Star-forming Region in Aquila (ell = 45 deg, b = 0 deg), 2010, ApJ, 723, 915

Roy A. et al., The Balloon-borne Large Aperture Submillimeter Telescope (BLAST) 2005: A 10 deg^2 Survey of Star Formation in Cygnus X, 2011, ApJ, 727, 114

Salpeter E. E., The Luminosity Function and Stellar Evolution., 1955, ApJ, 121, 161

Sandell G., Sievers A., Submillimeter Continuum Observations of NGC 7538, 2004, ApJ, 600, 269

Saraceno P., Andre P., Ceccarelli C., Griffin M., Molinari S., An evolutionary diagram for young stellar objects., 1996, A&A, 309, 827

Shirley Y. L., Evans N. J., II, Rawlings J. M. C., Gregersen E. M., Tracing the Mass during Low-Mass Star Formation. I. Submillimeter Continuum Observations, 2000, ApJS, 131, 249

Shu F. H., Self-similar collapse of isothermal spheres and star formation, 1977, ApJ, 214, 488

Shu F. H., Adams F. C., Lizano S., Star formation in molecular clouds - Observation and theory, 1987, ARA&A, 25, 23

Sibthorpe B. et al., AKARI and BLAST Observations of the Cassiopeia A Supernova Remnant and Surrounding Interstellar Medium, 2009, ArXiv e-prints

Smith N., Brooks K., 2008, The Carina Nebula: A Laboratory for Feedback and Triggered Star Formation.

Smith N., Egan M. P., Carey S., Price S. D., Morse J. A., Price P. A., Large-Scale Structure of the Carina Nebula, 2000a, ApJ, 532, L145

Smith N., Egan M. P., Carey S., Price S. D., Morse J. A., Price P. A., Large-Scale Structure of the Carina Nebula, 2000b, ApJ, 532, L145

Smith N., NASA , Team T. H. H., The carina nebula, 2007, MNRAS

Smith N., Povich M. S., Whitney B. A., Churchwell E., Babler B. L., Meade M. R., Bally J., Gehrz R. D., Robitaille T. P., Stassun K. G., Spitzer Space Telescope observations of the Carina nebula: the steady march of feedback-driven star formation, 2010a, MNRAS, 406, 952

Smith N., Povich M. S., Whitney B. A., Churchwell E., Babler B. L., Meade M. R., Bally J., Gehrz R. D., Robitaille T. P., Stassun K. G., Spitzer Space Telescope observations of the Carina nebula: the steady march of feedback-driven star formation, 2010b, MNRAS, 406, 952

Soifer B. T., Neugebauer G., Houck J. R., The IRAS view of the extragalactic sky, 1987, ARA&A, 25, 187

Sturm E., Lutz D., Genzel R., Sternberg A., Egami E., Kunze D., Rigopoulou D., Bauer O. H., Feuchtgruber H., Moorwood A. F. M., de Graauw T., ISO-SWS spectroscopy of ARP 220: a highly obscured starburst galaxy., 1996, A&A, 315, L133

Stutzki J., Guesten R., High spatial resolution isotopic CO and CS observations of M17 SW - The clumpy structure of the molecular cloud core, 1990, ApJ, 356, 513

Swinyard B. M. et al., In-flight calibration of the Herschel-SPIRE instrument, 2010, ArXiv e-prints

Swinyard B. M., Dohlen K., Ferand D., Baluteau J., Pouliquen D., Dargent P., Michel G., Martignac J., Ade P. A. R., Hargrave P. C., Griffin M. J., Jennings D. E., Caldwell M. E., 2003, in Presented at the Society of Photo-Optical Instrumentation Engineers (SPIE) Conference, Vol. 4850, J. C. Mather , ed, Society of Photo-Optical Instrumentation Engineers (SPIE) Conference Series, p. 698

Tachihara K., Onishi T., Mizuno A., Fukui Y., Statistical study of $C^{18}O$ dense cloud cores and star formation, 2002, A&A, 385, 909

The P. S., Bakker R., Antalova A., Studies of the Carina Nebula. IV - A new determination of the distances of the open clusters TR 14, TR 15, TR 16 and CR 228 based on Walraven photometry, 1980, A&AS, 41, 93

Thronson H. A., Jr., Harper D. A., Compact H II regions in the far-infrared, 1979, ApJ, 230, 133

Tovmassian H.., 1995, RevMexAA (Serie de Conferencias), 2, 83

Truch M. D. P., 2007, Ph.D. thesis, Brown University

Truch M. D. P. et al., 2007, in Bulletin of the American Astronomical Society, Vol. 38, Bulletin of the American Astronomical Society, p. 945

Truch M. D. P. et al., The Balloon-borne Large Aperture Submillimeter Telescope (BLAST) 2006: Calibration and Flight Performance, 2009, ApJ, 707, 1723

Trumpler R. J., Observational Evidence of a Relativity Red Shift in Class O Stars, 1935, PASP, 47, 249

van Altena W. F., Lee J. T., Lee J., Lu P. K., Upgren A. R., The velocity dispersion of the Orion Nebula cluster., 1988, AJ, 95, 1744

Van der Tak F. F. S., Menten K. M., Very compact radio emission from high-mass protostars. II. Dust disks and ionized accretion flows, 2005, A&A, 437, 947

Verschuur G. L., Measurements of Magnetic Fields in Interstellar Clouds of Neutral Hydrogen, 1969, ApJ, 156, 861

Visser A. E., Richer J. S., Chandler C. J., Completion of a SCUBA Survey of Lynds Dark Clouds and Implications for Low-mass Star Formation, 2002, AJ, 124, 2756

Walborn N. R., 1995, in Revista Mexicana de Astronomia y Astrofisica Conference Series, Vol. 2, V. Niemela, N. Morrell, & A. Feinstein , ed, Revista Mexicana de Astronomia y Astrofisica Conference Series, p. 51

Ward-Thompson D., André P., 1999, in ESA Special Publication, Vol. 427, P. Cox & M. Kessler , ed, The Universe as Seen by ISO, p. 463

Ward-Thompson D., Kirk J. M., Crutcher R. M., Greaves J. S., Holland W. S., André P., First Observations of the Magnetic Field Geometry in Prestellar Cores, 2000, ApJ, 537, L135

Ward-Thompson D., Scott P. F., Hills R. E., Andrģravee P., A Submillimetre Continuum Survey of Pre Protostellar Cores, 1994, MNRAS, 268, 276

Werner M. W., Becklin E. E., Gatley I., Matthews K., Neugebauer G., Wynn-Williams C. G., An infrared study of the NGC 7538 region, 1979a, MNRAS, 188, 463

Werner M. W., Becklin E. E., Gatley I., Matthews K., Neugebauer G., Wynn-Williams C. G., An infrared study of the NGC 7538 region, 1979b, MNRAS, 188, 463

Williams J. P., Blitz L., McKee C. F., The Structure and Evolution of Molecular Clouds: from Clumps to Cores to the IMF, 2000, Protostars and Planets IV, 97

Williams J. P., de Geus E. J., Blitz L., Determining structure in molecular clouds, 1994, ApJ, 428, 693

Woody D. P., Scott S. L., Scoville N. Z., Mundy L. G., Sargent A. I., Padin S., Tinney C. G., Wilson C. D., Interferometric observations of 1.4 millimeter continuum sources, 1989, ApJ, 337, L41

Yorke H. W., The dynamical evolution of H II regions - Recent theoretical developments, 1986, ARA&A, 24, 49

Young C. H. et al., A "Starless" Core that Isn't: Detection of a Source in the L1014 Dense Core with the Spitzer Space Telescope, 2004, ApJS, 154, 396

Zinnecker H., McCaughrean M. J., Wilking B. A., 1993, in E. H. Levy & J. I. Lunine , ed, Protostars and Planets III, p. 429

Zinnecker H., Yorke H. W., Toward Understanding Massive Star Formation, 2007, ARA&A, 45, 481

Zuckerman B., Evans N. J., II, Models of massive molecular clouds, 1974, ApJ, 192, L149

Zuckerman B., Palmer P., Radio radiation from interstellar molecules, 1974, ARA&A, 12, 279